HETEROEPITAXY OF InN ON SILICON (111) AND R-PLANE SAPPHIRE SUBSTRATES

DOCTOR OF PHILOSOPHY (PhD) DISSERTATION

ADEBOWALE OLUFUNSO AJAGUNNA

DEPARTMENT OF PHYSICS, UNIVERSITY OF CRETE
HERAKLION, 2011

Doctor of Philosophy (Ph.D) Dissertation

Heteroepitaxy of InN on silicon (111) and r-plane sapphire substrates

By

ADEBOWALE OLUFUNSO AJAGUNNA

Advisory Committee:

Alexandros Georgakilas (Advisor)
Professor, Physics Department, University of Crete

Nikos Flytzanis
Professor, Physics Department, University of Crete

Zekentes Konstantinos
Principal Researcher, Institute of Electronic Structure and Laser, FORTH

Examination Committee:

Alexandros Georgakilas
Professor, Physics Department, University of Crete

Nikos Flytzanis
Professor, Physics Department, University of Crete

Zekentes Konstantinos
Principal Researcher, Institute of Electronic Structure and Laser, FORTH

Panos Tzanetakis
Professor, Physics Department, University of Crete

Zaharias Chatzopoulos
Associate Professor, Physics Department, University of Crete

Thomas Kehagias
Associate Professor, Physics Department, Aristotle University of Thessaloniki

Eleftherios Iliopoulos
Assistant Professor, Physics Department, University of Crete

Department of Physics, University of Crete, Heraklion, Greece

June 2011

To

My wife

Bola

My Kids

Precious, Pleasant and Peace

who together bore the brunt of my long absence from home

and

The Almighty God

(Mt. 28:20b)

ABSTRACT

Among the group-III nitride (III-N) semiconductors, InN has been the least studied and also the most complex. However, InN is a promising material for sub-THz electronic devices due to the very high values of its electron low-field mobility (14,000 cm^2/V.s) and maximum drift velocity (5.2 x 10^7 cm/s). InN and InN-rich alloys are also very interesting for optoelectronic devices in the IR wavelength region of telecommunications, as well as tandem solar cell applications, due to its 0.65 eV bandgap. This PhD dissertation is based on the study of plasma assisted molecular beam epitaxy (PAMBE) of InN on Si (111) and *r*-plane $(1\bar{1}02)$ sapphire substrates. Epitaxial growth on silicon is interesting for low cost production and/or monolithic integration with Si integrated circuits (ICs). Growth of *a*-plane InN on *r*-plane $(1\bar{1}02)$ sapphire substrates can be used for realizing quantum well heterostructures, free from polarization induced electric fields. Also, it has been theoretically predicted that nitrogen stabilized non-polar surfaces could be free from electron accumulation.

Direct InN growth on Si (111), using the optimum conditions for InN growth on GaN (0001) – substrate temperature 400-450°C and stoichiometric III/V flux ratio – results to 3D growth mode and porous columnar InN epilayers with bad adhesion at the InN/Si interface. A two-step growth process was developed, consisting of nucleating a very thin InN layer on Si at low temperature under N-rich growth conditions, and the growth of the main epilayer at the optimum InN (0001) growth conditions. The fast coalescence of the initial 3D islands of InN results to a continuous 20 nm InN film on the Si (111) surface with low 10 x 10 μm^2 AFM rms surface roughness of 0.4 nm, which allows the main epilayer to be overgrown in step-flow growth mode, achieving an atomically smooth surface. The fast coalescence also assists defects annihilation near the InN/Si interface and 0.5 μm films exhibited threading dislocation (TD) density of $4.0x10^9$ cm^{-2} for the edge-type and $1.7x10^9$ cm^{-2} for the screw-type TDs. Similar defect densities were determined by TEM for InN films grown after initial deposition of an AlN/GaN nucleation layer on Si. However, those films exhibited significantly better electron mobility and lower crystal mosaicity according to XRD rocking curves.

The experiments of InN growth on *r*-plane $(1\bar{1}02)$ Al_2O_3 substrates revealed that different InN crystallographic orientations could be realized depending on the InN nucleation conditions. Single crystal cubic (001) InN was grown on *r*-plane sapphire by using one-step growth at ~ 400°C, while polar *c*-plane (0001) or semipolar *s*-plane $(10\bar{1}1)$ InN were observed by using a two-step growth process with InN nucleation at low temperature under N-rich or near stoichiometric III/V flux ratio conditions, respectively. Pure *a*-plane $(11\bar{2}0)$ InN films were realized only when *a*-plane GaN or AlN nucleation-buffer layers were initially grown on *r*-plane sapphire. The structural quality of the *a*-plane InN films improved with increasing epilayer thickness, which is attributed to interaction and annihilation of defects. However, the growth of *a*-plane InN proceeds in 3D growth mode resulting to increasing surface roughness with increasing film thickness. A comparative study of the thickness dependent electrical properties of *a*-plane InN films grown on *r*-plane Al_2O_3 and *c*-plane films grown on GaN/Al_2O_3 (0001) templates was carried out by room temperature Hall-effect measurements. For both InN orientations, a rather linear increase of the electron sheet density (N_S) with increasing thickness, consistent with a constant bulk concentration around 1 x 10^{19} cm^{-3} was observed. However, the electron

mobilities of the *c*-plane InN films were more than three times those of the *a*-plane films, attributed to the presence of higher dislocation density (1.4 x 10^{11} cm^{-2}) in the *a*-plane InN films. The analysis of the Hall-effect measurements, by considering the contribution of two conducting layers, indicates a similar accumulation of low mobility electrons with $N_S > 10^{14}$ cm^{-2} at the films' surface/interfacial region for both the *a*- and *c*-plane InN films. In general, similar electron concentrations were measured for all the different orientation InN films (polar *c*-plane, non-polar *a*-plane, semi-polar *s*-plane and cubic (001) InN). This suggests that similar surface/interfacial electron accumulation occurs independently of the InN crystallographic orientation, and the bulk donors are not related to the threading dislocations, since significant variations of defect densities occur for the different InN orientations. A SIMS investigation of a *c*-plane InN film exhibiting electron concentration of 1.09 x 10^{20} cm^{-3} excludes hydrogen as the possible donor since its concentrations was $6.5x10^{18}$ cm^{-3}. Only oxygen approached a concentration level near 10^{20} cm^{-3} and this might be the unintentionally incorporated donor.

Finally, the spontaneous growth of InN nanopillars (NPs) on Si (111) and *r*-plane sapphire substrates was investigated. Optimization of the different growth parameters resulted to well-separated (0001) InN NPs on Si (111) that exhibited photoluminescence. Almost in all cases, the growth rate of the InN NPs along the *c*-axis is multiple of the In-limited growth rate. A non-uniform amorphous Si_xN_y layer was inevitable under unoptimised growth conditions, leading to frequently observed NP misorientation (tilt) on Si substrates. Only *c*-axis oriented InN NPs were formed on the *r*-plane sapphire substrates.

In conclusion, the thesis has created new scientific knowledge for the heteroepitaxy of InN on Si (111) and $(1\bar{1}02)$ sapphire. Comparison with *c*-plane InN grown on GaN (0001) allowed the generic characteristics of InN to be extracted from the orientation-dependent ones.

ACKNOWLEDGEMENTS

My sincere gratitude goes foremost to my Advisor, Professor Alexandros Georgakilas, for giving me the privilege and benefits of working with him. I am extremely fortunate to have him as my supervisor. His keen interest in me, encouragements, motivation, support and guidance has made the completion of my doctoral studies possible.

I could not have carried out my research work without the help and support of my current and former MBE colleagues: Adam Adikimenakis, Manos Dimakis and George Tsiakatouras. Many thanks to Ms. Katerina Tsagaraki, who characterized most of my samples by scanning electron microscope (SEM), atomic force microscope (AFM) and X-ray diffractometer (XRD), and also taught me how to operate the AFM and XRD. My appreciation goes also to Ms. Maria Androulidaki, for the optical transmittance and photoluminescence measurements, as well as to Ms. Maria Kayambaki, for the capacitance-voltage (C-V) and current-voltage (I-V) measurements of my specimens. The invaluable comments and discussions with Professor Elefterios Iliopoulos and his help in many circumstances have also contributed in no little way to this research work. I will like to acknowledge the support of Dr. George Konstadinidis and Thanasis Kostopoulos regarding the fabrication of the devices. Special thanks to Ms. Marina Tzanakaki for her invaluable support administratively. I particularly would like to thank Messrs. Nikos Papadakis and Mihalis Sfendourakis for technical support at various times during the period of this work. I would like to express my appreciation to all members of the microelectronics research group (MRG) for their friendship and help all through the years. I will not forget the times we spent together. I wish you all the very best in your endeavours.

My deep appreciation to Professors Philomena Komninou, Thomas Kehagias and George Dimitrakopulos, as well as Ms. Andy Lotsari, from the Nanostructured Materials Microscopy Group (NMMG) of the Physics department at the Aristotle University of Thessaloniki, for the transmission electron microscopy (TEM) observations of some of my specimens.

I would like to thank my wife, Bola Ajagunna, and my kids for their perpetual love, patience, support and understanding during the course of this work. My deepest gratitude goes to my parents; Adebamibo and Rachael Ajagunna, for their encouragements and supports and to my siblings; Otuns, Obakemis, Benjamins and Oladejos, for their love and prayers. My gratitude also goes to my friends; Johnson and Bose Omisope, Biodun and Bisi Oloye, John Adesoye, Titi Ojeaga, Alexander and Eleni Melirrytou, Dinos and Debbie Roussos, Tom and Sheryl Black, all the brethren of Heraklion Church of Christ and Grace Covenant Centre, for their invaluable prayers and supports.

Finally, this doctoral thesis could not have been possible without the combined support, financially and otherwise, of the Greek State Scholarship Foundation (IKY) and Nigerian Federal Scholarship Board (FSB), under the Bilateral Education Agreement of Nigeria and Greece (BEA Scholarship). A research fellowship supported by the MORGAN (European Commission's FP7) project of the Institute of Electronic Structure and Laser (IESL, FORTH) was very important for the completion of this thesis. Finally, the Marie Curie RTN PARSEM (European Commission's FP6) assisted collaboration and scientific interaction with the University of Thessaloniki and other European groups is also gratefully acknowledged.

TABLE OF CONTENTS

Abstract --i

Acknowledgements ---iii

Table of Contents --iv

List of abbreviations --xi

Preface --xii

Chapter 1 Introduction --1

1.1 Historical review of the III-Nitride semiconductors' family ……………….2

1.2 Brief History of Indium Nitride (InN) ………………………………………5

1.3 Important properties and potential applications of InN and Alloys…………6

1.4 Objectives of the thesis ……………………………………………………..11

Chapter 2 Growth and Characterization Techniques of InN -----------------18

2.1 Introduction…………………………………………………………………..…19

2.2 InN Growth techniques…………………………………………………....19

2.2.1 Molecular Beam Epitaxy (MBE)…………………………………..…19

2.3 Characterization techniques…………………………………………….…26

2.3.1 Reflection high energy electron diffraction (RHEED)……………..…...26

2.3.2 X-ray Diffraction (XRD)……………………………………………….…28

2.3.3 Atomic Force Microscopy (AFM)………………………………….....31

2.3.4 Electron Microscopy (EM)…………………………………………..32

2.3.4.1 Scanning Electron Microscopy (SEM)………………………32

2.3.4.2 Transmission Electron Microscopy (TEM)………………….33

2.3.5 Electrical Measurement Techniques……………………………....34

2.3.5.1 Hall-Effect Measurements……………………………………34

2.3.5.2 Capacitance-Voltage Measurements (EC-V)………………...35

2.3.6 Optical measurement Techniques……………………………………………36

2.3.6.1 Photoluminescence (PL)……………………………………………..36

2.3.6.2 Optical Transmittance ……………………………………………….36

2.4 Concluding remarks………………………………………………………….37

Chapter 3 Background of the Molecular Beam Epitaxy (MBE) of InN------43

3.1 Epitaxial growth of InN: Substrates for InN epitaxy……………………….44

3.1.1 Sapphire substrates……………………………………………………..44

3.1.2 Silicon (111) substrates ……………………………………………..45

3.2 Epitaxial growth process…………………………………………..…..46

3.2.1 Growth modes in heteroepitaxy……………………………………..47

3.3 Substrates' surface preparations ……………………………………49

3.4 Determination of III/V flux ratio……………………………………49

3.5 Estimation of the MBE growth temperature ………………………..50

3.6 InN growth properties………………………………………………50

3.7 InAlN growth properties……………………………………………..52

3.8 Concluding remarks…………………………………………………52

Chapter 4 InN and InN/InAlN heterostructures on GaN/Al_2O_3 (0001)------- 55

4.1 Introduction……………………………………………………………..56

4.2 Experimental procedures……………………………………………….56

4.3 Morphological investigation…………………………………………………57

4.4 Structural characterisation of the films by HR-XRD………………………..60

4.5 Electrical characterisation of InN films………………………………….…..64

4.6 Origin of bulk donors in InN………………………………………….…..…65

4.7 Optical studies of (0001) InN layers……………………………….……..66

4.7.1 Low temperature photoluminescence measurements……….…………66

4.7.2 Optical transmittance measurements…………………………………..67

4.8 Growth of InAlN and InN based device heterostructures……………………68

4.9 Investigation of InN-rich InAlN Schottky diodes……………………………71

4.10 Growth of InN/InAlN heterostructures………………………………………73

4.11 Concluding remarks…………………………………………………………77

Chapter 5 Growth of InN on *r*-plane ($1\bar{1}02$) sapphire substrates -------------82

5.1 Introduction: Why non-polar III-nitrides?... 83

5.2 Experimental descriptions……………………………………………………84

5.3 The role of buffer layer on InN grown on *r*-plane sapphire………………….85

5.4 Effect of Growth Temperature (T_{sub}) on *a*-plane InN grown on *r*-plane sapphire……………………………………………………………………93

5.5 Effect of III/V flux ratio on *a*-plane InN grown on *r*-plane sapphire………..98

5.6 Effect of *in-situ* intermittent surface nitridation of *a*-plane InN during growth………………………………………………………………….102

5.7 Thickness dependence of the properties of *a*-plane InN grown by MBE…..104

5.7.1 Objective of the study and experimental procedures……………….104

5.7.2 Surface Morphology characterisation…………………………….....105

5.7.3 Structural properties analyses……………………………………....107

5.7.4 Structural Anisotropy investigation………………………………...109

5.7.5 Electrical properties investigation of *a*-plane and *c*-plane InN films.109

5.7.5.1 Hall-effect Measurements study of the InN films……….……….110

5.7.5.2 Modelling and analysis of the electrical properties of *a*-plane InN ..111

5.7.6 Optical properties investigation of *a*-plane InN…………………….115

5.7.6.1 Photoluminescence measurements of *a*-plane InN…………………116

5.7.6.2 Transmittance measurements of *a*-plane InN………………………116

5.8 Growth and properties of 3 μm thick *a*-plane InN grown on *r*-plane sapphire…………………………………………………………………..118

5.10 Microstructure of *a*-plane InN films on *r*-plane sapphire substrates……....123

5.11 Concluding remarks……………………………………………………...126

Chapter 6 Epitaxy of cubic (002) InN, polar (0001) InN and semipolar ($10\bar{1}1$) InN on *r*-plane ($1\bar{1}02$) sapphire substrates -------------------------132

6.1 Background knowledge and importance of semipolar InN ………………...133

6.2 Experimental descriptions………………………………………………..133

6.3 *In-situ* reflection high electron energy diffraction investigation………… ...134

6.4 X-ray diffraction Analyses ………………………………………………....136

6.5 Investigation of the surface morphology……………………………..…..139

6.6 Transmission electron microscopy investigations……………………..……141

6.6.1 Microstructures of the *c*-plane InN layer on *r*-plane sapphire substrate ……………………………………………………………………141

6.6.2 Microstructures of the *s*-plane InN layer on *r*-plane sapphire substrate ……………………………………………………………………142

6.7 Investigation of the electrical properties of the films……………………….145

6.8 Investigation of the optical properties of the films……………………….....145

6.9 Concluding remarks………………………………………………….…..146

Chapter 7 Nucleation and buffer layers for InN on Si (111) heteroepitaxy------149

7.1 Review of earlier work on InN/Si (111) epitaxy and Si surface properties...150

7.2 Investigation of single-step growth of InN on Si (111): Role of III/V flux ratio ………………………………………………………………………151

7.3 Study of two-step growth of InN on Si (111): Role of intermediate layer….159

7.4 TEM Study of InN film grown on Si (111) using GaN/AlN buffer layer…..163

7.5 Investigation of the role of thick GaN layer on the properties of InN film grown on Si (111) using GaN/AlN double buffer layer…………………….…167

7.6 Concluding remarks……………………………………………………...172

Chapter 8 Optimisation of InN nucleation for direct heteroepitaxy on Si-------176

8.1 Introduction to direct InN epitaxy on Silicon substrates…………………...177

8.2 Study of InN nucleation on Si (111) substrates…………………………….178

8.3 Heteroepitaxy of InN on Si (111) using different nucleation layers (NLs)..187

8.4 Transmission electron microscopy study of InN-on-Si (111) heterostructures ……………………………………………………………………………196

8.5 Concluding remarks……………………………………………………...201

Chapter 9 Growth of InN Nanopillars on Si (111) and *r*-plane ($1\bar{1}02$) Al_2O_3 substrates ---204

9.0 Introduction to InN Nanostructures……………………………………...205

9.1 Initial experiment on the spontaneous growth of InN NPs on Si (111)…….206

9.2 Investigation of the role of III/V flux ratio on InN NPs properties (N-flux constant)…………………………………………………………….…210

9.3 Investigation of the role of III/V flux ratio on InN NPs properties (In-flux constant)………………………………………………………………….211

9.4 The role of AlN nucleation layer on InN NPs properties (In-flux constant)..216

9.5 Conclusions for PAMBE growth of InN NPs on Si (111)………………….219

9.6 Growth of InN nanopillars on *r*-plane sapphire substrates…………………220

9.7 Concluding remarks……………………………………………………...224

Chapter 10 Summary of results ---228

10.1 Preamble…………………………………………………………………….229

10.2 InN and InN/InAlN heterostructures on GaN/Al_2O_3 (0001)………………..229

10.2.1 InN (0001) films on (0001) GaN/Al_2O_3 (0001)…………………….……229

10.2.2 InN/InAlN heterostructures on (0001) GaN/Al_2O_3 (0001)…………..…230

10.3 InN on *r*-plane ($1\bar{1}02$) sapphire substrates…………………………………230

10.3.1 The role of buffer layer on InN growth on *r*-plane sapphire………..230

10.3.2 Growth of *a*-plane InN grown on *r*-plane sapphire………………….231

10.3.3 Thickness dependent electrical properties of *a*-plane InN………..…232

10.4 InN films on Si (111) substrates……………………………………………232

10.4.1 Nucleation and buffer layers for InN on Si (111) heteroepitaxy……232

10.4.2 Optimisation of InN nucleation for direct heteroepitaxy on Si (111).232

10.5 InN Nanopillars on Si (111) and *r*-plane ($1\bar{1}02$) Al_2O_3 substrates…………….233

10.6 General conclusion for InN heteroepitaxial films……………………………..233

10.7 Possible future works………………………………………………………234

Appendices 235

Appendix 1 Physical parameters of Hexagonal InN, GaN and AlN 236

Appendix 2 List of peer-reviewed Publications in International Journals 238

Appendix 3 List of peer-reviewed Abstracts in International Conferences 239

Appendix 4 List of Invited Talks 243

LIST OF ABBREVIATIONS

2D or 3D	Two- or three-dimensional
2-DEG	Two-dimensional electron gas
III-N	III-nitride
III-face	Metal-faced
AFM	Atomic force microscopy
B-M	Burstein-Moss
BSFs	Basal plane stacking faults
CBE	Conduction band edge
CBED	Convergent beam electron diffraction
CBM	Conduction band minimum
CTEM	Conventional transmission electron microscopy
C-V	Capacitance-voltage
E_B	Branch point energy
ECR-MBE	Cyclotron resonance plasma-assisted molecular beam epitaxy
ECV	Electrochemical capacitance-voltage
E_g	Band gap
EM	Electron Microscopy
ETD	Edge type dislocation
FE-SEM	Field-emission scanning electron microscopy
FFT	Fast fourier transform
F_{In}	In flux
F_N	Flux of reactive nitrogen species
FWHM	Full-width at half maximum
HEMT	High electron mobility transistor
HFET	Heterojunction field-effect transistors
HJ	Heterojunction
HREELS	High-resolution electron-energy-loss spectroscopy
HRTEM	High resolution transmission electron microscopy

HR-XRD	High resolution X-ray diffraction
ICs	Integrated circuits
IDBs	Inversion domain boundaries
I-V	Current-voltage
LD	Laser diode
LED	Light emitting diode
LM	Lattice mismatch
LT-InN	Low temperature InN
N-face	Nitrogen faced
MBE	Molecular beam epitaxy
ML	Monolayer
MOVPE	Metal-organic vapour phase epitaxy
MQW	Multi-quantum well
NL	Nucleation layer
NPs	Nanopillars
PAMBE	Plasma assisted molecular beam epitaxy
PDs	Photodiodes
PL	Photoluminescence
P_{sp}	Spontaneous polarization
P_{pz}	Piezoelectric polarization
QDs	Quantum dots
RC	Rocking curve
RF	Radio frequency
RHEED	Reflection high energy electron diffraction
RT	Room temperature
SAED	Selected-area electron diffraction
sccm	Standard cubic centimetres per minute
SF	Stacking fault
SIMS	Secondary ion mass spectrometry

SL	Superlattice
STD	Screw threading dislocation
T	Transmittance
TM	Thermal expansion mismatch
T_{sub}	Growth or substrate temperature
UHV	Ultrahigh vacuum
UV	Ultraviolet
VBM	Valence band maximum
VPE	Vapour phase epitaxy
XTEM	Cross-sectional transmission electron microscopy

PREFACE

Group-III heterostructures of polar, semipolar and non-polar orientations have become very popular within the last decade due to their applications in the fabrication of highly efficient blue-green light-emitting diodes (LEDs), blue-violet laser diodes, solar-blind UV detectors, sensors and high performance power microwave transistors [1,2]. Recently, unprecedented attention has been drawn to the growth and characterisation of InN being a promising material for sub-THz electronic devices due to its very high values of low field mobility and maximum drift velocity of electrons [3,4]. The discovery [5,6] of lower than 1.9 eV bandgap for InN that approaches ~0.65 eV [7,8] has also widen the coverage of InN alloys (InGaN, InGaAlN and InAlN) over the electromagnetic spectrum from 0.65 to 0.62 eV; a feat expected to drive technological advancement in optoelectronic devices technology. However, before the use of InN for optical and electronic device applications we must understand and improve the heteroepitaxial growth, as well as the properties of InN.

In this thesis, growth of InN heterostructures was performed by nitrogen plasma assisted molecular beam epitaxy technique (PAMBE). The main objective of the research was to understand and control the growth and properties of InN-based heterostructures and nanostructures on new substrates and crystallographic orientations, such as Al_2O_3 $(1\bar{1}02)$ (*r*-plane) and Si (111). Comparisons of this work with the InN heteroepitaxy on GaN (0001) pseudo-substrates could identify the intrinsic/native InN properties and distinguish the influence of different lattice-mismatched substrates and growth processes used in InN heteroepitaxy. It was also aimed to advance our understanding for the growth and properties of InN-rich InAlN alloys' and to explore the growth of InN/InAlN heterostructures device applications, such as high electron mobility transistors (HEMTs).

The thesis was therefore focussed on the PAMBE growth and characterization of polar and non-polar InN heterostructures on sapphire and Si substrates. The surface morphology, structural, electrical and optical properties of the InN heterostructures were investigated. The characterization techniques included Normasky optical microscopy, atomic force microscopy (AFM), field-emission scanning electron microscopy (FE-SEM), high resolution X-ray diffraction (HR-XRD), Hall-effect, electrochemical capacitance-voltage (ECV), transmittance (TM) and photoluminescence (PL) measurements. Conventional and high resolution transmission electron microscopy (CTEM and HRTEM) investigations were also carried out on selected samples by collaborators from the Physics Department of Aristotle University of Thessaloniki.

The dissertation is outlined as follows: Chapter 1 deals with introduction to the InN and III-nitride semiconductor compounds and their general properties. The description of different experimental techniques, with emphasis on the PAMBE growth and the material characterisation methods employed in this work are outlined in Chapter 2. Epitaxial growth processes and preview of earlier work on InN shall be the focus of Chapter 3. The growth of InN and InAlN films and device heterostructures on GaN/Al_2O_3 (0001) substrates are discussed in Chapter 4. The experiments of InN growth on *r*-plane sapphire substrates and the characterisation results, including the study of the thickness dependent properties of *a*-plane InN with comprehensive comparison with the properties of *c*-plane InN of similar film

thicknesses, are discussed in Chapters 5 and 6. Chapter 7 concerns the growth of InN on Si (111) and the investigation of the effects of different III-nitride buffer/nucleation layers; while Chapter 8 will go further to discuss the optimization of growth conditions for direct InN-on-Si epitaxy (without intermediate layers of other III-nitrides like AlN). The study of the growth of InN nanopillars on Si (111) is articulated in Chapter 9 while the general conclusions of the dissertation are summarised in Chapter 10.

The growth experiments with PAMBE were carried out in the research laboratory of the Microelectronics Research Group (MRG) of the Institute of Electronic Structure and Laser (IESL) of the Foundation for Research and Technology-Hellas (FORTH) and the Physics department of the University of Crete at Heraklion-Crete. All the research equipment used for the studies belongs to the MRG laboratory, except of the CTEM and HRTEM microscopes that belong to the Physics Department laboratories of the Aristotle University of Thessaloniki.

References

1. O Ambacher, *J. Phys. D: Appl. Phys.* **31**, 2653–2710 (1998)
2. A. G. Bhuiyan, A. Hashimoto, A. Yamamoto, *J. Appl. Phys*. **94**, 2790 (2003).
3. B. R. Nag, *J. Cryst. Growth* **269**, 35 (2004)
4. V. M. Polyakov and F. Schwierz, *Appl. Phys. Lett*. **88**, 032101 (2006)
5. V. Yu. Davydov, A.A. Klochikhin, R.P. Seisyan, V.V. Emtsev, S.V. Ivanov, F. Bechstedt, J. Furthmüller, H. Harima, A.V. Mudryi, J. Aderhold, O. Semchinova, J. Graul, *Phys. Status Solidi (b)* **229**, R1 (2002)
6. J. Wu, W. Walukiewicz, K. M. Yu, J. W. Ager III, E. E. Haller, H. Lu, W. Schaff, Y. Saito, Y. Nanishi, *Appl. Phys. Lett.* **80**, 3967 (2002)
7. A. Georgakilas, in "*CAS 2008 Proceedings*" IEEE, 43 (2008)
8. E. Dimakis, *Ph.D Thesis*, Physics Department, University of Crete, Heraklion-Greece (2007)

1 Introduction

1.1 Historical review of the III-Nitride semiconductors' family

1.2 Brief History of Indium Nitride (InN)

1.3 Important properties and potential applications of InN and Alloys

1.4 Objectives of the thesis

1.1 Historical review of the III-Nitride semiconductors' family

The III-nitride (III-N) semiconductors' family belongs to the general III-V semiconductor's family, which combines elements of the group III and group V of the periodic table to form III-V compounds in binary, ternary or quarternary forms. They consist of the group-III arsenides, phosphines, nitrides, and antimonides. The III–V binary compounds are formed between the cations B, Al, Ga, In and the anions N, P, As and Sb. These semiconductor compounds possess a range of properties that are suitable for the most demanding electronic and optoelectronic technologies. The III-N semiconductors basically consist of the binary compounds InN, GaN and AlN and their alloys, and are usually of wurzite-structure (α-phase) [1], although they may also exist in cubic-phase (β-phase) like GaAs and InP with zincblende structure. Under ambient conditions, the wurzite is the thermodynamically stable structure for bulk AlN, GaN, and InN [2]. The cubic zincblende and the rocksalt or NaCl structure are possible metastable structures. The zincblende structure for GaN and InN could be stabilized by their epitaxial growth as thin films on (001) crystal planes of cubic substrates like Si, MgO, and GaAs [3,4] while the wurtzite polytype easily forms on (111) and (0001) crystal planes; following the crystallographic compatibility of the substrates' surface planes. The third rocksalt (or NaCl) structure can be induced in AlN, GaN, and InN at very high pressures [3,5,6].

In both the wurtzite and zincblende structures, each nitrogen atom is coordinated by four group III atoms and vice versa, making each atom the centre of a tetrahedron [7], as shown for the wurzite structure in Fig. 1.1(a). The main difference between the hexagonal and cubic structures occurs in the stacking sequence of the closest packed diatomic planes. For the wurtzitic structure, the stacking sequence of (0001) planes is ABABAB in the <0001> direction. For the zincblende structure, the stacking sequence of (111) planes is ABCABC in the <111> direction. The nature of the bonding is predominantly covalent with some ionic character. The cohesive energy per bond in the wurtzite crystal structure is 2.88 eV, 2.20 eV and 1.98 eV for AlN, GaN, InN, respectively [8,9].

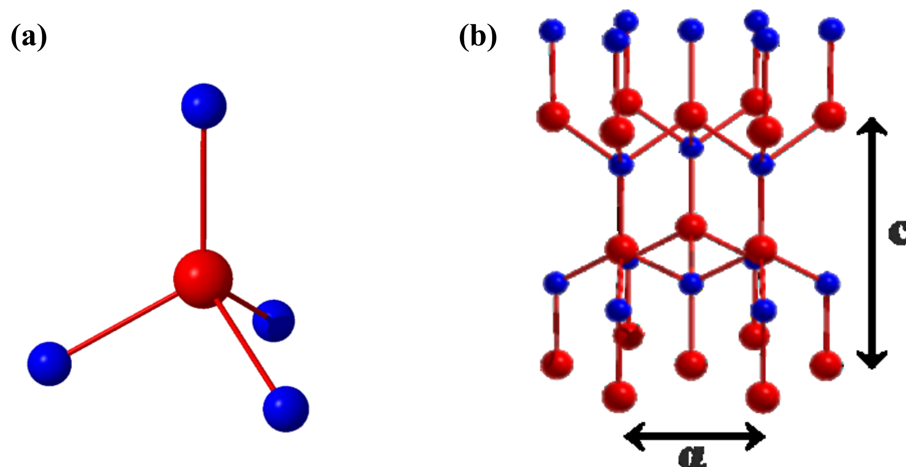

Figure 1.1 *Schematic diagrams showing (a) the tetrahedral bonding of the III-nitrides. Each group III atom (larger sphere) is coordinated by four nitrogen atoms (smaller sphere) and vice versa, which also holds for both wurzite and zincblende structures and (b) a wurzite structure with the c and a lattice constants designated.*

In a crystal lattice, the three lattice distances *a*, *b*, and *c,* which are used to denote the size of the unit cell in three dimensions, are referred to as the lattice constants. The cubic structure has only one lattice parameter, *a*, since the unit cell exhibits similar length in all sides, that is $a = b = c$. However, the hexagonal (wurtzite) crystal structure is defined by $a = b \neq c$ and therefore has only two lattice constants *a* and *c* [Fig. 1.1(b)]. '*c*' corresponds to the [0001] axis along the stacking direction while '*a*' is defined in the (0001) hexagonal closest packed planes perpendicular to the *c*-axis. The room temperature lattice parameters for the hexagonal and cubic structures of GaN, InN, and AlN as well as the hexagonal structures' internal parameter *u*, which is the anion-cation bond length along the [0001] axis, are summarised in Table 1.1. The different ionic radii of In, Ga and Al lead to the different lattice constants, bandgaps, and binding energies exhibited by InN, GaN and AlN [9]. The lattice constant values of III-nitrides may be also influenced by the growth conditions, impurity concentrations and film stoichiometry [10]. For example, the lattice constants of GaN grown with higher growth rates were found to be larger and an expansion of the lattice was observed in GaN heavily doped with Zn and Mg [3].

Table 1.1 Lattice constants of the cubic and hexagonal binary III-nitrides: AlN, GaN and InN. The hexagonal internal parameters (*u*) and the energy gaps (eV) of the nitrides are also given in the table.

	Hexagonal		Cubic	Internal parameter *u*	Energy gap (eV)	
	a(Å)	*c*(Å)	*a*(Å)		Hexagonal	Cubic
AlN	3.112 [11]	4.982 [11]	4.38 [13]	1.601 [11]	6.2 [14]	4.9 [13]
GaN	3.189 [11]	5.185 [11]	4.52 [13]	1.626 [11]	3.39 [15]	3.2 [13]
InN	3.525 [12]	5.705 [12]	4.98 [13]	1.612 [12]	0.65 [12]	0.56 [16]

Most III-nitride films and devices are grown on other substrates, such as silicon carbide (SiC), Si, and sapphire, since single crystals of InN, GaN and AlN are either not available or difficult to synthesise and very expensive. These substitute substrates usually result to high levels of extended defects, film strain, unintentional incorporation of impurities and point defects. The large mismatch of the in-plane lattice constants of III-nitrides, compared to those of the commonly used substrates, leads to the formation of extended defects, with densities up to five orders of magnitude higher than in other semiconductors [17]. Vertical lattice constant (*c*) mismatch has also been found to create additional crystalline defects, including inversion domain boundaries and stacking faults [18]. A high residual strain is typically present in the heteroepitaxial III-nitride films due to different thermal expansion coefficient of substrate and epilayer; leading also to micro-cracks and other defects on cooling down the sample after growth.

The thermal expansion coefficients perpendicular to *c*-axis of AlN, GaN and InN at 560 - 600K have already been reported [9,18,19] as 5.3×10^{-6} K^{-1}, 5.0×10^{-6} K^{-1} and 5.7×10^{-6} K^{-1} while 4.4×10^{-6} K^{-1}, 4.4×10^{-6} K^{-1} and 3.7×10^{-6} K^{-1} hold for the parallel to *c*-axis, respectively.

A notable feature of III-nitride materials is that devices may operate efficiently despite a high density of defects in the range up to 10^{10} cm^{-2} [20]. However, the

presence of these defects still affects the electronic and optical properties and limits the efficiency and lifetime of the devices [21]. This underscores the need to understand their defects' microstructure, formation mechanisms and ways of eliminating or reducing the defect density.

The common growth direction of wurzitic III nitrides is normal to the {0001} basal plane with atoms arranged in two closely spaced hexagonal bilayers A and B. Each bilayer consists of an atomic layer of cations and anions. Both wurzite and zincblende III-nitrides structures lack inversion symmetry and exhibit polar axes, the [0001] and <111>, respectively; depending on the atoms that terminate a bulk crystal surface, which could either be metal-faced (III-face) or nitrogen faced (N-face) as shown in Fig. 1.2. 'Metal-face' does not have the same meaning as 'metal-terminated', which gives a description of the actual surface structure or reconstruction [9]. Polarity affects the surface and bulk properties of nitrides, in terms of spontaneous polarization and etching, as well as some as-grown properties like defect incorporation during growth and the surface morphology. The presence of polarity results to the existence of spontaneous polarization (P_{sp}) charges and as a consequence, electric fields [22], which result to band bending and modify the carrier distribution. In the absence of strain, P_{sp} manifests as polarization charge at surface and hetero-interfaces of all III-nitride films and could be expressed as

$$P_{sp} = P_{sp}\, z \qquad (1.1)$$

However, as a result of the unavoidable residual strain that is generated in the III-nitride materials, due to lattice and thermal expansion mismatches with the substrate materials, 'piezoelectric polarization (P_{pz})' with direction dependent on the strain type (compressive or tensile) and the film's polarity will develop. This polarization could be expressed as

$$P_{pz}= e_{33}\varepsilon_z + e_{31}(\varepsilon_x +\varepsilon_y) \qquad (1.2)$$

where $\varepsilon_z = (c - c_o)/c_o$ is the strain along c-axis and $\varepsilon_x = \varepsilon_y = (a - a_o)/a_o$ is the in-plane strain, assumed to be isotropic, while c_o and a_o are are the equilibrium values of the lattice parameters [9,22]. The constants e_{31} and e_{33} are piezoelectric constants of the III-nitride.

The total polarization in the absence of external electric fields becomes

$$P = P_{sp} + P_{pz} \qquad (1.3)$$

Polarization could adversely affect III-nitride optoelectronic devices by developing electric fields which modify the band edges in heterostructures, leading to quantum confined Stark effect (in quantum well) or Franz-Keldysh effects (in uniform bulk semiconductors). However, polarization could also provide an advantage in the formation of two-dimensional electron gas (2-DEG) at interfaces (upper or lower) of nitride-based heterostructures without the use of doping, making possible the fabrication of high electron mobility transistor (HEMT) devices.

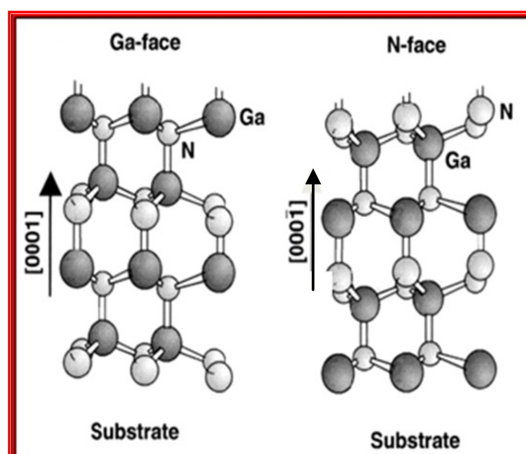

Figure 1.2 *Typical Ga-face and N-face wurzite structure showing the atomic arrangement of GaN atoms (Figure from O. Ambacher 1998 [10]).*

The potential of nitrides in the fabrication of optoelectronic and micro/nano-electronic devices has been widely reported [9,23-26]. A number of cutting-edge technologies and a vast area of applications has already been realized with group III-nitride compound semiconductors and their alloys [4,9]. The driving force for III-nitride semiconductors' research is device applications for emitters and detectors in the visible and ultraviolet (UV) regions of the optical spectrum and high-power RF amplifiers. In addition, using different proportions of metallic elements in the synthesis of the ternary or quaternary nitride alloys, the III-nitride semiconductors can provide a wide range of available band gaps for efficiently converting the broad solar spectrum into electricity, by tandem solar cell devices. The energy gaps of the basic nitride family comprising of InN, GaN, and AlN are stated in Table 1.1. Some other important properties that have accrued great importance to nitride materials are their high mechanical and thermal stability (for wide bandgaps) chemical inertness and radiation hardness [10], which make the III-nitrides significant materials for applications in harsh environment.

1.2 Brief History of Indium Nitride (InN)

InN is a very important member of the III-nitride semiconductors' family [27]. The study of InN began as early as 1938 [28]. Development in InN synthesis was slow [29,30] because direct interaction of metallic indium and nitrogen molecules in an inactivated form does not take place, even at rather high temperatures [31]. The extremely high dissociation pressure of InN [32-35] (or extremely high equilibrium vapor pressure of nitrogen [36,37]) does not permit use of very high temperatures for InN synthesis. During those early days of InN study, powder or small crystals of InN could only be realised. Hovel and Cuomo first reported the synthesis of InN with improved characteristics in 1972 [34]. Nevertheless, the inability to grow good crystal quality material deflected interest away from it; being polycrystalline and consisting of significant oxygen contamination [38,39]. The films also exhibited high free electron concentrations in the range of 10^{19} - 10^{21} cm^3, with corresponding relatively low electron mobility of less than 100 cm^2/Vs [39].

Up to the late 90's, InN was mainly synthesised by sputtering and the fundamental properties of InN have been the major focus. The earlier accepted intrinsic properties of InN were unavoidably determined from the consequently formed low quality materials. InN was evaluated to be a direct band gap semiconductor [40] with room temperature (RT) fundamental band gap of around 2 eV [40-42]. Marasina *et al*. [43] reported the sensitivity of InN to substrate temperature and determined that rapid dissociation of InN occurs above 600 °C while the growth of InN layer is not sustainable at 670 °C [43]. However, the development of more sophisticated epitaxial growth methods; like molecular beam epitaxy (MBE) and vapour phase epitaxy (VPE), has led to new experimental and theoretical investigations, making the observation of photoluminescence (which was never observable for InN) possible. Discussions of the band gap of InN therefore became prevalent, leading to the optical band gap review to 0.65 - 0.7 eV [44-48]. At present, high crystal quality InN with RT carrier density of 3.5 x 10^{17} cm^{-3} and corresponding Hall mobility of 2050 cm^2/Vs has been achieved by MBE [49].

1.3 Important properties and potential applications of InN and Alloys

InN is a very indispensable member of the III-nitride semiconductors family. It can be the constituent of a continuous alloy system of direct bandgap $In_xGa_{1-x}N$, $In_y Al_{1-y}N$, and $In_xAl_yGa_{1-x-y}N$ [Fig. 1.3]. These ternary and quaternary alloys cover a broad bandgap range of 0.65 - 6.2 eV that spans from UV to NIR wavelengths of the electromagnetic spectrum. This property makes them materials of choice for UV, violet, blue, green light emitting diodes (LEDs) and laser diodes (LDs) and also key materials for solar device applications or energy harvesting devices [50-54]. Heterostructures like $In_xGa_{1-x}N$(1.9eV)/Si(1.1) or $In_xGa_{1-x}N$(1.9eV)/$In_xGa_{1-x}N$(1.1eV) have already been proposed for a conversion efficiency of over 30% [53]. The first commercial target has been predicted to be multijunction solar cells with high efficiencies up to 70% [55] and could be achieved by using the whole $In_xGa_{1-x}N$ composition range in graded layer cells and/or with quantum well multilayers [56,57]. Such nitride-based solar cells would have the advantage of containing no poisonous elements like Arsenic and do not need toxic gases like Phosphine in the fabrication process. Hence, InN is a potential material for low cost high efficiency solar cell applications.

The newly reported InN bandgap (0.65-0.7eV) makes it compatible, together with its alloys, to the wavelengths used for transmission in optical fibers at 1263 – 1675 nm [54]. High speed laser diodes (LDs) and photodiodes (PDs) could be developed in the future for use in optical communication systems. InN and InN-rich InGaN electron mobility and minority carrier lifetime are also much less sensitive to irradiation compared with GaAs and GaInP [58-60]. The high irradiation resistance makes them ideal for space devices and nuclear reactor applications compared to GaN [58] and the conventional GaAs or GaInP presently being used, which rapidly become electrically insulating with increasing dose of energetic-particle irradiation such as electron, protons and $^4He^+$ [58-60].

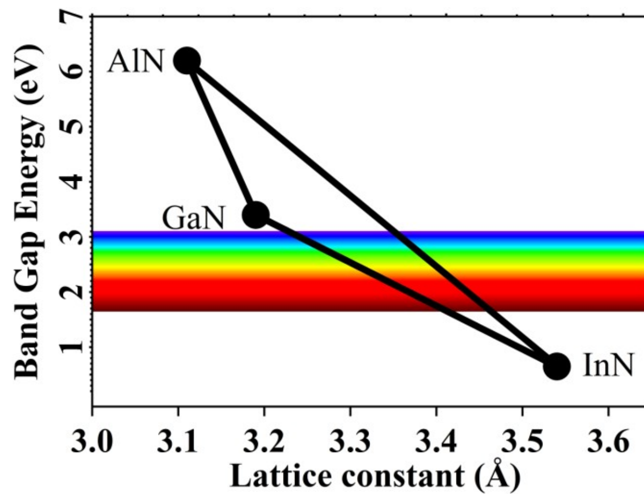

Figure 1.3 *The energy gap of the group III-nitride alloys as a function of the a-axis lattice constant, showing the possibility of III-nitride bandgap engineering for optoelectronic applications.*

InN exhibits the lowest electron effective mass among the III-nitrides (the electron effective mass at band edge, m_e*/m_o = 0.32 for AlN, 0.20 for GaN and 0.07 for InN) [58,61]. Such low electron effective mass should result to high electron mobility in InN. In 1994, Chin *et al*. had calculated the highest mobility of 4400 cm^2 / Vs at 300K and 30 000 cm^2 / Vs at 77K for InN whilst 1000 cm^2 / Vs and 6000 cm^2 / Vs were also proposed for GaN at 300K and 77K, respectively [62]. Current reports have projected the 300K electron mobility of InN to 4000 [63], 10 000 cm^2 / Vs [64] and 14000 cm^2/Vs [65] for materials with low carrier concentrations. The measurements of the field-induced non-equilibrium electron distribution and transport, using the "ensemble Monte Carlo (MC) method" [65-67] and "transient sub-picosecond Raman spectroscopy" [67], have led to electron drift velocity values ranging from 5 x 10^7 to 2 x 10^8 cm/s, which are higher than that of other group III-V semiconductors [65-67]. Foutz *et al.* by ensemble Monte Carlo method has also found that for a doping concentration of 10^{19} cm^{-3}, InN exhibits an extremely high peak velocity over a wide range of temperatures from 150 – 500K compared to GaAs, GaN and AlN; underscoring the superiority of InN transport characteristics [68]. Recently, a higher electron saturation velocity of approximately 5 x 10^7 cm/s (at 32 kV/cm) [65] has been calculated (see Fig. 1.4), in contrast to the earlier proposed value of 4.2 x 10^7 cm/s (at 65kV/cm) for InN with E_g = 1.9 eV [69]. InN therefore has an advantage for high frequency centimeter and millimeter wave devices. Transient Electron study has already predicted InN based FETs with extremely high speed and cut-off frequency of over 1THz for 0.1μm gates [68]. Therefore, the InN large spontaneous and piezoelectric polarization constants and large band offset with its alloys (due to its lower bandgap) are expected to be of added advantage in the fabrication of InN based HEMT Devices.

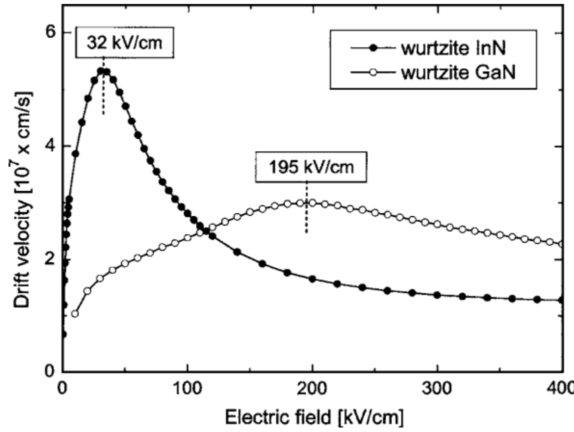

Figure 1.4 *Calculated steady-state drift velocity as a function of electric field strength for wurtzite InN and GaN at room temperature. Peak velocities of* $5.3x10^7$ *and* $3.0x10^7$ *cm/s are estimated for InN and GaN, respectively. (Figure from V. M. Polyakov and F. Schwierz 2006 [65]).*

Fundamental understanding of the surface and interface properties of InN is required for the design criteria of low dimensional devices [70]. The surface properties were never studied until after discovering, in year 2002, that InN has a lower band gap than the 1.9 eV commonly accepted [44,45]. Lu *et al*. plotted the sheet electron density against film thickness during investigation of the thickness dependent electrical properties of InN and found that the extrapolation to zero film thickness resulted to a non-zero sheet density greater than 2.5 x 10^{13} cm^{-2} [71]. This was the first observation of a strong excess sheet charge at the InN surface. Efforts to form Schottky contacts on InN by the same authors [71], using Ti, Al and Ni contacts, or capacitance-voltage (C-V) and Hg Probe measurements techniques failed. Hence they concluded that the behaviour may be similar to that of InAs where the Fermi level is pinned above the conduction band minimum (CBM) due to native donor surface defects [71]. The excess surface state density of InN was again experimentally confirmed by high-resolution electron-energy-loss spectroscopy (HREELS) [70] and attributed to the high location of the branch point energy (E_B) relative to the CBM, which causes the Fermi level at the surface to be pinned below E_B by donor type surface states [Fig. 1.5], resulting in downward band bending and the observed electron accumulation [72]. The E_B is located close to the average mid-gap energy across the entire Brillouin zone and is defined as the energy where surface states change their character from predominantly donor type (below) to predominantly acceptor type (above) [72,73]. The high branch point energy relative to the CBM in InN means that unintentional native defects will preferentially form as donors, generally resulting in high unintentional n-type bulk conductivity [72]. The concept of E_B is similar to the charge neutrality level for semiconductor proposed by Tersoff [74] or the Fermi stabilization energy (E_{FB}) [58,75], which is about 4.9 eV below vacuum and 0.9 eV above the conduction band edge (CBE) for InN [59,76] or the universal absolute energy, ε(+/-) [77] used by others. To achieve overall charge neutrality, the Fermi level at the surface is expected to lie in the vicinity of the branch-point energy. If the surface Fermi level is located below the branch point, some donor surface states will be unoccupied and hence positively charged: this surface charge must be balanced by a space charge due to downward band bending towards the surface, leading to an electron accumulation layer [72]. This contrast what has been observed

for other III–V semiconductor surfaces, where depletion layers normally occur due to their surface Fermi level being located in the band gap at the Γ-point [78]. The depletion of the conduction electrons allows the ionized acceptor-type surface states to be neutralized, leading to overall charge neutrality. According to Mahboob *et al*., The Fermi level (E_F) pinning occurs at 1.64 eV above the valence band maximum (VBM) and 0.89 eV above the CBM [70]. However, the surface Fermi level is not anomalously high in the overall band structure, but rather the Γ-point CBM is unusually low relative to the rest of the conduction band edge (CBE) [79]. HREELS indicates that the electron accumulation is independent of temperature above 300K [80]. Furthermore, the surface electron accumulation seems unaffected by chemical or physical treatments [60,70] and makes Hall effect measurements of InN films complicated. An InN film is not a homogeneous conductivity layer but, in general, the contribution from bulk and surface conductivity layers is considered [81].

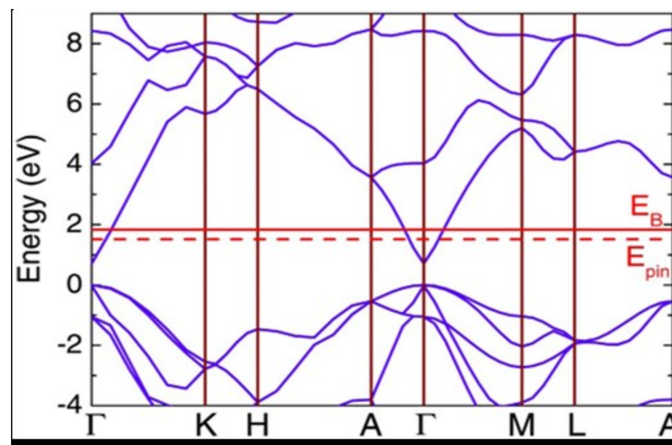

Figure 1.5 *Quasiparticle corrected density functional theory (QPC-DFT) band structure across the Brillouin zone with the determined branch point E_B and surface Fermi level pinning E_{pin} positions (Figure from King et al. 2008 [72]).*

The origin of the *n*-type residual doping has been investigated by many authors. They studied the role of impurities, point and extended defects. The nitrogen vacancy (V_N) has been proposed by first principle calculations [82-84] and experiments [73,74] as the lowest energy defect and can therefore be a major source of free electrons in as-grown InN or compensation donors in *p*-type doped InN material. To date, impurities, such as oxygen (O_N) [82,83,87-89], Silicon (Si_{In}) [83,89], and Hydrogen (H) [90-93] are being considered as donor sources. Hydrogen has been predicted to be a stable donor (acceptor) in *p* type (*n*-type) GaN and AlN, where it always compensates existing conductivity [77]. However, contrary to the H amphoteric behaviour in the other III-nitride materials, interstitial hydrogen as a shallow single donor or substitutional hydrogen as a double donor has been predicted for InN [94], under the consideration that H^0 and H^- always exhibit higher energy than H^+ [95]. Likewise, nitrogen antisite [96], is also among the proposed donor candidates.

It has been reported that the concentrations of existing O and/or H impurities in InN are too low to account for the high electron concentrations and as a consequence intrinsic defects such as N vacancies and/or dislocations could be important sources of free electrons in these samples [97-99]. Investigation of the

thickness dependence of the electrical properties of unintentionally doped InN showed increasing Hall mobility and reducing electron density with increasing film thickness [100,101]. The drastic reduction in the density of extended defects (and not the unintentional impurities) with increasing thickness has also been claimed to be responsible for such improvement [100,102]. Wang *et al*. [98] suggested edge-type dislocations as the more prominent candidate while Piper *et al*. indicated that dislocation lines also accommodate segregated V_N^+ defects [99]. Wang *et al*. have tried to study the role of dislocations by growing films under different III/V growth conditions to vary the density of extended defects and deep levels [103]. They reported that threading dislocations of edge-type character are possible source of electron degeneracy while other workers did not observe any discernable effect of dislocations on electron carrier density in their InN films [104,105] but proposed that unintentional impurities are more prone to be the cause.

The exhibited high concentrations of electrons at the surface and the bulk of InN films have enriched the InN electrical properties and may provide additional potential application fields. The optimum carrier density at which superconductivity is observed in *n*-type InN has been reported to be limited by the Mott transition (lower limit) and superconductivity to metal transition (upper limit) with corresponding electron concentrations of 2 x 10^{17} and 5 x 10^{20} cm^{-3}, respectively [106,107]. Moreover, the high surface electron accumulation could also be potentially explored for InN-based sensing applications [108-112]. Terahertz emission depends on the acceleration of the photoexcited carriers generated close to the surface of semiconductors by transient electric field dipole, which can be supplied in the case of InN by its inherent electron accumulation. Strong terahertz emission has been reported in both polar *c*-plane [113-116] and non-polar *a*-plane InN [117], opening the way for potential applications in electronic detector and emitting devices that are operating at THz radiation wavelength.

The presence of high electron concentrations in the bulk of InN makes *p*-type doping difficult and it has not been possible yet to grow InN layers free from background donors. To date, Mg and Si are the most important acceptors and donors for group III-Nitrides, respectively. Theoretically, Carbon (C_N) has been proposed to give rise to an acceptor level with hole activation energy increasing along the series from InN, GaN, and AlN [118]. Substitutional C on a N site (C_N) and Mg on an In site (Mg_{In}) have also been proposed as the most favourable sites for the C and Mg impurities, and they are consequently predicted to be single acceptors under most *n*-type layer concentration levels [89]. Mg doping has been proposed to have the capability of compensating the *n*-type conductivity in the bulk of InN and it is seen as a prospective means of achieving *p*-type doping in InN [88]. Mamutin *et al*. attempted Mg doping of WZ InN film grown by PAMBE [119]. *P*-type InN was not obtained and the Authors claimed only an improvement of InN:Mg crystal quality for Mg concentration range of 10^{19} – 3 x 10^{20} cm^{-3}. Increasing the Mg doping level over $10^{21}cm^{-3}$ deteriorated the InN crystal quality and surface morphology, causing a large concentration of Mg interstitials that resulted in an order of magnitude reduction of electron concentration but complete compensation was not achieved.

The first evidence of *p*-type doping of InN was reported, using electrolyte-based capacitance voltage measurements, by Jones *et al*. [120]. Doping of high

quality InN films with Mg has recently been carried out to achieve high resistivity and investigate compensation doping by Wang *et al.* [121], and they observed that the electron density decreases with Mg doping due to the effect of electron compensation. Further increase in the Mg flux led to increase in electron density as a result of Mg-related donor-like defects' formation [121]. However, a *p*-type bulk region in the film, surrounded by electron accumulation layers at the surface and interface has been discovered by such efforts [121-127]. It was determined that most of the Mg atoms occupied substitutional In sites [128]. The Mg concentration at which buried *p*-type region could be formed was from ~10^{18} to 3 x 10^{19} cm^{-3}. A lower Mg doping had no effect but a higher one begun to generate donor-like defects in the InN. Nevertheless, direct Hall-effect measurements of InN, despite such a buried *p*-type layer formation, still indicated net *n*-type conductivity due to the inherent surface and interfacial electron accumulation [120,121,126].

The non-polar orientation InN films are very promising, due to the expected elimination of polarisation effects along the non-polar growth directions, which could be of great benefit in the fabrication of optoelectronic devices [129] and the predicted potential for realizing InN surfaces without an electron accumulation layer [130]. Although the evidence of unpinned Fermi level for *in-situ* cleaved *a*-plane InN surfaces has been reported [131], it has not yet been experimentally verified in heteroepitaxially grown InN surfaces [132].

To date, there is an insurmountable challenge towards the realization of InN based devices due to inability to control the doping as required for realizing a *pn* diode: "No InN *pn* diode, no InN-based LEDs and LDs".

1.4 Objectives of the thesis

InN is an important semiconductor material for electronic and optoelectronic applications. This has stimulated research on the epitaxial growth and properties of InN heterostructures-nanostructures. The starting point of this thesis was a previous one on the "Physical mechanisms in molecular beam epitaxy and properties of InN (0001) films" [12], which established the basic understanding for InN growth on GaN (0001) pseudo-substrates. The objective of the present work is to understand and control the growth and properties of InN-based heterostructures and nanostructures on different substrates and/or crystallographic orientations, with emphasis on the new substrates for InN heteroepitaxy of Al_2O_3 $(1\bar{1}02)$ (*r*-plane sapphire) and Si (111). This work could identify the intrinsic/native InN properties and distinguish the influence of different lattice-mismatched substrates and growth processes used in InN heteroepitaxy. The work also aimed to advance our understanding of InN and InN-rich alloys' properties on *c*-plane GaN pseudo-substrates and to exploit the development of heterostructures for device applications, such as HEMTs. The work can be divided in three parts.

The first study was aimed at the optimization of InN heteroepitaxial growth on *c*-plane GaN pseudo-substrates. The major emphasis deals with studying the thickness dependence of the morphological, structural, electrical and optical properties of *c*-plane InN. The growth and properties of $In_xAl_{1-x}N$ films, covering the range of $0.12 \leq x \leq 0.80$, were also investigated on *c*-plane GaN pseudo-substrates. First experiments

on the growth of $In_xAl_{1-x}N$/InN heterostructures for HEMT devices were accomplished.

In the second study, the heteroepitaxial growth of InN on Al_2O_3 $(1\bar{1}02)$, i.e. *r*-plane sapphire, substrates was investigated. The growth studies were focused on examining the effects of substrate surface treatments, the III-nitride nucleation conditions/material and the use of a buffer layer, before growing the main InN film. The *r*-plane sapphire surface treatments employed consisted of high temperature annealing and surface nitridation. Depending on the conditions used to initiate the growth on *r*-plane sapphire, it has been found possible to grow InN films with the non-polar *a*-plane $(11\bar{2}0)$ orientation, as well as with the polar *c*-plane (0001), the semipolar *s*-plane $(10\bar{1}1)$ and cubic (002) orientations. Using optimised growth conditions, the thickness dependent properties of non-polar *a*-plane InN layers, grown on *r*-plane sapphire, were investigated and compared with the results obtained for the polar *c*-plane InN layers grown on GaN (0001) pseudo-substrates. This study was also aimed at investigating the non-polar InN transport properties in order to confirm or not the predicted non-existence of surface electron accumulation on non-polar surfaces [133]. The electrical activity/effects of crystalline defects, due to the lattice mismatched growth on the various substrates, could be also evaluated by comparing the transport properties of different orientation InN films.

The third study concerns the heteroepitaxy and the properties of InN thin films and nanopillars on Si (111) substrates. A significant effort was devoted to study the role of nucleation and buffer layers on the InN epilayer grown on Si (111) substrate. Although AlN appears as the best nucleation material on Si (111) for III-N epitaxial growth, using a large bandgap AlN layer at the interface creates a barrier for vertical current conduction through the InN-on-Si interface that may be required for some device applications. The presence of intermediate layers of other III-nitrides will also not allow forming actual Si/InN heterojunctions that may be interesting to have an active role in some types of devices, e.g. solar cells. For this reason, it is important to also control the direct growth of InN on Si. Thus a comprehensive study of the direct nucleation of InN on Si (111) surfaces was carried out to identify the various conditions that are suitable for the growth of InN thin films and nanopillars. The realized optimum nucleation conditions were applied to grow high crystalline quality InN thin films and nanopillars (NPs) on Si (111) and their properties were studied. For the growth of InN NPs, the role of III/V flux ratio, substrate temperature and nucleation conditions, were studied. The determined conditions for NPs growth on Si (111) were also evaluated for InN deposition on *r*-plane sapphire substrates.

References

1. John E. Ayers, *Heteroepitaxy of semiconductors: Theory, Growth, and Characterisation*, CRC Press, Taylor & Francis Group, Boca Raton (USA) Chapter 2 (2007)
2. T. L. Tansley, *in "Group III nitrides"*, edited by J. H. Edgar, INSPEC, London UK, pg.35-42 (1994)
3. Bernard Gil (ed.),"*Group III Nitride Semiconductor Compounds: Physics and Applications*", Oxford University Press, New York. Chapter 2 pg 20-21 (1998)
4. Hadis Morkoç, *Handbook of Nitride Semiconductors and Devices – Vol 1: Materials Properties, Physics and Growth*, WILEY-VCH GmbH & Co, Weinheim- Germany, Chapter 1 (2008)
5. D. Elwell and M. M. Elwell, *Prog. Cryst. Growth Charact*. **17**, 53 (1988)
6. A. M. Saitta and F. Decremps, *Phys. Rev. B* **70**, 035214 (2004)
7. D. A. Neumayer and J. G. Ekerdt, *Chem. Mater.* **8**, 9-25 (1996)
8. W. A. Harrison, *Electronic Structure and Properties of Solids*, Dover, New York, Chapter 7, pg. 174–179 (1980)
9. O Ambacher, *J. Phys. D: Appl. Phys.* **31**, 2653–2710 (1998)
10. E. Dimakis, E. Iliopoulos, K. Tsagaraki, A. Adikimenakis, and A. Georgakilas, *Appl. Phys. Lett.* **88**, 191918 (2006)
11. I. Vurgaftman, J. Meyer, L. Ram-Mohan, *J. Appl. Phys.* **89**, 5815 (2001)
12. E. Dimakis, *Ph.D Thesis*, Physics Department, University of Crete, Heraklion-Greece, Chapter 1 (2007)
13. D.J. As, *in "Optoelectronic Properties of Semiconductors and Superlattices"*, series editor M.O.Manasreh, Taylor & Francis Books, Inc., New York, Vol. 19, chapter 9, pg. 323-450 (2003)
14. W.M. Yim, E.J. Stofko, P.J. Zanzucchi, J.I. Pankove, M. Ettenberg, S.L. Gilbert, *J. Appl. Phys*. **44**, 292 (1973)
15. H.P. Maruska, and J.J. Tietjen, *Appl. Phys. Lett*. **15**, 327 (1969)
16. J. Schörmann, D. J. As, and K. Lischka, P. Schley and R. Goldhahn, S. F. Li, W. Löffler, M. Hetterich, and H. Kalt, *Appl. Phys. Lett.* **89**, 261903 (2006)
17. V. Potin, P. Vermaut, P. Ruterana, G. Nouet, *J. Electron. Mater.* **27**, 266 (1998)
18. S. Kasap and P. Capper (Eds.), *Springer Handbook of Electronic and Photonic Materials*, Springer Science + Business Media, Inc., NewYork, Chapter 32 (2006)
19. A. U. Sheleg, V. A. Savastenko, *Vestsi Akad. Nauk, Set. Fiz.-Mat. Nauk USSR* **3**, 126 (1976)
20. S. D. Lester, F.A. Ponce, M. G. Craford, and D. A.Steigerwald, *Appl. Phys. Lett.* **66**, 1249 (1995)
21. S.J. Rosner, E.C. Carr, M.J. Ludowise, G. Girolami, H. Erinkson, *Appl. Phys. Lett.* **70** (1997) 420
22. F. Bernardini, V. Fiorentini and D. Vanderbilt, *Phys. Rev. B* **56** R10 024 (1997)
23. S. C. Jain, M. Willander, J. Narayan, and R. V. Overstraeten, *J. Appl. Phys.* **87**, 965 (2000)
24. S. J. Pearton, J. C. Zolper, R. J. Shul, and F. Ren, *ibid.* **86**, 1(1999)
25. S. Strite and H. Morkoc, *J. Vac. Sci. Technol. B* **10**, 1237 (1992)
26. S. N. Mohammad and H. Morkoc, *Prog. Quantum Electron.* **20**, 361 (1996)
27. E. Dimakis, E. Iliopoulos, K. Tsagaraki, Th. Kehagias, Ph. Komninou, and A. Georgakilas, *J. Appl. Phys.* **97**, 113520 (2005).

28. R. Juza and H. Hahn, Z. Anorg. *Allg. Chem*. **239**, 282 (1938)
29. R. Juza and A. Rabenau, Z. Anorg. *Allg. Chem*. **285**, 212 (1956)
30. J. Pastrnak and L. Souckova, *Phys. Status Solidi* **3**, K71 (1963)
31. N. A. Gorjunova, *Slosnye Almazopodobnye Poluprovodniki*, Moscow (1964)
32. J. B. McChesney, P. M. Bridenbaugh, and P. B. O'Connor, *Mater. Res. Bull*. **5**, 783 (1970)
33. R. D. Jones and K. Rose, *J. Phys. Chem. Solids* **48**, 587 (1987)
34. H.J. Hove, J.J. Cuomo, *Appl. Phys. Lett*. **20**, 71 (1972)
35. A. Yamamoto, T. Shin-ya, T. Sugiura, A. Hashimoto, J. Cryst. Growth **189/190**, 461 (1998)
36. H. Lu, W. J. Schaff, J. Hwang, H. Wu, W. Yeo, A. Pharkya and L. F. Eastman, *Appl. Phys. Lett*. **77**, 2548 (2000)
37. S.V. Ivanov, T.V. Shubina, V.N. Jmerik, V.A. Vekshin, P.S. Kop'ev and B. Monemar, *J. Cryst. Growth* **269**, 1 (2004)
38. V.A. Tyagi, V.A. Eustigneev, A.M. Krasilo, A.F. Andreeva, V.Y. Malatidiou, *Sov. Phys. Semicond*. **11**, 1257 (1977)
39. K.L. Westra, R.P.W. Lawson, M.J. Brett, J. *Vac. Sci. Technol*. **A8**, 1730 (1988)
40. J. W. Trainor and K. Rose, *J. Electron. Mater.* **3**, 821 (1974)
41. N. Puychevrier and M. Menoret, *Thin Solid Films* **36**, 141 (1976)
42. T. L. Tansley and C. P. Foley, *J. Appl. Phys*. **59**, 3241 (1986)
43. L. A. Marasina, I. G. Pichugin, and M. Tlaczala, *Krist. Tech.* **12**, 541 (1977)
44. V.Yu. Davydov, A.A. Klochikhin, R.P. Seisyan, V.V. Emtsev, S.V. Ivanov, F. Bechstedt, J. Furthmuller, H. Harima, A.V. Mudryi, J. Aderhold, O. Semchinova, J. Graul, *Phys. Status Solidi (b),* **229**, R1 (2002)
45. J. Wu, W. Walukiewicz, K. M. Yu, J. W. Ager III, E. E. Haller, H. Lu, W. J. Schaff, Y. Saito, and Y. Nanishi, *Appl. Phys. Lett.* **80**, 3967 (2002)
46. T. Matsuoka, H. Okamoto, M. Nakao, H. Harima, and E. Kurimoto, *Appl. Phys. Lett.* **81**, 1246 (2002)
47. M. Hori, K. Kano, T. Yamaguchi, Y. Saito, T. Araki, Y. Nanishi, N. Teraguchi, and A. Suzuki, *Phys. Status Solidi (b)* **234**, 750 (2002)
48. A. Georgakilas, in "*CAS 2008 Proceedings*" (IEEE, 2008) 43
49. J. Wu, W. Walukiewicz, W. Shan, K. M. Yu, J. W. Ager, S. X. Li, E. E. Haller, H. Lu, and W. J. Schaff, *J. Appl. Phys*. **94**, 4457 (2003)
50. I. Akasaki, H. Amano, N. Koide, M. Kotaki, and K. Manabe, *Physica B* **185**, 428 (1993)
51. S. Nakamura, M. Senoh, and T. Mukai, *Jpn. J. Appl. Phys*. **Part 2 32**, L8 (1993)
52. S. Nakamura, M. Senoh, S. Nagahama, N. Iwasa, T. Yamada, T. Matsushita, H. Kiyoku, and Y. Sugimoto, *Jpn. J. Appl. Phys*. **Part 2 35**, L74 (1996)
53. A. Yamamoto, M. Tsujino, M. Ohkubo, and A. Hashimoto, *Sol. Energy Mater. Sol. Cells*. **35**, 53, (1994)
54. A. G. Bhuiyan, A. Hashimoto, and A. Yamamoto, *J. Appl. Phys*., **94,** 2779 (2003)
55. E. Tiras, D. Zanatob, S. Mazzucato, N. Balkan, W.J. Schaff, *Superlatt. Microstruct.* **36**, 473–485 (2004)
56. S. Nakamura, T. Mukai and M. Senoh, *Appl. Phys. Lett.* **64**, 1687 (1994)
57. S. Nakamura, M. Senoh, S. Nagahama, N. Iwasa, T. Yamada, T. Matsushita, H. Kiyoku, Y. Sugimoto, T. Kozaki, H. Umemoto, M. Sano and K. Chocho, *Japan. J. Appl. Phys*. **36** L1568 (1997)
58. Junqiao Wu, *J. Appl. Phys*. **106**, 011101 (2009)

59. J. Wu, W. Walukiewicz, K. M. Yu, W. Shan, J. W. Ager, E. E. Haller, H. Lu, W. J. Schaff, W. K. Metzger, and S. Kurtz, *J. Appl. Phys*. **94**, 6477 (2003)
60. S. X. Li, K. M. Yu, J. Wu, R. E. Jones, W. Walukiewicz, J. W. Ager, W. Shan, E. E. Haller, H. Lu, and W. J. Schaff, *Phys. Rev. B* **71**, 161201 (2005)
61. J. Wu, W. Walukiewicz, W. Shan, K. M. Yu, J. W. Ager, E. E. Haller, H. Lu, and W. J. Schaff, *Phys. Rev. B* **66**, 201403 (2002)
62. V. W. L. Chin, T. L. Stanley and T. Osotchan, *J. Appl. Phys*. **75**, 7365, (1994)
63. B. R. Nag, *J. Crys. Growth* **269** (2004)
64. W. Liang and K. T. Tsen, D. K. Ferry, Hai Lu and William J. Schaff, *Appl. Phys. Lett.* **84**, 3681 (2004)
65. V. M. Polyakov and F. Schwierz, *Appl. Phys. Lett*. **88**, 032101 (2006)
66. Z. Yarar, *Phys. Status Solidi (b)* **244**, 3711 (2007)
67. K. T. Tsen, C. Poweleit, D. K. Ferry, H. Lu, and W. J. Schaff, *Appl. Phys. Lett.* **86**, 222103 (2005)
68. B. E. Foutz, S. K. O'Leary, M. S. Shur and L. F. Eastman, *J. Appl. Phys.* **85**, 7727, (1999)
69. S. K. O'Leary, B. E. Foutz, M. S. Shur, and L. F. Eastman, *J. Mater. Sci.: Mater. Electron.* **17**, 87 (2006)
70. I. Mahboob, T. D. Veal, C. F. McConville, H. Lu, and W. J. Schaff, *Phys. Rev. Lett.* **92**, 036804 (2004)
71. H. Lu, W. J. Schaff, L. F. Eastman, and C. E. Stutz, *Appl. Phys. Lett.* **82**, 1736 (2003)
72. P. D. C. King, T. D. Veal, P. H. Jefferson, S. A. Hatfield, L. F. J. Piper, C. F. McConville, F. Fuchs, J. Furthmüller, F. Bechstedt, H. Lu and W. J. Schaff, *Phys. Rev. B* **77**, 045316 (2008)
73. W. Mönch, *Semiconductor Surfaces and Interfaces, Springer,* Berlin (2001)
74. J. Tersoff, *Phys. Rev. B* **30**, 4874 (1984)
75. W. Walukiewicz, *Appl. Phys. Lett*. **54**, 2094 (1989)
76. W. Walukiewicz, *Physica (Amsterdam)* **302B**, 123 (2001)
77. C. G. Van de Walle and J. Neugebauer, *Nature (London)* **423**, 626 (2003)
78. H. Lüth, *Surfaces and Interfaces of Solid Materials* (Springer, Berlin, 1995)
79. T. D. Veal, I. Mahboob, L. F. J. Piper, and C. F. McConville, H. Lu and W. J. Schaff, *J. Vac. Sci. Technol. B* **22**, 2175 (2004)
80. L. F. J. Piper, T. D. Veal, I. Mahboob, C. F. McConville, H. Lu and W. J. Schaff, *J. Phys. Rev. B* **70**, 115333 (2004)
81. C.H. Swartz, R.P. Tompkins, N.C. Giles, T.H. Myers,H. Lu, W.J. Schaff, L.F. Eastman, *J. Crystal Growth* **269**, 29–34 (2004)
82. D. W. Jenkins and J. D. Dow, *Phys. Rev. B* **39**, 3317 (1989)
83. C. Stampfl, C. G. Van der Walle, D. Vogel, P. Krueger, and J. Pollmann, *Phys. Rev. B* **61**, R7846 (2000)
84. X. M. Duan and C. Stampfl, *Phys. Rev. B* **77**, 115207 (2008)
85. T. L. Tansley and R. J. Egan, *Phys. Rev. B* **45**, 10942 (1992)
86. A. Yamamoto, T. Tanaka, K. Koide, A. Hashimoto, *Phys. Status Solidi (a)* **194**, 510 (2002)
87. M. Yoshimoto, H. Yamamoto, W. Huang, H. Harima, J. Saraie, A. Chayahara, and Y. Horino, *Appl. Phys. Lett.* **83**, 3480 (2003)
88. V. Cimalla, M. Niebelschütz, G. Ecke, V. Lebedev, O. Ambacher, M. Himmerlich, S. Krischok, J. A. Schaefer, H. Lu, and W. J. Schaff, *Phys. Status Solidi (a)* **203**, 59–65 (2006)

89. X. M. Duan and C. Stampfl, *Phys. Rev. B* **79**, 035207 (2009)
90. D. C. Look, H. Lu, W. J. Schaff, J. Jasinski, and Z. Liliental-Weber, *Appl. Phys. Lett.* **80**, 258 (2002)
91. E. A. Davis, S. F. J. Cox, R. L. Lichti, and C. G. Van der Walle, *Appl. Phys. Lett.* **82**, 592 (2003)
92. S. P. Fu, T. J. Lin, W. S. Su, C. Y. Shieh, Y. F. Chen, C. A. Chang, N. C. Chen, and P. H. Chang, *J. Appl. Phys.* **99**, 126102 (2006)
93. G. Pettinari, F. Masia, M. Capizzi, A. Polimeni, M. Losurdo, G. Bruno, T. H. Kim, S. Choi, A. Brown, V. Lebedev, V. Cimalla, and O. Ambacher, *Phys. Rev. B* **77,** 125207 (2008)
94. A. Janotti and C. G. Van de Walle, *Appl. Phys. Lett.* **92**, 032104 (2008)
95. S. Limpijumnong, C. G. Van der Walle, *Phys. Status Solidi (b)* **228**, 303 (2001)
96. T. L. Tansley and C. P. Foley, *Proceedings of the 3rd International Conference on Semi-Insulating III-V Materials*, Warm Springs, Oregon, p. 497 (1984)
97. J. Wu, W. Walukiewicz, S. X. Li, R. Armitage, J. C. Ho, E. R. Weber, E. E. Haller, Hai Lu, William J. Schaff, A. Barcz and R. Jakiela, *Appl. Phys. Lett.*, **84**, 2805 (2004)
98. H. Wang, D. S. Jiang, L. L. Wang, X. Sun, W. B. Liu, D. G. Zhan, J. J. Zhu, Z. S. Liu, Y. T. Wang, S. M. Zhang, and H. Yang, *J. Phys. D: Appl. Phys*. **41**, 135403 (2008)
99. L. F. J. Piper, T. D. Veal, C. F. McConville, H. Lu, and W. J. Schaff, *Appl. Phys. Lett.* **88**, 252109 (2006)
100. W. J. Schaff, X. Chen, D. Hao, K. Matthews, T. Richards, L. F. Eastman, H. Lu, C. J. Cho, and H. Y. Cha, *Phys. Status Solidi (b)* **245**, 868 (2008)
101. H. Lu, W. J. Schaff, L. F. Eastman, J. Wu, W. Walukiewicz, D. C. Look, and R. J. Molnar, *Mater. Res. Soc. Symp. Proc*. **743**, L4.10 (2002)
102. R. E. Jones, S. X. Li, L. Hsu, K. M. Yu, W. Walukiewicz, Z. Liliental- Weber, J. W. Ager, E. E. Haller, H. Lu, and W. J. Schaff, *Physica B* **376–377**, 436 (2006)
103. X. Wang, S-B. Che, Y. Ishitani, and A. Yoshikawa, *Appl. Phys. Lett*. **90**, 151901 (2007)
104. C.S. Gallinat, G. Kobmuller and J.S. Speck, *Appl. Phys. Lett*. **95**, 022193 (2009)
105. V. Darakchieva, T. Hofmann, M. Schubert, B. E. Sernelius, B. Monemar, P. O. Å. Persson, F. Giuliani, E. Alves, H. Lu, and W. J. Schaff, *Appl. Phys. Lett*. **94**, 022109 (2009)
106. Takashi Inushima, *Phys. Status Solidi (c)* **4**, 660 (2007)
107. T. Inushima, N. Kato, D. K. Maude, H. Lu, W. J. Schaff, R. Tauk, Y. Meziani, S. Ruffenach, O. Briot, W. Knap, B. Gil, H. Miwa, A. Yamamoto, D. Muto, Y. Nanishi, M. Higashiwaki, T. Matsui, *Phys. Status Solidi (b)* **243**, 1679 (2006)
108. H. Lu, W. J. Schaff, and L. F. Eastman, *J. Appl. Phys*. **96**, 3577 (2004)
109. C. F. Chen, C. L. Wu, and S. Gwo, *Appl. Phys. Lett*. **89**, 252109 (2006)
110. O. Kryliouk, H. J. Park, H. T. Wang, B. S. Kang, T. J. Anderson, F. Ren, and S. J. Pearton, *J. Vac. Sci. Technol. B* **23**, 1891 (2005)
111. Y. S. Lu, C. C. Huang, J. A. Yeh, C. F. Chen, and S. Gwo, *Appl. Phys. Lett*. **91**, 202109 (2007)
112. Y. S. Lu, C. L. Ho, J. A. Yeh, H. W. Lin, and S. Gwo, *Appl. Phys. Lett*. **92**, 212102 (2008)
113. R. Ascazubi, I. Wilke, K. Denniston, H. Lu, and W. J. Schaff, *Appl. Phys. Lett.* **84**, 4810 (2004)

114. X. Mu, Y. Ding, K. Wang, D. Jena, and Y. B. Zotova, *Opt. Lett*. **32**, 1423 (2007)
115. V. M. Polyakov and F. Schwierz, *Semicond. Sci. Technol*. **22**, 1016 (2007)
116. G. Matthaus, V. Cimalla, B. Pradarutti, S. Riehemann, G. Notni, V. Lebedev, O. Ambacher, S. Nolte, and A. Tuennermann, *Opt. Commun*. **281**, 3776 (2008)
117. H. Ahn, Y. P. Ku, C. H. Chuang, C. L. Pan, H. W. Lin, Y. L. Hong, and S. Gwo, *Appl. Phys. Lett*. **92**, 102103 (2008)
118. L.E. Ramos, J. Furthmüller, L.M.R. Scolfaro, J.R. Leite, and F. Bechstedt, *Phys. Rev. B* **66**, 075209 (2002)
119. V. V. Mamutin, V. A. Vekshin, V. Y. Davydov, V. V. Ratnikov, Y. A. Kudriavtsev, B. Y. Ber, V. V. Emtsev, and S. V. Ivanov, *Phys. Status Solidi (a)* **176**, 373 (1999)
120. R. E. Jones, K. M. Yu, S. X. Li, W. Walukiewicz, J. W. Ager, E. E. Haller, H. Lu, and W. J. Schaff, *Phys. Rev. Lett*. **96**, 125505 (2006)
121. X. Wang, S. B. Che, Y. Ishitani, and A. Yoshikawa, *Appl. Phys. Lett*. **90**, 201913 (2007)
122. P. A. Anderson, C. H. Swartz, D. Carder, R. J. Reeves, S. M. Durbin, S. Chandril, and T. H. Myers, *Appl. Phys. Lett*. **89**, 184104 (2006)
123. P. D. C. King, T. D. Veal, P. H. Jefferson, C. F. McConville, H. Lu, and W. J. Schaff, *Phys. Rev. B* **75**, 115312 (2007)
124. X. Wang, S. B. Che, Y. Ishitani, and A. Yoshikawa, *Appl. Phys. Lett*. **91**, 242111 (2007)
125. J. W. L. Yim, R. E. Jones, K. M. Yu, J. W. Ager, W. Walukiewicz, W. J. Schaff, and J. Wu, *Phys. Rev. B* **76**, 041303(R) (2007)
126. X. Wang, S. B. Che, Y. Ishitani, and A. Yoshikawa, *Appl. Phys. Lett*. **92**, 132108 (2008)
127. J. W. Ager, N. Miller, R. E. Jones, K. M. Yu, J. Wu, W. J. Schaff, and W. Walukiewicz, *Phys. Status Solidi (b)* **245**, 873 (2008)
128. T. Miyajima, S. Uemura, Y. Kudo, Y. Kitajima, A. Yamamoto, D. Muto, and Y. Nanishi, *Phys. Status Solidi (c)* **5**, 1665 (2008)
129. P. Waltereit, O. Brandt, A. Trampert, H. T. Grahn, J. Menniger, M. Ramsteiner, M. Reiche and K. H. Ploog, *Nature* **406**, 865 (2000)
130. D. Segev and C. G. Van de Walle, *Europhys. Lett.* **76**, 305 (2006)
131. C.-L. Wu, H.-M. Lee, C.-T. Kuo, C.-H. Chen, and S. Gwo, *Phys. Rev. Lett*. **101**, 106803 (2008)
132. A. O. Ajagunna, E. Iliopoulos, G. Tsakatouras, K. Tsagaraki, M. Androulidaki, and A. Georgakilas, *J. Appl. Phys.* **107**, 024506 (2010)
133. C. G. Van de Walle and D. Segev, *J. Appl. Phys*. **101**, 081704 (2007)

2 Growth and Characterization Techniques of InN

2.1 Introduction

2.2 III-Nitride Growth techniques

2.2.1 Molecular Beam Epitaxy (MBE)

2.3 Characterization techniques

2.3.1 Reflection high energy electron diffraction (RHEED)

2.3.2 X-ray Diffraction (XRD)

2.3.3 Atomic Force Microscopy (AFM)

2.3.4 Electron Microscopy (EM)

2.3.4.1 Scanning Electron Microscopy (SEM)

2.3.4.2 Transmission Electron Microscopy (TEM)

2.3.5 Electrical Measurement Techniques

2.3.5.1 Hall-Effect Measurements

2.3.5.2 Capacitance-Voltage Measurements (ECV)

2.3.6 Optical measurement Techniques

2.3.6.1 Photoluminescence (PL)

2.3.6.2 Optical Transmittance

2.4 Concluding remarks

2.1 Introduction

In this chapter, common growth techniques for InN and its alloys are presented with emphasis on the MBE, which is the growth technique explored in this work. A brief description of the different characterization techniques employed during the course of the thesis is also given.

2.2 InN Growth techniques

Many techniques, such as sputtering [1-5], metalorganic vapour phase epitaxy or chemical vapour deposition (MOVPE or MOCVD) [6-9], plasma-assisted MOVPE [10-12], laser-assisted MOVPE [13,14], hydride vapour phase epitaxy (HVPE), which was used in the first demonstration of InN epitaxial growth in 1977 [15,16] and involves the reaction of hot gaseous metal chlorides like InCl (from hot HCl + In = InCl) with ammonia gas (NH_3), pulsed laser ablation or pulsed laser deposition (PLD) [17,18] and molecular beam epitaxy (MBE) [19-23], have been used to prepare InN thin films and/or nanostructures on various substrates. The first growth method by which the earlier experimental properties of InN were based is sputtering [2,3,24] and the samples were polycrystalline.

Remarkable progress in the growth of high quality epitaxial InN films by a variety of methods has recently been achieved. The most successful among all growth methods are molecular beam epitaxy (MBE) and metal-organic chemical vapour deposition (MOCVD). High quality InN crystalline films have been achieved by both MBE [25,26] and MOVPE or MOCVD [9].

The MBE is the growth technique employed for all the investigations in this work. This technique, which is briefly described in the following, is basically an ultra high vacuum deposition method, where the fluxes of atoms or molecules from solid or gas sources are incident on the substrate in the form of beams that could be interrupted instantaneously.

2.2.1 Molecular Beam Epitaxy (MBE)

A traditional GaAs MBE system is an ultrahigh vacuum (UHV) evaporation system containing solid sources, called “Knudsen cells” or “K-cells”, which are used to evaporate species like Ga, In, Al, As_4 as well as doping materials like Be and Si for *p*- and *n*-doping, respectively [27]. In the case of III–nitrides, the nitrogen is supplied by a N_2 or NH_3 gas source and such MBE system is usually called gas source MBE [28]. The schematic of a typical III-nitrides MBE system is shown in Fig. 2.1. When metalorganic chemical beams are used for the supply of group III element sources, the name “metalorganic molecular beam epitaxy (MOMBE)” or “chemical beam epitaxy (CBE)” applies [29,30]. The MBE process involves the heating of the K-cells to evaporate the elements in form of atomic or molecular beams. The beams of atoms or molecules of the constituent elements are condensed and reacted on the surface of a heated single crystal substrate held by the manipulator. The manipulator permits the rotation of the substrate during the growth process in order to enhance uniform thickness and composition of the intended material. MBE growth is carried out at relatively low T_{sub} under conditions far from thermodynamic equilibrium unlike epitaxial growth techniques, such as liquid phase epitaxy (LPE) that proceed at conditions near thermodynamic equilibrium [31].

MBE depends on the kinetics of the surface processes that occur when the impinging beams react with the outermost atomic layers of the substrate [32] and is a very slow technique with typical growth rates in the range of 0.25 – 1.25 μm/h. In comparison to MOCVD and other growth techniques being used in the III-nitride semiconductor research, MBE allows lower deposition temperatures (typically from RT to 1000°C), layer thickness control to the sub-monolayer level, and actual flux measurement from the sources with an ion gauge flux monitor. MBE technique also has the advantage of being compatible with a wide range of surface analysis techniques such as, reflection high energy electron diffraction (RHEED), quadrupole mass spectrometry (QMS) for gas analysis, and Auger electron spectrometry (AES).

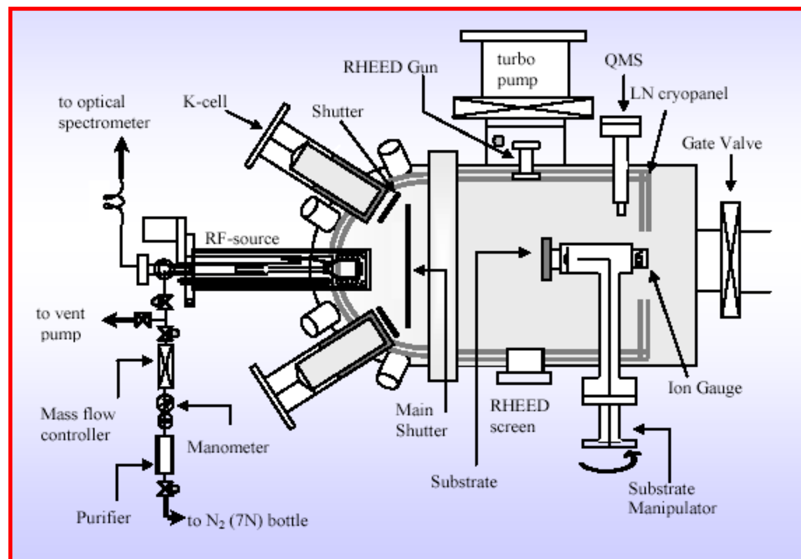

Figure 2.1 *Schematic diagram of a typical RF-MBE system, showing the several components (Figure from Georgakilas et al. 2003 [33]).*

Due to the inert nature and strong N-N bond of molecular nitrogen (N_2), the need to break N_2 to atomic species or nitrogen containing molecule with weaker bonds is important in MBE growth [34,35], leading to some modifications of the conventional MBE method by installing additional component, such as radio-frequency (rf) or electron cyclotron resonance (ECR) microwave plasma sources to activate nitrogen species [33,36]. In an ECR-microwave plasma-assisted MBE system, the ionic nitrogen species are formed by passing molecular nitrogen at a pressure $\geq 10^{-4}$ Torr through the ECR source at 2.45 GHz [37]. The source is compact [Fig. 2.2(a)], allowing it to be inserted into the source flange and through the cryoshroud of an MBE chamber in such a way as to have a direct line of sight to the substrate and thereby minimise recombination through collisions [38]. The main disadvantage of ECR sources is the high energetic ions (60 eV) bombardments of the growing films, leading to the displacement of bulk atoms [36,37].

As an alternative to ECR, the rf-plasma source (also called nitrogen plasma source) typically employs 13.56 MHz rf coil to couple energy into the plasma discharge region [33] and offers negligible radiation damage by producing nitrogen radicals with energies in the region of 2 eV [37]. Electrodeless discharge, together with a pyrolytic boron nitride (PBN) discharge tube capped with a PBN exit plate

(aperture), as shown in Fig. 2.2(b), is used to minimize contamination [39]. Nitrogen is introduced into the PBN tube and the RF energy at 13.56 GHz is inductively coupled through a water-cooled copper coil to create the plasma [33]. The generation rate of the reactive atomic nitrogen strongly depends on the aperture size and density while small aperture size coupled with high aperture density is preferable to obtain higher production of reactive atomic nitrogen with less nitrogen ions [36]. In the case of the Ammonia (NH_3) or dimethylhydragen gas source MBE, cracking promotes molecular N_2 generation that should be avoided [40].

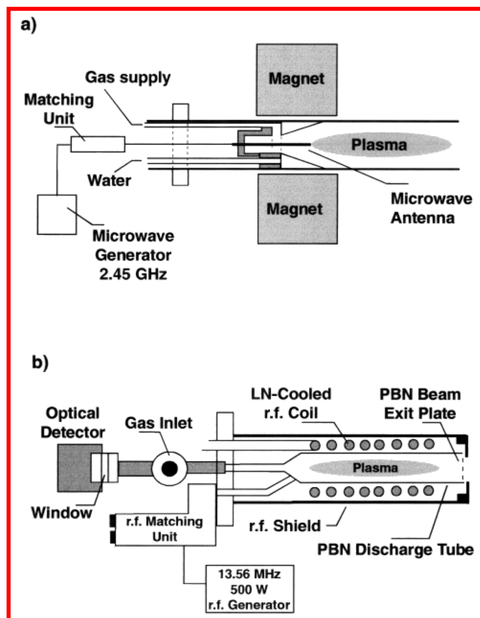

Figure 2.2 *(a) Schematic diagram of an ECR source (2.45 GHz) and (b) rf plasma source (13.56 MHz) for producing nitrogen radicals. (Figure from O. Ambacher 2003 and the references therein [37]).*

The photographic image of the Riber 32P MBE system used for the epitaxy of InN in this thesis is shown in Fig. 2.3. The system consists of the conventional Knudsen cells [Fig. 2.1]; inside of which porcelain boron nitride (PBN) crucible are inserted. Solid group-III materials of Al, Ga and In are stored in the crucibles. Also installed in the system are Be and Si doping sources. The temperature of each effusion cell can be ramped up to ~1500°C, although lower temperature is employed for the supply of molecular or atomic beam (evaporation) during growth, which depends on the vapour pressure of the element. The temperatures of the cells as well as that of the rotatable manipulator (growth or substrate temperature) are computer-controlled.

An Oxford Applied Instruments HD-25 RF plasma source with operating power up to 600 W was installed on it to activate the nitrogen gas and supply active nitrogen. The nitrogen flow rate in the plasma source was controlled by a 2.0 standard cubic centimetres per minute (sccm) range MKS mass flow controller. The RF source is equipped with a Kodial window that has a direct line of sight to the discharged tube through the gas feed tube [33,41]. The investigated heterostructures and nanopillars were grown using nitrogen flow spanning 0.1 to 1.35 sccm and operating RF-power range from 300 to 400 W. The plasma source was always operating in the high brightness mode, which is also the preferred mode of operation during growth of nitrides [41]. The exact composition of the nitrogen beam from the plasma source can be very important for the PAMBE growth [33]. The qualitative investigation of the concentration of the active nitrogen species; in terms of the metastable molecular nitrogen (N_2*) and atomic nitrogen (N), and their dependence on the RF source operating conditions has been carried out by Illiopoulos *et al.* The measured

integrated intensities of the respective emissions as a function of RF power and nitrogen flow rate are shown in the contour map of Fig. 2.4 [41]. The concentration of excited molecular nitrogen increases monotonically with both RF power and nitrogen flow [Fig. 2.4(a)], while the concentration of atomic nitrogen is rather insensitive to the gas flow and depends on the RF power coupled to the source [Fig. 2.4(b)].

Figure 2.3 *Photographic image of the Riber 32P MBE system used for the epitaxy of the InN heterostructures and nanopillars reported in this work. It consists of the conventional Knudsen cells for the supply of In, Ga and Al atomic beams with two additional sources for Be and Si. An Oxford Applied Instruments HD-25 RF plasma source is employed to produce atomic nitrogen species. The equipment is installed in a 100 m^2 clean room of class 1000.*

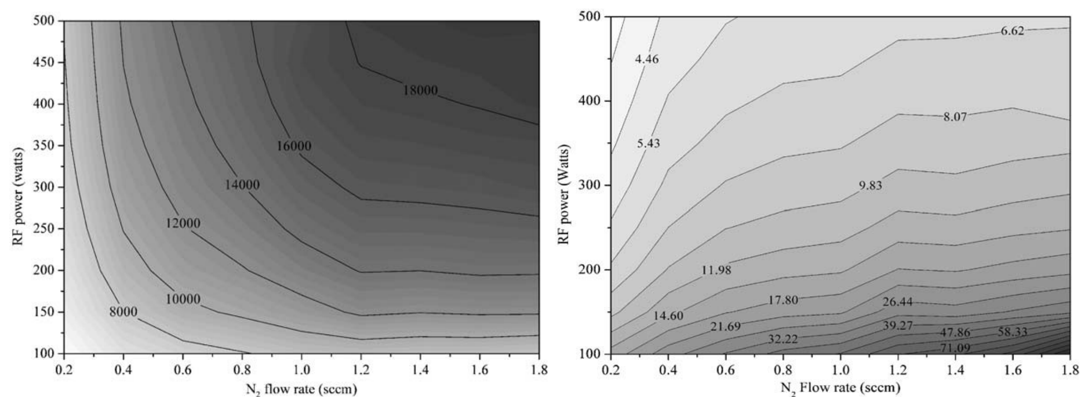

Figure 2.4 *(a) Integrated intensity of excited molecular species optical transitions as a function of RF power and nitrogen gas flow rate. (b) Ratio of excited molecular to atomic nitrogen optical emission intensities as a function of RF power and nitrogen gas flow rate (Figure from Iliopoulos et al. 2005 [41]).*

Comparison investigations of the metastable molecular and atomic nitrogen [Fig. 2.5(a)] with GaN growth rates [Fig. 2.5(b)] as a function of the nitrogen flow rate suggest that excited molecular species are primarily responsible for GaN growth

[41]. These results, which should also be applicable to the III-nitride semiconductors group in general, show that the plasma source can be tuned to operate in conditions where mainly excited nitrogen molecules are present or where excited molecules and atomic nitrogen co-exists in the plasma cavity. Nitrogen ions consisting of ionized molecules (N_2^+) and atoms (N^+) were not observed by Illiopoulos *et al*. because of the weak character of the plasma's ionic content [41].

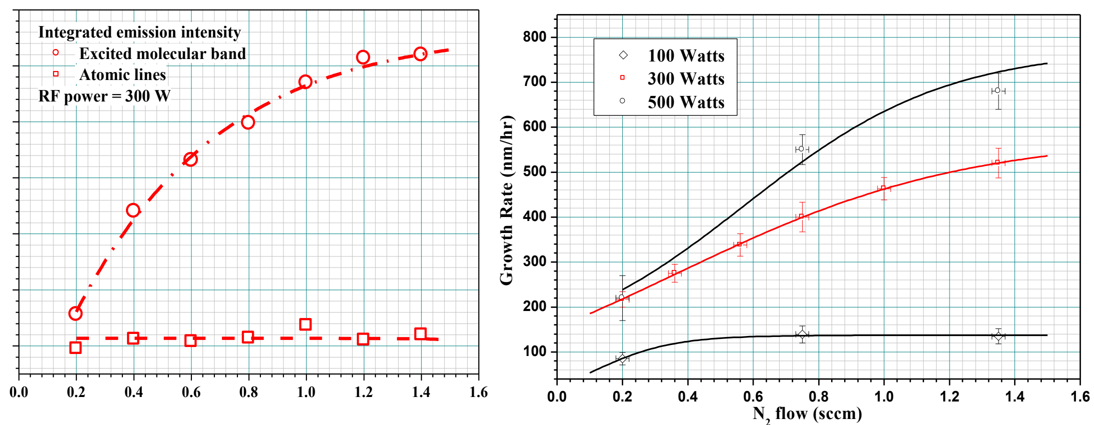

Figure 2.5 *(a) Excited molecular and atomic integrated emission intensities for 300W RF power as a function of nitrogen gas flow rate (b) Growth rates of gallium nitride films as a function of nitrogen flow rates for RF power levels equal to 100, 300 and 500 W. (Figure from Iliopoulos et al. 2005 [41]).*

The MBE growth chamber is pumped from a turbo-molecular pump, ion pump and Titanium sublimation pump. Liquid nitrogen is used to cools the chamber walls (cryopanel) to cryogenic temperatures which prevents evaporation from the large surface area of the cryopanel. Moreover, stray or unwanted impurity atoms in the chamber looses their thermal energy and stick (freeze) to the panel on collision with the walls; considerably improving the purity of the growth chamber. All growth experiments were performed in UHV with background pressure of 10^{-11} Torr. However, during growth, the typical pressure in the growth chamber can increase up to 1.5 – 4.5 x 10^{-5} Torr due to the introduction of nitrogen species. A quadrupole mass spectrometer (QMS) from Hidden analytical and reflection high energy electron diffraction (RHEED) from STAIB Instrumente are also installed in the growth chamber for *in-situ* analyses. The MBE equipment is installed in ~ 100 m^2 clean room of class 1000.

The major advantage of the MBE is that the growth surface could be kept clean by the UHV; thus the pressure of the vacuum environment surrounding the growing crystal must be kept as low as possible to avoid contamination that might affect electrical properties, film morphology and even whether or not epitaxial growth takes place. Due to the requirement of infrequent collisions of atomic beam with impurity atoms in the MBE, sustaining an ultra-high vacuum environment in the growth chamber is of utmost importance. The allowable residual gas pressure to preserve the existence of molecular beams requires the free mean path (λ) of the residual gas molecules to be larger than the distance between vapour source and substrate [Fig. 2.6] defined by λ according to the kinetic gas theory to be [27, 42]

$$\lambda = \frac{RT}{2^{1/2}\pi.N_A.p.\sigma^2} \quad \text{cm} \tag{2.1}$$

where R is the gas constant = 8.31 Joule/mole.K, N_A is the number of molecules in one mole of gas (Avogadro's number) with a value 6.02 x 10^{23} molecules/mole, T the room temperature = 300 K, k is the Boltzmann constant = 1.38 x 10^{-23} JouleK^{-1}, σ a collision diameter typically of the order of 2 to 5 angstroms and is taken as 300 pm for nitrogen [38] and p the gas pressure in Torr. Since the basic relation describing residual gas in an imperfect vacuum [42] is the ideal gas ($pV = RT = N_A kT$), equation (2.1) becomes

$$\lambda = \frac{k.T}{2^{1/2}\pi.p.\sigma^2} = \frac{k.T}{p(Torr).\sigma^2\ (\AA^2)} \quad \text{cm} \tag{2.2}$$

For example, a mean-free path (λ) of 7.8 cm is determined for a pressure (p) of approximately 10^{-3} Torr. This distance should increase as p reduces in accordance with Fig. 2.7. For our MBE system, the chosen mean-free path of 12 cm, which corresponds to a vacuum pressure of ~ 6.5 x 10^{-4} Torr, prevents collisions between residual gas molecules and vapour beam and permit the substrate to be reached by the beam. This region is marked with red arrow in Fig. 2.7.

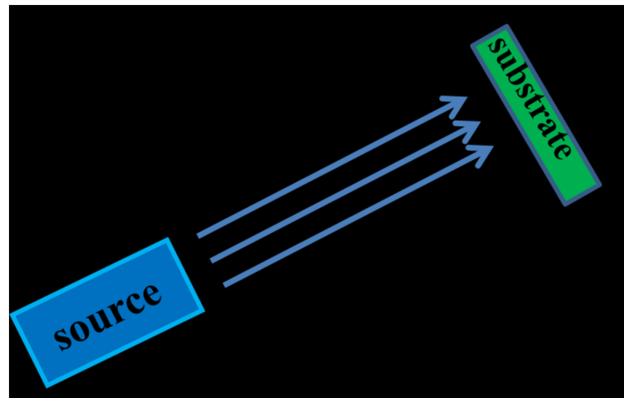

Figure 2.6 *Illustration of the mean-free path (λ) of the molecular beam from the vapour source (K-cell) to the growth surface of the substrate. The typical λ of the PAMBE used for this work is 12 cm.*

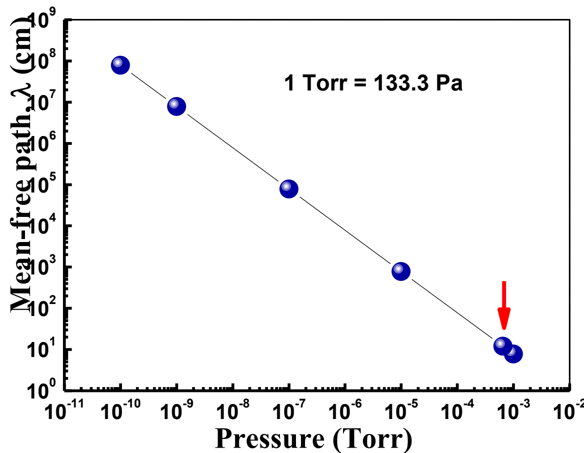

Figure 2.7 *The mean-free path (λ) of atoms as a function of growth chamber pressure. The red arrow indicates the allowable region the PAMBE growth conditions must satisfy.*

Different unwanted gases (impurities), such as oxygen (O), carbon (C) and hydrogen (H), in atomic and/or molecular form, are commonly observed in MBE growth chambers and it is impossible to completely remove them. Unfortunately, the existence of these impurities in a large amount could lead to unintentional doping of the as-grown crystal or in a worst scenario, epilayer contamination, structural defects and even non-occurrence of epitaxial growth. The incorporation of residual gases depends also on the sticking coefficient of the gases into the film material and the incidence rate of impurity atoms or molecules, which has to be much smaller than that of the evaporated atoms in order to avoid the incorporation of unwanted gas molecules into the growing film. The incident rate of impurity atoms or molecules can be calculated when the partial pressure (p_{imp}) of the unwanted gas is known by using the expression [27,43]

$$R = p_{imp}\sqrt{\frac{N_A}{2\pi M_{imp}.k.T_{imp}}} = 3.513 \times 10^{22}\frac{P_{imp}(\text{Torr})}{\sqrt{M_{imp}(\text{g}).T_{imp}(\text{K})}} \text{ cm}^{-2}\text{ s}^{-1} \quad (2.3)$$

where M_{imp} and T_{imp} are the molecular weight and the temperature of the impurities, respectively. For example the rate of collisions of molecules of O_2 on the substrate is equal to ~ 3.5 x 10^9 $cm^{-2}s^{-1}$, if $p_{O2} = 10^{-11}$ Torr, M_{O2} = 16 and T_{O2} = 300K. The growth of epitaxial layers requires sufficiently pure and uncontaminated growth process to permit the concentration of unwanted impurities to be well below dopant concentrations and the finite background pressure establishes the purity of the growth [42]. The UHV MBE with base pressure of 10^{-11} Torr, employed in this study, reduced the effect of such unwanted gas molecules or other impurity contamination to a negligible level, leading to the growth of high purity InN heterostructures and nanostructures.

The number of atoms evaporated per second on heating up a metallic source can be estimated by also using [44]

$$J_a = \frac{P_{III}.A.N_A}{(2\pi.R.T_{III}.M_{III})^{1/2}} = 3.51 \times 10^{22}\frac{P_{III}(\text{Torr}).A(\text{cm}^2)}{\sqrt{M_{III}.T_{III}(\text{K})}} \text{ s}^{-1} \quad (2.4)$$

where P_{III} is the equilibrium vapour pressure of the III-element at the cell temperature T_{III}, A is the surface area of the crucible's orifice, and M_{III} is the molecular or atomic weight of the element. The corresponding flux of atoms incident on the substrate surface can be determined by the number of incident atoms per unit time per unit area as [44]

$$J_{III} = \frac{J_a}{\pi\lambda^2} = \frac{P_{III}.A}{l^2(2\pi^3.R.T_{III}.M_{III})^{1/2}} = 1.118 \times 10^{22}\frac{P_{III}(Torr).A(\text{cm}^2)}{\lambda(\text{cm})^2[T_{III}(K).M_{III}]^{1/2}} \text{ cm}^{-2}\text{s}^{-1} \quad (2.5)$$

where l is the distance between the thermal evaporator (source) and the substrate. In the case of metallic Indium (In) where M_{In} = 114.82, if the beam equivalent pressure (BEP) or P_{In}, which is measurable by the Bayard Alpert gauge installed in the growth chamber of the MBE, is 6 x 10^{-4} Torr when the In source temperature (T_{In}) is at 800°C, then the typical number of incident In atoms impinging on the substrate during growth will be 3.08 x 10^{14} $cm^{-2}s^{-1}$, assuming that λ = 12 cm and A = 2 cm^2. It should be mentioned that the effusion cell temperature plays a very important role in controlling the value of J_{III} at every point in time.

The growth rate of III-nitride compound semiconductors can be estimated using [45]

$$GR_{III} = \frac{J_{III}.t_{ML}}{N_s} \quad (2.6)$$

where t_{ML} and N_s are the monolayer thickness and surface density of the material, respectively. For hexagonal InN (0001), the $t_{ML} = \frac{c}{2}$ = 2.85 Å (where c is the lattice constant along the [0001] axis of the hexagonal unit cell), $N_s = 2/\sqrt{3}\,a^2 = 9.2 \times 10^{14}$ cm^{-2} (where a is the lattice constant in the plane perpendicular to the c-axis) and J_{In} has been previously estimated as 3.08×10^{14} $cm^{-2}s^{-1}$ when the In effusion cell temperature is 800°C. The growth rate can therefore be estimated as 0.96 Å/s. While this growth rate is basically J_{In} dependent, the growth rate of InN can also be determined indirectly from that of GaN growth under Ga-rich growth conditions [Fig. 2.5(a)] by using the expression:

$$GR_{InN} = GR_{GaN} \frac{c_{InN}}{c_{GaN}} \left(\frac{a_{InN}}{a_{GaN}}\right)^2 \quad (2.7)$$

This method of determining InN growth rate is valid only on the conditions that the growth of InN occurs with similar RF power and nitrogen gas flow rate as those employed for GaN growth. The growth rate of AlN also can be obtained in a similar way by changing the parameters of InN in equation 2.7 to those of AlN to have

$$GR_{AlN} = GR_{GaN} \frac{c_{AlN}}{c_{GaN}} \left(\frac{a_{AlN}}{a_{GaN}}\right)^2 \quad (2.8)$$

2.3 Characterization techniques

In this section, the characterisation techniques employed to determine the properties of the InN and alloys *in-situ* and *ex-situ* are discussed.

2.3.1 Reflection high energy electron diffraction (RHEED)

Developed by Nishikawa and Kikuchi in 1928 [46], the reflection high energy electron diffraction (RHEED) is a very crucial *in-situ* ultra-high vacuum (UHV) characterisation method that gives information on surface structure during the growth of epitaxial film and one of the components that makes MBE versatile, especially in the growth of high quality thin films. RHEED consists of an electron gun (electron source) and phosphor fluorescence screen that detects the reflected beam from the sample's surface [47] and permits direct observation of the substrate's or sample surface structure during growth, enabling the *in-situ* study and control of the growth process down to sub-monolayer scale. RHEED diffraction patterns can be obtained from layers as thin as few tens of angstroms [48] down to less than 1Å [49]. A high energy beam of electrons (5-100 keV) with wavelengths smaller than prominent crystalline interplanar spacing is directed at a low angle (1-3°) to the surface and scattered on a fluorescent screen. The low angle of incidence prevents electron loss into the sample's bulk. The reciprocal lattice degenerates into lattice rods normal to the surface plane because of the two dimensionality of the surface [50]. A fraction of the electron beam is diffracted (scattered) by the atoms at the surface and interferes constructively to form a regular diffraction pattern on the screen as shown

schematically in Fig. 2.4(a). Given that the Bragg equation is $\lambda = 2d\sin\theta$, the angles of scattering by a crystal can be determined. The distance between adjacent streaks in reciprocal space could also be simply defined by $2\frac{\pi}{a}$, where a is the surface lattice constant. The corresponding wavelength (λ) to an accelerating voltage V (volts) is expressed as [51]

$$\lambda \approx \frac{12.247}{\sqrt{V\,(1+10^{-6}V)}}\ [\mathring{A}] \tag{2.9}$$

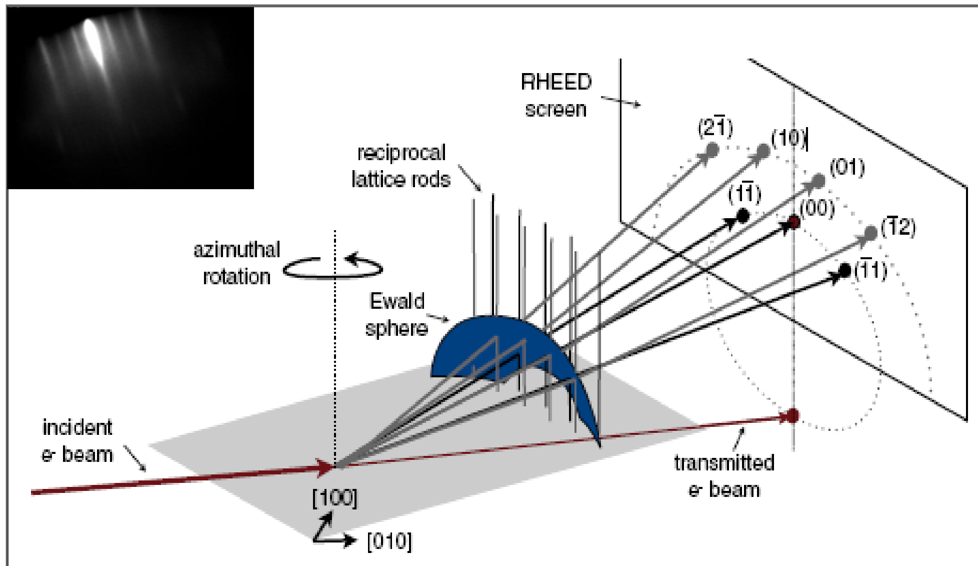

Figure 2.4 *Schematic illustration of the formation of a RHEED pattern (Figure from* Ingle *et al. 2010 [52]). The inset is the 3x3 reconstruction diffraction pattern obtained after the growth of a 100 nm AlN film on Si (111) substrate during this work.*

The real surface lattice structure is always different from the structure of the bulk material due to rearrangements of the surface atoms (reconstructions), making the top layer to be of different periodicity. A 3x3 reconstruction RHEED diffraction pattern obtained from the surface of a 100 nm AlN film grown on Si (111), during one of the experiments carried out in this work, is depicted in the inset.

There are mainly two types of diffraction pattern obtainable form RHEED; Transmission-reflection diffraction and true reflection-diffraction [51,53]. They result to spotty and elongated streaks patterns, respectively. The transmission-reflection diffraction applies to rough surfaces, leading to the concurrent transmission and reflection of beam through the three dimensionally grown surfaces [Fig. 2.5(a)] and resulting to spotty RHEED pattern. However, only reflection diffraction is responsible for smooth two-dimensional (2D) surfaces, leading to streaky diffraction pattern [Fig. 2.5(b)]. During operation, the electron beam of RHEED is at the grazing incidence while the molecular beams impinge almost normally on the substrate, avoiding interference with the flow of molecular beams in the deposition chamber.

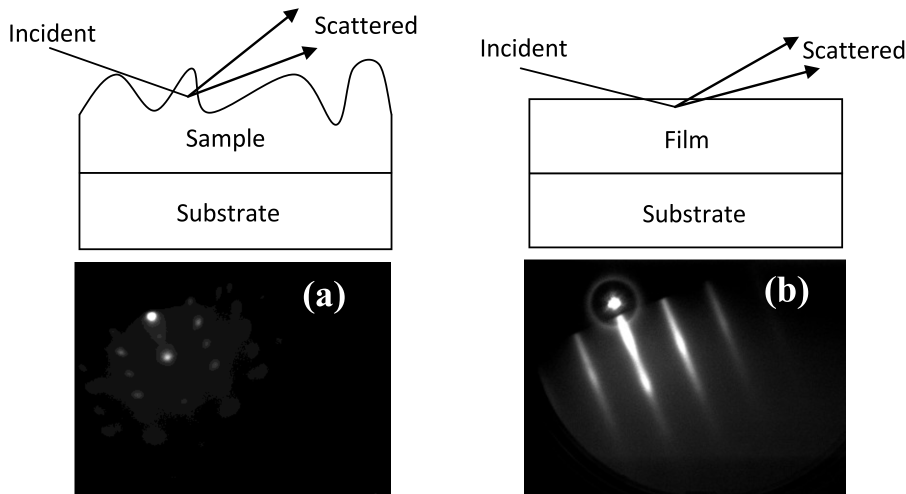

Figure 2.5 *Schematic diagrams and RHEED patterns of (a) Transmission-reflection diffraction: spotty diffraction pattern from a three dimensional (3-D) growth of InN on Si. The high intensity bright spots in the pattern represent the spots where many scattered electrons reach the detector (screen) and (b) True reflection diffraction: streaky RHEED pattern obtained for InN grown directly on Si (111).*

2.3.2 X-ray Diffraction (XRD)

X-ray diffraction is a very popular and important *ex-situ* non-destructive technique for structural characterisation of crystals. The spacing between atoms or atomic size in a crystal and the wavelength of the incident beam should be similar in order to produce significant diffraction [54]. The wavelength (λ) of X-rays, which is of the same order of magnitude (0.1-10 nm) with the size of atoms or spacing (*d*) between planes in a crystal, makes X-ray diffraction useful for producing diffraction pattern and probing the structural arrangement of atoms in a wide range of materials. The most important advantage of X-ray diffraction over diffraction techniques, such as low energy electron diffraction (LEED) and reflection high energy electron diffraction (RHEED), is that the interpretation of the measured intensity profiles is not hampered by the multiple-scattering effects that play an important role in electron diffraction [55], since electrons are deflected by the electric and magnetic fields present in a crystal lattice. An additional advantage is that X-rays can penetrate deep into materials and provide information about the internal structure, i.e. buried layers and interfaces, with little or no damage done to the structure [56]. X-ray diffraction can also be used, in conjunction with dynamic simulations, for the extraction of the compositions, strains, and thicknesses of individual layers in multilayer device structures [38].

X-rays can be generated in a cathode ray tube by using a heated filament to produce electrons, which are accelerated toward a target by using a high voltage difference between the filament and the target, causing a bombardment of the target material with electrons [57]. Electrons with sufficient energy dislodge inner shell electrons of the target material and characteristic X-ray spectra are produced when outer shell electrons replace them. The emitted spectra consist of several components but the most commonly used are the K_α and K_β. K_α has a slightly shorter wavelength

and higher intensity than K_β. The wavelengths of the X-rays are characteristic of the target material, which may be Cu, Fe, Mo or Cr.

The electron cloud surrounding each atom in the 3-D crystal (sample) acts as scattering centres for the X-rays [54]. Constructive interference occurs between the scattered (diffracted) X-rays when the Bragg's Law ($n\lambda = 2d \sin \theta$) is satisfied, that is, the path length difference for beams diffracted from different atoms must be an integral multiple of the X-ray wavelength. The intensity of diffracted X-rays signal is measured, using a scintillation detector, and converted to a count rate using a computer monitor output device. In a rocking curve (RC) measurement, the sample is rotated about the ω-axis of the X-ray diffractometer and the diffracted intensity is measured as a function of the angle ω [38]. For a ω-2θ measurement, which is used to confirm the structural orientation of a crystal, the sample is rotated at an angle $\omega = \theta$ and the detector at an angle 2θ relative to each other and a profile consisting of different intensity peaks can be measured when the geometry of incident rays leads to constructive interference of the diffracted beam. In general, the positions, intensities and full-width at half maximum (FWHM) values of the intensity peaks in the scan graph are used to characterise the structural properties of the sample.

The crystal mosaicity can be evaluated from the XRD ω-scan measurements (rocking curves) [58]. The broadening in the diffraction peak of ω-scan can be caused by microstructural defects (such as dislocations and point defects), wafer curvature, limited size (e.g small layer thickness), instrument resolution and compositional variation [54]. For *c*-plane InN, the screw dislocations with a Burgers vector b = [0001] result in a tilt of lattice planes[26], which in turn reflects itself in the FWHM of symmetric X-ray ω-scans or more accurately, in Williamson-Hall plots of the FWHM of ω-scan with increasing order. The egde dislocations, having Burgers vector $b = \frac{1}{3}\langle 11\bar{2}0 \rangle$, induced a twist of lattice planes [26]. Unfortunately, the twist is more difficult to measure directly by XRD, since it is accessible only via either a chi-scan of a reflection plane perpendicular to (0001), (such as $[1\bar{1}00]$ in transmission geometry) or by a phi-scan of one of these planes in grazing incidence [54]. This kind of measurements, and even the skew geometry method [54,59], is beyond the capability of the HRXRD equipment used. Alternatively, the symmetric (0002) and asymmetric $(10\bar{1}5)$ reflections were used in this thesis for estimating the mosaicity of the different films and nanopillars investigated. It is important to note that unlike the $000l$ reflections, the broadening of the $10\bar{1}l$ (where l = 1, 2,… 5) reflection is sensitive to both screw-type and edge-type threading dislocations in III-nitrides [54,58,60]. Moreover, in the case of the non-polar *a*-plane, semipolar *s*-plane and cubic InN grown and investigated during the course of this work, only the symmetric RC around the $(11\bar{2}0)$, $(10\bar{1}1)$ and (002) reflections, respectively, were obtained.

Two types of XRD exist; namely, the standard powder diffractometer and high resolution (HR) diffractometer. Both consist of the X-ray source, slits and detector [Figs. 2.6 and 2.7]. The goniometer serves as sample holder and permits rotational, translational, vertical and horizontal adjust movement of the sample and separates the source from the detector. The major difference is that the former is a low resolution diffractometer with incident beam divergence (δ) of approximately 0.5^o and a considerable radiation wavelength spread ($\Delta\lambda$) that makes it difficult to measure weak peaks near a substrate peak [54], although it gives high-intensity data for non-oriented samples.

On the other hand, the high resolution (HR) diffractometer consists of two monochromators, which eliminate unwanted wavelengths and permits a drastic reduction of δ (0.003°) and $\Delta\lambda$, and an additional crystal analyser [Fig. 2.7], which allows a high resolution measurement [54].

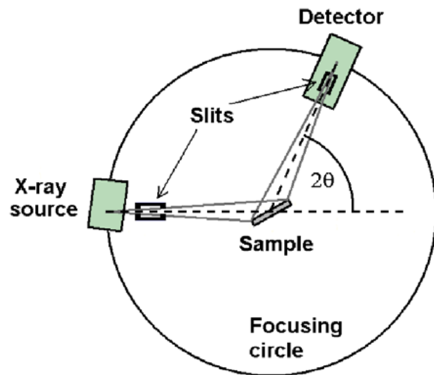

Figure 2.6 *XRD geometry for powder diffraction with no incident beam monochromator (Figure from Moram and Vickers 2009 [54]).*

XRD is ideal for the characterization of III-nitride due to its non-destructive nature and high strain sensitivity [54]. Effective measurement can still be taken despite the presence of relatively weak or broad diffraction peaks, multiple defect types and a non-spherical wafer curvature. The various samples investigated in the thesis were characterised using the high resolution BEDE D1 triple-axis X-ray diffractometer (HR-XRD) with Cu $K\alpha$ radiation (λ = 1.54056 Å). Three types of measurements, consisting of the ω scan (also called the rocking curve scan), ω-2θ scan and 2θ scan were carried out. During the measurement of the ω-scan, the detector remains stationary without the analyser slits while the sample is rotated about the ω-axis. The full width at half maximum (FWHM) is used to gauge the crystal-quality of the material under investigation. For the ω-2θ scan mode, both sample and detector (with analyser slits) are rotated to obtain diffraction profile featuring different 2θ values that can be used to investigate structure, crystallinity or preferred orientation of an epilayer. This scan mode probes exhibits less broadening in the diffraction peaks, compared to the ω-scan, and an increasing scattering vector. The broadening in this scan mode is mainly caused by lattice constant non-uniformity or strain. In the case of 2θ scan measurements, only the detector (with analyser slits) is rotated and is mainly useful for precise lattice parameter determination, providing information about lattice mismatch between the film and the substrate, and consequently, the inherent residual strain and stress in a crystal.

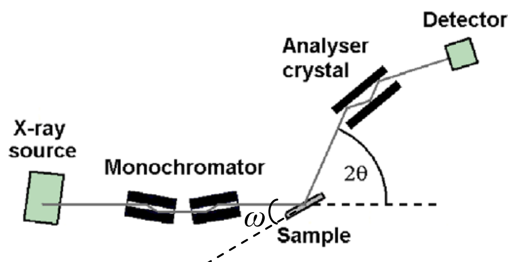

Figure 2.7 *Geometry for high-resolution diffraction (HR-XRD) with incident beam monochromator, precision goniometer and an optional analyser crystal (Figure from Moram and Vickers 2009 [54]).*

2.3.3 Atomic Force Microscopy (AFM)

The atomic force microscope (AFM) was invented by Binning *et al.* in 1986 [61] and is used like other microscopy techniques to characterise the surface morphology and the growth mode of epitaxial layers. It is one of the different possible modes of operation in scanning probe microscopy (SPM) method, where the tip interacts with the sample's surface through a physical phenomenon and measures a physical quantity like current or force that is related with the interaction [38], thereby creating an image of the surface morphology of the sample under investigation with the aid of an appropriate software. Unlike the scanning tunnelling microscope (STM) that measures the tunnelling current, the AFM measures the forces acting between a conducting sharp tip attached to the free end of a cantilever and a sample. The sensitivity and resolution of AFM depends majorly on the properties and dimensions of the cantilever as well as the tip. The AFM can be operated in a number of imaging modes [62]; namely, static or contact modes and dynamic or non-contact modes, such as tapping mode - where the cantilever oscillates at its resonant frequency. Tapping mode operation limits the damage done to the surface and the tip compared to contact mode operation.

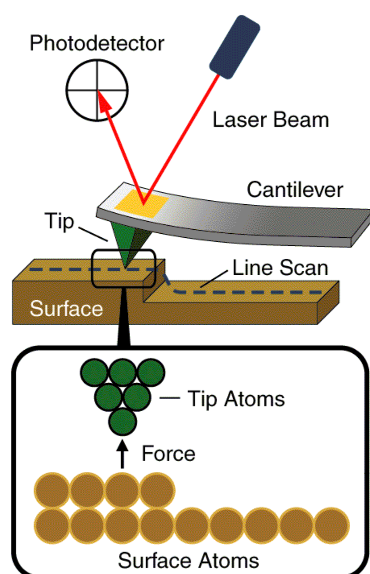

Figure 2.8 *Schematics of an AFM cantilever, tip and sample's surface (Figure from MANSIC Project [63]).*

Attractive or repulsive forces may result when the tip is brought very close to the surface that is to be examined, causing a positive or negative deflection of the cantilever [62]. A feedback mechanism is employed to adjust the tip-to-sample distance in order to maintain a small but constant force between the tip and the sample during scanning operations [51]. A photodetector detects the deflection by means of a reflected laser beam from the backside of the cantilever as shown in Fig. 2.8.

The commercially available AFM consists of a digital signal processor (DSP) that drives the AFM in real-time, the analogue-to-digital (ADC) and digital-to-analogue converters (DAC) for a two-way signals translation between the scanner head and the DSP card, the piezoelectric scanner that is driven by a high voltage amplifier and a dual monitor computer interface that permits data or images display. AFM has an excellent resolution for atomic-scale surface profiling of both conducting and insulating surfaces and demonstrates resolution more than 1000 times better than

the optical diffraction limit. The AFM employed in this work was operated in the tapping mode and it is a Digital Instrument Multimode IIIa Nanoscope system.

2.3.4 Electron Microscopy (EM)

Electron microscopy has been employed in both surface and structural analysis of materials since its inception. Basically, two major forms of EM exist in the form of scanning electron microscopy (SEM) and transmission electron microscopy (TEM) Both are briefly discussed.

2.3.4.1 Scanning Electron Microscopy (SEM)

Scanning electron microscope (SEM), as the name entails, scans the sample surface with a high-energy electrons beam, which interacts with the atoms of the sample, producing signals that contain information about the sample's topography, composition and other properties. These signals include secondary electrons, backscattered electrons, characteristic X-rays (used for elemental analysis) and continuum X-rays, and light (Cathodoluminescence (CL)), diffracted backscattered electrons [64]; which is being used to determine crystal structures and orientations of minerals [65]. Backscattered electrons and secondary electrons are the commonly used signals for imaging the samples and are basically employed in the primary and secondary mode imaging operation of SEM [66], respectively. In the primary mode, the interaction of an electron from the beam with the nucleus of the material results to Coulombic attraction that causes electron deflection; following Rutherford elastic scattering. Some of these electrons will be backscattered and re-emerge from the surface of the sample. The scattering angle's strong dependence on the atomic number of the nucleus permits the primary electrons arriving at the detector to give imaging information about the topology and composition of the sample. On the other hand, the high energy incident electrons interact with the loosely-bound conduction band (CB) electrons in the sample, giving them a limited amount of energy inorder to escape from the atom. Only those secondary electrons that are produced within a few nanometers from the surface are capable of escaping from the sample and thereby permitting high resolution topographical images to be detected. This secondary electron imaging operation is the most common SEM imaging mode.

SEM set-up can also have an additional unit commonly referred to as the energy-dispersive X-rays analyser (EDXA or EDS), which is used for qualitative and quantitative elemental analysis of material samples [64]. Its working mechanism is based on the fact that elements exhibit different atomic structure that can be characterised by analyzing the emission of X-rays. To stimulate the emission of characteristic X-rays from a sample, a high-energy electron beam is focused into the sample being studied. The incident beam may excite an electron in an inner shell, ejecting it from the shell while creating a hole where an electron from the outer shell with higher-energy fills. The difference in energy between the higher-energy shell and the lower energy shell is released in the form of X-ray photons. The energy of the emitted X-rays is characteristic of the atomic number of the emitting element. Using EDS software, a spectrum of the relative counts (intensity) versus energy of the detected x-rays is obtained and used to provide quantitative information about the elements present at a given area on the sample or map the abundance of a particular element as a function of position.

A JEOL JSM 7000F field-emission high resolution scanning electron microscope (FE-SEM), equipped with an oxford instruments INCA EDXA system, was used to study the morphological properties of the samples.

2.3.4.2 Transmission Electron Microscopy (TEM)

TEM has long been a powerful research tool for the study of thin films' mechanism of formation and structural conditions. Although a destructive technique, it is very popular and important in the study of materials growth as well as the incorporations of defects, such as dislocations, stacking faults, twin boundaries and grain boundaries in heteroepitaxial layers. TEM images are produced using a beam of high energy electrons (energies 100 keV - 1 MeV) that is incident on a sample in the form of a very thin foil (thickness <100 nm). Heteroepitaxial films can be observed in either cross-sectional or plan-view sample geometries. The prepared sample must be stable under irradiation by the high-energy electron beam, which can sometimes cause phenomena such dislocation glide, formation of vacancies, and alloy clustering [67,68].

Conventional TEM (CTEM) can be used to obtain images showing local variations in diffracting power due to electrons scattering in the strained region around dislocations, stacking faults or other defects in the crystal [69]. In diffraction contrast CTEM under two-beam conditions, an aperture inserted at the back focal plane of the objective lens permits the selection of only one beam to form image. Use of the beam transmitted directly through the image results to bright field images whereas if the diffracted beam is used to form the image, a dark field image results. Different types of contrast arise due to crystal non-uniformities such as compositional variations, voids or inclusions, thickness variations, or extended defects. Another useful CTEM technique utilizes the Moiré patterns that are formed by the interference of diffracted beams from overlapping distinct crystals. Moiré patterns can be employed to produce an effective magnification of the misfit between parallel families of crystal planes with different interplanar spacings (*d*-spacings) and are thus very useful in strain measurements. Selected area electron diffraction (SAED) patterns can also be obtained from any region of the specimen by using a selected aperture. The SAED pattern gives information about the epitaxial relationship of heterostructures [70] and is affected by the strain, epilayer misorientations (tilt or twist) relative to the substrate, formation of superlattices, etc.

In addition to diffraction contrast, defects and interfaces can be examined at atomic scale by high resolution TEM (HRTEM) which utilizes the phase contrast produced by the interference of the transmitted and multiple diffracted beams [71]. The point resolution of usual 200 kV TEM instruments is limited by lens aberrations, mechanical and electrical instabilities to around 0.2 nm, which makes difficult the examination of very localized atomic arrangements around defects such as dislocations. However, the development of spherical aberration correctors for electromagnetic lenses has led to the development of more sophisticated HRTEM and scanning TEM (STEM) microscopes with sub-Angstrom resolution [72]. The capabilities of HRTEM and HR-STEM todate are employed for the nanoscale determination of the elastoplastic behaviour of epitaxial layers. For this purpose quantitative HRTEM (qHRTEM) techniques of strain mapping have been developed [73]. Furthermore, the analytical capabilities of modern day STEM instruments have

been amplified through the developments in spectroscopic techniques such as energy dispersive x-ray spectroscopy (EDXS) and electron energy loss spectroscopy (EELS).

The TEM and HRTEM structural characterization of the InN samples investigated in this work were performed by collaborators (Prof. Ph. Komninou, Prof. Th. Kehagias and Prof. G. P. Dimitrakopulos) from the Aristotle University of Thessaloniki's Physics department, using 200 kV JEOL 2011 LaB_6 and Jeol 2010F FEG microscopes. The specimen preparations were performed by tripod polishing followed by low-energy ion milling. The approaches used for the microstructural studies include SAED, dark- and bright field CTEM, as well as HRTEM in cross-sectional sample geometry (XTEM).

2.3.5 Electrical Measurement Techniques

In this work the main electrical measurements techniques used to investigate the transport properties and other electrical properties of the InN heterostructures and/or devices are the Hall-effect and electrochemical C-V measurements. These techniques are briefly described in the following.

2.3.5.1 Hall-Effect Measurements

The Hall-effect is named after American physicist Edwin Hall, who discovered the phenomenon in 1879 [74] and is the most widely used technique to measure the transport properties of epitaxial layers. Hall measurements data over a wide temperature range (4.2–300 K) could give insight to the imperfections, uniformity and carrier scattering mechanisms in a material, but its basic use is to determine the carrier concentration, and mobility of semiconductor materials. The Hall-effect is based on the fact that electrical currents are affected by magnetic fields and it occurs when a magnetic field is applied perpendicular to the flow of current. The field causes the Lorentz force on the moving charge carriers, which induces a potential difference, called Hall voltage, in a direction perpendicular both to the current flow and the applied magnetic field.

The Hall coefficient could be experimentally determined and related to the electrical parameters through $R_H = r_H/ne$ and the resistivity through $\mu_H = R_H/\rho$, where n is the free-carrier concentration, e is the unit of electrical charge, μ_H is the Hall mobility, and r_H is the Hall scattering factor (usually assumed to be unity). Knowing the Hall coefficient helps to determine the carrier type and density of the material. The drift mobility is the average velocity per unit electric field at low electric field and is related to the Hall mobility through the Hall scattering factor by $\mu_H = \mu r_H$. The Hall scattering factor depends on the details of the scattering mechanisms that limit the drift velocity. As the carriers travel through a semiconductor, they encounter various scattering mechanisms that govern the carrier mobility in the electronic system. The major scattering mechanisms [75] that generally govern the electron transport in group III–V semiconductors is also valid for InN; such as ionized-impurity scattering, polar longitudinal-optical (LO) phonon scattering, acoustic phonon scattering (through the deformation potential that arises from the energy change of the band edges induced by strain associated with acoustic phonons), piezoelectric scattering (that arises from the electric fields that are produced by the strain associated with phonons in a crystal without inversion symmetry), and defects (dislocations and native point defects). The advantage of Hall measurements lies in providing average values of carrier density and mobility.

The low magnetic field (0.3 T) Hall-effect measurements set-up used to characterize the transport properties of the InN layers in this work is shown in Fig. 2.8(a). The equipment is computer-controllable. All measurements were taken at room temperature after soldering four small indium contacts at the edges of carefully cut 3 mm x 3 mm film pieces, using the van der Pauw geometry [76] shown in Fig. 2.8(b).

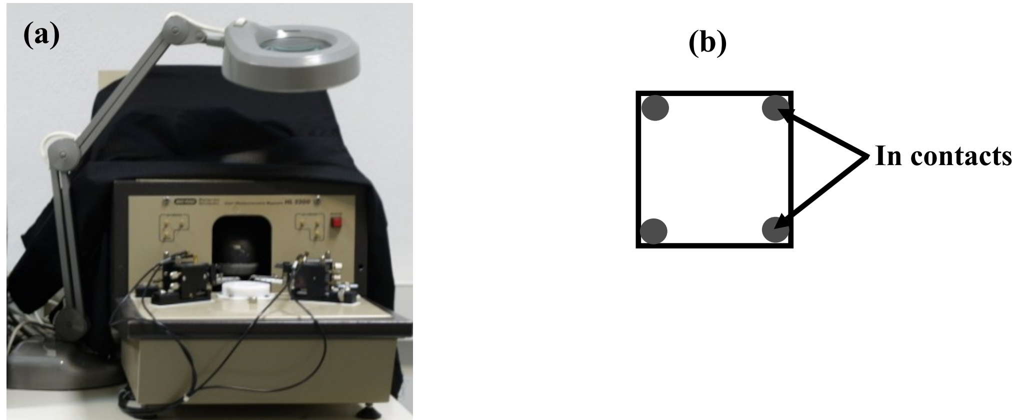

Figure 2.8 *Photographic image of the Hall-effect measurements set-up used to characterize the electrical properties of the InN samples.*

2.3.5.2 Capacitance-Voltage Measurements (CV)

The Capacitance versus Voltage (C-V) measurement technique is the method used to determine the carrier distribution in semiconductor materials and it is based on the analysis of capacitance-voltage behaviour of the depletion region of a reversed-biased Schottky barrier, which allows the extraction of the "doping profile" in a semiconductor [77]. The maximum depth to which a carrier profile can be measured by the C-V technique is limited by the avalanche breakdown field at high bias but this limitation can be overcome by capacitance-voltage measurements during electrochemical etching process of the sample (ECV) [78]. The ECV method measurement, although a destructive technique, is widely used for the measurement of the carrier concentration in semiconductors with low and high doping level [79]. It was developed by Ambridge and Factor [80] to overcome the depth limitation in depletion C-V profiling by using an electrolyte barrier to measure the carrier density and to etch the material in a controlled electrolytic process. The electrolyte solution usually performs the dual function of etching the surface at a controlled rate as well as providing a Schottky barrier contact suitable for measurement of the carrier concentration. An *ac* signal is superimposed on the dc bias to measure the capacitance and hence the carrier concentration of the semiconductor material which can also allow the depletion width to be calculated without ramping the *dc* bias.

The Biorad PN4300 Profile Plotter was employed for the ECV profiling of InN in this work. A 0.01 M electrolyte solution of potassium hydroxide is placed in contact with the wafer. Only surface ECV was done without etching the material, using similar depletion approximation calculations applicable to Schottky diode. The capacitance is determined by superimposing a small-amplitude *ac* voltage (v) of frequency typically ~ 0.3 - 5 kHz on the applied *dc* voltage V. The width of the depletion region can be obtained from

$$W = (\varepsilon_s \,.\, \varepsilon_o \,.\, A) / C \qquad (2.10)$$

and the carrier density measurement could be extracted by using;

$$N_d\,(W) = C^3 / (e.\ \varepsilon_s \,.\, \varepsilon_o \,.\, A^2.\ dC/dV) \qquad (2.11)$$

or

$$N_d\,(W) = 2 / [e.\ \varepsilon_s \,.\, \varepsilon_o \,.\, A^2.\ d(1/C^2)/dV] \qquad (2.12)$$

where W is the depletion width, C is the junction capacitance, A is the depletion area, ε_o is the permittivity of free space and ε_s is the relative permittivity of the semiconductor. The doping density was obtained from the slope of dC/dV from the C-V curve or the slope of the plot of $1/C^2$ as a function of the bias voltage.

2.3.6 Optical Measurement Techniques

The optical characterisation of the samples investigated in this work was carried out by photoluminescence and transmittance measurements. These techniques are briefly described below.

2.3.6.1 Photoluminescence (PL)

Photoluminescence (PL) is the emission of light from a material under optical excitation [81] and is one of the most important techniques of verifying heteroepitaxial suitability of a material for optical device applications, such as LED and Laser diodes [38]. It detects optical transitions from higher energy electronic states to lower energy electronic states. In the PL set-up, a laser with energy above the bandgap of the sample to be investigated is used to excite electron-hole pairs, leading to recombination of the excess carriers. Consequently, photons with characteristic energies associated with the electronic transitions in the sample are emitted. Low temperature measurements permit the whole spectroscopic information to be gathered by minimizing thermally activated non-radiative recombination processes that lead to the broadening of the PL spectra. The intensity of the PL signal provides information on the quality of surfaces and interfaces [81]. The PL spectra reported in this work were obtained by using He–Cd continuous-wave (cw) laser at 325 nm (35 mW) and a monochromator with 600 grooves/mm grating blazed at 2 µm. The measurements were taken with a special liquid nitrogen (LN_2) cooled InGaAs PIN photodiode detector with a maximum responsivity at 1.92 µm and a lock-in amplifier. Except otherwise stated, the measurements were carried out in a cryostat at 20K.

2.3.6.2 Optical Transmittance

The optical transmission measurements are usually used to determine the absorption coefficients of semiconductors. The transmitted light is measured as a function of wavelength or photon energy. The mathematical expression for the transmission is $T(E) = I/I_o$, where I is the intensity of the transmitted light and I_o is the intensity of the incident light. The transmittance data of InN films were used to estimate the absorption coefficients using

$$T(E) \sim exp\ (-\alpha d) \qquad (2.13)$$

$$\alpha(E) \sim -\ lnT(E) \times 1/d \qquad (2.14)$$

where d is the InN thickness, T is the transmittance and a is the absorption coefficient. Assuming the reflection remains constant, the optical bandgap energy (E_g) can be determined from absorption coefficient by using the Tauc's relation [82]

$$\alpha(E) \sim (h\nu - Eg)^{N} \tag{2.15}$$

where $h\nu$ = photon energy, and N = ½ and 2 for direct and indirect gap materials, respectively [83]. Since InN is a direct gap material, its $\alpha(E)$ should have a square root dependence on E, making the $\alpha(E)^2$ to exhibit a linear dependence on E. Then equation (2.6) becomes

$$\alpha(E)^2 \sim E - Eg \tag{2.16}$$

The extrapolation of this linear part to the abscissa gives the value of the absorption edge or optical bandgap (E_{go}). The optical bandgap energy determined for InN films in this thesis were all extracted by this method. The infrared optical transmittance measurements carried out in this work were done at ambient temperature after the back-side optical polishing of the sample, using a PERCKIN-ELEMER spectrophotometer with spectral range of 250 - 3200 nm, which is installed at the IESL, FORTH facilities.

2.4 Concluding remarks

All InN heterostructures and nanopillars presented in this work were grown by PAMBE. Except otherwise stated, the characterisation procedures employed have been discussed. The surface structure of the InN samples were always monitored *in-situ* by the reflection high energy electron diffraction (RHEED) attached to the MBE. The crystal orientations and quality of the InN were investigated by high resolution x-ray diffraction (HR-XRD) while the atomic force microscopy (AFM) and/or scanning electron microscopy (SEM) techniques were employed to understand the surface morphological properties and growth modes. InN microstructures were also studied with the aid of both conventional and high resolution transmission electron microscopy (TEM and HRTEM, respectively) by collaborators in Aristotle University of Thessaloniki. The electrical properties were determined by Hall-effect and ECV measurements at room temperature. The optical properties were evaluated with the use of photoluminescence (PL) and Infrared optical transmittance (T) spectroscopy.

References

1. F. Fischer and F. Schröter, *Ber. Deutsch Chem. Ges.* **43** 1465 (1910)
2. B.R. Natarajan, A.H. Eltoukhy, J.E. Greene and T.L. Barr**,** *Thin Solid Films*, **69**, 201 (1980)
3. C. P. Foley and T. L. Tansley, *Appl. Surf. Sci.* **22/23** 663 (1985)
4. T. J. Kirstenmacher, S. A. Ecelberger and W. A. Bryden, *J. Appl. Phys.* **74** 1684 (1993)
5. O. Takai, K. Ikuta and Y. Inoue, *Thin Solid Films*, **318**, 148 (1998)
6. T. Matsuoka, *in "GaN and Related Materials*", edited by S. J. Pearton, Gordon and Breach, New York , pg. 53–59 (1997)
7. A. Koukitu, T. Taki, N. Takahashi, and H. Seki, *J. Cryst. Growth* **197**, 99 (1999)
8. A. Yamamoto, Y. Murakami, K. Koide, M. Adachi, and A. Hashimoto, *Phys. Status Solidi (b)* **228**, 5 (2001)
9. A. Yamamoto, T. Tanaka, K. Koide, and A. Hashimoto, *Phys. Status Solidi (a)* **194**, 510 (2002)
10. Q. Guo and A. Yoshida, *Jpn. J. Appl. Phys*., Part 1 **33**, 2453 (1994)
11. T. Tsuchiya, M. Ohnishi, A. Wakahara, and A. Yoshida, *J. Cryst. Growth* **220**, 191 (2000)
12. M. Sato, *Jpn. J. Appl. Phys*., Part 2 **36**, L658 (1997)
13. X. Li, B. Zhou, K. S. A. Butcher, E. Florido, N. Syakir, and T. L. Tansley, *Proceedings of the Australian Compound Optoelectronic Materials Devices Conference*, Sydney, Australia, December 12–14, pg. 43 (1994)
14. A. G. Bhuiyan, T. Tanaka, A. Yamamoto, and A. Hashimoto, *Phys. Status Solidi (a)* **194**, 502 (2002)
15. L. A. Marasina, I. G. Pichugin, and M. Tlaczala, *Krist. Tech*. **12**, 541 (1977)
16. N. Takahashi, R. Matsumoto, A. Koukitu, and H. Seki, *Jpn. J. Appl. Phys*., Part 2 **36**, L743 (1997)
17. D. Feiler, R. S. Williams, A. A. Talin, H. Yoon, and M. S. Goorsky, *J. Cryst. Growth* **171**, 12 (1997)
18. P. Bhattacharya, T. K. Sharma, S. Singh, A. Ingale, and L. M. Kukreja, *J. Cryst. Growth* **236**, 5 (2002)
19. E. Dimakis, E. Iliopoulos, K. Tsagaraki, and A. Georgakilas, *Phys. Status Solidi (a)* 203, 1686 (2006)

20. Y. Saito, H. Harima, E. Kurimoto, T. Yamaguchi, N. Teraguchi, A. Suzuki, T. Araki, and Y. Nanishi, *Phys. Status Solidi (b)* **234**, 796 (2002)

21. G. Koblmüller, C. S. Gallinat, S. Bernardis, and J. S. Speck, G. D. Chern, E. D. Readinger, H. Shen, and M. Wraback, *Appl. Phys. Lett*. **89**, 071902 (2006)

22. H. Lu, W. J. Schaff, and L. F. Eastman, *J. Appl. Phys*. **96**, 3577 (2004)
23. K. Xu, W. Terashima, T. Hata, N. Hashimoto, Y. Ishitani, and A. Yoshikawa, *Phys. Status Solidi (c)* **0**, 377 (2002)

24. K. S. A. Butcher, M.Wintrebert-Fouquet, P. P-T. Chen, T. L. Tansley, and S. Srikeaw, *Mater. Res. Soc. Symp. Proc*. **693**, 341 (2002)

25. H. Lu, W. J. Schaff, L. F. Eastman, J. Wu, W. Walukiewicz, K. M. Yu, J. W. Auger III, E. E. Haller, and O. Ambacher, *Abstract of the 44th Electronic Material Conference*, Santa Barbara, CA, June 26–28, (2002)

26. E. Dimakis, J.Z. Domagala, A. Delimitis, Ph. Komninou, A. Adikimenakis, E. Iliopoulos, A. Georgakilas, *Superlatt. Microstruct.* **40**, 246 (2006)

27. S. Mader *in "Epitaxial growth Part A – Materials Science Series"*, Edited by J. W. Matthews, Academics Press, New York Chapter 2.1 (1975)

28. R. F. Davis, M. J. Paisley, Z. Sitar, D. J. Kester, K. S. Ailey, K. Linthicum, L. B. Rowland, S. Tanaka, and R. S. Kern, *J. Cryst. Growth* **178**, 87 (1997)

29. C. R. Abernathy, J. D. MacKenzie, and S. M. Donovan*, J. Cryst. Growth* **178**, 74 (1997)

30. J. Aderhold, V. Yu. Davydov, F. Fedler, H. Klausing, D. Mistele, T. Rotter, O. Semchinova, J. Stemmer, and J. Graul, *J. Cryst. Growth* **222**, 701 (2001)

31. M. A. Herman and H. Sitter, *Molecular Beam Epitaxy: fundamentals and current status",* Springer Series in Materials Science 7, 2nd Edition, Springer-Verlag Berlin Heidelberg, Germany*,* Springer, New York, Chapter 1 (1996)

32. M. A. Herman and H. Sitter, *in Molecular Beam Epitaxy: Fundamentals and Current Status,* Springer Series in Materials Science 7*,* edited by M B Panish, 1st Edition, Springer-Verlag Berlin Heidelberg New York, (1989)

33. A. Georgakilas, H. M. Ng, Ph. Komninou, in "Nitride semiconductors: *Handbook on Materials and Devices"*, Edited by P. Ruterana, M. Albrecht, J. Neugebauer , Wiley-VCH, Berlin, Chap 3, p. 107 (2003)

34. J. B. McChesney, P. M. Bridenbaugh, and P. B. O'Connor, *Mater. Res. Bull*. **5**, 783 (1970)

35. N. A. Gorjunova, *Slosnye Almazopodobnye Poluprovodniki*, Moscow (1964)

36. A. G. Bhuiyan, A. Hashimoto, and A. Yamamoto, *J. Appl. Phys*., **94,** 2779 (2003)

37. O Ambacher, *J. Phys. D: Appl. Phys*. **31** 2653–2710 (1998)

38. J. E. Ayers, *Heteroepitaxy of Semiconductors – Theory, growth and Characterization*, CRC Press Taylor & Francis Group, USA. Chapter 6 pg 227- 279 (2007)

39. W. E. Hoke, P. J. Lemonias, and D. G. Weir, *J. Cryst. Growth* **111**, 1024 (1991)

40. N. Grandjean, J. Massies, and M. Leroux, *Appl. Phys. Lett*. **69**, 2071 (1996)

41. E. Iliopoulos, A. Adikimenakis, E. Dimakis, K. Tsagaraki, G. Konstantinidis, A. Georgakilas, *J. Cryst. Growth* **278**, 426 (2005)

42. K-N Tu, J.W. Mayer and L.C. Feldman, *in "Electronic Thin Film Science: for Electrical Engineers and Material Scientists",* Macmillan Publishing Company, USA. Pg 394 (1992)

43. J.R. Arthur, *Surface Science* **500**, 189–217 (2002)

44. A.Y. Cho, *in* "*The Technology and Physics of Molecular Beam Epitaxy*", edited by E.H.C Parker, Plenium Press, New York, Chapter 1 (1985)

45. E. Dimakis, *Ph.D Thesis*, Physics Department, University of Crete, Heraklion-Greece, Chapter 1 (2007)

46. Nishikawa and Kikuchi, *Nature (London)* **121**, 1019 (1928)

47. E.J. Scheibner, L.H. Germer and C.D. Hartman, *Rev. Sci. Instrum*. **31**, 112 (1960)

48. D. B. Dove *in "Epitaxial growth Part A – Materials Science Series"*, Edited by J. W. Matthews, Academics Press, New York, Chapter 3.4 (1975)

49. R. C. Newman and D. W. Pashley, *Phil. Mag*. **46**, 917 (1955)

50. G. Bauer and G. Springholz,*Vacuum* **43**, 357 (1992)

51. M. A. Herman and H. Sitter, *Molecular Beam Epitaxy: fundamentals and current status",* Springer Series in Materials Science 7, 2nd Edition, Springer-Verlag Berlin Heidelberg, Germany*,* Springer, New York, Chapter 4 (1996)

52. N. J. C. Ingle, A. Yuskauskas, R. Wicks, M. Paul and S. Leung, *J. Phys. D: Appl. Phys*. **43**, 133001 (2010)

53. G.M. Minchev, L.M. Trendafilov, M.I. Dencheva-Zarkova, *Proceeding of the 2nd International workshop on MBE growth physics and technology,* Warsaw, Poland October 21 – 25, (1996)

54. M A Moram and M E Vickers *Rep. Prog. Phys*. **72**, 036502 (2009)

55. K. Heinz, *Appl. Phys. A* **41**, 3 (1986)

56. E. Vlieg, A. Van't ent, A.P. de Jongh, H. Neerings and J.F. van der Veen, *Nuclear Instruments and Methods in Physics Research A* **262**, 522 (1987)

57. B D Cullity and S R Stock *in "Elements of X-Ray Diffraction"*, 3rd edition, (Englewood Cliffs, NJ: Prentice-Hall) (2001)

58. V. Srikant, J. S. Speck, and D. R. Clarke, *J. Appl. Phys.* **82**, 4286 (1997)

59. P.F. Fewster, J. Appl. Crystallogr. 22 (1989) 64

60. H Heinke, V Kirchner, S Einfeldt and D Hommel, *Phys. Status Solidi (a)* **176**, 391 (1999)

61. G. Binning, C.F. Quate, Ch. Gerber, *Phys. Rev. Lett.* **56**, 930 (1986)

62. Franz J. Giessibl, *Rev. Mod. Phys.* **75**, 949 (2003)

63. MANSiC Project http://www.mansic.eu/documents/PAM1/Frangis.pdf

64. J. Goldstein, D. Newbury, D. Joy, C. Lyman, P. Echlin, E. Lifshin, L. Sawyer, and J. Michael, *in "Scanning Electron Microscopy and X-Ray Microanalysis"*, 3rd edition, Kluwer Academic, New York, Chapter 1 (2003)

65. A. J. Schwarz, M. Kumar, and B. L. Adams, *in "Electron Backscatter Diffraction in Material Science",* Kluwer Academic/Plenum Publishers, New York (2000)

66. David C. Joy, *Ultramicroscopy* **37**, 216 (1991)

67. T.M.Smeeton, M.J. Kappers, J.S. Barnard, M.E. Vickers., C.J. Humphreys, *Appl. Phys. Lett.* **83**, 5419 (2003)

68. Th. Kehagias, Ph. Komninou, P. Grigoriadis, G. P. Dimitrakopulos, J. G. Antonopoulos, and Th. Karakostas, *Interface Science* **3**, 195-201 (1995)
69. D. B. Williams and C. B. Carter, *in "Transmission Electron Microscopy-A Textbook for Materials Science"* , 750 pp., Plenum Press, New York, NY (1996).
70. G. P. Dimitrakopulos, Th. Kehagias, A. Ajagunna, J. Kioseoglou, I. Kerasiotis, G. Nouet, A. P. Vajpeyi, Ph. Komninou, and Th. Karakostas, *Phys. Status Solidi (a)* **207**, 1074 (2010)
71. J. C. H. Spence, *"High Resolution Electron Microscopy",* 3rd edition, Oxford University Press (2003)
72. Nobuo Tanaka, *Sci. Technol. Adv. Mater*. **9**, 014111 (2008)
73. S. Kret, P. Ruterana, C. Delamarre, T. Benabbas, and P. Dluzewski, *in "Strain, Chemical Composition, and Defects Analysis at Atomic Level in GaN-based Epitaxial Layers", in Nitride Semiconductors: Handbook on Materials and Devices,* eds. Pierre Ruterana, Martin Albrecht, and Jörg Neugebauer, WILEY , Chapter 9, (2006)

74. E.H. Hall, *American Journal of Mathematics,* **2**, 287 (1879)

75. K. A. Wang, Y. Cao, J. Simon, J. Zhang, A. Mintairov, J. Merz, D. Hall, T. Kosel, and D. Jena, Appl. Phys. Lett. **89**, 162110 (2006)

76. NIST online, http://www.nist.gov/pml/semiconductor/hall_resistivity.cfm

77. D. K Schroder, *"Semiconductor Material and Device Characterization"*, 3rd Ed. John Wiley & Sons, Inc. New Jersey Chapter 2 (2006)

78. N. Sieber and H. E. Wulf, *Phys. Status Solidi (a)* **126**, 213 (1991)

79. P. Blood, *Semicond. Sci. Technol.* **1**, 7 (1986)

80. T. Ambridge and M. Faktor, *J. Appl. Electrochem*. ***5,*** 319 (1975)

81. T.H. Gfroerer, *in* "*Encyclopedia of Analytical Chemistry",* edited by RA Mayers, John Wiley & Sons Ltd, Chichester, 9209 (2000)

82. J. Tauc and A. Menth, *Non Cryst. Solids* **569**, 8 (1972)

83. J. Tauc, *in "Amorphous and liquid semiconductors"*, Plenum Press New York, pg. 171 (1974)

3 Background of the Molecular Beam Epitaxy (MBE) of InN

3.1 Epitaxial growth of InN: Substrates for InN epitaxy

3.1.1 Sapphire substrates

3.1.2 Silicon (111) substrates

3.2 Epitaxial growth process

3.2.1 Growth modes in heteroepitaxy

3.3 Substrates' surface preparations

3.4 Determination of III/V flux ratio

3.5 Estimation of the MBE growth temperature

3.6 InN growth properties

3.7 InAlN growth properties

3.8 Concluding remarks

3.1 Epitaxial growth of InN: Substrates for InN epitaxy

In MBE, thin films are grown by the supply of the constituent elements in the form of incident molecular or atomic beams on a substrate surface maintained at an elevated temperature in ultrahigh vacuum. Epitaxial growth occurs by the diffusion of the incident atoms on the surface and their incorporation at proper sites extending the crystal of the underlying single crystalline substrate. The major problem in III-nitrides thin film growth is the non-availability of sufficiently large single-crystal substrates for homoepitaxial growth. The lack of substrates leads to heteroepitaxial growth, which has always resulted to problems caused by lattice mismatch (*LM*) and thermal expansion mismatch (TM). Additional problems, such as inversion domains, arise when the polar III-V compounds are grown heteroepitaxially on non-polar substrates, such as Si [1].

The common expression for determining *LM* or lattice misfit (f) is

$$f = (a_{substrate} - a_{epilayer})/a_{epilayer} \quad (3.1)$$

where $a_{substrate}$ and $a_{epilayer}$ are the corresponding in-plane lattice periodicities of substrate and epilayer, respectively. The LM is responsible for most of the defects that are introduced *in-situ* during the growth process, whilst TM may also induce defects or adhesion problems when samples are cooled down from the growth temperature to room temperature at the end of the growth. TM between substrate and nitride is the usual origin of the residual stress that occurs in the epilayer upon cooling. To date, no ideal substrate exists for InN heteroepitaxial growth. InN is grown on foreign material single crystalline substrates, since no InN substrate material is available to promote homoepitaxial growth. The heteroepitaxy of high quality planar InN heterostructures requires layer-by-layer-growth and achieving a high crystalline quality material needs an atomically smooth and clean substrate surface. At present, sapphire and SiC substrates pre-dominate the heteroepitaxial growth of III-nitrides. In what follows, a brief introduction of the two substrates used for InN heteroepitaxy in this work is discussed.

3.1.1 Sapphire substrates

Sapphire (Al_2O_3) is the most extensively used substrate material for the epitaxial growth of III-nitrides. The large lattice and thermal mismatch existing between III-nitrides and sapphire is expected to generate an extremely high density of structural defects. However, the good quality crystals of sapphire together with its transparency, stability at high temperature and availability at relatively low cost have made it a substrate of choice for III-nitrides growth. InN has not been grown directly on sapphire substrates in most reported works. An intermediate nucleation/buffer layer made up of AlN or GaN or the combination of both materials [2] has been used to improve adhesion and microstructure of the InN films. The existing LM of about -25% in-between sapphire and InN is effectively reduced to -13% and -11% by growth on an AlN or GaN buffer layer, respectively. The possibility of growing high quality nitride thin films using sapphire of different orientations is of keen interest in nitride research. *C*-plane (0001), *m*-plane $(1\bar{1}00)$ and *r*-plane $(1\bar{1}02)$ Al_2O_3 are the most common sapphire orientations being presently employed for III-nitrides epitaxy. The schematic drawing of common crystallography planes for III-nitride family is

shown in Fig. 3.1. The crystallography planes of substrates are very important in general, since overgrown layer almost always follow the structure of the underlying substrate material.

3.1.2 Silicon (111) substrates

Silicon substrates have excellent crystal quality and are available with low cost, in large sizes (up to 12 inch in diameter), cleavable and the (111) surface exhibits only 8% LM with (0001) InN. The accurately known characteristics, good thermal conduction (approximately 3 times larger than that of sapphire) as well as the advanced technology should make Si the most appropriate substrate material for InN heteroepitaxy. Si (111) exhibits a diamond crystal structure and among the commonly available form or orientations of Si, only the Si (111) permits the III-nitride epilayer grown on it to naturally evolve in the hexagonal (0001) orientation. The potential drive for the integration of InN excellent properties with Si technologies, particularly, in the areas of electron devices, solar cells, light emission and detection devices; at the optical-fiber telecommunication wavelengths, coupled with the very low LM in comparison to other substrates, should motivate the development of InN heteroepitaxial structures on this substrate material.

In conclusion, the heteroepitaxial growth of InN is a practical necessity and the choice of substrate is crucial. The purpose of this work is to optimize the growth of InN on Al_2O_3 (both *r*- and *c*-plane orientations) and Si(111) substrates for device applications and investigate the effect of substrate material and orientation on the various properties of InN. InN heterostructures and nanostructures on these substrates are discussed from chapters 4 to 9 of the thesis.

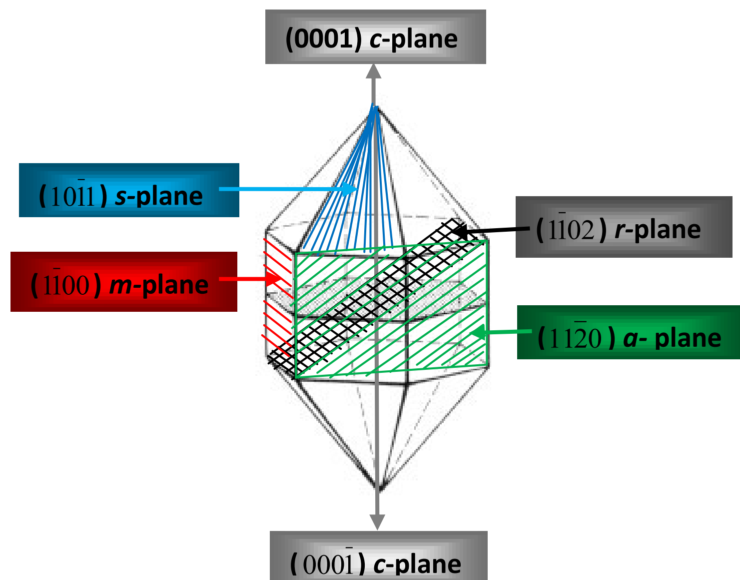

Figure 3.1 *Schematic diagram of the common crystallography planes of III-nitride materials.*

3.2 Epitaxial growth Process

Epitaxial growth is governed by series of physical processes and depends on thermodynamics and kinetics. When a material growth process is initiated in the MBE, atomic and/or molecular beams of the constituent elements of the material impinge on the substrate surface, which is placed on a substrate holder with the capability to heat the substrate up to 800 - 900°C. Fig. 3.2(a) shows a figurative description of the epitaxial growth process. Deposited atoms (adatoms) on the surface will diffuse in it and preferably bond to the lattice sites with higher bonding energy on the substrate's surface. Some of the adatoms may desorb away from the substrate's surface when favourable lattice site for incorporations are not readily available and depending on the characteristic residence time on the surface.

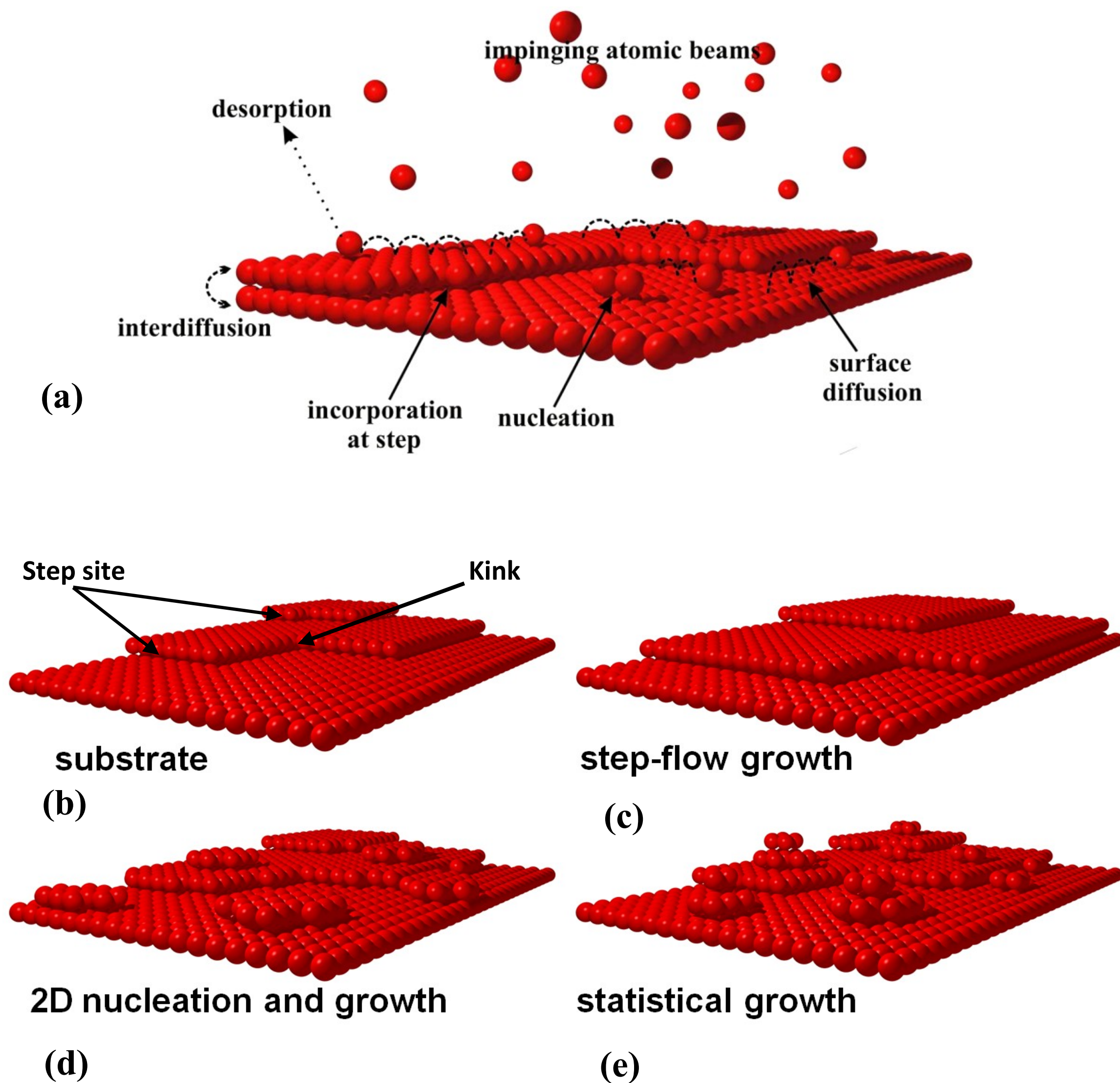

Figure 3.2 *Schematic diagram of epitaxial growth process: (a) General description, (b) 'kinks' and 'steps' on the high crystalline substrate's surface, (c) step-flow 2D growth of crystalline material, (d) growth via 2D-islands nucleation (e) statistical growth due to random incorporation of adatoms to form amorphous materials.*

‘Kinks’ and ‘Steps’ are high-energy binding sites that provide favourable sites for atoms to bond (chemisorption). They are of great importance in thin film growth because incorporation occurs more easily at lattice step edge or kink [3]. The black arrows in the schematic diagram of the substrate’s surface, which is shown in Fig. 3.2(b), point to the examples of kink and steps on a substrate’s surface. If the adatoms diffusion length is small, compared to the distance of steps, then aggregation of such atoms on the crystal’s (or substrate’s) surface results to nucleation of two-dimensional (2D) islands [Fig. 3.2(c)]. As the growth process continues, subsequent atoms could condense directly on the 2D nuclei and increase their lateral size to form large 2D islands [Fig. 3.2(d)] that could eventually merge into a complete atomic plane or monolayer. However, random incorporation of adatoms into different sites on the substrates’ surface (statistical growth), leading to non-oriented islands, causes the formation of non-crystalline (amorphous) material [Fig. 3.2(e)].

3.2.1 Growth modes in heteroepitaxy

The understanding of the mode of growth and structure of the very initial stages of an oriented layer is the key to the realization of epitaxy [4]. The growth mode of a nucleating heteroepitaxial layer is determined majorly by the properties of the surfaces and interfaces involved [5]. The surface energy is one of the two factors that determine the heteroepitaxial growth characteristics. Surface energy is the extra energy expended to create a surface and determines whether one material wets another to form a uniform adherent layer [6]. Very low surface energy material (such as oxides and organic materials) tends to wet a higher surface energy material (such as metal) while the latter will naturally form clusters on the former. Surface energy is related to bond energy (binding energy) and the number of bonds broken in creating the surface. Difference in the surface energy of film and substrate could cause the atoms of the film to prefer to bond to each other rather than to the atoms of the substrate; leading to the formation of atomic clusters (3D nuclei) of the film on the substrate. The surface energy depends also on the orientation of the surface and may be altered by surface adlayers and surface treatment prior to or during growth. Thermodynamically, the growth mode of the epitaxial material is determined by the minimum surface energy configuration, but the growth mode of the epitaxial material may also be controlled kinetically by the atomic diffusion.

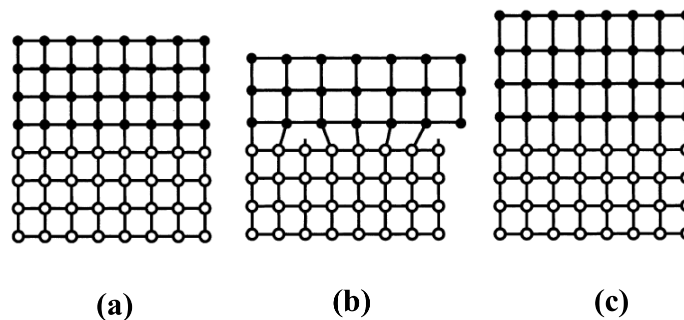

Figure 3.3 *Cross-section schematic of atomic arrangement in various modes of epitaxial growth: (a) lattice-matched or commensurate growth, (b) lattice-mismatched or relaxed growth; (c) lattice-mismatched strained pseudomorphic growth (After J.R. Arthur (2002)[8]).*

The other important factor that determines the growth mode is the strain energy. Heteroepitaxial semiconductors typically contain elastic strains, due to lattice mismatch and thermal mismatch [7]. A film lattice-matched to the substrate shares similar atomic order with the substrate, leading to 2D commensurate growth [Fig. 3.3(a)]. An incommensurate growth occurs when the epilayer has a significantly large mismatch with the substrate, consequently causing separated multilayer islands to be formed rather than a wetting layer (2D growth mode). In the case of a small lattice mismatch strain, a pseudomorphic growth (whereby the film adopts the two-dimensional spacing of the substrate [8]) could occur initially [Fig. 3.3(c)] until a critical thickness is reached when the increasing strain as growth proceed leads to the generation of misfit dislocations at the epilayer/substrate interface that results to lattice distortion (partial or fully relaxed heteroepitaxial layer) [Fig. 3.3(b)].

An important difference between homoepitaxy and heteroepitaxy is that heteroepitaxy requires nucleation of a new phase on the substrate surface, which influences the growth mode and hence, the morphology and structural properties of heteroepitaxial layers [1]. E. Bauer [9] classified the various growth modes that are possible during deposition into three as: (i) layer-by-layer growth; which occurs when the substrate surface energy is higher than that of the deposit [Fig. 3.4(a)]. In this case, islands of monolayer height coalesced before a new layer can nucleate on top of them. (ii) Three dimensional (3D); which occurs when substrate surface energy is lower than that of deposit [Fig. 3.4(b)], leading to the growth of many discrete islands with many atomic layers prior to coalescence. (iii) A combined scenario consisting of the former followed by the latter; which is considered to arise from high strain energy in the deposit layer that consequently leads to nucleation of 3D nuclei on top of the initial, strained monolayer [Fig. 3.4(c)]. These three growth modes are traditionally referred to as Frank–van der Merwe (FM) [10] Volmer-Weber (VW) [11] and Stranski–Krastanov (SK) [12] growth modes [13], respectively. Equilibrium considerations dictate that mismatched heteroepitaxial material will usually grow in a VW or SK mode, with a rough surface, pinholes or trenches due to the coalescence of irregular islands, unless the epitaxial layer wets the substrate and the lattice mismatch is small [14]. However, the mismatch (strain effect) between film and substrate can be reduced or removed by growing graded buffer layer [8].

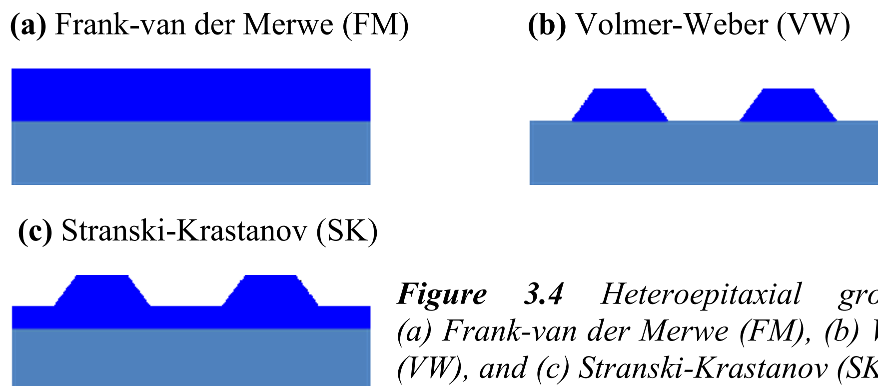

Figure 3.4 *Heteroepitaxial growth modes: (a) Frank-van der Merwe (FM), (b) Volmer-Weber (VW), and (c) Stranski-Krastanov (SK).*

3.3 Substrates' surface preparations

The InN heterostructures reported herein were deposited on either *r*-plane sapphire substrates or 2-3 μm thick GaN(0001) buffer layer grown by MOVPE on *c*-plane sapphire substrates (hereafter referred to as "GaN pseudo-substrates") or Si (111). Preparation of the substrate surface prior to deposition is a critical step since the surface must be relatively free of crystal imperfections and impurities to promote homogeneous nucleation and low-defect growth. Substrates with polished and chemically cleaned surfaces according to the standards of the semiconductors' industries were purchased and used in our experiments.

Nevertheless, an additional cleaning was carried out at the lab before the introduction of substrates in the MBE system, to remove contaminants that may have accumulated on the surface during transportation and storage. A degreasing procedure employed for the sapphire substrates was always the same, irrespective of their crystallographic orientation. The substrates were usually first dipped into a solution of TCE, kept at 90 °C, for 10 minutes. Afterwards, they were always rinsed in acetone and propanol in sequential order for 10 minute each. This process was always followed by thorough rinse in deionized water (DI). The same cleaning method was adopted for the GaN pseudo-substrates.

The Si substrates preparation process was carried out by using an entirely different chemical cleaning method from that of sapphire substrates or GaN pseudo-substrates. The Si substrates were initially immersed for 10 minutes in a 3:1 solution of H_2SO_4 : H_2O_2 kept at 90 °C followed by a rinse in DI. This step assists to first degrease the Si surface and then cover it with a thin oxide layer. Afterwards, the resulting oxide layer is removed by dipping the substrates in a 10 : 1 solution of H_2O : HF for 5 minutes and then the substrates are rinsed again in DI several times. Treatment of Si surface with HF solution leads to hydrogen terminated hydrophobic surface and prevents the cleaned Si surface from being oxidized prior to loading into the MBE preparation chamber.

After the chemical cleaning of the Si and/or sapphire substrates, they were always immediately loaded into the loading chamber of the MBE for further surface preparation with heat treatment that is aimed at removing any adsorbed gases, especially in the form of H_2O, prior to onward transfer to the growth chamber. In the growth vacuum, the final thermal surface cleaning of the substrates takes place at higher temperatures; usually within the range of 800 - 900°C, in order to remove any other form of impurity that may be present on the surface and create atomically clean, well-ordered surfaces. The growth on Si(111) substrates requires that after this step, on ramping down the temperature to about 750°C, 7x7 reconstruction pattern should be observed *in-situ* by the RHEED [15]. This reconstruction is an ordered atomic structure on the Si (111) surface and it depends mainly on the substrate temperature and the adsorbed species. During the course of this work, the observation of 7x7 reconstruction on the Si (111) surface prior to growth initiation was found absolutely necessary for a successful epitaxial growth process.

3.4 Determination of III/V flux ratio

All atomic fluxes were determined in terms of equivalent GaN, AlN, and InN growth rates in units of nm/hr from thickness measurements of GaN, AlN and InN

films grown under metal-rich and N-rich conditions at temperatures that favour incorporation of all arriving atoms without thermal decomposition. The method of determination of the III and N atoms has been analytically described elsewhere [16,17].

3.5 Estimation of the MBE growth temperature

The growth temperature (or substrate temperature, T_{sub}) employed for the development of this work was determined from the thermocouple attached to the MBE manipulator, which is not in contact with the rotating substrate. The thermocouple was calibrated by using the conventional In and Al melting points of 160°C and 660°C, respectively to determine the real substrate temperature [16,18]. When compared with the computer controlled temperature readout, the real temperature was found to be 100°C higher than the thermocouple reading. The real temperatures are stated throughout this work.

3.6 InN Growth Properties

InN is the most difficult to synthesize among the III–nitrides due to its several orders higher nitrogen equilibrium vapour pressure over InN compared to AlN and GaN [19]. This high equilibrium N_2 vapour pressure [20] and low InN dissociation temperature [21] makes the growth of high crystal quality InN film difficult; since material quality is well known to increase with temperature. The PAMBE, employed for InN growth in this work, permitted the use of low substrate temperature required to avoid decomposition.

It is well known that surface diffusivity of the Ga and N adatoms is enhanced when there is a metallic double layer on the (0001) surface during GaN growth [22,23]. The double Ga adlayer is secured by using excess Ga flux [$F_{Ga} > F_N$, Ga-rich condition] [23]. The excess Ga atoms are desorbed from the surface, since the Ga desorption rate is much higher than the GaN decomposition rate ($R_{GaN\text{-}decomposition} < R_{Ga\text{-}desorption}$) at the used substrate temperature (T_{sub}) during growth of approximately 800°C. The reverse is the case for InN, where the growth is not sustainable under *In-rich* growth conditions since InN decomposition rate is higher than In-desorption rate ($R_{InN\text{-}decomposition} > R_{In\text{-}desorption}$) [16,24]; leading to difficulty in the growth of InN. InN is therefore more sensitive to growth temperature and III/V flux ratio compared to other nitride semiconductors. The crystalline quality improves with increased growth temperature up to the dissociation limit of InN [25,26]. Substrate temperature significantly influences the crystallinity, surface morphology, growth rate, electrical and other properties of as-grown InN film. The studies of the epitaxial growth of InN on GaN templates by both MOCVD [21] and PAMBE [16] showed that the growth mode of InN is controlled by the T_{sub} and III/V flux ratio. Growth at low temperature (< 400°C) proceeds through nucleation and fast coalescence of 3D islands due to the limited surface mobility of In adatoms. At higher T_{sub} (400-500°C), for $F_N > F_{In}$, the growth proceeds through sparse nucleation of 3D islands due to enhanced In adatoms mobility while for $F_N = F_{In}$, layer-by-layer growth is followed. At substrate temperatures higher than 450°C, the fluxes of atoms on the surface are effectively changed and the InN growth is no longer sustainable. At temperatures higher than approximately 500°C, In accumulates on the surface [16,27]. Rapid dissociation occurs above 500°C and no deposition of InN layer occurs above 600°C.

A two-step growth method is the standard method for the heteroepitaxial growth of thin films and is commonly used to reduce lattice or thermal expansion mismatch between epilayer and substrate. It consists of the deposition of a low temperature thin intermediate (or nucleation) layer prior to the epitaxy of the main layer at high temperature. The intermediate layer is expected to uniformly cover the substrate surface and to promote layer-by-layer growth of the final epilayer. A single step growth consists of direct deposition of InN on the substrate at high substrate temperatures (400 - 435°C) under stoichiometric In/N flux ratio, while a two-step growth method employs a thin nucleation or buffer layer grown at low T_{sub} with $F_{In}/F_N \leq 1$, to provide high density of nucleation centers. The main epilayer InN is grown in the second step at a higher temperature (400-500°C) but usually under stoichiometric In/N flux ratio [16,24,28]. By definition, a nucleation layer is a thin initial (wetting) layer deposited directly on the substrate while a buffer layer refers to the thick layer usually deposited to improve the crystalline and electronic properties of the final epilayer. For example, a buffer layer separates the highly defective initial or nucleation layer from the top layer of a device active region. Both single-step and two-step growth methods have been used for the epitaxy of InN in this work.

A self-regulating mechanism for InN growth on GaN (0001) has been reported [28]. As depicted in Fig. 3.5, under conditions of high In-adatoms' surface mobility, In-adatoms migrate from in-between InN islands regions to the top surface of the islands themselves so that equal "fluxes" of In and N atoms are provided to maintain a low energy In-stabilized surface, and regulating in that way the growth rate along the [0001] direction and the surface coverage with InN. Efficiently mobile In-adatoms diffuse along the GaN surface to form InN regions with stoichiometry of incoming In and N atoms on the growth front [Fig. 3.5]. Use of T_{sub} of approximately 430°C has been reported to enhance the In-adatoms' mobility without InN decomposition, whilst stoichiometric III/V flux ratio (F_{In} /F_N ~1) makes possible the complete substrate's surface coverage, leading to smooth surface morphology, as a result of step-flow growth mode with 1ML-height steps found on the surface of the InN epilayer. Depending on substrate temperature and III/V flux ratio conditions, InN may be grown as compact film, or separated 3D islands (or pillars).

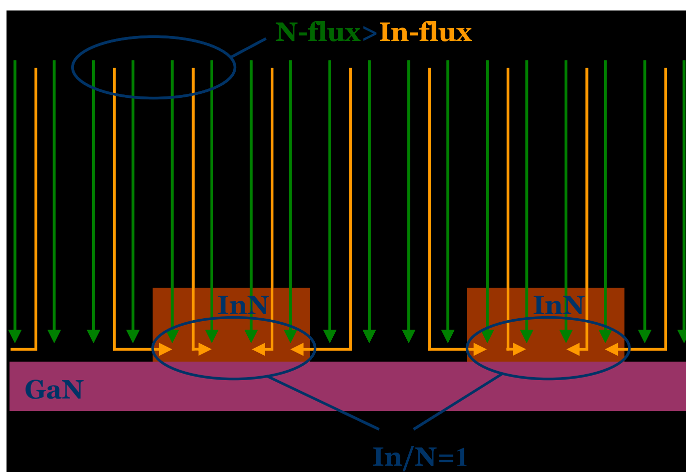

Figure 3.5 Self-regulating mechanism of InN growth on GaN (0001) by molecular beam epitaxy [28].

3.7 InAlN growth Properties

The ternary Indium-Aluminium Nitride alloys system (InAlN) is of particular interest for both optoelectronic and high frequency electronic devices. However, the development of InAlN films in the entire composition range is still challenging due to reasons related to the miscibility gap in the alloy system that leads to phase separation. Similar to what was obtained for InGaN growth [29-31], InAlN films exhibit problems of In incorporation and may also exhibit phase separation. Experimentally, the ternary InAlN film growth difficulty is due to the combined effects of strain and wide difference in AlN and InN growth temperatures. Metallic In has been observed to fill the dislocation lines resulting from relaxation of the lattice mismatch in InAlN film grown on GaN template [32,33]. Moreover, avoiding In-rich growth, which results in continuous metallic In accumulation and eventually in the disruption of epitaxial growth, is difficult at the T_{sub} required for high quality InAlN growth. Therefore, the delicate optimization of growth conditions for high quality InAlN film growth has been also considered in this work. Optimised InAlN films of different In compositions are required for the fabrication of electron device heterostructures, such as the High Electron Mobility Transistors (HEMTs).

3.8 Concluding remarks

In conclusion, the present quality of epitaxial films of InN and heterostructure interfaces needs further improvement for device applications. The understanding and optimization of the InN and InAlN growth is needed in order to develop InN-based device technology and this work contributes in this direction.

References

1. J. E. Ayers, *Heteroepitaxy of Semiconductors – Theory, growth and Characterization*, CRC Press Taylor & Francis Group, USA. Chapter 4 pg 114-117 (2007).
2. A. G. Bhuiyan, A. Hashimoto, and A. Yamamoto, *J. Appl. Phys.* **94**, 2779 (2003)
3. K-N Tu, J.W. Mayer and L.C. Feldman, *Electronic Thin Film Science: for Electrical Engineers and Material Scientists,* Macmillan Publishing Company, USA Chap 5. Pg 100 (1992)
4. D. W. Pashley *in "Epitaxial growth Part A – Materials Science Series"*, Edited by J. W. Matthews, Academics Press, New York Chapter 1 (1975)
5. J. E. Ayers, *Heteroepitaxy of Semiconductors – Theory, growth and Characterization*, CRC Press Taylor & Francis Group, USA. Chapter 2 pg 32 (2007).
6. K-N Tu, J.W. Mayer and L.C. Feldman, *Electronic Thin Film Science: for Electrical Engineers and Material Scientists* Macmillan Publishing Company, USA Chap 2. Pg 21 (1992)
7. J. E. Ayers, *Heteroepitaxy of Semiconductors – Theory, growth and Characterization*, CRC Press Taylor & Francis Group, USA. Chapter 2 pg 19-20 (2007).
8. J.R. Arthur, *Surface Science* **500**, 189 (2002)
9. E. Bauer, *Z. Kristallogr.* **110**, 372 (1958)
10. F.C. Frank and J.H. van der Merwe, *Proc. R. Soc. London A*, **198**, 216 (1949)
11. M. Volmer and A. Weber, Keimbildung in übersättigten Gebilden, *Z. Physik Chem.* **119**, 277 (1926)
12. E. Bauer and H. Poppa, *Thin Solid Films* **12**, 167 (1972)
13. C. Ratsch and J. Venables, *J. Vac. Sci. Technol. A*, **21**, S96 (2003)
14. J. E. Ayers, *Heteroepitaxy of Semiconductors – Theory, growth and Characterization*, CRC Press Taylor & Francis Group, USA. Chapter 4 pg 132 (2007).
15. J. Grandal, M.A. Sánchez-García, *J. Cryst. Growth* **278**, 373 (2005)
16. E. Dimakis, E. Iliopoulos, K. Tsagaraki, Th. Kehagias, Ph. Komninou, and A. Georgakilas, *J. Appl. Phys.* **97**, 113520 (2005).
17. A.O. Ajagunna, A. Adikimenakis, E. Iliopoulos, K. Tsagaraki, M. Androulidaki, A. Georgakilas, *J. Crystal Growth* **311**, 2058 (2009)
18. E. Dimakis, K. Tsagaraki, E. Iliopoulos, Ph. Komninou, Th. Kehagias, A. Delimitis, A. Georgakilas, *J. Crystal Growth* **278**, 367 (2005)
19. O. Ambacher, M. S. Brandt, R. Dimitrov, T. Metzger, M. Stutzmann, R. A. Fischer, A. Miehr, A. Bergmajer, and G. Dollinger, *J. Vac. Sci. Technol. B* **14**, 3532 (1996)
20. J. B. McChesney, P. M. Bridenbaugh, and P. B. O'Connor, Mater. *Res.Bull.* **5**, 783 (1970)
21. L. A. Marasina, I. G. Pichugin, and M. Tlaczala, *Krist. Tech*. **12**, 541 (1977)
22. T. Zywietz, J. Neugebauer and M. Scheffler, *Appl. Phys. Lett.* **73**, 487 (1998)
23. G. Koblmüller, R. Averbeck, H. Riechert, and P. Pongratz, *Phys. Rev. B* **69**, 035325 (2004)
24. E. Dimakis, G. Konstantinidis, K. Tsagaraki, A. Adikimenakis, E. Iliopoulos, and A. Georgakilas, *Superlattices Microstruct*. **36**, 497 (2004).

25. H. Lu, W. J. Schaff, J. Hwang, H. Wu, W. Yeo, A. Pharkya, and L. Eastman, *Appl. Phys. Lett*. **77**, 2548 (2000).
26. Y. Saito, H. Harima, E. Kurimoto, T. Yamaguchi, N. Teraguchi, A. Suzuki, T. Araki, and Y. Nanishi, *Phys. Status Solidi (b)* **234**, 796 (2002)
27. E. Iliopoulos, A. Adikimenakis, E. Dimakis, K. Tsagaraki, G. Konstantinidis, A. Georgakilas, *J. Cryst. Growth* **278**, 426 (2005)
28. E. Dimakis, E. Iliopoulos, K. Tsagaraki, and A. Georgakilas, *Appl. Phys. Lett.* **86**, 133104 (2005).
29. I. Ho and G. B. Stringfellow, *Appl. Phys. Lett*. **69**, 2701 (1996)
30. S. Yu. Karpov, *MRS Internet J. Nitride Semicond. Res*. **3**, 16 (1998)
31. D. Doppalapudi, S. N. Basu, K. F. Ludwig, and T. D. Moustakas, *J. Appl. Phys*. **84**, 1389 (1998)
32. S.-L. Sahonta, G. P. Dimitrakopulos, Th. Kehagias, J. Kioseoglou, A. Adikimenakis, E. Iliopoulos, A. Georgakilas, H. Kirmse, W. Neumann, and Ph. Komninou, *Appl. Phys. Lett*. **95**, 021913 (2009)
33. P. D. C. King, T. D. Veal, A. Adikimenakis, Hai Lu, L. R. Bailey, E. Iliopoulos, A. Georgakilas, W. J. Schaff, and C. F. McConville, *Appl. Phys. Lett.* **92**, 172105 (2008)

4 InN and InN/InAlN heterostructures on GaN/Al_2O_3 (0001)

4.1 Introduction

4.2 Experimental procedures

4.3 Morphological investigation

4.4 Structural characterisation of the films by HR-XRD

4.5 Electrical characterisation of InN films

4.6 Origin of bulk donors in InN

4.7 Optical studies of (0001) InN layers

4.7.1 Low temperature photoluminescence measurements

4.7.2 Optical transmittance measurements

4.8 Growth of InAlN and InN based device heterostructures

4.9 Investigation of InN-rich InAlN Schottky diodes

4.10 Heteroepitaxial growth of InN-based HEMT structures

4.11 Concluding remarks

4.1 Introduction

In this chapter, the detailed studies carried out on the molecular beam epitaxy of InN on 2800 nm thick MOVPE GaN pseudo-substrates are discussed. The major investigation was centred on the thickness dependent properties of *c*-plane InN films. While some authors have reported the thickness dependence of the electrical properties of InN grown on sapphire [1,2], little or nothing has been done concerning the dependence of other properties on thickness [3]. Even those who worked on the thickness dependence of the electrical properties of InN only covered a narrow range of thickness; like 10-80 nm [4] and 500 - 4500 nm [5]. In the other cases, scattered information about *c*-plane InN is given and the samples were grown under a variety of conditions, using different growth techniques, substrate materials, substrate temperatures, III/V flux ratios and even buffer layers [6-9]. Hence, making such investigation as the present one that uses InN with nominal thickness range of 30 – 5000 nm grown under similar conditions is of great importance in the study of the properties of InN. Thicknesses lower than 30 nm are exempted since accurate characterisation measurements become very difficult and the possibility of strong interaction of the material properties with that of the substrate's surface and interfacial properties exist, which could lead to results that are difficult to analyse or interpret for reaching reliable conclusions.

In this Chapter, we examine thickness dependent properties of InN (0001), covering an extended range of thickness in a systematic comparative study, for the first time. The InN properties investigated as functions of film thickness are surface roughness, crystal mosaicity, electrical and optical properties. Furthermore, the growth of InAlN films with different In composition from InN-rich regime to AlN-rich regime is also investigated. The control of the InN and InAlN growth is aimed at achieving InN-based device heterostructures. Some results on the growth and characterisation of InN-based Schottky diode and HEMT structures are also presented.

4.2 Experimental procedures

As a first step, the conventional substrate's surface *ex-situ* cleaning, according to section 3.3 [10], was employed for all the GaN (0001) pseudo-substrates. The GaN (0001) pseudo-substrates (or templates) consisted of a 2.8 μm GaN (0001) buffer layer grown by MOVPE on Al_2O_3 (0001) substrate [Fig. 4.1]. Each substrate was introduced into the multi-chamber MBE system and outgassed up to 650°C in the preparation chamber, prior to transfer to the growth chamber for thermal surface cleaning at 820°C. A 40 nm thick GaN layer was always first grown on the Ga-polar GaN (0001) pseudo-substrates to improve the smoothness and purity of the GaN surface prior to InN growth initiation at the optimum growth conditions of 420°C and stoichiometric III/V flux ratio. The typical growth structure is shown in Fig. 4.1. The method of determination of the III/V flux ratio has been previously discussed (Section 3.3.2). The nominal thickness of the as-grown InN films was in the range from 30 nm to 5000 nm.

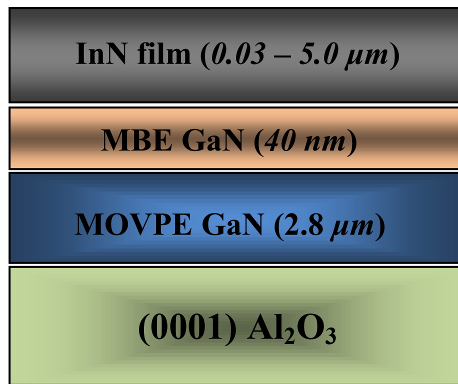

Figure 4.1 *Heteroepitaxial structure of the c-plane InN films of different thicknesses on GaN pseudo-substrates consisting of 2.8 μm GaN grown on Al_2O_3 (0001) by MOVPE.*

4.3 Morphological investigation

Prior to the *ex-situ* investigations of the as-grown InN, all the layers were etched in HCl solution in order to avoid possible contribution of In droplets to any of the investigated films' properties. In droplets could form when the In/N flux ratio slightly exceeds one. The FE-SEM micrograph of Fig. 4.2 is representative for the smooth surface morphology of all samples. The corresponding 5x5 μm^2 AFM images of the films are shown in Fig. 4.3. It is very evident that the epitaxy of the films proceeded in the step-flow growth mode with the InN surface morphology consisting of monolayer height steps and terraces around spiral hillocks. The early stage of the InN growth was characterised with high density hillocks, which appeared to exhibit increment in size and decrement in density per surface area as the film thickness increases. The hillocks considerably reduced in density (ρ) by two orders from 1.30 x 10^9 cm^{-2} to 1.2 x 10^7 cm^{-2} as the InN film thickness increased from 30 nm to 1000 nm, respectively [Fig. 4.4(b)]. The surface area between hillocks exhibited surface steps consistently, although in the cases where the density of hillocks is very high (i.e. for the 30 nm layer) the observation of the steps was not clear [Fig. 4.3]. The hillocks observed on the surfaces of these samples are similar to the hillocks observed in InN [11] and GaN (0001) [10,12] growth by MBE, and may indicate step-flow growth around the screw-type threading dislocation (STD) [10,13]. In general, the reduction of the density of hillocks and simultaneous increase in the average size of hillocks observed with increasing InN film thickness have similarly been reported for GaN films by Roskowski *et al.* [14].

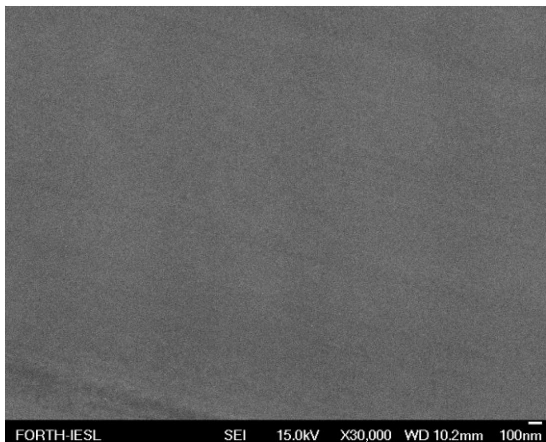

Figure 4.2 *FE-SEM micrograph for the 1000 nm thick c-plane InN film, showing the typical surface morphology of the InN-on-GaN (0001) films.*

The reduction of hillocks' density in thicker films, as shown in Figs. 4.3 and 4.4(a), is attributed to the improved coalescence of the initial islands with growth time and probably a reduction in the screw-type threading dislocation (STD) density, since hillocks have been associated with STDs in III-nitrides [10,15-17]. Even though the AFM has been proposed as a useful technique for determining the type, density, and distribution of dislocations near the surface of GaN layers [16], further investigation by a more reliable study like the transmission electron microscopy of these InN epilayers is required to explicitly associate the observed hillocks with STDs, since the density of STD is not expected to change significantly along the growth direction of the InN films [18]. Dimakis *et al.* [18], by transmission electron microscopy, have previously observed a similar STD density at both the interface and surface regions of a high crystal quality 10 μm thick InN epilayer grown on Al_2O_3 (0001) substrate.

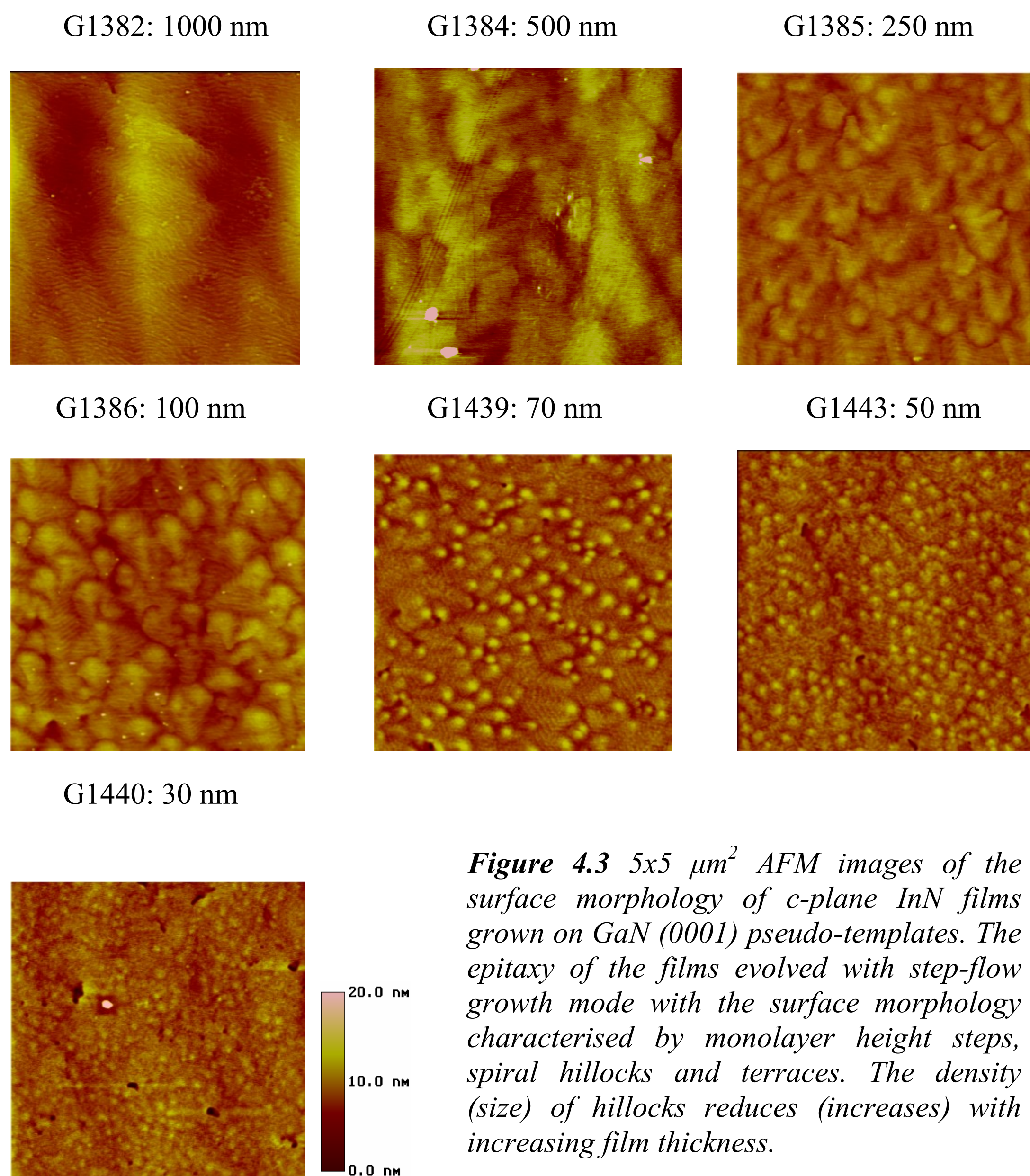

Figure 4.3 *5x5 μm² AFM images of the surface morphology of c-plane InN films grown on GaN (0001) pseudo-templates. The epitaxy of the films evolved with step-flow growth mode with the surface morphology characterised by monolayer height steps, spiral hillocks and terraces. The density (size) of hillocks reduces (increases) with increasing film thickness.*

The rms surface roughness values of the films were deduced from the 2x2 μm^2 AFM micrographs of their surfaces and plotted against InN epilayer thickness as shown in Fig. 4.4(b). The exhibited reduction in the surface roughness with increasing film thickness, and the fact that rms roughness values are generally below 0.55 nm is an indication of enhanced coalescence of the initially formed islands into a continuous film grown under the two-dimensional (2D) step-flow growth mode. Comparatively, our results agree with the reduction of surface roughness with increasing thickness observed by Heying *et al.* [12] and Roskowski *et al.* [14] for GaN (0001) films grown on Al_2O_3 and AlN/SiC substrates, respectively. The InN surface roughness has been associated with the existing macroscopic surface spiral-hillocks defects by Wang *et al.*, who studied InN films grown at different temperatures on GaN (0001) pseudo-substrates [16].

Fig. 4.5(a) shows the surface of the thickest 5000 nm InN film. The film exhibits higher density of hillocks (ρ = 6.2 x 10^8 cm^{-2}), compared to the 1000 nm film of Fig. 4.3, deviating sharply from the previously observed reduction in hillocks density with film thickness. In addition, formation of micro-holes is apparent on the surface. The observed difference in the surface morphology of the film, in comparison to others in Fig. 4.3, is attributed to the difficulty of keeping stable optimum growth conditions for long time in thicker InN samples, which probably resulted to different III/V flux ratio on the surface. It is well known that the III/V flux ratio plays a decisive role on the III-nitride semiconductors' surface morphology [10,19,20]. Nonetheless, 2D step-flow growth mode was still maintained during the growth, as evident from the inset of Fig. 4.5, leading to a smooth surface morphology with rms surface roughness of 0.96 nm and 1.5 nm deduced from the 2x2 μm^2 and 5x5 μm^2 AFM scans, respectively. The higher rms roughness exhibited by the 5000 nm InN layer is attributed to the high density of hillocks and micro-holes apparent on the film's surface [Fig. 4.5].

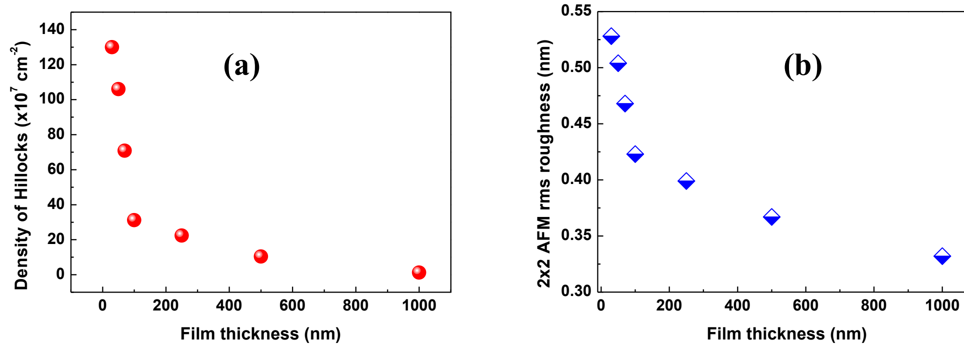

Figure 4.4 *AFM characterisation of the surface morphology of c-plane InN films grown on GaN(0001) pseudo-templates: (a) Plot of the estimated density of hillocks from the 5x5 μm^2 micrographs as a function of film thickness, and (b) 2x2 μm^2 AFM rms surface roughness versus film thickness for c-plane InN-on-GaN(0001) pseudo-templates. The density of hillocks observed on the films' surfaces and the rms surface roughness similarly reduce with increasing film thickness.*

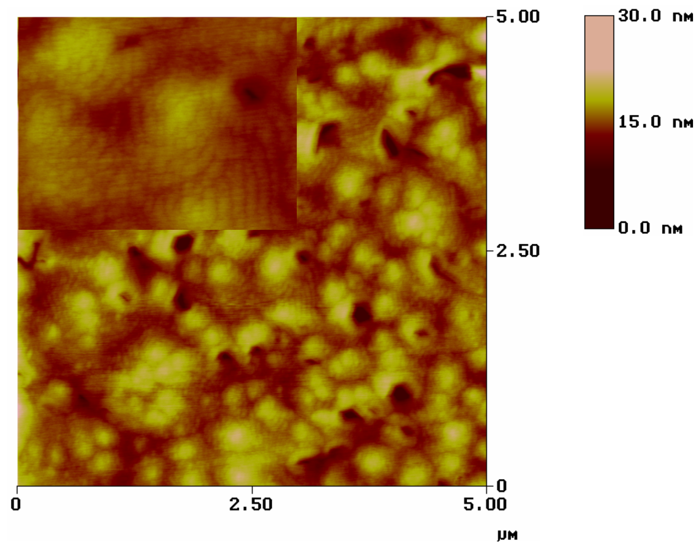

Figure 4.5 *5x5 μm² AFM micrograph showing the surface morphology of the 5000 nm thick c-plane InN film G1424 grown on GaN(0001) pseudo-substrate. The rms roughness of the surface is 1.50 nm. The inset is the enlarged image, which indicates that the growth of the thick InN film followed a step-flow mode.*

4.4 Structural characterisation of the InN films by HR-XRD

The ω-2θ HRXRD scans, presented in Fig. 4.6, confirmed that all the films are single phase (0001) InN. No additional peaks co-exist with that of InN{000*l*}, except those of GaN{000*l*}, AlN(0001) and Al_2O_3(0006), which originate from the MOVPE GaN pseudo-substrates used for the InN films' epitaxy.

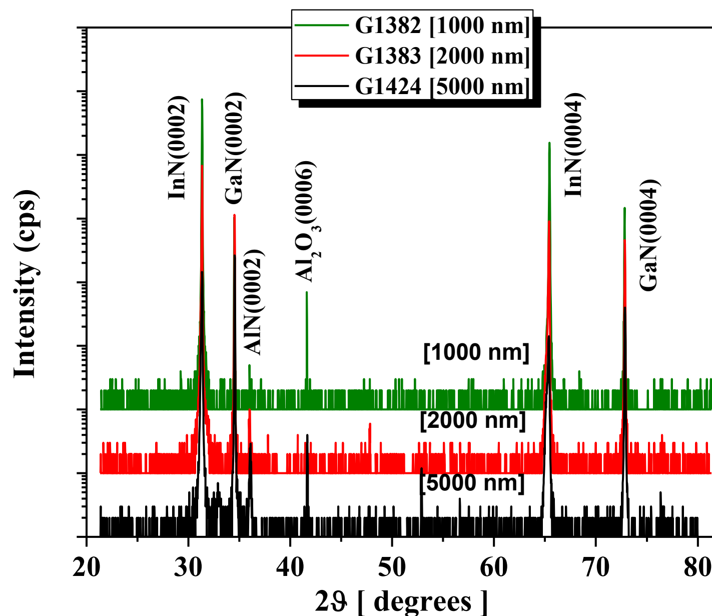

Figure 4.6 *ω-2θ HRXRD scans for the thick film samples G1382 (1000 nm), 1383 (2000 nm) and 1424 (5000 nm) which are representative of the other film samples.*

The egde dislocations, having Burgers vector $b = \frac{1}{3}\langle 11\bar{2}0 \rangle$, induce a twist of lattice planes [17]. Unfortunately, the twist is more difficult to measure directly by XRD, since it is accessible only via either a chi-scan of a reflection plane perpendicular to (0001), (such as $[1\bar{1}00]$ in transmission geometry) or by a phi-scan of one of these planes in grazing incidence [21]. This kind of measurements, even the skew geometry method [22], is beyond the capability of the HRXRD equipment used. Alternatively, the asymmetric $(10\bar{1}5)$ reflection can be used for a rough comparison of the twist and consequently, the edge dislocation density in the different samples. It is important to note that unlike the $000l$ reflection, the broadening of the $10\bar{1}l$ (where l = 1, 2,… 5) reflections is sensitive to both screw-type and edge-type threading dislocations in III-nitrides [21,23,24].

The mosaicity of the InN films was examined by obtaining both symmetric rocking curves, RCs (ω-scans) around the (0002) reflection and asymmetric RCs around the $(10\bar{1}5)$ reflection. Fig. 4.7 shows the symmetric and asymmetric RCs obtained for the thickest 5000 nm sample with FWHM of 450 and 324 arcsec, respectively. The FWHM values of the symmetric (star symbol) and asymmetric (circle symbol) reflections, measured for the various InN films, are plotted as functions of film thickness in Fig. 4.8. The FWHM of the $(10\bar{1}5)$ RC, which is affected by both screw and edge dislocations, is generally higher in comparison to the FWHM of the (0002) RC, except for the 5000 nm thick film [Fig. 4.7]. The asymmetric $(10\bar{1}5)$ RC FWHM values decreased from 1044 to 324 arcsec as the film thickness increased from 30 nm to 5000 nm, respectively.

The broadening of the diffraction peak of RCs can be caused by microstructural defects (such as dislocations and point defects), wafer curvature, limited size (e.g small layer thickness), instrument resolution and compositional variation [21]. Instrument resolution is 1-2 orders of magnitude better compared to the measured large FWHM values. The effect of the wafer curvature for given residual biaxial strain should increase with increasing epilayer's thickness. In the MBE growth of InN, no significant deviations from the crystal's stoichiometry are usually expected and all samples were grown under the same conditions. it is assumed that the variation in the InN composition and point defects effects on the broadening are minimal and can be overlooked. Broadening of the RCs from the limited sample's size can be estimated by the equation [21]

$$B = \frac{(1/t)}{|k_{hkl}|} \qquad (4.1)$$

where B is the integral breadth of the line in radians, t is the sample thickness and k_{hkl} is the magnitude of the scattering vector. The FWHM values derived by Eq. (4.4) are more than an order of magnitude smaller than the experimental $(10\bar{1}5)$ RC FWHM, indicating that the decreasing FWHM with thickness cannot be attributed to film thickness effects, but should rather be associated with improvement of InN structural quality with thickness.

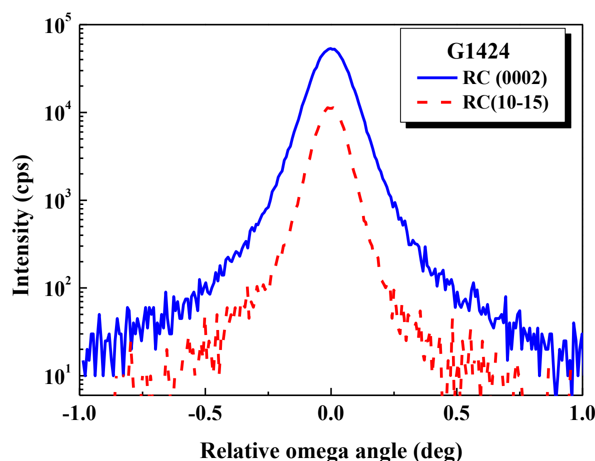

Figure 4.7 *HRXRD symmetric and asymmetric rocking curves (RCs) obtained for the 5000 nm InN film with FWHM of 450 and 324 arcsec, respectively.*

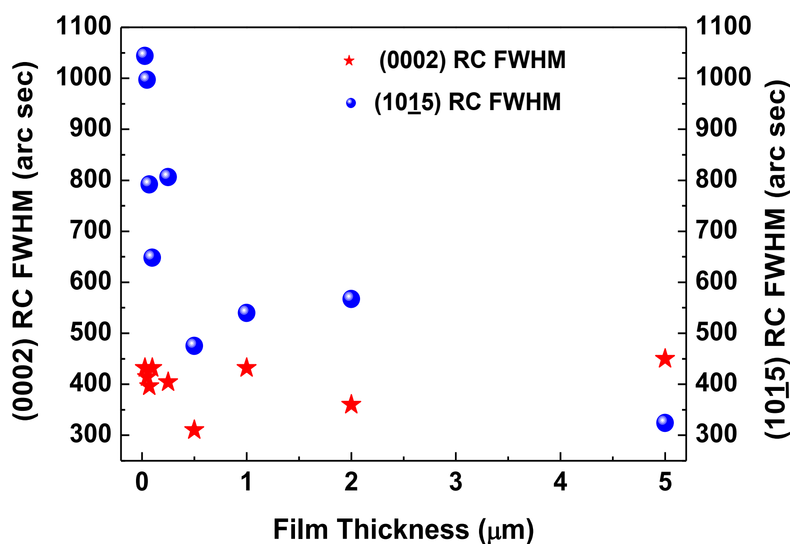

Figure 4.8 *Plots of the symmetric (0002) (star symbol) and asymmetric* $(10\bar{1}5)$ *(circle symbol) RC FWHM values versus InN film thickness. (0002) RC FWHM maintains a roughly similar values while the* $(10\bar{1}5)$ *RC FWHM decreases significantly with increasing film thickness.*

On the contrary the corresponding (0002) RC FWHM maintains lower and roughly constant values in all the films, relative to the $(10\bar{1}5)$ RCs, with an average width of about 390 arcsec [Fig. 4.8]. A decrease of the (0002) RC FWHM values may be concluded up to 500 nm thickness (310 arcsec), above which the FWHM increases again. These results suggest that the STD density does not change significantly with

film thickness, in agreement with the electron microscopy observations results of Dimakis *et al*. [17], although experimental condition variation, such as III/V flux ratio, substrate defect density, etc., may affect the result. The increased FWHM for the samples thicker than 500 nm may also indicate a difficulty to keep stable optimum growth conditions for long time, as required in the thicker samples. It may also be related to strain inhomogeneities in the thicker films, e.g. due to gradual relaxation of a residual misfit strain. Moreover, the significantly lower and roughly similar symmetric (0002) RC widths, in comparison to the FWHM of the asymmetric $(10\bar{1}5)$ RC, is also an indication that the ETDs component of the asymmetric $(10\bar{1}5)$ RC may be the dislocation type that dominates the structure of the InN films. The reduction in the FWHM of the InN $(10\bar{1}5)$ RC is also in agreement with the well known reduction of the ETD density with increasing InN thickness [25].

In general, the measured small FWHM values for the symmetric and assymetric RCs, with respect to film thickness, show that all the InN epilayers are of state-of-the-art material quality. For the 500 nm thick sample, the lattice constants *c* and *a* were determined as 5.71 Å and 3.52 Å, respectively, using the extended Bond method [26], indicating that the InN layer is compressively strained on the GaN pseudo-substrates [27,28].

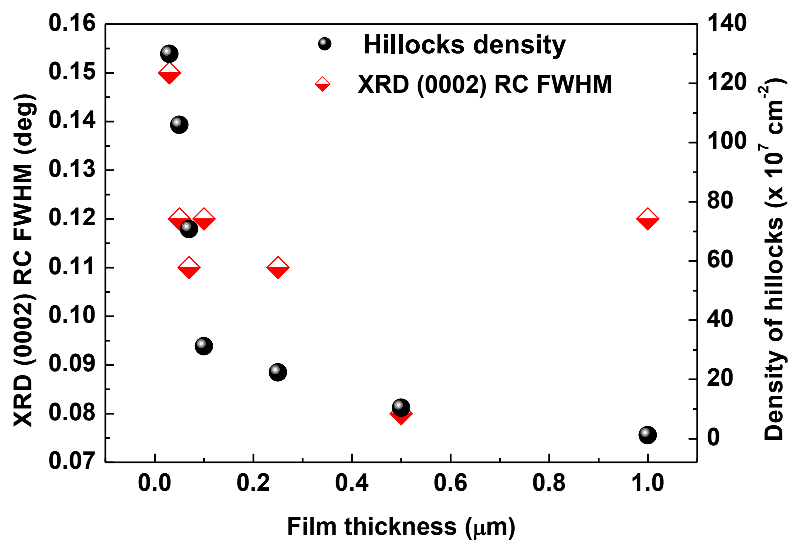

Figure 4.9 *Plots of the symmetric (0002) RC FWHM values (which correspond to lattice tilt from screw dislocations) and the density of the observed surface hillocks (from the AFM micrographs of Fig. 4.3) as functions of InN film thickness.*

To investigate the relationship between the observed surface hillocks from the AFM [Fig. 4.3] with screw-type dislocations, the (0002) symmetric RC FWHM values, which correspond to lattice tilt from screw component dislocations, and the density of the hillocks are together plotted against InN film thickness in Fig. 4.9. A similar trend can be seen for several samples but there are also significant deviations. We suggest that the appearance of hillocks on the AFM micrographs depends on the density of STDs but is also a very sensitive function of the exact growth conditions

(T_{sub} and III/V flux ratio). Slight unintentional variations of these growth conditions affect the visibility of STDs and thus counting the surface hillocks in AFM micrographs is not a safe method for extraction of STD density. A direct measurement technique, such as transmission electron microscopy, is needed to extract the density of screw dislocations in the InN films.

4.5 Electrical Characterisation of InN films

The Hall-effect characterisation data of the InN films at room temperature (RT) are plotted versus film thickness in Figs. 4.10 and 4.11. These are the experimentally measured values of sheet density (N_{S_meas}) and mobility (μ_{meas}). From the N_{S_meas} values and the known thickness t of the samples, the apparent electron concentration $N_{ap} = N_{S_meas} / t$ may be determined for each sample, assuming a homogeneous conductivity InN layer, which is not the actual situation [29].

Fig. 4.10 shows that the measured sheet carrier density maintains an almost linear relationship with thickness that spans a wide range of film thickness from 30 nm to 5000 nm, which is an indication of the existence of constant carrier concentration in the bulk of the layers. The extrapolation of the linear fit of the figure to the N_{S_meas} intercept (depicted by line symbol in Fig. 4.10) yielded a non-zero value of 1.58 x 10^{14} cm^{-2}, which is indicative of the surface electron accumulation that exists in the InN layers [5,30].

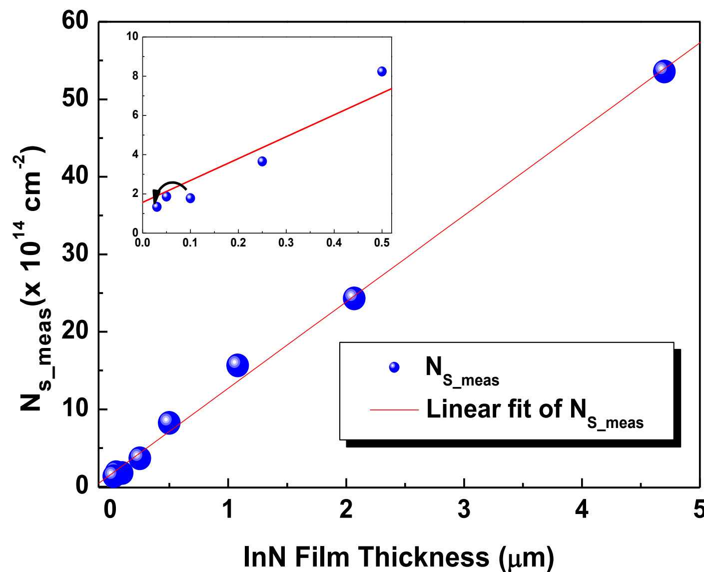

Figure 4.10 *The electron sheet density (N_{S_meas}) as extracted by room temperature Hall-effect measurements for InN films of different thicknesses. A linear fit (line symbol) intercepts the N_{S_meas} axis at 1.58 x 10^{14} cm^{-2}. The inset is an expansion of the plot for the lower thickness range of 30 to 500 nm.*

The inset of Fig. 4.10 shows a zoomed view of the lower thickness films up to 250 nm. A strange ‘kink’ denoted by a black arrow is noticeable in the inset. The measured N_s increased almost linearly with increasing thickness above 100 nm, but it also increased for the 50 nm sample, similarly to the results found for *a*-plane films

[31], which are described in Chapter 5. This peculiar behaviour was understood by considering the contribution of two conducting layers with different current densities and mobilities, one corresponding to a surface/interface conductivity layer with equivalent conductance of a 50 nm InN film, exhibiting low mobility and sheet density of ~10^{14} cm^{-2} and the remaining layer corresponding to a constant bulk donor concentration of ~10^{19} cm^{-3} [31]. This analysis will be discussed comprehensively in Chapter 5 of this work and the results shall be compared with those of *a*-plane orientation InN films.

The plots of the μ_{meas} and N_{ap} as functions of film thickness are shown in Fig 4.11. The measured electron mobility (μ_{meas}) increased monotonically with increasing InN thickness from 242 to 1824 cm^2/V.s as the film thickness increased from 30 nm to 5000 nm. The corresponding N_{ap} values decreased simultaneous from 4.45 x 10^{19} to 1.07 x 10^{19} cm^{-3}. The high mobility values of the InN films are found to be consistent with theory and are attributed to low compensation ratio [32] and low dislocation density [33,34]. However, the fast increase of measured mobility with increasing InN thickness is mainly the effect of the weighted averaging of the two conductivity layers' contributions in Hall-effect measurements. The saturation of the Hall mobility at film thicknesses quite above 100 nm indicates that at higher film thickness, the role of the low mobility interfacial/surface layer is negligible [31]. The occurrence of a weaker improvement of electron mobility at thicknesses above 100 nm is related to improving structural quality with increasing InN thickness. The highest carrier mobility of 1824 cm^2/Vs was measured for the thickest 5000 nm film sample at RT with a corresponding carrier density of 1.07 x 10^{19} cm^{-3}. This value is lower in comparison with the 2370 cm^2/Vs reported for an MBE grown 4400 nm InN sample, with significantly lower electron concentration of 2.8 x 10^{17} cm^{-3} [5]. Considering that scattering by ionized donors should be significantly higher for the $N_{ap} \approx 10^{19}$ cm^{-3} samples, the similarity of the mobility values suggests a very high compensation ratio for the sample with 2.8 x 10^{17} cm^{-3} reported by Ref 5.

4.6 Origin of bulk donors in InN

Secondary ion mass spectrometry (SIMS) investigation was carried out, by Mr. Michał A. Borysiewicz at the Institute of Electron Technology (Department of Micro- and Nanotechnology of Wide Bandgap Semiconductors) in Warsaw (POLAND), on a 600 nm InN film (sample G1902) grown on a GaN (0001) pseudo-substrate. This sample exhibited an electron concentration of 1.09 x 10^{20} cm^{-3} according to Hall-effect measurements. The SIMS measurements shown in Fig. 4.11(b) revealed that only the O (oxygen) concentration in the film is approaching the 10^{20} cm^{-3} level, while H and Si concentrations are 6.5 x 10^{18} cm^{-3} and ~ 10^{18} cm^{-3}, respectively, indicating that hydrogen can be excluded as the bulk donor source. These results indicate that oxygen should be the unintentionally incorporated donor.

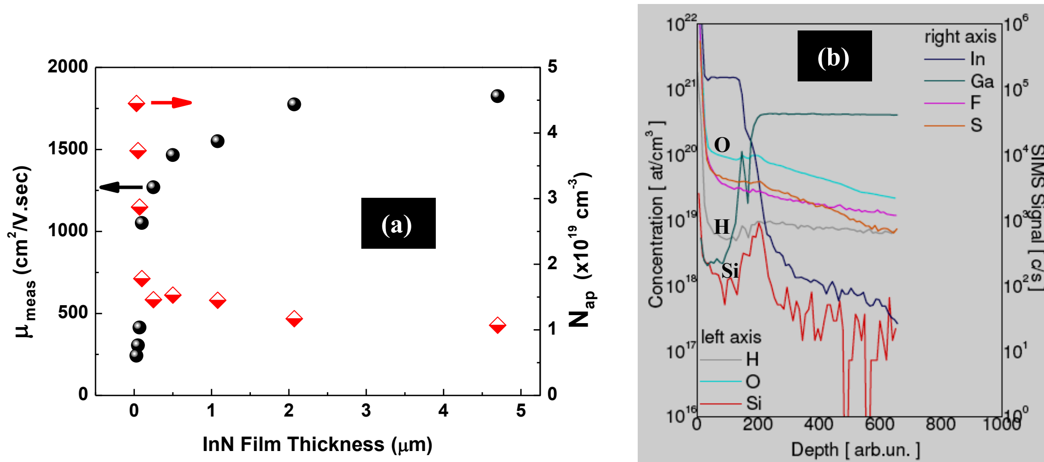

Figure 4.11 *(a) Plots of the apparent mobility (μ_{meas}) and electron concentration (N_{ap}) extracted by Hall-effect measurements (assuming a uniform conductivity InN layer) versus InN film thickness. (b) SIMS depth profiles for a 600 nm InN sample G1902 grown on GaN pseudo-substrate with estimated values of the H, O, and Si concentrations in the film. Electron concentration of 1.09 x 10^{20} cm^{-3} was determined from the Hall-effect measurements for the film, which coincides with the SIMS value for O in the film and indicates that the oxygen impurities incorporated during growth were responsible for the observed high electron degeneracy.*

4.7 Optical Studies of (0001) InN layers

4.7.1 Low temperature photoluminescence measurements

The 20K PL spectra of the *c*-plane InN films of different thicknesses are shown in Fig. 4.12(a). All the InN films exhibited similar broad spectra due to the high carrier concentration. Some differences in the spectra might be due to variations in the impurity and defect contents of the layers. The total PL integrated intensity as a function of InN film thickness is shown in Fig. 4.12(b). The trend of increasing PL intensity with epilayer thickness is attributed to improvement of the crystalline quality but also to the larger amount of material excited as thickness increases.

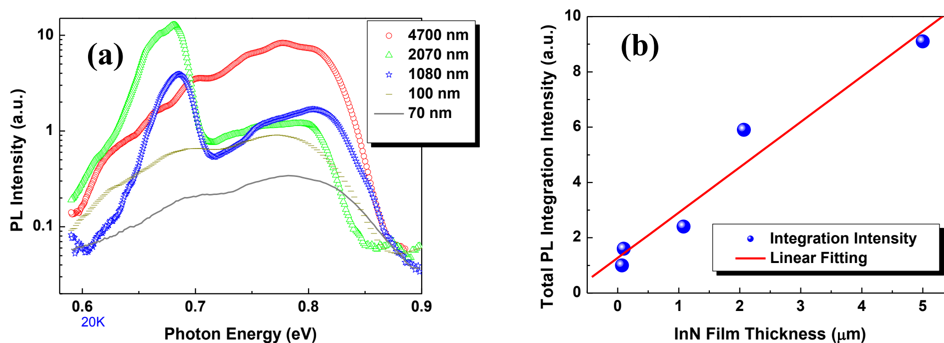

Figure 4.12 *PL measurements at 20K for the c-plane InN films: (a) PL spectra showing that all the films exhibited peaks irrespective of their thickness and (b) Total PL integration intensity showing that the PL intensity increased with thickness.*

4.7.2 Optical transmittance measurements

The three InN films G1382, G1383 and G1424 with epilayer thicknesses of 1000, 2000 and 5000 nm and apparent electron carrier concentrations of 1.45 x 10^{19} cm^{-3}, 1.17 x 10^{19} cm^{-3} and 1.07 x 10^{19} cm^{-3}, respectively, were investigated by optical transmittance measurements. The InN films with thickness above 1000 nm were chosen, in order to minimise measurement errors. The optical transmittance spectra were recorded in the wavelength region of 1000 - 2200 nm at 300K, as shown in Fig. 4.13(a), after the backside-polishing of the substrates to minimize scattering of the light. The well defined absorption edge of the spectra suggests that the films are of good crystal quality. The transmission spectra also exhibited interference fringe patterns. Below the band gap of the semiconductor, light interference within the thin films modulates both the reflection and transmission spectrum, resulting to the formation of ripples, while the high absorption coefficient above the band gap causes the film to absorb any multiple reflections of the light [35]. The amplitude of the fringe pattern was smaller for the 1000 nm film.

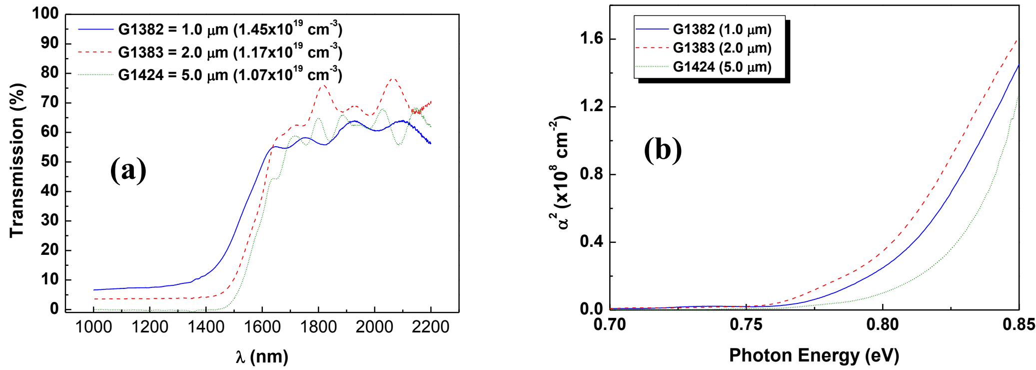

Figure 4.13 *(a) Optical transmittance spectra for the c-plane InN films with thicknesses of 1000 nm, 2000 nm and 5000 nm and (b) Plots of the square of absorption coefficient (α^2), calculated from the optical transmittance data, versus photon energy.*

The optical transmittance data were used to calculate the absorption coefficient α (E), following the steps described in subsection 2.3.6 of Chapter 2. Then, the absorption edge (E_{go}) was determined for each sample from the plot of α^2 versus $h\nu$, as shown in Fig. 4.13(b), under the assumption of parabolic bands and direct bandgap of InN. The value of E_{go} was slightly reduced by ~ 9 meV as film thickness increased from 1000 nm (0.802 eV) to 2000 nm (0.793 eV). The E_{go} of the 5000 nm film was at 0.819 eV, blue-shifted from the other two by 17 meV and 26 meV, respectively. Considering that the conventional band gap of InN films is ~0.65 eV [36], the high electron concentration of these thick films should play a role in the blue-shifting of the E_g due to Burstein-Moss effect. The Burstein-Moss shift (B-M shift) of 53.7, 49.9 and 48.5 meV was calculated for the 1000, 2000 and 5000 InN films, respectively, using B-M shift $\Delta E_g(n) \approx 2.2x10^{-8} n^{1/3}$ from Ref. 37, where n is the electron concentration. The estimated actual bandgap (E_g) values become 0.748, 0.743 and 0.771 eV, respectively. These results indicate that band filling effect, according to the

used expression of Ref 37, cannot fully account for the E_g observed for G1382, G1383, and G1424 above the ~0.65 eV value.

As a result of the large lattice constant mismatch between InN and the GaN (0001) pseudo-substrate, the InN films are expected to be relaxed at the growth temperature. However, several factors can cause in-plane strain, which consequently results to bandgap shift in InN [38-40]. For example, InN films could exhibit in-plane biaxial strain due to thermal expansion coefficients (TECs) mismatch and/or due to the lattice mismatch with the underlying substrates [27,28,41]. Compressive strain in InN films grown on GaN/Al_2O_3 substrates is known to arise during cooling, after the end of growth, due to the different TECs of InN and sapphire [27,28]. The observed increase of E_g should be partially related to the compressive residual strain [38].

4.8 Growth of InAlN and InN based device heterostructures

For InN-based device applications, there exist a need for heterostructures including larger bandgap materials to provide barriers that could allow the generation and confinement of carriers within the heterostructures [42]. The candidates could be GaN, AlN, or their alloys with InN. The significant lattice mismatch between these compounds and InN is expected to result in large piezo-electric polarisation in the strained layers (in polar structures) [43], which is very important for HEMT device applications. InAlN exhibits a higher band gap than InGaN and lager polarization difference with InN for the same In mole fraction, allowing to achieve a higher two-dimensional electron gas (2DEG) at the InAlN/InN heterojunction (HJ) compared to an InGaN/GaN HJ. Also, it is known that for the larger bandgap III-nitride materials, like GaN, AlN and InAlN, it is possible to form Schottky barriers by metal contacts on the surface. Schottky contacts are required for the gates to control the channel charge in HEMT devices. In this work, we studied HJs of InN with GaN, AlN and InAlN barrier layers. The growth and properties of InAlN films are discussed in the following sections.

The ternary Indium-Aluminium nitride alloys system (InAlN) is of particular interest for both optoelectronic and high frequency electronic devices. However, the development of InAlN films in the entire composition range is still challenging due to reasons related to the miscibility gap in the alloy system that leads to phase separation, in a similar way to what was obtained for InGaN growth [44-46]. Growing high quality InAlN films needs high substrate temperatures, which often lead to problems of In incorporation. Experimentally, the ternary InAlN film growth difficulty is due to the combined effects of strain and wide difference in AlN and InN growth temperature [47]. Therefore, the delicate optimization of the growth conditions for high quality InAlN film heteroepitaxy is embarked upon in this work. We aim to eventually employ the optimized conditions to grow InAlN/InN heterostructures for electron devices.

$In_xAl_{1-x}N$ films with different mole fractions of InN (x = 0.13 – 0.8) were grown on GaN (0001) pseudo-substrates by finding a balance in between the growth temperature and materials' fluxes to avoid the formation of metallic droplets. Growth temperatures in the range of 450 - 600°C were investigated. The average thickness of the grown InAlN layers was 150 nm.

A FE-SEM micrograph showing the surface of an InAlN film (sample G1786) with 16% InN content is shown in Fig. 4.15(a). The cross-sectional view of another InAlN film (sample G1861) with 70% InN content is shown in Fig. 4.15(b). These

images are typical for all the InAlN epilayers. They indicate that uniform InAlN layers with good adhesion on the GaN (0001) surface can be grown.

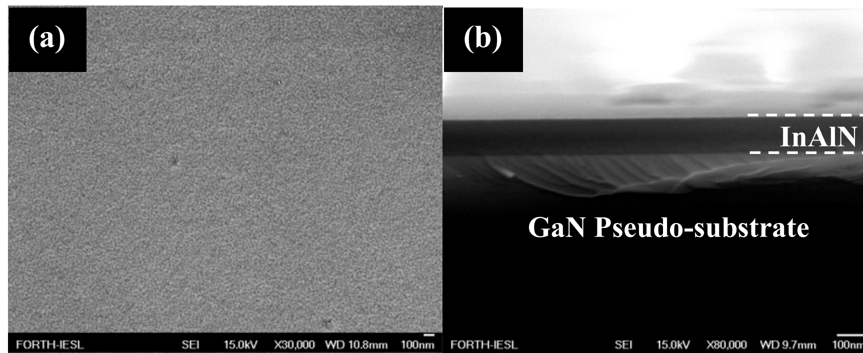

Figure 4.15 *FE-SEM micrographs showing (a) the surface of a 150 nm InAlN layer with 16% InN content and (b) a cross-section of an InAlN layer with 70% InN content. The images are representative of the InAlN layers discussed in this section.*

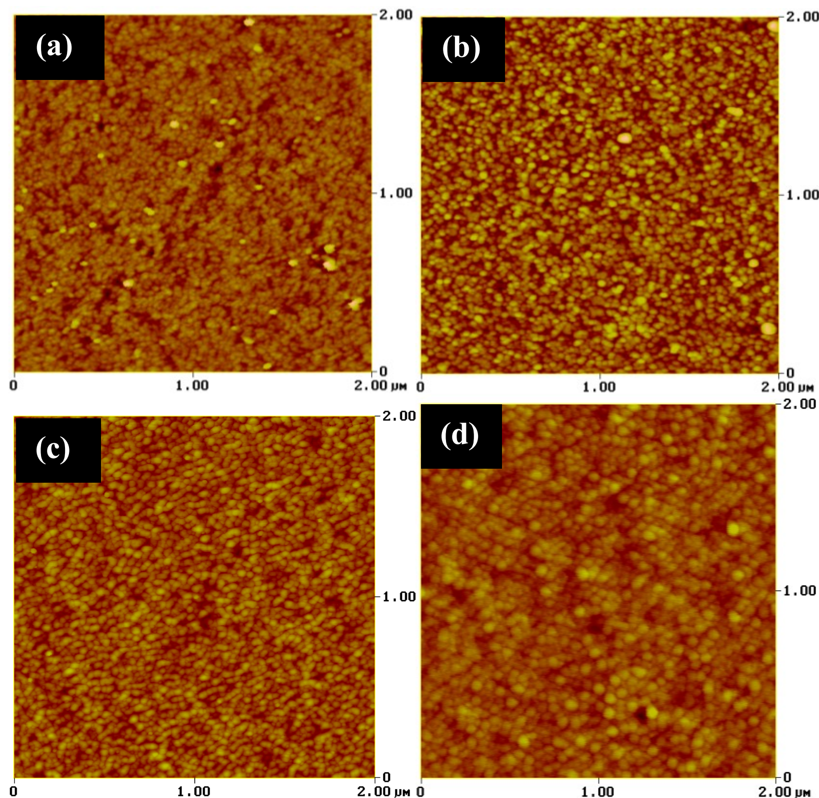

Figure 4.16 *2x2 μm² AFM micrographs showing the surface morphology of (a) InAlN sample G1866 with 20% InN content, (b) InAlN sample G1863 with 30% InN content, (c) InAlN sample G1861 with 70% In content and (d) InAlN sample G1860 with 80% InN content. The images are representative of all the InAlN layers discussed in this section with characteristic surface roughness grains attributed to the slightly N-rich growth conditions adopted for the epitaxial growth to prevent In droplets formation.*

The 2x2 μm² AFM micrographs of the surfaces of four InAlN films are shown in Fig. 4.16. The typical surface roughness grains observed for all the InAlN layers are attributed to the slightly N-rich growth conditions employed to prevent metallic In

droplets formation on the surfaces of the films. The AFM images of Figs. 4.16 (a) to 4.16(d) correspond to InAlN layers with 20, 30, 70 and 80% InN content, respectively. The rms surface roughness of each one was determined as 2.1, 4.96, 1.53 and 0.70 nm, respectively. This indicates that modest surface roughness was obtained in each of the layers, compared with results reported in the literature [48].

The InN mole fraction in the InAlN alloys was determined by HR-XRD, using GaN as reference. The determined In incorporation varied from approximately 12.7 to 80.0%, as shown by the HR-XRD theta-2theta profile scans of Fig. 4.17. All alloys exhibited two Bragg peaks arising from InAlN (0002) and GaN (0002), which correspond to the InAlN epilayer and the GaN pseudo-substrate, respectively. No double peaks were observed in any of the diffraction spectra, which may suggest lack of phase separation in the layers. However, the large widths of the peaks suggest significant inhomogeneities in the alloys. The samples identity numbers and the corresponding InN percentage as estimated from the HR-XRD diffraction spectra are given in the figure.

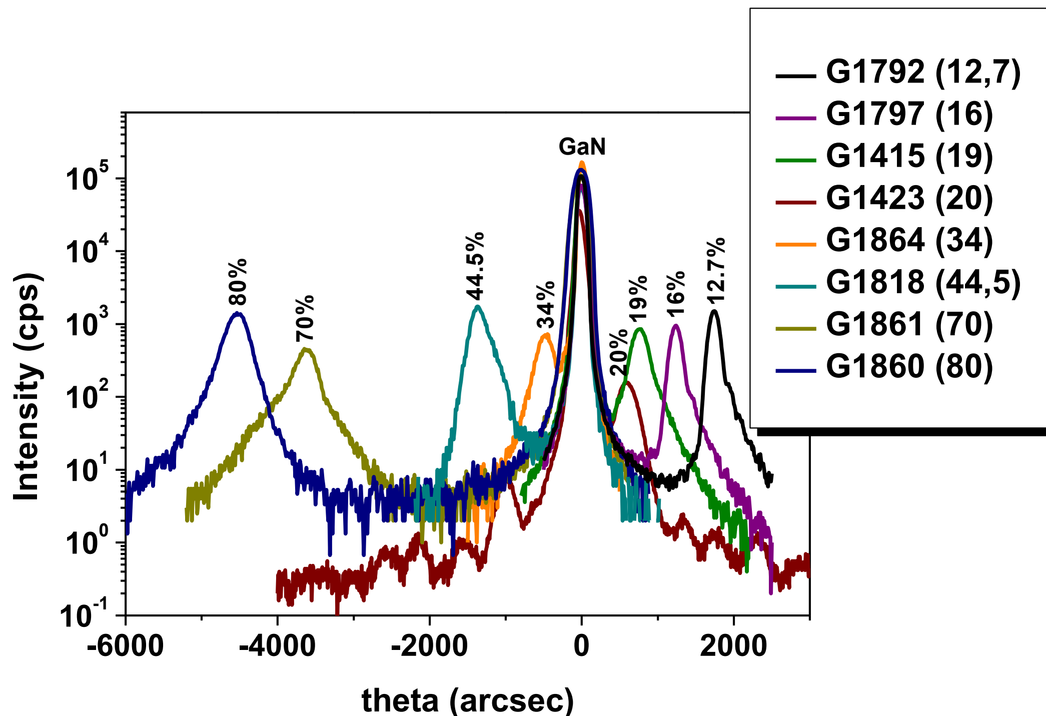

Figure 4.17 *HR-XRD theta-2theta scans for InAlN layers grown on GaN (0001) pseudo-substrates with InN content ranging from 12.7 to 80.0%. Each InAlN diffraction peak is labelled accordingly in the figure.*

Low and room temperature PL measurements of the InAlN layers were carried out. The PL spectra of sample G1797 (16% InN) is shown in Fig. 4.18. The InN content in sample G1797 was evaluated by the PL to be 15.6% [49,50], which is close to the 16% determined by the HR-XRD. Sample G1797 gives blue emission at 20K and both blue and yellow at room temperature. The PL peak at low temperature occurs at 3.913 eV.

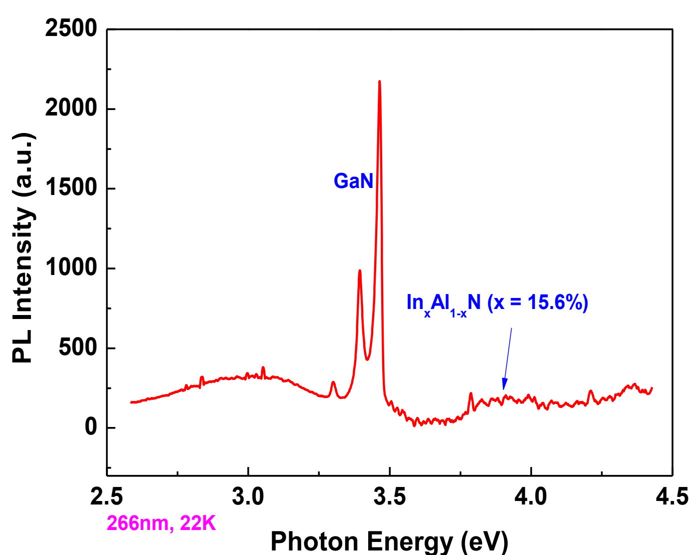

Figure 4.18 *PL measurements for $In_xAl_{1-x}N$/GaN layer at 22K for sample G1797. 15.6% InN content was determined by PL which is close to the 16% estimation by the HR-XRD.*

In general, the results of these investigations indicated that different composition InAlN layers can be grown on (0001) GaN pseudo-substrates by MBE. The optimised growth conditions for the InAlN films were then employed for the growth of InAlN/InN heterostructures.

4.9 Investigation of InN-rich InAlN Schottky diodes

According to published data, both InN-rich InGaN and InAlN alloys exhibit electron accumulation at the surface in a similar way to InN. InN content of 39% [51] and 43% [52,53] have been reported to correspond to flatband condition of undoped InGaN while 59% [52] has been estimated for Mg-doped InGaN. In the case of InAlN, the determined flatband condition lies around 59% [54] for the undoped, and 70% [55] for the Mg-doped InAlN. Above (below) these points, surface electron accumulation (depletion) occurs in both InGaN and InAlN. This underscores the need to properly engineer the InAlN heterostructures for device applications. One of the aims of this work is to determine whether Schottky barrier contacts can be made on InAlN layers and InAlN/InN heterostructures.

Two $In_{0.83}Al_{0.17}N$ samples G1904 and G1905 were grown on Ga-faced n^+-GaN/Al_2O_3 (0001) pseudo-substrates with the epitaxial structures shown in Figs. 4.19(a) and 4.19(b), respectively. A 0.5 μm GaN buffer layer was first grown under Ga-rich growth conditions at 810°C to reduce the surface roughness and improve the purity of the GaN layers. The $In_{0.83}Al_{0.17}N$ epilayer was then grown at 450°C. In the case of G1905, a 1 nm AlN cap layer was grown at ambient temperature to ensure that the AlN is non-conducting (amorphous).

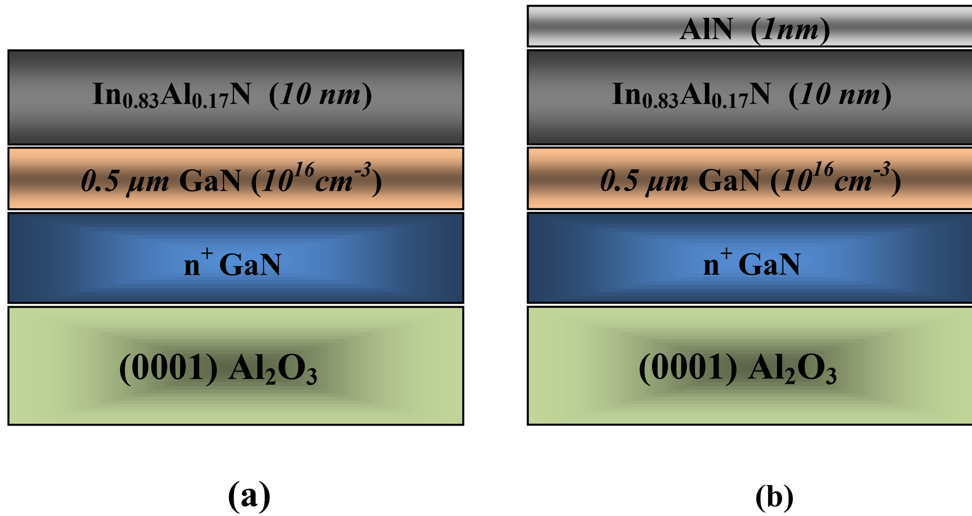

Figure 4.19 *Schematics of the InAlN/GaN heterostructures used for Schottky contacts processing: (a) G1904 without AlN cap layer (b) G1905 with a 1 nm AlN cap layer.*

After the growth process, conventional ultraviolet (UV) contact lithography, high-voltage e-gun evaporation of metals, and lift-off techniques were employed *ex-situ* for the fabrication of Schottky diodes. Mesa formation was accomplished by using a Ti/Ni (5 nm/ 50 nm) hard mask. The mesa isolation was performed by reactive ion etching (RIE) for 80 min, using BCl_3/Cl_2 (7:1) plasma at 10 mTorr and 50 W. The mesa length was usually 1µm. The hard mask was removed with a $HCl/HNO_3/HF$ (6.6/2.4/1) solution. E-gun evaporation was used to deposit the rectifying contact (30 nm Ni/100 nm Au) while multilayer system, consisting of 30 nm Ti/ 170 nm Al/ 40 nm Ni/50 nm Au, was deposited on the n^+-GaN and employed as the ohmic contact. Schottky contacts were of circular geometry with different diameters (50, 100, 175 and 250 µm). Capacitance-voltage (C-V) and current-voltage (I-V) measurements at RT were employed for the characterization of the Schottky contacts and the epitaxial heterostructures.

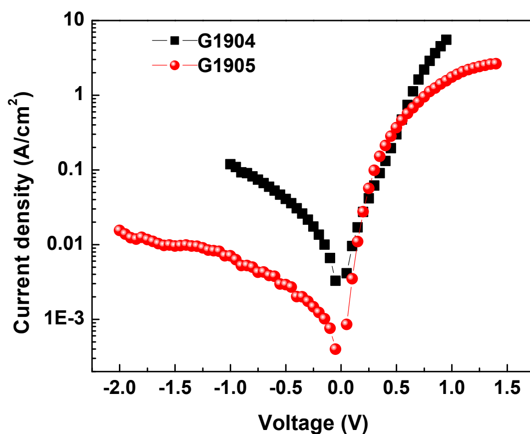

Figure 4.20 *I-V characteristics of the Schottky diodes fabricated on the InN-rich InAlN layers. G1904 exhibits Schottky diode ideality factor and barrier height of 4.18 and 0.52 eV, respectively, while 2.29 and 0.57 eV apply in the case of G1905. Very leaky diodes were generally obtained for G1904 compared to G1905.*

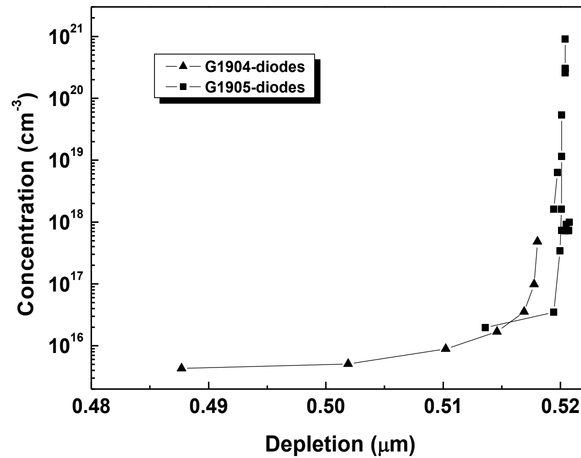

Figure 4.21 *ECV measurements of Schottky diode samples G1904 and G1905 before and after fabrication. The measurements were taken after the photolithography processing of the samples.*

The typical rectifying character exhibited by the I-V characteristics of the fabricated contacts are shown in Fig. 4.20. The best diode was observed for a radius corresponding to 100 µm in the case of G1905 and 250 µm for G1904. The leakage current was relatively high in both devices, although reasonable for the large radius employed. The reverse current density was 16 mA/cm^2 for a reverse bias voltage of -2V in the case of G1905 while G1904 exhibited higher reverse current density of 122 mA/cm^2 at much lower reverse bias voltage of -1V, indicating a higher leakage current in sample G1904 that is without AlN cap layer. C-V measurements on the InAlN diodes were carried out at a frequency equal to 1 MHz. As shown in the carrier profile of Fig. 4.21, the epitaxial layers were fully depleted down to the interface with the n^+-GaN buffer layer.

The room temperature ideality factor (n) and Schottky contact barrier height (Φ_b) of diode G1904 were determined as 4.59 and 0.42 eV, respectively, using thermionic emission theory [56] while G1905 exhibited 2.29 and 0.57 eV, respectively. The high ideality factor values suggest significant tunnelling currents at the contacts. The comparison of the results indicates that the use of thin AlN cap layer significantly improved the Φ_b and the ideality factor.

4.10 Growth of InN/InAlN heterostructures

HEMTs rely on the use of heterojunctions (HJs) formed between two semiconductors of different bandgaps. This section describes exploratory experiments for the formation of heterostructures, which employ an InN layer where carriers might be confined, as required for the realization of a HEMTs structures. Four samples were grown on GaN (0001) pseudo-substrates. The epitaxial structures of the samples are described in Table 4.1. A lattice matched $In_{0.18}Al_{0.82}N$ buffer layer was always first deposited on the GaN pseudo-substrate, except in the case of sample G1879, where $In_{0.7}Al_{0.3}N$ was used. The $In_xAl_{1-x}N$ buffer layer was expected to either electrically isolate the substrate (x=0.18) or to absorb the major part of lattice mismatch between

InN and GaN (x=0.70), so that InN could be coherently strained. Table 4.1 comprehensively describes the epitaxial structures of the samples.

Table 4.1 *Description of the grown InN/InAlN heterostructures*

Sample	Growth Structure
G1576	15 nm GaN/20 nm InN/100 nm GaN/100 nm $In_{0.18}Al_{0.82}N$/GaN template
G1577	15 nm AlN/20 nm InN/100 nm GaN/100 nm $In_{0.18}Al_{0.82}N$ /GaN template
G1879	20 nm $In_{0.7}Al_{0.3}N$/5 nm InN/25 nm $In_{0.7}Ga_{0.3}N$/200 nm $In_{0.7}Al_{0.3}N$/GaN template
G1880	20 nm $In_{0.18}Al_{0.82}N$ / 1ML InN/(1ML InN/5ML GaN) x5 / 200 nm $In_{0.18}Al_{0.82}N$/GaN template

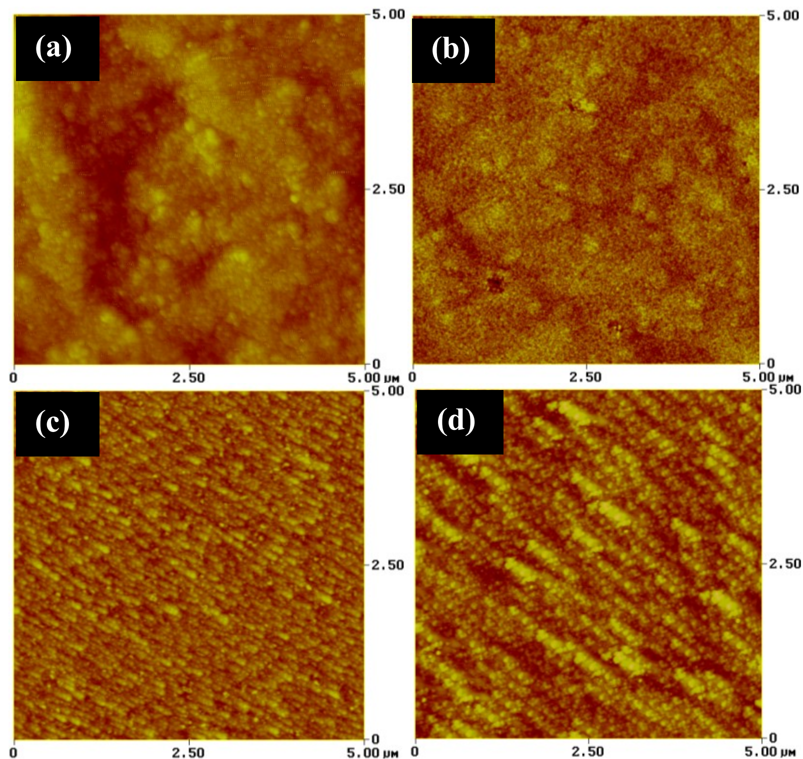

Figure 4.22 *5 x 5 μm^2 AFM micrographs showing the surface of the samples consisting of InAlN/InN heterostructures grown on (0001) GaN pseudo-substrates: (a) G1576, (b) G1577, (c) G1879 and (d) G1880. The rms roughness (z-axis full scale) for these samples was 0.77 nm (7.53 nm), 0.82 nm (12.41 nm), 1.52 nm (12.85 nm) and 6.06 nm (49.45 nm), respectively.*

All the InN layers thicker than 1nm were grown at approximately 430°C. The InGaN and InAlN layers employed were grown with T_{sub} in the range of 420 - 450°C. In the case of sample G1880, an InN/GaN superlattice (SL) structure was grown, as a possible electron channel layer. We know that strain relaxation of InN on GaN (0001) starts from the first ML [57]. However, Yoshikawa *et al.* [58] reported that 1 ML of InN can be grown without strain relaxation above the conventional InN decomposition temperature, if inserted in-between GaN layers. Based on these findings, G1880 SL structure was grown at 500°C using 1ML of InN interwoven with

5ML of GaN in the makeup of the SL, indicating that six InN wells are inserted in the GaN matrix. The top surface consists of a 20 nm $In_{0.18}Al_{0.82}N$ cap layer [Table 4.1].

The 5x5 μm^2 AFM images of the surfaces of the samples are shown in Fig. 4.22. The surfaces of the samples G1576 [Fig. 4.22(a)] and G1577 [Fig. 4.22(b)] were very smooth with rms surface roughness of 0.77 nm and 0.83 nm, respectively. Samples G1879 [Fig. 4.22(c)] and G1880 [Fig. 4.22(d)] exhibited higher rms roughness of 1.52 nm and 6.06 nm, respectively. It is important to note that no metallic indium accumulation was observed on the surface of any of these heterostructures.

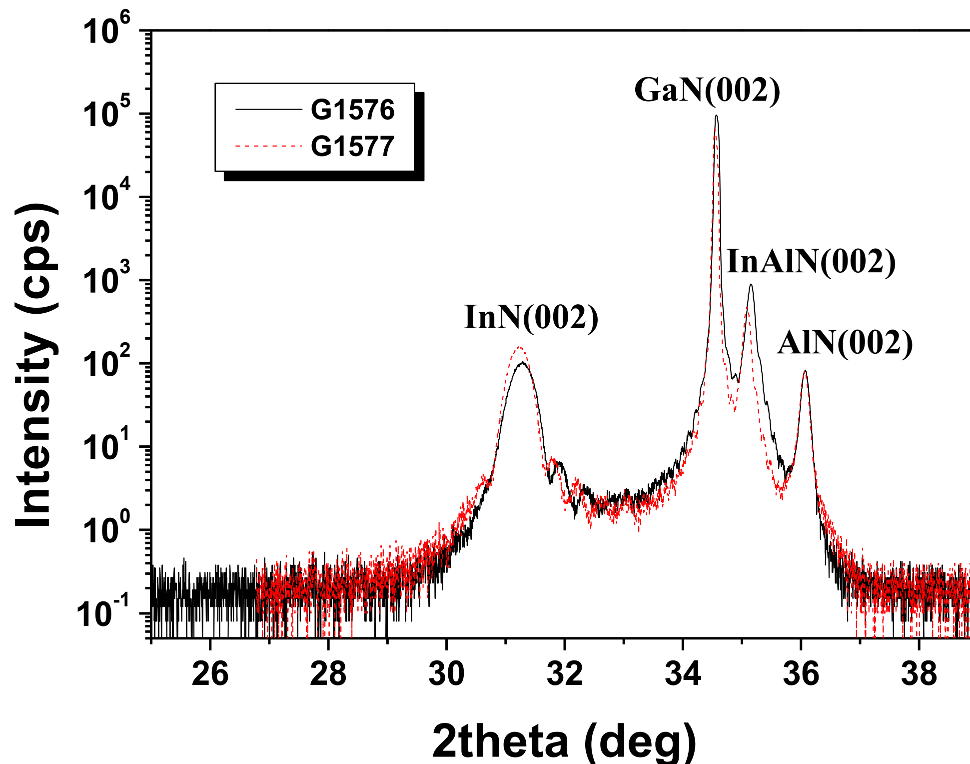

Figure 4.23 *HRXRD theta-2theta scans for the InN/InAlN heterostructure samples G1576 and G1577 [Table 4.1].*

The heterostructures were investigated by HRXRD. Since samples G1576 and G1577 differed only in the cap layer material, the theta-2theta symmetric (0002) scans are shown together for comparison in Fig. 4.23. The presence of thickness interference fringes is evidence for flat and abrupt interfaces between the different layers of the heterostructure. The excellent alignment of the diffraction profile of both samples is also a good indication that the growth was consistent and reproducible. The observation of the InN layer peak, despite its only 20 nm thickness, suggests that it is of high crystal quality. Moreover, the peak of the 100 nm InAlN layer with expected In incorporation of 18% is clearly visible and the narrowness of the peak indicates that it is of high structural quality also. The GaN and AlN peaks originated from the GaN-pseudo-substrates. From the graphs, the InN active layer thickness in G1576 and G1577 were estimated as 21 nm and 23 nm, respectively, which are in good

agreement with the nominal value of 20 nm. The InN mole fraction of the alloys was determined as 17.2% and 17.6%, respectively, which also conform to the expected 18%.

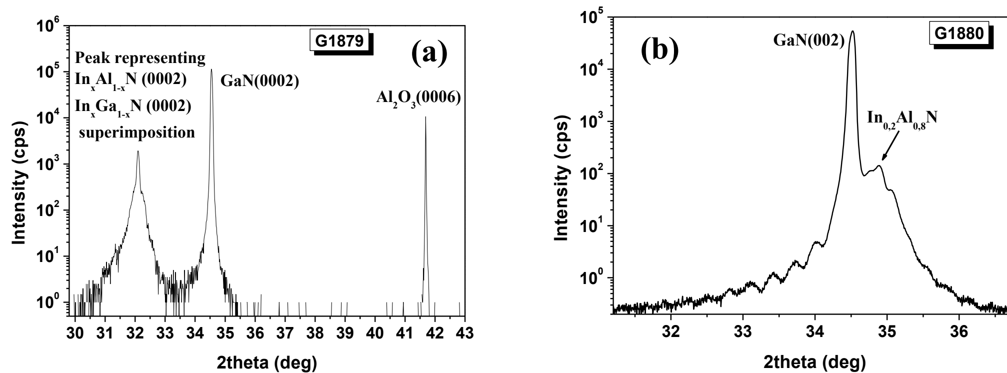

Figure 4.24 *HRXRD theta-2theta scans for the InN/InAlN heterostructure samples: (a) sample G1879 and (b) sample G1880. The structure of the samples is shown in Table 4.1.*

The diffraction profiles of samples G1879 and G1880 are shown in Figs. 4.24(a) and 4.24(b), respectively. Two of the diffraction peaks observed for sample G1879 correspond to the GaN buffer layer and the Al_2O_3 substrate. Since the expected peaks from the $In_{0.7}Ga_{0.3}N$ and $In_{0.7}Al_{0.3}N$ layers of the heterostructure are enveloped by the third broad-based peak observed at 32.09 degree to the left-hand side of the GaN peak in Fig. 4.24(a), this third peak is assigned to both alloys. In the case of sample G1880 in Fig. 4.24(b), the observed satellite peaks in the theta-2theta scan indicate that a multi-quantum well (MQW) structure was grown. The InN component of the SL is not observable because of the extremely small thickness of this layer. The estimated 20% InN content in the InAlN layer is close to the expected value of 18%.

Table 4.2 *AFM and Hall-effect results for the InN/InAlN heterostructure samples. AFM_{rms} is the rms roughness extracted from 5 x 5 μm^2 AFM scans, R_s, N_s and μ are the sheet resistance, sheet density and mobility determined from the Hall-effect measurements.*

Sample	AFM_{rms} (nm)	R_s (Ω/sq)	N_s (cm^{-2})	μ (cm^2/Vs)
G1576	0.77	468	9.15×10^{13}	150
G1577	0.83	379	6.03×10^{13}	300
G1879	1.52	15	-	-
G1880	6.06	6954	4.62×10^{12}	200

In order to gain an insight into the electrical properties of the structures, Hall-effect measurements were conducted on the samples at room temperature and the results are given in Table 4.2. Sheet electron density (N_s) ranging from 10^{12} to high 10^{13} cm^{-2} was measured in the heterostructures, with corresponding mobility range of

150 to 300 cm^2/Vs. The extremely low sheet resistance of G1879 indicates some problems in the measurements or the electrical properties of this structure.

The results for sample G1577 are very interesting considering that the lattice mismatch strain of the 20 nm InN layer is fully relaxed and high defect content should exist in this layer. These values are higher than the values reported to date for InN-based heterojunction field-effect transistors (HFET) channel of 2.6 x 10^{13} cm^{-2} and 209 cm^2/Vs by Lin *et al.* [59].

4.11 Concluding remarks

InN heteroepitaxial growth on GaN (0001) pseudo-substrates was carried out in order to study the dependence of InN properties on layer thickness and to establish a set of material data that could be used in comparative studies for analysis and understanding of the properties of InN films grown on Si (111) and *r*-plane sapphire substrates. InN on *c*-plane GaN pseudo-substrates corresponds to the state-of-the-art InN material. Thickness range of 30 - 5000 nm was investigated. The epitaxy of the films proceeded in the step-flow growth mode with surface morphology characterised by monolayer height steps, terraces and spiral hillocks. The early stage of the InN growth was characterised by high density hillocks, which appeared to exhibit increment in size and decrement in density per surface area as the film thickness increases. The visibility of hillocks on the AFM micrographs of the surface is related to the presence of screw dislocations but also to the used growth conditions (substrate temperature and III/V flux ratio).

The measured small FWHM values for the symmetric and assymetric RCs, with respect to film thickness, show that all the InN epilayers are of state-of-the-art material quality.

Surface electron accumulation of approximately 10^{14} cm^{-2} was determined in the InN (0001) layers. The measured electron mobility (μ_{meas}) increased from 242 to 1824 $cm^2V^{-1}sec^{-1}$ as the film thickness increased from 30 nm to 5000 nm and the corresponding apparent electron concentration (N_{ap}) values decreased from 4.45 x 10^{19} to 1.07 x 10^{19} cm^{-3}, respectively. The fast increase in the Hall mobility, as thickness increased from 30 nm to 100 nm, is due to the weaker contribution of the low mobility surface/interface conductivity layer to the overall conductivity. The critical thickness at which both electrical quantities begin to saturate is 100 nm.

A SIMS investigation carried out on an InN film exhibiting electron concentration of 1.09 x 10^{20} cm^{-3} revealed that only the O (oxygen) concentration in the film is approaching the 10^{20} cm^{-3} level, while H and Si concentrations are 6.5 x 10^{18} cm^{-3} and ~ 10^{18} cm^{-3}, respectively. The results exclude hydrogen and Si but supports oxygen as the source of bulk donors in InN.

Optical studies of the thicker 1000 - 5000 nm InN films by transmittance measurements indicate a similar bandgap at approximately 0.75 eV after Burstein-Moss shift correction. Departure of the bandgap obtained for the InN film from the conventional 0.65 eV value was attributed in part to a bandgap shift resulting from compressive strain due to InN and sapphire thermal expansion coefficients' mismatch.

The growth of InN based heterostructures including large bandgap materials of InAlN, AlN and GaN as barriers, were also investigated. InAlN alloys with InN content from approximately 13 to 80.0% were controllably grown on GaN (0001) templates. Ni-based Schottky contacts were successfully fabricated on 10 nm $In_{0.83}Al_{0.17}N$ layer grown on GaN (0001) template. Use of a 1 nm AlN barrier

enhancement layer demonstrated the best diode, leading to Schottky contact with ideality factor and barrier height of 2.29 and 0.57 eV, respectively, for a diameter of 100 μm. Both values deteriorated to 4.59 and 0.42 eV, respectively, when the cap layer was exempted, confirming AlN cap layer as an efficient Schottky barrier enhancement layer on InN-rich InAlN.

The advantage of III-nitride band gap engineering between 0.65 eV for InN to 6.2 eV for AlN allows the InAlN alloy to be used as barrier layer and the low bandgap InN material as channel for InN-based HEMT structures. Four different InN/InAlN heterostructures grown for an exploratory study exhibited flat and abrupt interfaces, according to HR-XRD theta-2theta scans. Hall-effect measurements exhibited electron sheet carrier density and mobility of 6.03 x 10^{13} cm^{-2} and 300 $cm^2V^{-1}sec^{-1}$, respectively, for an heterostructure consisting of 15 nm AlN/20 nm InN/100 nm GaN/100 nm $In_{0.18}Al_{0.82}N$ /GaN template. These values are relatively higher than the best values of 2.6 x 10^{13} cm^{-2} and 209 cm^2/Vs reported to date for InN-based heterojunction field-effect transistors.

Reference

1. V. Cimalla, V. Lebedev, F. M. Morales, R. Goldhahn and O. Ambacher, *Appl. Phys. Lett*. **89**, 172109 (2006)
2. W. Liu, R. J. N. Tan, C. B. Soh, and S. J. Chua, *Appl. Phys. Lett*. **97**, 042110 (2010)
3. S. Yamaguchi, M. Kariya, S. Nitta, T. Takeuchi, C. Wetzel, H. Amano, and I. Akasaki, *J. Appl. Phys*. **85**, 7682 (1999)
4. H. Lu, W. J. Schaff, L. F. Eastman, J. Wu, W. Walukiewicz, V. Cimalla, and O. Ambacher, *Appl. Phys. Lett*. **83**, 1136 (2003)
5. G. Koblmüller, C. S. Gallinat, S. Bernardis, J. S. Speck, G. D. Chern, E. D. Readinger, H. Shen, and M. Wraback, *Appl. Phys. Lett*. **89**, 071902 (2006)
6. A. Knübel, R. Aidam, V. Cimalla, L. Kirste, M. Baeumler, C-C. Leancu, V. Lebedev, J. Wallauer, M. Walther, and J. Wagner, *Phys. Status Solidi (c)* **6**, 1480 (2009)
7. I. Gherasoiu, M. O'Steen, T. Bird, D. Gotthold, A. Chandolu, D. Y. Song, S. X. Xu, M. Holtz, S. A. Nikishin, and W. J. Schaff, *J. Vac. Sci. Technol*. A **26**, 399 (2008)
8. T. A. Komissarova, T. V. Shubina, V. N. Jmerik, S. V. Ivanov, L. I. Ryabova, D. R. Khokhlov, A. Vasson, J. Leymarie, T. Araki, and Y. Nanishi, *Semiconductors* **43**, pp. 285 (2009)
9. T-C P. Chen, C. Thomidis, J. Abell, W. Li, T.D. Moustakas, *J. Cryst. Growth* **288**, 254 (2006)
10. A. Georgakilas, H. M. Ng, Ph. Komninou, in "Nitride semiconductors: *Handbook on Materials and Devices"*, Edited by P. Ruterana, M. Albrecht, J. Neugebauer , Wiley-VCH, Berlin, Chap 3, p. 107 (2003)
11. C. S. Gallinat, G. Koblmüller, J. S. Brown, and J. S. Speck, *J. Appl. Phys.* **102**, 064907 (2007)
12. B. Heying, E. J. Tarsa, C. R. Elsass, P. Fini, S. P. DenBaars, and J. S. Speck, *J. Appl. Phys.* **85**, 6470 (1999)
13. P.Q. Miraglia, E.A. Preble, A.M. Roskowskic, S. Einfeldt, S.H. Lim, Z. Liliental-Weber, R.F. Davis, *Thin Solid Films* **437**, 140 (2003)
14. A.M. Roskowski, P.Q. Miraglia, E.A. Preble, S. Einfeldt, R.F. Davis, *J. Cryst. Growth* **241**, 141 (2002)
15. B. S. Simpkins, E. T. Yu, P. Waltereit, J. S. Speck, *J. Appl. Phys*. **94**, 1448 (2003)
16. X. Wang, S.-B. Che, Y. Ishitani, and A. Yoshikawa, *Appl. Phys. Lett*. **90**, 151901 (2007)
17. E. J. Tarsa, B. Heying, X. H. Wu, P. Fini, S. P. DenBaars, and J. S. Speck, *J. Appl. Phys.* **82**, 5472 (1997)
18. E. Dimakis, J. Domagala, A. Delimitis, Ph. Komninou, A. Adikimenakis, E. Iliopoulos, A. Georgakilas, *Superlattices and Microstruct*. **40**, 246 (2006)
19. B. Heying, R. Averbeck, L. F. Chen, E. Haus, H. Riechert, and J. S. Speck, *J. Appl. Phys.* **88**, 1855 (2000)
20. B. Heying, I. Smorchkova, C. Poblenz, C. R. Elsass, P. Fini, S. DenBaars, U. Mishra and J. S. Speck, *Appl. Phys. Lett*. **77**, 2885 (2000)
21. M A Moram and M E Vickers *Rep. Prog. Phys*. **72**, 036502 (2009)
22. P.F. Fewster, J. Appl. Crystallogr. **22**, 64 (1989)
23. V. Srikant, J. S. Speck, and D. R. Clarke, *J. Appl. Phys.* **82**, 4286 (1997)

24. H Heinke, V Kirchner, S Einfeldt and D Hommel, *Phys. Status Solidi (a)* **176**, 391 (1999)
25. V. Lebedev, V. Cimalla, T. Baumann, and O. Ambacher, F. M. Morales, J. G. Lozano, and D. González, *J. Appl. Phys*. **100**, 094903 (2006)
26. N. Herres, L. Kirste, H. Obloh, K. Kohler, J. Wagner, P. Koidl, *Mat. Sci. Eng*. B **91**, 425 (2002)
27. E. Dimakis, E. Iliopoulos, K. Tsagaraki, A. Adikimenakis, and A. Georgakilas, *Appl. Phys. Lett*. **88**, 191918 (2006)
28. E. Dimakis, J. Domagala, E. Iliopoulos, A. Adikimenakis, and A. Georgakilas, *Phys. Status Solidi* (a) **204**, 1996 (2007)
29. C.H. Swartz, R.P. Tompkins, N.C. Giles, T.H. Myers,H. Lu, W.J. Schaff, L.F. Eastman, *J. Crystal Growth* **269**, 29–34 (2004)
30. V. Darakchieva, T. Hofmann, M. Schubert, B. E. Sernelius, B. Monemar, P. O. Å. Persson, F. Giuliani, E. Alves, H. Lu, and W. J. Schaff, *Appl. Phys. Lett*. **94**, 022109 (2009)
31. A. O. Ajagunna, E. Iliopoulos, G. Tsakatouras, K. Tsagaraki, M. Androulidaki, and A. Georgakilas, *J. Appl. Phys*. **107**, 024506 (2010)
32. B. R. Nag, *J. Cryst. Growth* **269**, 35 (2004)
33. V.W. L. Chin, T.L. Tansley and T. Osotchan, *J. Appl. Phys*. **75**, 7365 (1994)
34. S. Vitanov, M. Nedjalkon and V. Palankovski, *NMA 2006, LNCS* **4310**, 197 (2007)
35. J. F. Muth, J. D. Brown, M. A. L. Johnson, Z. YU, R. M. Kolbas, J. W. Cook, JR and J. F. Schetzina, *MRS Internet J. Nitride Semicond. Res*. 4S1, G5.2 (1999)
36. A. Georgakilas, in "*CAS 2008 Proceedings*" IEEE, 43 (2008)
37. B. Monemar, P. P. Paskov and A. Kasic, *Superlattices and Microstruct*. **38,** 38 (2005)
38. C. S. Gallinat, G. Koblmüller, J. S. Brown, S. Bernardis, J. S. Speck, G. D. Chern, E. D. Readinger, H. Shen, and M. Wraback, *Appl. Phys. Lett*. **89**, 032109 (2006)
39. P. P.-T. Chen, K. S. A. Butcher, M. Wintrebert-Fouquet, R. Wuhrerb, M. R. Phillips, K. E. Prince, H. Timmers, S. K. Shrestha, B. F. Usher, *J. Cryst. Growth* **288**, 241 (2006)
40. A. Kadir, T. Ganguli, R. Kumar, M. R. Gokhale, A. P. Shah, S. Ghosh, B. M. Arora, and A. Bhattacharya, *Appl. Phys. Lett.* **91**, 111913 (2007)
41. P. Specht, R. Armitage, J. Ho, E. Gunawan, Q. Yanga, X. Xu, C. Kisielowski, E.R. Weber, *J. Cryst. Growth* **269**, 111 (2004)
42. Md. T. Hasan, A. G. Bhuiyan, A. Yamamoto, *Solid-State Electronics* **52**, 134 (2008)
43. J. Kuzmik and A. Georgakilas, IEEE Transactions on Electron Devices **58**, 720 (2011)
44. H. Chen, R. M. Feenstra, J. Northrup, J. Neugebauer, and D. W. Greve, *MRS Internet J. Nitride Semicond. Res.* **6**, 11 (2001)
45. I. Ho and G. B. Stringfellow, *Appl. Phys. Lett*. 69, 2701 (1996)
46. D. Doppalapudi, S. N. Basu, K. F. Ludwig, and T. D. Moustakas, *J. Appl. Phys*. 84, 1389 (1998)
47. S.-L. Sahonta, G. P. Dimitrakopulos, Th. Kehagias, J. Kioseoglou, A. Adikimenakis, E. Iliopoulos, A. Georgakilas, H. Kirmse, W. Neumann, and Ph. Komninou, *Appl. Phys. Lett.* **95**, 021913 (2009)
48. M. Higashiwaki and T. Matsuil, *Jpn. J. Appl. Phys*., **43**, L768 (2004)

49. E. Iliopoulos, A. Adikimenakis, C. Giesen, M. Heuken, and A. Georgakilas, *Appl. Phys. Lett.* **92**, 191907 (2008)
50. M. Androulidaki, N. T. Pelekanos, K. Tsagaraki, E. Dimakis, E. Iliopoulos, A. Adikimenakis, E. Bellet-Amalric, D. Jalabert, and A. Georgakilas, *Phys. Status Solidi (c)* **3**, 1866 (2006)
51. L. R. Bailey, T. D. Veal, P. D. C. King, C. F. McConville, J. Pereiro, J. Grandal, M. A. Sánchez-García, E. Muñoz, and E. Calleja, *J. Appl. Phys*. **104**, 113716 (2008)
52. P. D. C. King, T. D. Veal, H. Lu, P. H. Jefferson, S. A. Hatfield, W. J. Schaff, C. F. McConville, *Phys. Status Solidi (b)* **245**, 881 (2008)
53. T. D. Veal, P. H. Jefferson, L. F. J. Piper, C. F. McConville, T. B. Joyce, P. R. Chalker, L. Considine, H. Lu, and W. J. Schaff, *Appl. Phys. Lett*. **89**, 202110 (2006)
54. P. D. C. King, T. D. Veal, A. Adikimenakis, H. Lu, L. R. Bailey, E.Iliopoulos, A. Georgakilas, W. J. Schaff, and C. F. McConville, *Appl. Phys. Lett*. **92**, 172105 (2008)
55. P. D. C. King, T. D. Veal, W. J., and C. F. McConville, *Phys. Status Solidi (b)* **246**, 1169 (2009)
56. J. Kuzmik, A. Kostopoulos, G. Konstantinidis, J.-F. Carlin, A. Georgakilas, and D. Pogany, *IEEE Trans. Electron Devices* **53**, 422 (2006)
57. E. Dimakis, E. Iliopoulos, and K. Tsagaraki, Th. Kehagias and Ph. Komninou and A. Georgakilas, *J. Appl. Phys.* **97**, 113520 (2005)
58. A. Yoshikawa, S. B. Che, W. Yamaguchi, H. Saito, X. Q. Wang, Y. Ishitani, and E. S. Hwang, *Appl. Phys. Lett*. **90**, 073101 (2007)
59. Y. S. Lin, S. H. Koa, C. Y. Chan, S. S. Hsu, H. M. Lee, and S. Gwo, *Appl. Phys. Lett.* **90**, 142111 (2007)

5 Growth of InN on *r*-plane ($1\bar{1}02$) Al_2O_3 substrates

5.1 Introduction: Why non-polar sapphire substrates?

5.2 Experimental descriptions

5.3 The role of buffer layer on InN grown on *r*-plane sapphire

5.4 Effect of Growth Temperature (T_{sub}) on *a*-plane InN grown on *r*-plane sapphire

5.5 Effect of III/V flux ratio on *a*-plane InN grown on *r*-plane sapphire

5.6 Effect of *in-situ* intermittent surface nitridation of *a*-plane InN during growth

5.7 Thickness dependence of the properties of *a*-plane InN grown by MBE

5.7.1 Objective of the study and experimental procedures

5.7.2 Surface Morphology characterisation

5.7.3 Structural properties analyses

5.7.4 Structural Anisotropy investigation

5.7.5 Electrical properties investigation of *a*-plane InN

5.7.5.1 Hall-effect Measurements study of the *a*-plane InN films

5.7.5.2 Modelling and analysis of the electrical properties of *a*-plane InN

5.7.6 Optical properties investigation of *a*-plane InN

5.7.6.1 Photoluminescence measurements of *a*-plane InN

5.7.6.2 Transmittance measurements of *a*-plane InN

5.8 Growth and properties of 3 μm thick *a*-plane InN grown on *r*-plane sapphire

5.10 Microstructures of *a*-plane InN films on *r*-plane sapphire substrates

5.11 Concluding remarks

5.1 Introduction: Why non-polar III-nitrides?

Polarization, which can be either spontaneous or piezoelectric, induces electric fields along the polar *c*-axis of III-nitride semiconductor heterostructures and reduces the efficiency of light emitting devices. Group-III nitrides heterostructures of non-polar orientation therefore hold great promise for the fabrication of highly efficient light-emitting diodes (LEDs) and laser diodes (LDs) due to the absence of internal electric fields and consequently, the possibility of achieving high electron and hole wavefunctions overlap that yields high optical transition probability [1,2]. Zero-internal field has recently been demonstrated in non-polar InGaN/GaN multi-quantum wells (MQWs) grown on *r*-plane sapphire substrate [3], making the possibility of growing high quality non-polar MQWs the key factor to solve the efficiency limitation in conventional *c*-plane GaN based light emitting diodes. *A*-plane InGaN/GaN MQW green LEDs have already been successfully grown on *r*-plane sapphire and device characteristics of these green LEDs have been reported [4].

Recently, unprecedented attention has been drawn to InN growth and characterisation among the III-nitrides group due to its very promising properties for the development of advanced electronic and optoelectronic devices [5]. The development of non-polar heterostructures based on InN is very interesting considering the elimination of the polarisation induced internal fields. Moreover, evidence of unpinned Fermi level for *in-situ* cleaved *a*-plane InN surfaces [6] has confirmed the predicted potential of realizing InN surfaces without an electron accumulation layer [7,8]; underscoring the importance of investigating the heteroepitaxial growth of InN of *a*-plane or *m*-plane orientations. Even though a lot have already been done in the growth and characterisation of *a*-plane $(11\bar{2}0)$ GaN and $(11\bar{2}0)$ AlN, *a*-plane $(11\bar{2}0)$ InN has enjoyed very little attention in spite of the well known overall potentials. Most of the works already done on InN are related to its growth on *c*-plane (0001) [9,10]. High crystal quality *a*-plane InN growth on *r*-plane $Al_2O_3(1\bar{1}02)$ seems to be more tricky and difficult to realize, in comparison to *c*-plane InN growth and often leads to undesired InN orientation(s).

Previous studies of *a*-plane InN growth have mainly focused on direct InN growth on *r*-plane Al_2O_3 without the use of any intermediate layer [11,12], and this mostly yielded InN layers with either dominant cubic phase or a mixture of both cubic and hexagonal-phases. Cubic InN (β-InN), nevertheless, could enhance further expansion of the applications of InN and its alloys having been predicted to exhibit lower band gap energy at about 0.58 eV [13]. Interestingly, Zhu et al. have reported the growth of single crystalline *a*-plane InN on *r*-plane sapphire by MOCVD, employing 3 minutes nitridation of the sapphire surface at 600°C, without use of any intermediate layer [14]. Using electron cyclotron resonance plasma-assisted molecular beam epitaxy (ECR-MBE) to grow *a*-plane $(11\bar{2}0)$ InN on nitridated *r*-plane $(1\bar{1}02)$ sapphire, Watanabe *et al.* [12] have shown that the nitridation of the sapphire produced a cubic (001) AlN interfacial layer, which caused the subsequent InN to have its *a*-axis normal to the interface.

Other researchers have investigated the growth of *a*-plane InN on *r*-plane sapphire, using intermediate layers of III-nitride compounds. For example, Lu *et al.* [15] studied the heteroepitaxial growth of *a*-plane InN on *r*-plane sapphire using AlN

nucleation layer and an additional GaN buffer layer by MBE technique and reported the formation of only *a*-axis oriented wurtzite-type InN $(11\bar{2}0)$ film. Shikata *et al.* [16] employed GaN underlayer to grow *a*-plane InN on *r*-plane sapphire using nitrogen plasma RF-MBE and reported the PL emission energy as low as 0.62 eV, compared to the conventional (0001) InN band gap energy of 0.65 eV, attributing the red shift of the PL peak to the Franz–Keldysh effect. They also suggested that the observed high surface roughness being exhibited by as-grown *a*-plane InN films is due to the occurrence of three-dimensional (3D) growth mode resulting from the large lattice mismatch between InN $(11\bar{2}0)$ and GaN $(11\bar{2}0)$. However, same lattice misfit of approximately 11% holds for both *c*- and *a*-plane InN film grown on GaN and yet a smooth surface is still obtained in the case of the *c*-plane InN, as a result of step-flow growth mode achieved under stoichiometric III/V flux ratio condition. This suggests that lattice mismatch strain is not the only cause of the 3D growth mode typical of *a*-plane InN films on *r*-plane sapphire substrates. The role of In-adlayer on the morphological and structural properties of PAMBE grown non-polar *a*-plane InN on free-standing *a*-plane GaN substrates has been investigated by Koblmüller *et al.* [17]. They reported the enhancement of surface adatoms diffusion under In-rich growth conditions, leading to reduction in film mosaicity and the basal-stacking fault density of the *a*-plane InN layers [17].

In spite of these efforts, the so far reported results for the morphological, structural and electrical properties of *a*-plane InN are significantly inferior compared to the current state of the art properties of *c*-plane InN [18,19]. Since very few reports are available on non-polar InN and the so far synthesized *a*-plane InN films are of poor crystallinity, it is very essential that more work be done to improve the understanding of epitaxial growth of *a*-plane InN. The use of appropriate *r*-plane sapphire surface treatment; consisting of nitridation, nucleation layers, and/or optimisation of an appropriate buffer layer could promote the growth of high quality, single crystalline non-polar *a*-plane InN. The challenges and results obtained from the epitaxy of high quality InN on *r*-plane sapphire are discussed in the following.

5.2 Experimental description

The *r*-plane sapphire surface *ex-situ* and *in-situ* cleaning method has been discussed in section 3.31. The role of sapphire surface nitridation vis-à-vis the use of intermediate layers, comprising of InN or GaN or AlN or GaN/AlN, is investigated. During this study, it was discovered that using LT-InN intermediate layer do not result to *a*-plane film but to InN of different crystallographic orientations. Therefore, these set of samples with InN buffer layers will not be discussed until the next chapter (Chapter 6) of this work. In this chapter, attention will only be paid on the growth process that promotes the epitaxy of single-crystal *a*-plane InN on *r*-plane sapphire. Many studies were carried out to understand the growth and properties of *a*-plane InN, addressing such issues as: the role of buffer layers, substrate temperature, III/V flux ratio, *in-situ* intermittent nitridation of InN during growth, the microstructure of *a*-plane InN and the dependence of *a*-plane InN properties on film thickness. The study involves the investigation of the surface morphology and the structural, electrical and optical properties of InN using different characterisation techniques. In the following, these various investigations are briefly discussed.

5.3 The role of buffer layer on InN growth on *r*-plane sapphire

InN samples were grown on $(1\bar{1}02)$ sapphire substrates by PAMBE. The $(1\bar{1}02)$ sapphire surface was always nitridated for 15 minutes at 900°C before the commencement of the InN deposition. Different buffer layers were employed. The details of the buffer layers' growth conditions are given in Table 1. All the InN samples were grown under the same optimum conditions applicable for *c*-plane InN (Section 4.2) with nominal thickness of 500 nm each.

Table 5.1 *Description and growth conditions of the buffer layers employed for PAMBE of InN on r-plane* $(1\bar{1}20)$ *sapphire substrates.*

Sample Identity	***Buffer layer***	***III-flux Growth rate***	***N-flux Growth rate***	***Growth Temp. (°C)***
G1503 = A	1000 nm HT-GaN	470 nm/h	470 nm/h	810
G1511 = B	35 nm LT-GaN	470 nm/h	470 nm/h	550
G1628 = C	35 nm HT-GaN / 50 nm HT-AlN	470 nm/h / 430 nm/h	470 nm/h / 430 nm/h	810/850
G1629 = D	50 nm HT-AlN	430nm/h	430 nm/h	850

The RHEED patterns of all the InN films were typically spotty as shown in Fig. 5.1; indicating that their growth proceeded with 3D growth mode, resulting to rough surfaces. However, it is noteworthy that whenever only GaN is used as an intermediate layer, as in the case of samples A and B, the patterns tend to become streaky [Fig. 5.1(a)] while the use of AlN, as in the case of samples C and D, always results to purely spotty RHEED pattern [Fig. 5.1(b)].

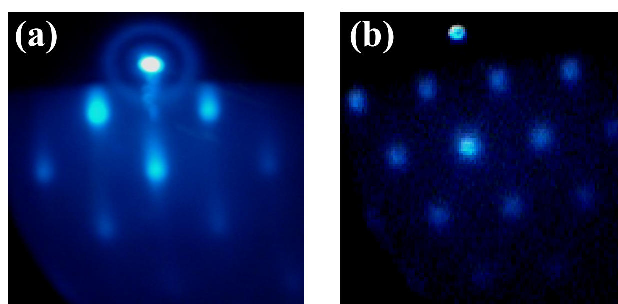

Figure 5.1 *Typical spotty RHEED patterns observed during the growth of a-plane InN samples on r-plane sapphire substrates using (a) GaN buffer layer - samples A and B (b) AlN buffer layer - samples C and D. The departure from a streaky pattern signifies a rough surface and 3D growth mode.*

The morphology of the InN samples was characterised by both FE-SEM and AFM. Fig. 5.2 shows the FE-SEM micrograph for the cross-sectional view of sample B, which is representative of the rest of the samples, and indicates that a compact InN film was grown on *r*-plane sapphire in spite of the spotty RHEED pattern observed during the InN epitaxial growth. The 35 nm GaN intermediate layer in-between the sapphire substrate and the 500 nm thick InN film is indicated by the white arrow in Fig. 5.2. It is also clearly visible that a good interfacial adhesion exists in-between the substrate and the InN epilayer.

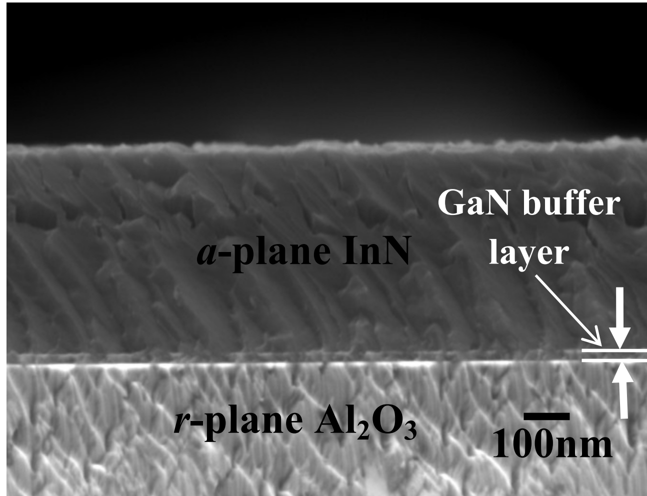

FIG. 5.2 Scanning Electron Microscopy cross-sectional view of the a-plane InN film B grown on r-plane sapphire. The image is also representative of the structures of the other three films. The white arrow points to the 35 nm GaN buffer layer employed.

The 5 x 5 μm^2 AFM micrographs and the rms surface roughness of the *a*-plane InN films are shown in Fig. 5.3 and Table 5.2, respectively. In all cases, the surface morphology appears to consist of grains with size depending on the buffer layer employed for the InN epilayer growth. The grainy structure of the surface morphology appears homogeneous for each film sample. The film using 35nm GaN buffer layer exhibited the smallest grain size and consequently, the lowest rms surface roughness value of 3.24 nm (see Table 5.2). It is evident that the growth of these films must have proceeded with nucleation and coalescence of three dimensional (3D) islands. The grainy nature of the surface morphology of each sample is consistent with the spotty RHEED pattern observed *in-situ* during the growth. The absence of surface morphology anisotropy in all of the samples indicates equivalent adatoms' diffusion length along both in-plain *c*- and *m*-axis of the InN layers in contrast to what is expected for nonpolar GaN surfaces [20]. This may also be related to the fact that similar lattice misfit strain of approximately 11%, exists along both the in-plane *c*- and *m*- directions for growth of *a*-plane InN on GaN. This result contrasts the anisotropic morphology [21-23] with pits [23-25] typically observed for *a*-plane GaN growth on *r*-plane sapphire or the striated surface morphology observed for *m*-plane InN grown by PAMBE on *m*-plane GaN substrates [26]. However, recent reports indicate that *a*-plane InN films grown by MOVPE on *r*-plane sapphire substrates also exhibit stripe features along the *c*-axis and surface undulation along the *m*-axis [27,28].

The as-grown InN on $Al_2O_3(1\bar{1}02)$ samples were characterised by HR-XRD. Typical ω-2θ scan profiles for all the samples are shown in Fig. 5.4. No InN peak along orientation other than $[11\bar{2}0]$ is observable; signifying that all the deposited InN overlayers are wurtzite-structured single crystals of *a*-plane orientation with the *a*-axis perpendicular to the substrate's surface. Fig. 5.4(a) shows the diffraction profile for sample B. The various peaks observable from the scan are labelled accordingly in the figure. Similar diffraction peaks to that of sample B were also obtained for sample A, except that the intensity of the diffraction peak of the GaN buffer layer was stronger and comparable to that of the $Al_2O_3\,(1\bar{1}02)$ shown in Fig.5.4(a). The higher diffraction intensity of the 1μm GaN buffer layer of E is attributed to its higher thickness (see Table 5.1). For sample C, which employed a GaN/AlN buffer layer, only the diffraction peaks related to $(1\bar{1}02)$ Al_2O_3, $(11\bar{2}0)$ InN, $(2\bar{2}04)$ Al_2O_3, $(11\bar{2}0)$ GaN,

and $(11\bar{2}0)$ AlN planes were observed, as shown in Fig 5.4(b); indicating that single crystalline InN was also deposited. The diffraction peaks obtained for sample D are very similar to that of C, except that the GaN buffer layer peak observed and labelled in Fig. 5.4(b) is absent, since only an AlN buffer layer was employed. It also worth mentioning that from the X-ray diffraction, the respective buffer layers of GaN and/or AlN employed were found to be purely *a*-plane III-nitrides [Fig. 5.4], indicating well nucleated buffer layers.

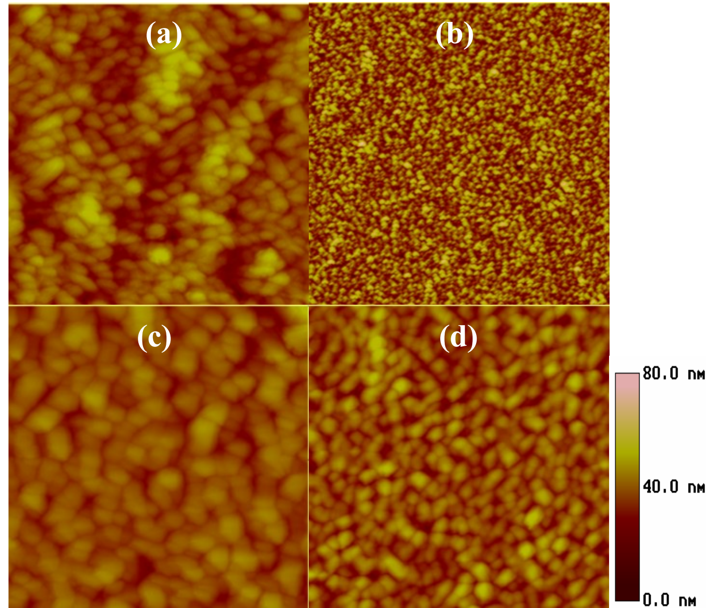

Figure 5.3 *AFM 5x5 μm² micrographs of the InN films with (a) 1 μm GaN buffer layer (sample A) (b) 35 nm GaN buffer layer (sample B) (c) GaN/AlN buffer layer (sample C) and (d) AlN buffer layer (sample D).*

The HR-XRD RCs around the $(11\bar{2}0)$ peak for X-ray beam incidence along the in-plane *c* [0001] direction, of the four *a*-plane samples, are shown in Fig. 5.5. Table 5.2 gives the measured FWHM for X-ray beam incidence along both in-plane *c* [0001] and *m* $[1\bar{1}00]$ directions. Firstly, it is clearly evident that sample C exhibited the narrowest $(11\bar{2}0)$ FWHM of 0.46° along the in-plane *c* [0001] direction with very high peak intensity, while samples A and B follow with 0.52° and 0.53°, respectively. Sample D was found to be of the poorest quality with FWHM of 0.80°. The $(11\bar{2}0)$ RC measurements, taken along the orthogonal in-plane *m* $[1\bar{1}00]$ direction, resulted to significant increase of the FWHM only for film C, which exhibited a value of 0.75° (see Table 5.2). This is an indication of the existence of structural anisotropy in the InN film of sample C.

Interestingly, though the XRD analysis of the underlaying 1 μm GaN buffer layer of sample A exhibits strong structural anisotropy with the $(11\bar{2}0)$ RC FWHM along the orthogonal in-plane *c* (0001) and *m* $(1\bar{1}00)$ orientations determined as 0.25° and 0.40°, respectively, the overgrown *a*-plane InN epilayer obviously did not demonstrate structural anisotropy (see Table 5.2). The results show that the use of thick 1000 nm (sample A) or thin 35 nm (sample B) GaN buffer layers did not introduce structural anisotropy to the top InN layer. Hence, the strong structural

anisotropy observed in sample C, which employed a thin GaN/AlN intermediate layer, could have mainly originated from the AlN nucleation layer as a result of evolutionary growth. Sample D, which employed a thin AlN buffer layer demonstrated mild degree of such anisotropy. This finding suggests that the use of AlN as nucleation layer tends to increase the structural anisotropy in the InN epilayers.

Table 5.2 *Summary of the overall characterisation result data obtained for 500 nm a-plane InN film samples grown on r-plane sapphire substrates using different buffer layers. $(11\bar{2}0)$ RC_{FWHM} is the full width at half maximum values for the rocking curves of $(11\bar{2}0)$ InN reflection measured along the orthogonal in-plain c-[0001] and m-$[1\bar{1}00]$ orientations, R_{rms} is the rms surface roughness values determined from 5 x 5 μm^2 AFM scans, E_{peak} and PL_{FWHM} are the energy of the PL peak and the full width at half maximum value of the PL spectra, respectively, E_g is the band gap energy calculated from the transmittance spectra while n_d and μ are the apparent electron concentration and mobility as determined from Hall-effect measurements, respectively.*

Sample Identity	$(11\bar{2}0)$ RC_{FWHM} [0001]	$(11\bar{2}0)$ RC_{FWHM} $[1\bar{1}00]$	R_{rms} (nm)	E_{peak} (eV)	PL_{FWHM} (meV)	E_g (eV)	n_d (x $10^{19}cm^{-3}$)	μ ($cm^2/V.s$)
G1503 (A)	0.52°	0.53°	10.57	0.639	62.3	0.826	1.76	415
G1511 (B)	0.53°	0.54°	3.24	0.629	66.5	0.740	1.49	325
G1628 (C)	0.46°	0.75°	8.35	0.635 / 0.718	64.3/103	0.834	1.24	630
G1629 (D)	0.80°	0.85°	15.89	0.735	115	0.780	1.74	425

The lack of structural anisotropy in the InN film grown on a structurally anisotropic 1 µm-thick GaN buffer layer (sample A) is attributed to the approximately similar lattice misfit (f ~ 11%) between *a*-plane InN and *a*-plane GaN along both the in-plane *c* and *m* axes, unlike what occurs in the growth of *a*-plane GaN or AlN on *r*-plane Al_2O_3 [29]. The *f* for the heteroepitaxy of *a*-plane GaN on *r*-plane Al_2O_3 along the *c*- and *m*-plane directions is +16% and +1.2%, respectively, while for the heteroepitaxy of *a*-plane AlN on *r*-plane Al_2O_3 is -2.8% and 13.1%, respectively. This large difference in lattice mismatch (for heteroepitaxy on *r*-plane sapphire) is expected to inherently promote uneven growth rate along the *c* and *m* in-plane directions of the III-nitride materials. The creation of different misfit strain relaxation defects along the *c* and *m* axes of the *a*-plane GaN film grown on *r*-plane sapphire substrate has been recently reported [29,30]. From the kinetics point of view, the strong in-plane anisotropy of nonpolar GaN surfaces has also been attributed solely to anisotropic Ga adatoms' diffusion barrier along both *a*- and *m*-plane axes [20].

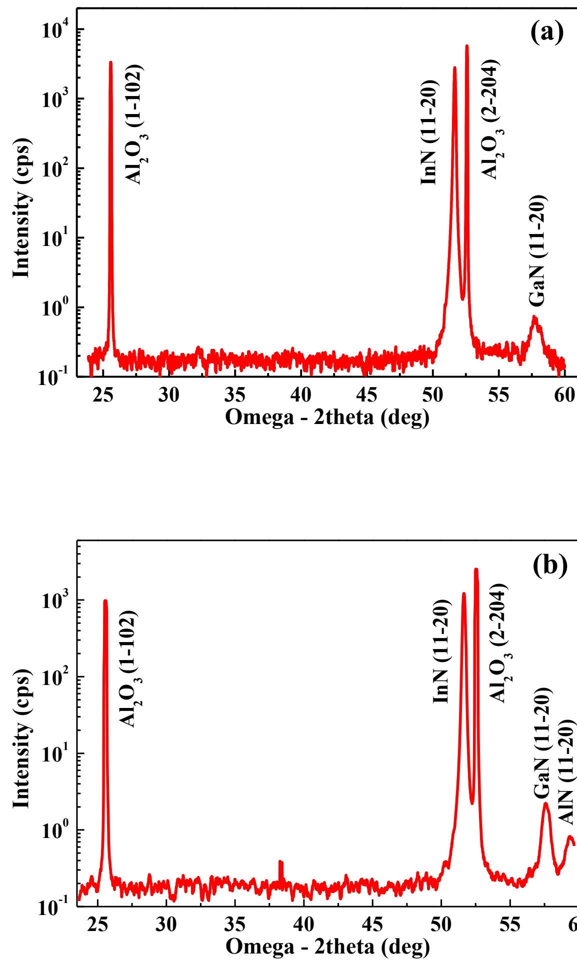

Figure 5.4 *HR-XRD (ω-2θ) scans for the a-plane InN films grown on r-plane sapphire; (a) 35 nm GaN buffered sample B, representative also of the 1 µm GaN buffered sample A (b) GaN/AlN buffered sample C, representative also of the AlN buffered sample D. The respective GaN and/or AlN buffer layers employed are also found to be of pure a-plane orientation.*

The HRXRD results given in Table 5.2 contradict the slightly lower FWHMs along the *m*-orientation compared to *c*-orientation reported by Koblmüller *et al*. for *a*-plane InN grown on *a*-plane GaN substrates [17] but is consistent with that of Darakchieva *et al*., who reported the anisotropic dependence on the azimuth angle with minimum RC FWHM along [0001] and maximum along $[1\bar{1}00]$ for *a*-plane InN films grown on *r*-plane sapphire [31]. According to Table 5.2, the anisotropy of the XRD RC FWHM value only becomes significant when AlN buffer layer is used.

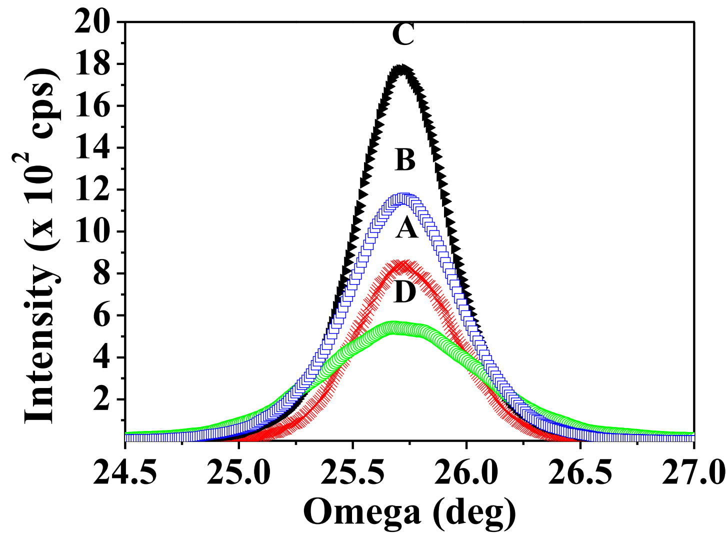

Figure 5.5 *HR-XRD RC in the region of* ($11\bar{2}0$) *reflection for X-ray beam incidence along the in-plane c(0001) orientation of a-plane InN samples grown on r-plane sapphire substrates. The FWHM for samples A, B, C and D are 0.52^o, 0.54^o, 0.46^o and 0.80^o, respectively. Significant structural anisotropy was observed only between the orthogonal in-plane c [0001] and m [$1\bar{1}00$] directions of sample C that employed GaN/AlN buffer layer [see Table 5.2].*

The effect of buffer layer type on the electrical properties of the InN films was also studied by Hall-effect measurements at 300K. The Hall mobilities and the corresponding apparent electron carrier concentrations (determined from the measured sheet carrier density values, assuming a homogeneous layer) for all the samples are given in Table 5.2. The electron concentration was rather similar in all samples, with important differences appearing only for the electron mobility values. The lower electron mobility values exhibited by sample B is far from expected when compared to the result obtained for film samples D, which exhibited significantly larger XRD RC FWHM values and thus inferior structural quality. Sample C (GaN/AlN buffer layer), which exhibited the narrowest XRD ($11\bar{2}0$) RC FWHM (Table 5.2) along the *c*-axis, exhibited also the highest mobility and lowest concentration of electrons. The Hall mobility of 630 cm^2/Vs is the highest obtained to date for *a*-plane InN compared. The highest value reported to date varies from 55 to 283 cm^{2}V^{-1}s^{-1} for MOVPE grown *a*-plane InN [14,27,32] and from 250 to 422 cm^{2}V^{-1}s^{-1} for films grown by MBE [15,33,34]. This means that the presence of structural anisotropy along the *c* and *m* axes may not have an adverse effect on the electrical properties of the film. The exhibited higher electron mobility may be attributed to a reduced crystal defect density in the InN film grown on the thin GaN/AlN intermediate layer between the *a*-plane InN and *r*-plane sapphire substrate. However, it should be pointed out that an InN film is not a homogeneous conductivity layer since there are contributions from the bulk conductivity as well as from interfacial and surface conductivity layers [34,35]. The presence of the large bandgap AlN layer at the interface may have affected the contribution of interfacial conductivity and thus improved the apparent overall results. Finally, all the *a*-plane InN films being

investigated in this study still show inferior electrical properties compared to *c*-plane InN, especially in terms of Hall mobility. For example, electron mobility of 1466 $cm^2/V.s$ has been obtained for a *c*-plane InN of similar thickness grown on MOVPE GaN template in a separate study [34]. This is attributed to higher defect density in the *a*-plane films.

The optical characterisation of the *a*-plane films by PL measurements at 20K is shown in Fig. 5.6(a). The PL emission intensities of samples C and D with GaN/AlN and AlN intermediate layers are weak, leading to times 5 magnifications of their spectra for clear visibility. Nonetheless, single PL emissions energy peak are observed for A, B, and D at 0.639 eV, 0.629 eV, and 0.735 eV, respectively. Film C exhibited main PL energy peaks at 0.635 eV and another peak that is very weak at 0.718 eV. Film B grown on the 35 nm GaN buffer layer demonstrates the strongest PL intensity, follow by film E also with GaN buffer layer but of higher thickness. The extremely weak PL emissions observed for films C and D are attributed to the existence of more non-radiative electron-hole pair recombination defective centres in the layers. The PL peaks relationship with the type of buffer employed for the InN growth is shown in Fig. 5.6(b). Only the main peak of C is accounted for in the figure. Films that employed GaN buffer layer exhibit red-shifted energy peaks compared with when AlN buffer layers are employed.

The FWHM of the PL spectra was estimated to give insight to the crystal quality of the films. The FWHM observed for A, B, C and D are 62.3 meV, 66.5 meV, 64.3 meV and 115 meV, respectively, as given in Table 5.2. Fig. 5.6(b) shows the FWHM as a function of buffer layer type used. Only the main peak of Film C is accounted for in the plot. It is clearly evident that the use of single buffer layer of GaN (samples A and B) improves the structural quality of the films compared to single AlN buffer layer, since A and B demonstrated lower PL spectra FWHM values. Direct growth of *a*-plane InN on a sole AlN buffer layer (Film D) manifested the poorest film quality with FWHM of 115 meV in agreement with the HRXRD analyses of the films [Table 5.2].

To understand the PL behaviour of the films better, the squared of the absorption coefficient (a^2) versus energy (E) curve shown in Fig. 5.6(c) was obtained from the optical transmission measurements of the films and used to determine the appropriate absorption edges of the *a*-plane InN layers. The optical bandgap of films A, B, C, and D were determined as 0.826, 0.740, 0.834 and 0.780 eV, respectively. It is critical that the optical bandgap does not coincide with the PL energy peak of the films, indicating that the PL emissions observed did not emanate from band-to-band electron-hole pairs recombination. The generally observed blue-shift of the optical bandgap, compared with the conventional absorption edge of InN (0.65 eV), is attributed to Burstein-Moss shift, since all the samples exhibited degenerate electron density at low 10^{19} cm^{-3}.

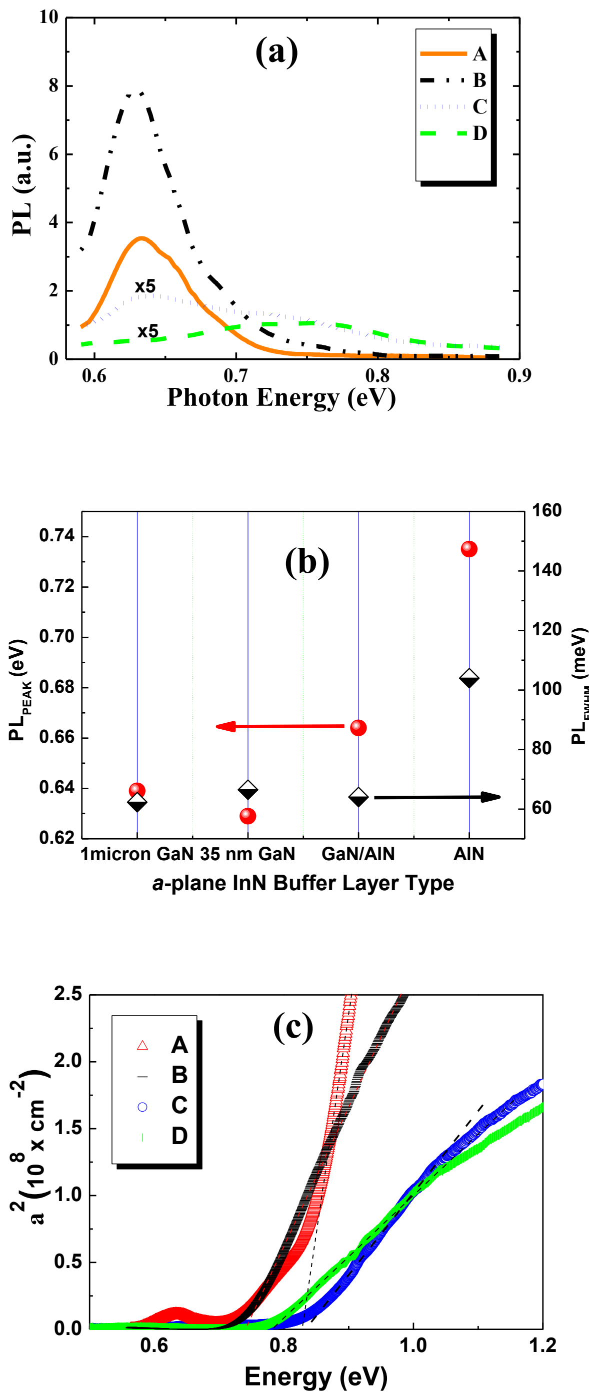

Figure 5.6 *(a) 20K PL spectra of a-plane InN films grown on r-plane sapphire substrates, using different buffer layers. The spectra of samples C and D are very weak and have been magnified 5 times to become apparent in the plot (b) Effect of buffer layer type on the energy and FWHM of the PL peak. Only the data for the main PL peak of Sample C are used (c) Approximate square of the absorption coefficient versus photon energy as extracted from RT optical transmittance measurements of the a-plane InN films. The optical band gap energy of samples A, B, C, and D was each estimated as 0.826, 0.740, 0.834 and 0.780 eV, respectively, from the intercept of the linear fit of the* a^2 *with the energy axis (shown by dotted lines).*

The strongest PL of samples B and A [Fig. 5.6(a)] and the more abrupt absorption edge [Fig. 5.6(c)] suggest the better crystalline quality of these samples, in comparison to samples C and D, contrary to the Hall mobility results. It is speculated that the weighted average of the different conductivity layer contributions may have been modified by changing the interfacial layer and electron mobility results. An increased defect density of the interfacial InN region may also deteriorate the low mobility contribution and affect the apparent mobility. In particular, the contribution of multiple conductivity layers could be the only way to explain the better electron mobility observed for sample D compared to sample B [Table 5.2].

In this study, the existence of lattice mismatch between the intermediate layers and *r*-plane sapphire substrates was found to play a very important role in the growth and properties of *a*-plane InN. It is evident that growth on GaN/AlN buffer layer produced InN material with the best electrical characteristics but its inherent structural anisotropy is a source of concern and could have contributed to the extremely weak PL emissions observed for the film. Use of high-thickness 1 μm GaN buffer for *a*-plane InN epitaxy on *r*-plane sapphire did not demonstrate any significant advantage over the alternative use of low-thickness (35 nm) GaN buffer. However, only the use of low thickness GaN buffer resulted to *a*-plane InN layer with the lowest surface roughness, complete absence of structural anisotropy, comparably good electrical properties and highest PL intensity; making it considerably a better buffer layer choice among the buffer layer materials investigated. Unless otherwise stated, low thickness (20 - 50 nm) GaN buffer layer were always employed for the study of growth properties of *a*-plane InN on *r*-plane sapphire embarked upon in this work. This optimised buffer layer has been used to grow *a*-plane InN of different film thicknesses in order to investigate the thickness dependence of non-polar *a*-plane InN properties [34]. The detailed results of this study shall be discussed later in this Chapter.

5.4 Effect of Growth Temperature (T_{sub}) on *a*-plane InN growth on *r*-plane sapphire

The In-polar (0001) InN has been known to be a very temperature sensitive material with the decomposition temperature limit generally accepted to be at around 450°C [36-38] while that of the N-polar counterpart is reported to be at ~100°C higher temperature [39,40]. It is therefore important also to study and understand the optimum growth temperature (T_{sub}) required for high quality *a*-plane InN epitaxy on *r*-plane Al_2O_3. The results obtained from the investigation of the effects of T_{sub} on the properties of epitaxial *a*-plane InN layers on *r*-plane sapphire are hereunder discussed.

In order to investigate the effect of T_{sub} on the growth of *a*-plane InN, three samples of InN, G1377, G1407 and G1445, were grown with T_{sub} in the range of 420 - 450°C, under similar In/N flux ratio of unity. The intermediate layer employed was a 20 nm GaN layer grown at low T_{sub} of 550°C and thereafter annealed at higher growth temperature to improve its crystal quality. Figs. 5.7(a) and 5.7(b) are the RHEED patterns obtained for the *r*-plane sapphire and the LT-GaN buffer layer, respectively. Table 5.3 gives the different samples grown and investigated in this experiment and their characteristics. At growth initiation, Volber-Weber growth mode was always observed for all the three InN samples [Fig.5.7(c)]. As growth continues, the spotty patterns become elongated [Fig. 5.7(d)] and tend to becoming streaky

within approximately 15 minutes of growth [Fig. 5.7(e)], which indicates that the formed three-dimensional InN islands tend to coalescence into continuous film at a nominal thickness of approximately 60 nm. The RHEED intensity during growth was decreasing continuously with growth time when the substrate temperatures of 440 °C (G1407) and 450 °C (G1377) were employed, respectively. The darkening of the RHEED patterns, despite the fact that a stoichiometric III/V flux ratio was employed, indicates the possibility of gradual accumulation of metallic In on the surface, due to thermal decomposition of InN. On the other hand, the intensity showed a stable brightness for T_{sub} = 420 °C, used for sample G1445.

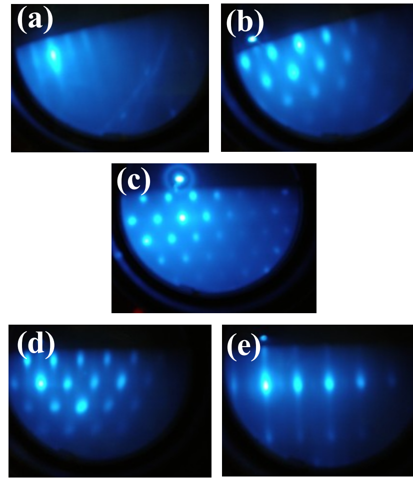

Figure 5.7 *Typical evolution of RHEED patterns in the growth of a-plane InN on r-plane sapphire substrate: (a) streaky pattern for the r-plane sapphire substrate, (b) spotty pattern for the GaN buffer layer, (c) spotty pattern immediately after InN growth initiation, (d) pattern consisting of elongated-spots and (e) streaks developed in between the elongated spots after the growth of ~ 60 nm InN.*

The target thickness for each of the samples was 1000 nm but due to the initiation of InN decomposition at the growth temperatures of samples G1377 and G1407, the growth was discontinued. The easiest way of identifying the point at which *a*-plane InN decomposition sets in, by the RHEED, is the observation of a transformation of the modulated-streaks in the RHEED pattern [Fig. 5.7(e)] to a spotty one with the evolution of time. The onset of *a*-plane InN decomposition can also be identified by direct observation of the substrate's surface during growth process through a glass window facing the MBE manipulator (substrate holder). The InN film's surface normally appears dark and mirror-like. The point at which the dark reflective colour begins to transform slowly to a silvery surface is the onset of *a*-plane InN decomposition. It is important to note that In-accumulation as a result of In-rich growth of InN could also lead to this observation. Care must be taken to ensure that such change is not due to excessive supply of In atoms to the substrate's surface. By ensuring good control of the III/V ratio and sticking to stoichiometric III/V flux ratio, the three samples being discussed were grown.

It should be noticed that during MBE growth, the substrate is radiatively heated from a hot filament and the RF plasma. The deposition of the low bandgap InN film will permit the absorption and emission of radiation in comparison to the initial sapphire substrate and thus the actual substrate temperature will change with time. An

increase of the actual substrate temperature is expected as the InN film thickness increases, due to increase absorption of thermal radiation.

Table 5.3 *Growth and characterisation data for InN films grown at different substrate temperatures (T_{sub}). Surface condition is the description of the as-grown surface morphology of the films as determined by optical microscopy and SEM, T is the target thickness, t is the obtainable thickness with or without decomposition, R_{rms} is the rms value of the InN surface roughness as estimated from 10 x 10 μm^2 AFM micrographs, RC_{FWHM} is the FWHM of the XRD ($11\bar{2}0$) rocking curve along the in-plane c-axis, E_{PL} is the photoluminescence peak energy at 20K, PL_{FWHM} is the FWHM of the PL peak, n_d is the apparent carrier concentration determined from Hall-effect measurements and μ is the Hall mobility.*

Sample	Surface condition	T_{sub} (°C)	T (nm)	t (nm)	R_{rms} (nm)	RC_{FWHM}	E_{PL} (eV)	PL_{FWHM} (meV)	n_d ($x10^{19}cm^{-3}$)	μ ($cm^2/V.s$)
G1377	Fully decomposed + cracks + In accumulation	450	1000	260	16.79	0.98°	-	-	-	-
G1407	Partial decomposition + No In accumulation	440	1000	775	3.5	0.70°	0.78	84.5	2.40	499
G1445	Smooth + No decomposition	420	1000	1000	3.4	0.59°	0.64	97.3	3.12	377

Table 5.3 gives the growth details and the general characterisation results for the three *a*-plane InN films. Fig. 5.8 shows the images of the as-grown film samples taken by Normasky microscope. Film G1377 exhibits very rough surface morphology due to initiation of InN decomposition, In accumulation and existence of micro-cracks on the film surface as shown in Fig. 5.8(a), suggesting that the used T_{sub} of 450°C was too high. Attempt to etch away the accumulated metallic In on the surface with HCl, prior to optical and Hall-effect measurements, resulted to the InN material been etched away leaving only the 20 nm GaN nucleation layer on the sapphire substrate. This explains why other results, besides XRD, are not available for the film in Table 5.3. Reduction of the T_{sub} from 450°C to 440°C sustained the growth of film G1407 up to 775 nm thickness before decomposition occurred. G1407 typically exhibited rough decomposed and smooth undecomposed regions on its surface as shown in Figs. 5.8(b), 5.8(d) and 5.8(e). Figure 5.8(d) was taken by a conventional digital CCD camera. No metallic droplet or In accumulation was observed on the surface in general. The decomposed region is generally delaminated. The images of the good region are shown in Figs. 5.8(b), 5.8(d) and 5.8(e) with the white broken circle. All the available characterisation results for sample G1407 [Table 5.3], were carried out on the undecomposed region. Only the *a*-plane InN sample G1445, grown at 420°C, reached the targeted 1000 nm film thickness and the film did not exhibit any sign of decomposition on its surface [Fig. 5.8(c)]. For this film, *T* (nm) = *t* (nm) as shown in Table 5.3.

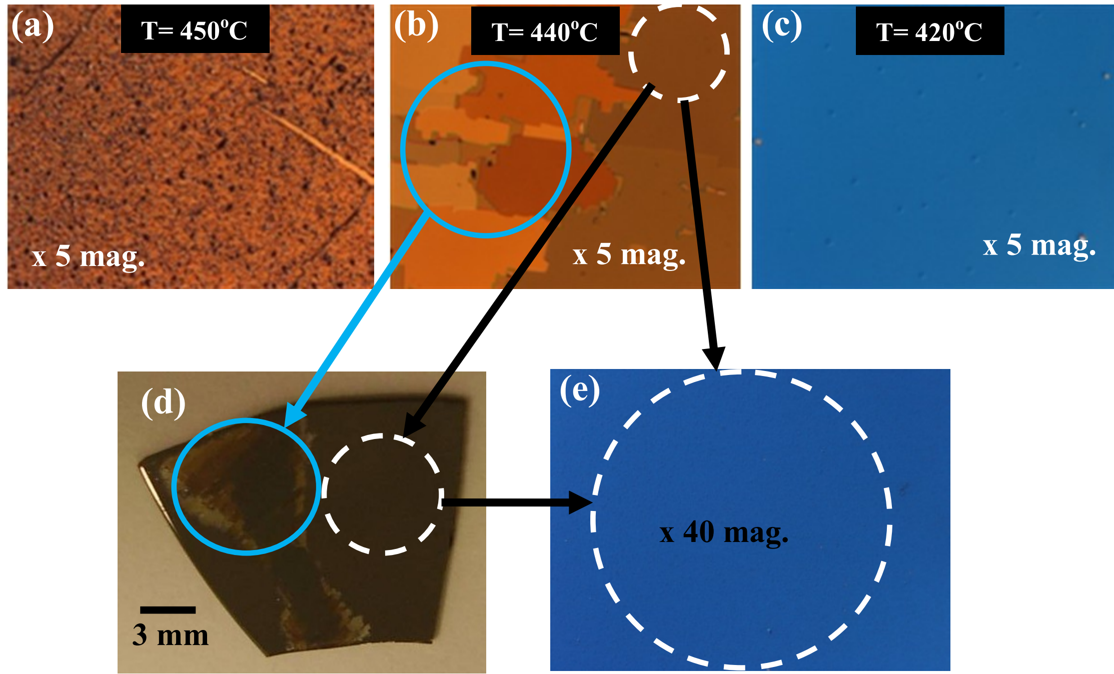

Figure 5.8 *Normasky optical microscopy plan-view images of a-plane InN films grown at different T_{sub}: (a) G1377 grown at 450°C shows a rough surface morphology and microcracks (b) G1407 grown at 440°C exhibited co-existence of both decomposed (closed circle) and undecomposed (broken circle) areas (c) G1445 grown at 420°C manifested smooth surface morphology (d) Conventional digital camera plan-view image of G1407 showing both decomposed and undecomposed surface regions (e) Normasky optical microscopy of the smooth, undecomposed region of G1407. Only the smooth region, shown with broken white circles was used to investigate the properties of G1407 given in Table 5.3.*

The 10 x 10 µm^2 AFM micrographs of the three samples are shown in Fig. 5.9. All the films exhibited a typical *a*-plane InN granular surface morphology [34]. Although the sizes of the surface roughness grains are uniform for each sample, it is clearly evident that reduction of grain size occurs with decreasing T_{sub}. The rms surface roughness results are given in Table 5.3. Film G1377 that exhibited partial decomposition in its entire surface region has the highest rms surface roughness of 17 nm. The lower temperature samples G1445 (T_{sub} = 420°C) and G1407 (T_{sub} = 440°C); using the undecomposed area of G1407, exhibited similar rms roughness values of 3.4 nm and 3.5 nm, respectively.

From the HRXRD analysis of the films, the *a*-plane orientation was confirmed for the three films. The $(11\bar{2}0)$ rocking curve FWHM values of 0.59 and 0.7° were obtained for G1445 and the good region of G1407, respectively, while G1377 exhibited a FWHM of 0.98° [Table 5.3]. The lower FWHM of G1445 may be related to the higher thickness of the InN layer [34]. However, improved electrical properties were exhibited by G1407 as shown in Table 5.3. Since the electrical mobility of *a*-plane InN has been demonstrated to improve with thickness [34], the higher electron mobility for sample G1407 is attributed to the higher T_{sub} employed for the growth. A mobility difference of 100 cm^2/Vs is a very significant increase for *a*-plane InN due to the low mobility values obtained in comparison to *c*-plane InN of similar thickness

[15,34]. This result indicates that higher growth temperature also improves the electrical properties of *a*-plane InN, similar to what has been observed for *c*-plane InN [39,41,42].

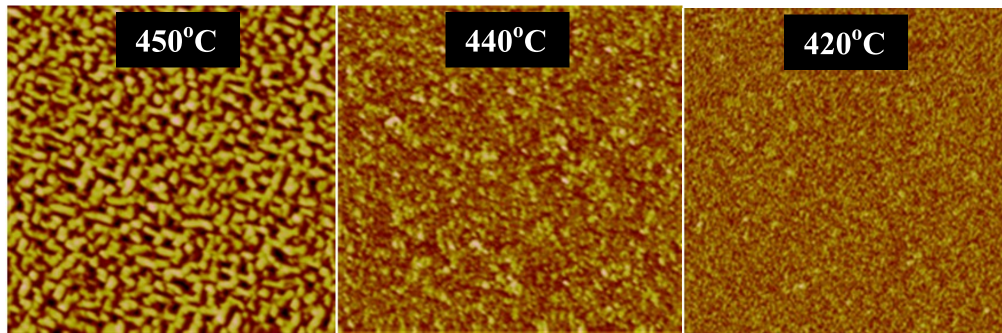

Figure 5.9 *10x10μm² AFM micrographs for a-plane InN samples grown at different temperatures on r-plane sapphire. The rms roughness values are 16.8 nm for G1377grown at 450°C, 3.5 nm for the non-decomposed part of G1407 grown at 440°C and 3.4 nm for G1445 grown at 420°C. Reduction of surface grain sizes with decreasing substrate temperature is observed. The micrographs z-axis full scale showed 130 nm, 43 nm and 99 nm, respectively.*

The 20K PL spectra of the three samples are shown in Fig. 5.10. G1445 with moderate T_{sub} exhibited PL photon energy peak at 0.647 eV, while that of G1407 is blueshifted as much as 122 meV and occurred at 0.769 eV. G1377 grown at 450°C was completely delaminated from the substrate on etching it with HCl to remove In droplets from the surface and could not be investigated. In both cases broad PL spectra due to the high carrier concentration and high defect densities were obtained. Similarly high PL FWHM values were observed for G1407 and G1445 at 85 and 97 meV, respectively [Table 5.3]. However, the PL emission intensity of G1445 was found to be more than six times higher than that of G1407 [Fig. 5.10.], suggesting a superior crystalline quality for sample G1445.

To further investigate the sensitivity to T_{sub} of both *c*- and *a*-plane InN, another experiment was conducted in which similar growth conditions were employed for the epitaxial growth of 500 nm thick *c*-plane InN (G1848) and *a*-plane InN (G1851) layers. T_{sub} of 440°C was used to grow sample G1848 on a Ga-polar GaN pseudo-substrate and sample G1851 on 50 nm GaN grown by MBE on *r*-plane sapphire substrate. It was observed that the growth of the *a*-plane InN was not sustainable after attaining to approximately 340 nm thickness due to InN decomposition. However, the *c*-plane InN film was very stable at this temperature throughout the growth process. From this study, it is evident that the decomposition limit for *a*-plane InN is lower than that of *c*-plane InN by approximately 30°C. A growth window of about 370°C - 420°C is proposed for the molecular beam epitaxy of high crystalline quality *a*-plane InN without surface decomposition.

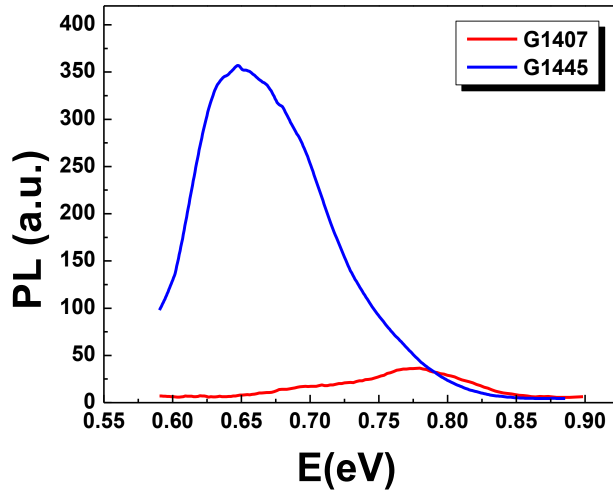

Figure 5.10 *20K PL spectra of a-plane InN films G1407 and G1445 grown at 440 and 420°C, respectively. G1377 grown at 450°C was completely delaminated from the substrate on etching it with HCl to remove In droplets from the surface and could not be investigated.*

5.5 Effect of III/V flux ratio on *a*-plane InN growth on *r*-plane sapphire

The role of III/V flux ratio in the growth of high crystal quality *a*-plane InN was investigated. All samples were grown at 420°C on *r*-plane sapphire substrates, using GaN nucleation layer. The thickness of the samples is approximately 350 nm. The used III/V flux ratio was varied from 0.42 to 0.80. The growth conditions and general results for all the investigated samples are given in Table 5.4.

Table 5.4 *Growth details and characterisation results for 350 nm thick a-plane InN films grown with different III/V flux ratios, from 0.42 to 0.80, on r-plane sapphire substrates at 420°C. R_{rms} is the rms value of the InN surface roughness as estimated from both 2x2 and 10 x 10 μm² AFM micrographs, RC_{FWHM} is the FWHM of the XRD $(11\bar{2}0)$ rocking curve along the in-plane c-axis or m-axis. n_d is the apparent carrier concentration determined from Hall-effect measurements at 300K and μ is the Hall mobility.*

Sample	***III/V flux ratio***	***R_{rms} (nm) 2x2/10x10 μm²***	***RC_{FWHM}***		***n_d (10^{19}cm³)***	***μ (cm²/V.s)***
			c-axis	**m-axis**		
G1517	0.80	1.22/1.18 nm	0.83°	1.19°	5.90	375
G1518	0.65	2.79/3.36 nm	0.76°	1.35°	7.65	270
G1519	0.50	3.47/5.15 nm	0.80°	1.36°	5.76	280
G1515	0.42	4.56/8.61 nm	0.85°	1.29°	8.13	300

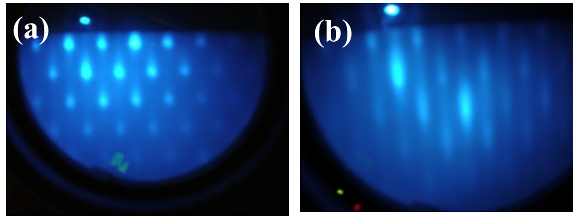

Figure 5.12 *RHEED pattern exhibited by films (a) G1515 and (b) G1517 that employed III/V flux ratio of 0.8 and 0.42, respectively, indicating that 3D growth mode was followed in the entire growth of G1515.*

The FE-SEM micrographs of the samples' cross-sections are shown in Fig. 5.11 and reveal that all the samples are compact films. The non-formation of columnar or nanopillars (NPs) structure, even under the highly N-rich growth conditions, is attributed to the low growth temperature employed, which prevented sufficient adatoms surface diffusion on the substrate's surface and adatoms migration to the top of the initially formed InN 3D islands. Consequently, the islands eventually coalesced to form a 2D morphology as growth process continued. This understanding could also be explained by the *in-situ* RHEED patterns of all the films that evolved gradually from spotty to modulated-streaky pattern. Improvement in the streakiness of the diffraction pattern occurs as the III/V flux ratio increases from 0.42 [Fig.5.12(a)] to 0.80 [Fig. 5.12(b)], which also indicates reduction in the surface roughness of the InN layers with increasing III/V flux ratio, in a similar way to *c*-plane InN [43-45]. A close look at the cross-sectional image obtained for the InN samples in Fig. 5.11 obviously depicts this fact and also indicated a very smooth surface and sharper interface for the InN layer G1517 (III/V = 0.80), compared to other samples.

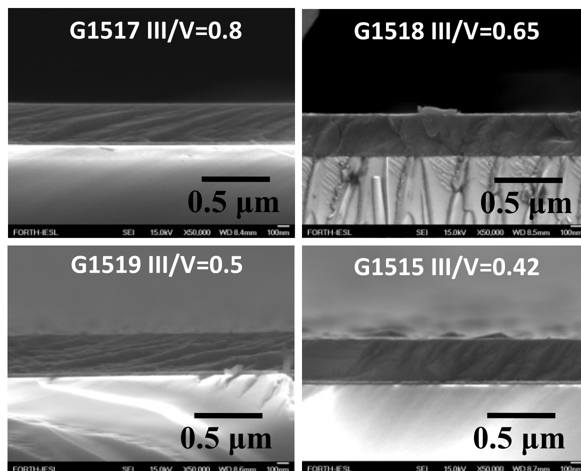

Figure 5.11 *SEM cross-sectional micrographs of a-plane InN films grown on r-plane sapphire using varied III/V flux ratio, as depicted in the respective image and Table 5.4.*

The 5x5 µm^2 AFM micrographs of all the InN films are shown in Fig. 5.13. It is evident that each film exhibited distinct surface morphology characterised by roughness resulting from 3D growth mode, which consist of circular surface grains. The apparent grain sizes reduced with increasing III/V flux ratio due to improved coalescence of the grains, in agreement with the RHEED pattern observations. Both 2 x 2 and 10 x 10 µm^2 AFM rms surface roughness of the InN film samples are given in Table 5.4 and the relationship with III/V flux ratio is obvious in Fig. 5.14(a). The lowest rms roughness value was obtained when the III/V flux ratio is 0.8 and at this point both AFM scales (2 x 2 and 10 x 10 µm^2) gives the same value, which indicate that G1517 exhibited the smoothest and most uniform surface morphology.

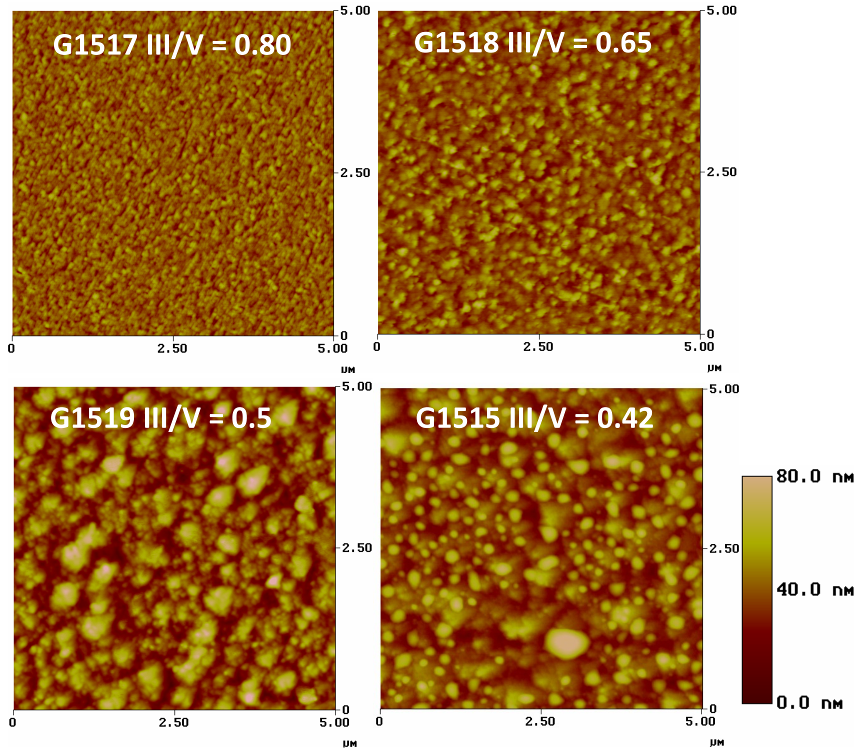

Figure 5.13 *5x5 μm^2 AFM scans for the surface of a-plane InN films grown on r-plane sapphire, using different III/V flux ratios. The AFM micrographs were taken after the samples have been etched in HCl to ensure non-existence of metallic In on the surface, although such accumulation was not expected for the InN layers grown under N-rich conditions.*

It is important to note that under In-rich growth condition the surface morphology of *a*-plane InN exhibits bunch lines resulting from grains that are fused together, as shown in Fig. 5.15(a) while the formation of a well defined grainy surface morphology always characterise films grown under stoichiometric III/V flux ratio [34], as shown in Fig. 15(b).

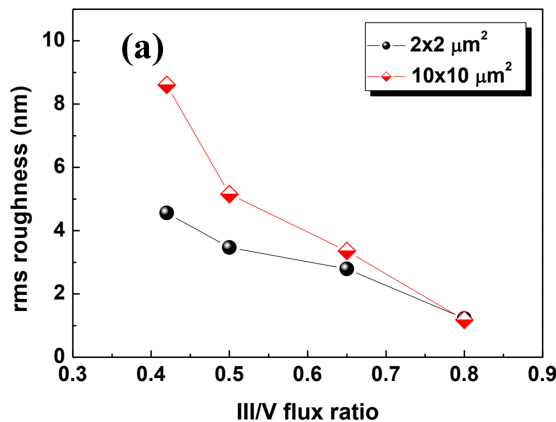

Figure 5.14 *Plot of rms surface roughness as a function of III/V flux ratio for a-plane InN films grown on r-plane sapphire, using GaN buffer layer.*

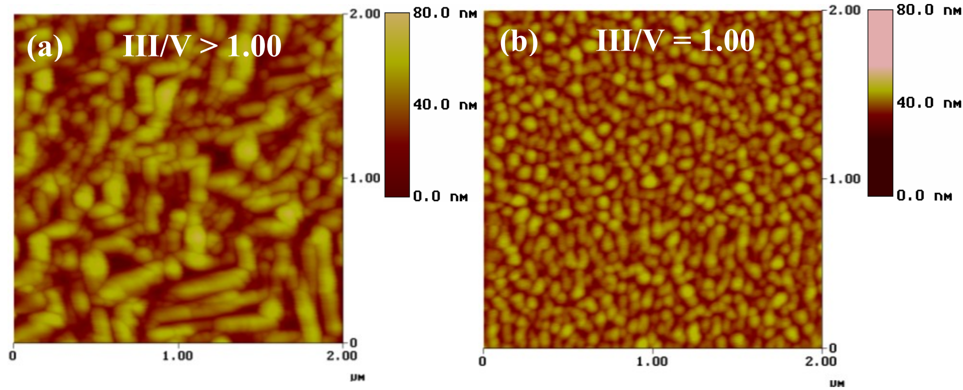

Figure 5.15 *2x2 µm^2 AFM scans for the surface of a-plane InN films grown on r-plane sapphire, using (a) III/V flux ratio > 1 and (b) III/V flux ratio = 1. The AFM micrographs were taken after the samples have been etched in HCl to ensure non-existence of metallic In on their surfaces.*

HR-XRD measurements of both ω scans (RCs) and ω-2θ scans were carried out on the films. The ω-2θ scans manifested only the peaks of InN $(11\bar{2}0)$ along with additional peaks from the used sapphire substrate; Al_2O_3 $(1\bar{1}02)$, Al_2O_3 $(2\bar{2}04)$, and GaN $(11\bar{2}0)$ buffer layer, in a similar way to Fig. 5.4(a). This observation confirms the *a*-plane orientation of the InN layers. The respective $(11\bar{2}0)$ RC FWHM measured along the in-plane *c*- and *m*-axes is given in Table 5.4. No significant difference in the FWHM values of the samples is observed, along the two orthogonal in-plane *c*-(0001) and *m*-$(1\bar{1}00)$ orientations of the *a*-plane InN as the In/N flux ratio decreases. However, all the samples exhibited structural anisotropy [Table 5.4], which contradicts what has been observed for *a*-plane InN films grown on *r*-plane sapphire substrates under stoichiometric flux ratio [34]. Examination of the azimuthal dependence of the HRXRD $(11\bar{2}0)$ RC FWHM, using $-45 \geq \Phi \leq 45$, resulted to the plot of the RC FWHM as a function of azimuth angle shown in Fig. 5.16. The lowest value corresponds to the measurement along the in-plain *c*-axis (Φ = - 45) and the highest to the in-plain *m*-axis (Φ = 45). A reference *a*-plane InN sample G1503 of 0.5 µm thickness, grown under stoichiometric flux ratio, is also plotted in Fig. 5.16 for effective comparison. It is very discernible that significant structural anisotropy exists only in *a*-plane InN films grown under N-rich conditions (III/V flux ratio ≤ 0.8) while it is obviously absent in the stoichiometrically grown reference sample (III/V flux ratio = 1).

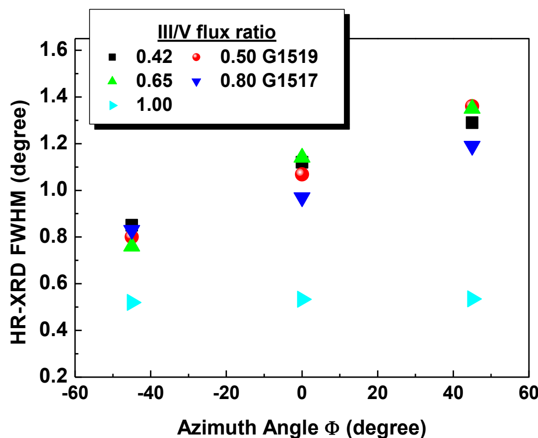

Figure 5.16 *Structural anisotropy behaviour of a-plane InN films grown on r-plane sapphire, using different III/V flux ratio. The result for a 0.5 µm a-plane InN layer grown under stoichiometric III/V flux ratio is inserted for comparative purpose.*

The Hall-effect results for the *a*-plane films are given in Table 5.4 and Fig. 5.17. All the films exhibited very poor mobility and high concentration of electron in the 10^{19} cm^{-3} range. Comparatively, the samples do not show any monotonic dependence of electron concentration and Hall mobility on the used III/V flux ratio. However, the best values were determined for sample G1517 (III/V flux ratio = 0.80), indicating that the *a*-plane film G1517 is of superior crystal-quality compared to other samples. It should be stated that these samples did not exhibit PL emission, which indicates a poor crystalline quality.

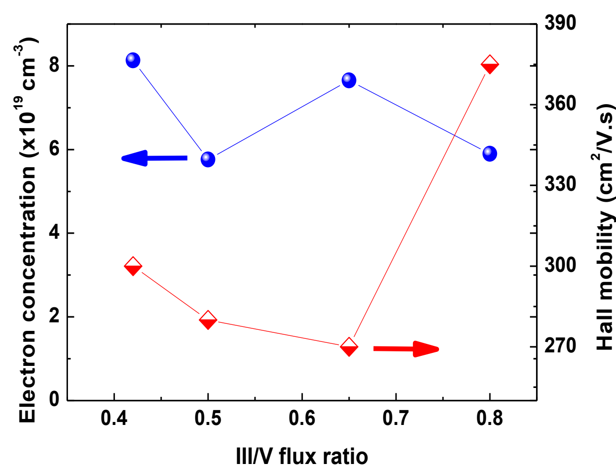

Figure 5.17 *Electron carrier concentration and Hall mobility as functions of III/V flux ratio for a-plane InN films grown on r-plane sapphire substrate, using GaN buffer layer.*

5.6 Effect of *in-situ* intermittent surface nitridation of *a*-plane InN during growth

Based on the low surface roughness obtained for *a*-plane InN when grown under slightly N-rich condition with III/V ratio of 0.8 (as earlier described in section 5.5), the effect of *in-situ* intermittent surface nitridation during the growth of *a*-plane InN was investigated. The aim was to further optimise the growth conditions that could result to high quality *a*-plane InN with smoother surface morphology. Two 1 µm thick *a*-plane InN films were grown with or without intermittent nitridation steps on *r*-plane sapphire substrates. The growth conditions and the results of this investigation are given in Table 5.5. In the case where surface nitridation applies, the intermittent nitridation was carried out every 10 minutes, for 20 seconds, during the growth process.

Whenever intermittent surface nitridation was employed, a spotty RHEED pattern rapidly transformed to streaky pattern; indicating that the nitridation may enhance the coalescence of the 3D islands, i.e the apparent surface grains that typify *a*-plane films' surface morphology [34]. Fig. 5.18 shows the AFM micrographs obtained for the two *a*-plane InN films; G1445 = A and G1513 = B, which were grown under similar conditions except for the fact that B was not subjected to the *in-situ* nitridation process that was applied to A. The AFM investigation revealed a smoother surface morphology when the nitridation process was applied, as in the case of sample A [Fig. 5.18(a)], even though both are characterised by granular surface morphology arising from 3D growth mode. The 2x2 μm^2 AFM rms surface roughness is estimated as 2.60 nm and 10.29 nm for A and B, respectively, indicating that the absence of *in-situ* growth surface nitridation increased the roughness four times [Fig. 5.18 and Table 5.5]. However, the decrease of rms roughness in sample D is related to

decrease in the size and increase in the density of islands that appear as grains in the AFM micrographs. Apparently, a redistribution of material at the surface should occur during nitridation, resulting to a smoother surface morphology with smaller 3D islands, approaching 2D-like characteristics. However, the observed rms roughness indicates that 3D growth mode is active in both samples.

***Table 5.5** Summary of the characterisation results of a-plane InN films grown with or without in-situ intermittent nitridation of sample's surface. R_{rms} is the rms surface roughness estimated from the 2x2 μm^2 AFM scans of each film, RC_{FWHM} is the XRD $(11\bar{2}0)$ rocking curve FWHM value along the in-plane c-axis, E_{PL} is the PL peak at 20K, n_d and μ are the apparent electron concentration and mobility estimated from Hall-effect measurements, respectively.*

Sample	*III/V flux ratio*	*Nitridation Treatment*	RC_{FWHM}	R_{rms} *(nm)*	n_d *($10^{19}cm^3$)*	μ *($cm^2/V.s$)*	E_{PL} *(eV)*
A G1445	1	Yes	0.59 °	2.60	3.12	377	0.635/ 0.683
B G1513	1	No	0.43 °	10.29	1.13	422	0.631

Fig. 5.18(c) shows a plot of the rms roughness determined for the films as a function of the AFM scan area. Both film exhibited almost similar rms roughness from one scan area to the other and evidently tend to saturation at the 10x10 μm^2 region, indicating uniform surface morphology with no large defects.

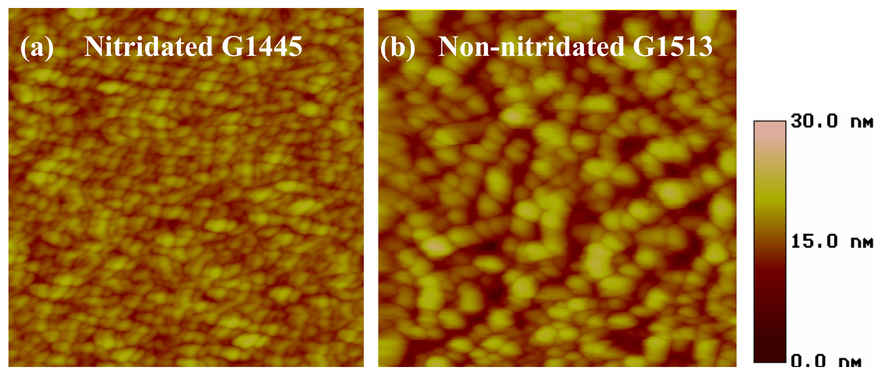

While the use of intermittent surface nitridation step during the epilayer's growth achieves significant smoothening of *a*-plane InN films surface morphology, such a step does not improve other properties of the film as shown in Table 5.5. The HRXRD (11-20) RC FWHM along the in-plane *c*-axis of the unnitridated sample B is lower than the nitridated sample A, indicating that B is of higher crystal quality. The unnitridated sample B also demonstrated the best electrical properties compared to the nitridated sample A, confirming the superior quality of B.
Intermittent surface nitridation was found to cause a doubling of the electron density of film A in comparison to the unnitridated film B. This indicates possible accumulation of donor impurities during the growth interruption and nitridation periods. Although both films manifested PL emissions, only sample B exhibited a single peak compared to the double peaks of sample A [Table 5.5].

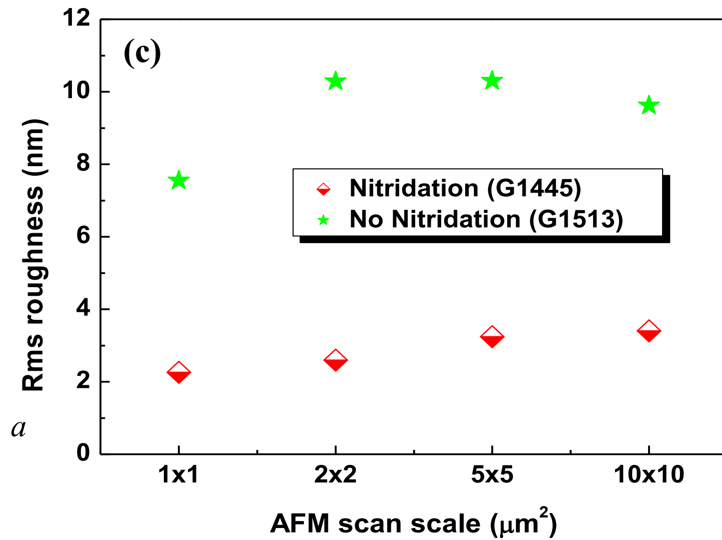

Figure 5.18 *2x2 μm² AFM micrographs of a-plane InN film (a) G1445 and (b) G1513 grown with and without in-situ intermittent surface nitridation, respectively. (c) Plot of the measured rms roughness as function of the AFM scan scale for both films.*

Finally, the investigation shows that the use of interruptive surface nitridation steps during *a*-plane InN growth does not cause any improvement in the properties of the resulting film, except for the achievement of lower rms roughness surfaces. On the contrary, a deterioration of the electrical properties and the crystal mosaicity is observed.

5.7 Thickness dependence of the properties of *a*-plane InN grown by MBE

The dependence of the properties of *c*-plane InN films, grown by various techniques, on thickness have been investigated by many authors. The transport properties have been found to improve with increasing *c*-plane InN film thickness, but only few reports exist for the dependence of the structural properties on the epilayer's thickness [40,41,46-48]. Concerning non-polar *a*-plane InN films, only Lu *et al*. have conducted research on their thickness dependent properties [15]. They reported the room temperature Hall mobility of 270 cm^2/Vs for *a*-plane InN and also observed that increasing film thickness did not lead to apparent improvement of the electrical properties of their *a*-plane InN films due to a rather constant density of defects along the growth direction; contrary to what has been observed in *c*-plane InN [19,49].

5.7.1 Objective of the study and experimental procedures

This chapter is aimed at discussing the extensive study carried out on the effect of film thickness on the growth, surface morphology, structural, electrical, and optical properties of *a*-plane InN films grown by PAMBE on *r*-plane sapphire substrates. This systematic study is aimed at improving the understanding of heteroepitaxy and properties of *a*-plane InN films. InN films with thickness of 50 nm (G1514), 100 nm (G1512), 500 nm (G1511) and 1000 nm (G1513) were grown, using an optimised 35 nm *a*-plane GaN buffer layer that yielded the best overall InN properties in section 5.3. The InN films were all grown under the optimum conditions applicable to the *c*-plane InN films discussed in Chapter 4. The *in-situ* RHEED patterns observed during the growth of the *a*-plane InN films are similar to those of Fig. 5.1(a) and indicated that the growth of the *a*-plane InN films followed a three-dimensional (3D) growth mode.

5.7.2 Surface Morphology characterisation

The surface morphology of the films was characterised by AFM. Fig. 5.19 presents the 2 x 2 μm^2 AFM micrographs of the four *a*-plane InN films, which provide a clear visibility of the grainy appearance of the surface morphology. The root-mean-square (rms) surface roughness values were estimated from the 10 x 10 μm^2 AFM scans and plotted against film thickness in Fig. 5.20(a). The rms surface roughness increases monotonically from 1.69 nm for the 50 nm film to 9.62 nm for the 1000 nm film. The lateral (width) and vertical (height) dimensions of the apparent roughness grains on the AFM images of Fig. 5.19 increased with increasing thickness of the InN epilayer, as shown in Fig. 5.20(b), while their size and spatial distributions also became less uniform; the lowest rms surface roughness of 1.69 nm was obtained for the thinnest 50 nm *a*-plane InN film. Overall, the reduction in the density of roughness grains on the *a*-plane InN surface, as the film thickness increases, and the corresponding increase in surface roughness may be attributed to the continuous expansion of the initial InN 3D islands/grains as growth evolves, following a 3D growth mode.

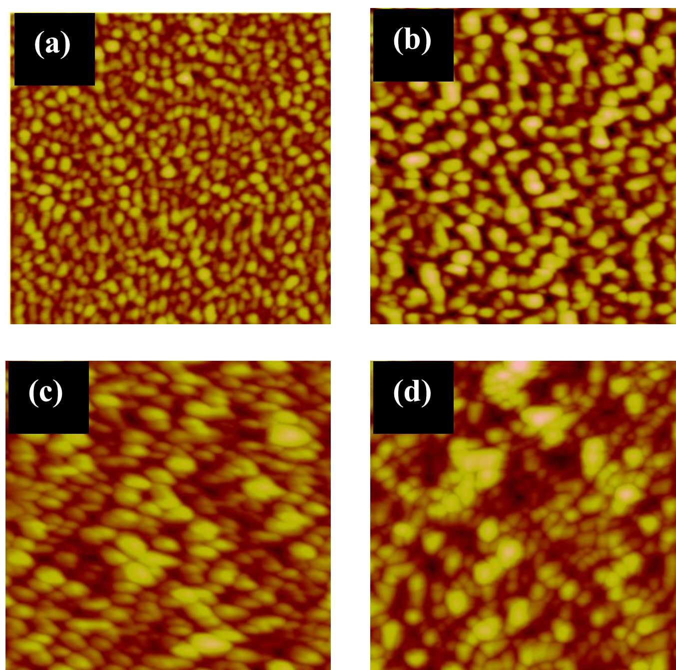

Figure 5.19 *2x2 μm^2 AFM micrographs showing the surface morphology of the a-plane InN films grown on r-plane sapphire with thicknesses (a) 50 nm, (b) 100 nm, (c) 500 nm, and (d) 1000 nm. The z-axis full scale is 10 nm, 40 nm, 55 nm, and 80 nm, respectively.*

The grainy features of the *a*-plane InN surface morphology, shown in Fig. 5.19, agree with the spotty *in-situ* RHEED pattern evolution; indicating that in spite of the stoichiometric III/V flux ratio growth conditions employed, the *a*-plane InN growth on *r*-plane sapphire substrates proceeds through the nucleation, growth and coalescence of 3D InN islands, in contrast to the two-dimensional (2D) step-flow mode usually maintained during the heteroepitaxial growth of *c*-plane InN films [Fig.

4.3]. The rms surface roughness determined from 2 x 2 μm^2 AFM scans of the *c*-plane InN films of similar thicknesses, which is generally below 1 nm, is compared with those of the *a*-plane films in Fig. 5.21. It can be deduced that while the roughness of the *c*-plane InN is more or less constant with increasing layer thickness, the surface roughness of the *a*-plane films increases due to the enlargement of the roughness grain sizes with thickness. This work assists to understanding that the surface roughness of InN is dependent on film orientation and differs even under similar growth conditions.

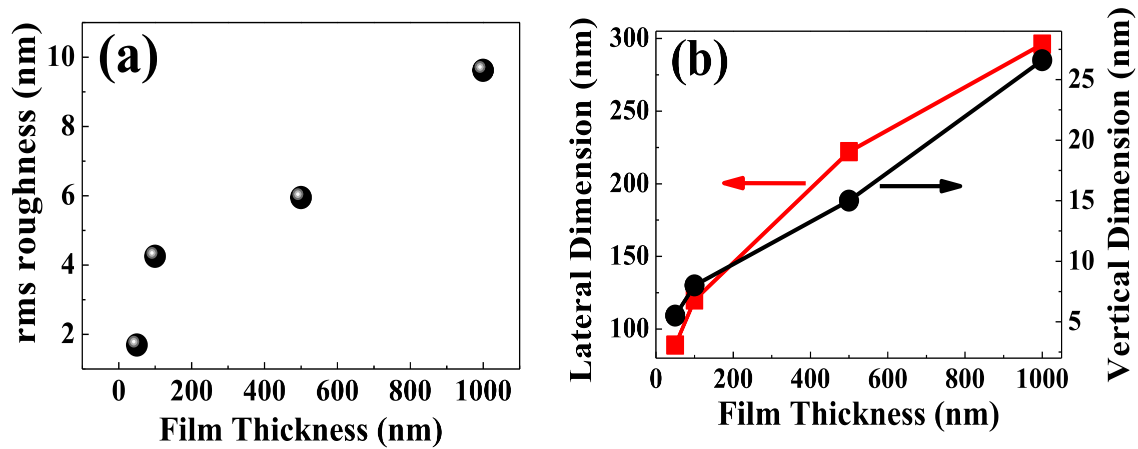

Figure 5.20 *(a) Rms surface roughness of the a-plane InN films versus film thickness, as determined from 10 x 10 μm² AFM scans, and (b) The magnitude of the lateral (width) and vertical (height) dimensions of apparent surface grains versus the a-plane InN film thickness.*

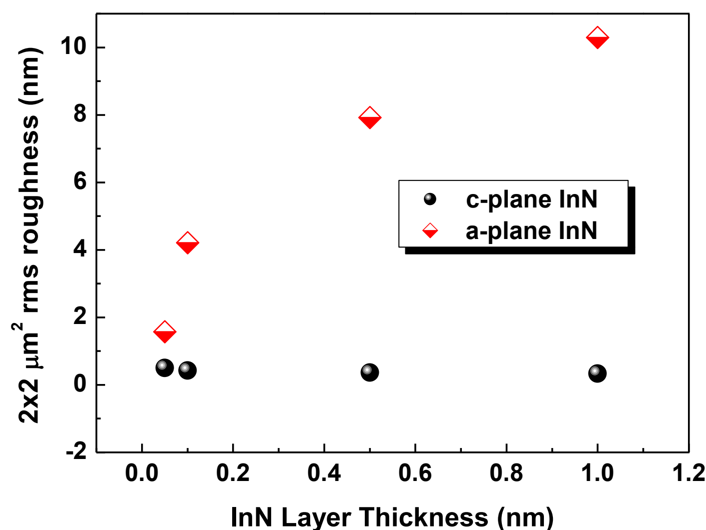

Figure 5.21 *Comparative 2x2 μm² AFM rms roughness dependence on thickness for both a- and c-plane InN layers. The thickness range of the layers is 50 - 1000 nm.*

The heteroepitaxial growth of III-nitride films on non-polar orientations typically results in anisotropic characteristics of the surface morphology as well as of the microstructure. This is due to different diffusivity of the adatoms on the surface [20] and possible differences in the lattice mismatch strain and its relaxation [29]

along the *c*-axis and its orthogonal in-plane direction. The anisotropic properties have been observed in *a*-plane GaN [23] as well as in *m*-plane InN [26] and have been attributed to differences of the lateral growth rate along the *m*- and *c*-axes on the *a*-plane surface and the *a*- and *c*- axes on the *m*-plane surface. Such anisotropy was not observed in the *a*-plane InN films grown in the present work, using a 35 nm GaN nucleation layer on *r*-plane sapphire, as evident from Figs. 5.3(b) and 5.19.

5.7.3 Structural properties analyses

HR-XRD was employed to analyse the thickness dependent structural properties of the InN samples. In order to confirm the expected *a*-plane orientation of the films, θ-2θ scans covering an extensive range of Bragg angle θ were carried out. The results revealed that all samples consist of single-crystal *a*-plane InN films. The θ-2θ scan for the 1000 nm *a*-plane InN film is shown in Fig. 5.22(a) and is representative of all the *a*-plane films. From this figure, the epitaxial orientation relationship of the InN epilayers, grown on the *r*-plane sapphire substrates with a GaN nucleation buffer layer, was determined as $(11\bar{2}0)$ InN // $(11\bar{2}0)$ GaN // $(1\bar{1}02)$ Al_2O_3. The low intensity peak at 2θ = 57.729° corresponds to the *a*-plane $(11\bar{2}0)$ orientation of wurzite GaN and reveals that the 35 nm GaN buffer is also *a*-plane oriented.

Table 5.6 *HR-XRD and Hall-effect measurements characterisation results for non-polar a-plane and polar c-plane InN films of different thickness grown on r-plane and c-plane sapphire substrates, respectively, under stoichiometric III/V flux ratio. t is the film thickness,* $(11\bar{2}0)RC_{FWHM}$ *is the FWHM of the HR-XRD* $(11\bar{2}0)$ *RCs along the in-plane c-axis for the a-plane InN films and* $(0002)RC_{FWHM}$ *is the FWHM of the HR-XRD RC around the (0002) reflection for the c-plane InN films.* N_{ap} *is the apparent electron concentration* $N_{ap} = N_{S_meas} / t$ *that was determined for each sample from the measured sheet density values (* N_{S_meas} *) determined from Hall-effect measurements at 300K and* μ_{meas} *is the measured mobility.*

t (nm)	a-plane InN films				c-plane InN films			
	μ_{meas} (cm^2/V.s)	N_{S_meas} (x$10^{14}cm^{-2}$)	N_{ap} (x$10^{19}cm^{-3}$)	$(11\bar{2}0)$ RC_{FWHM} (arcsec)	μ_{meas} (cm^2/V.s)	N_{S_meas} (x$10^{14}cm^{-2}$)	N_{ap} (x$10^{19}cm^{-3}$)	(0002) RC_{FWHM} (arcsec)
50	144	2.5	4.9	7200	305	2.0	3.7	552
100	235	1.9	1.9	5040	1051	1.7	1.7	462
500	325	7.5	1.5	1800	1466	8.2	1.5	310
1000	422	11.3	1.1	1440	1550	15.7	1.4	432

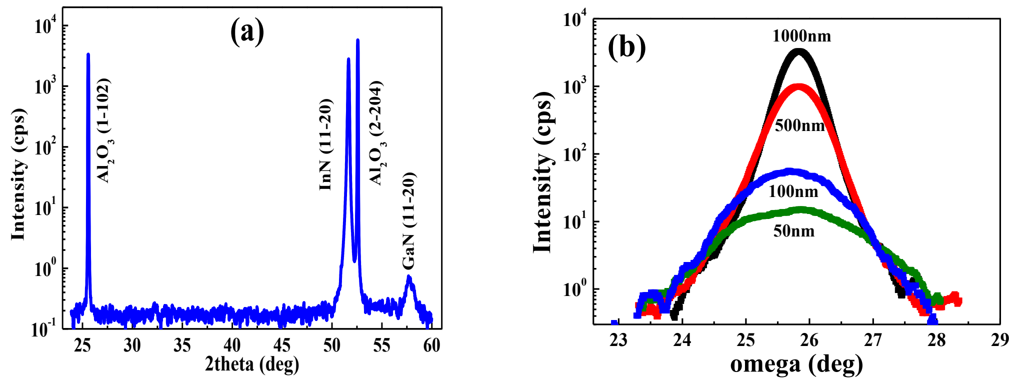

Figure 5.22 *(a) HR-XRD (θ-2θ) scan for the 1000 nm a-plane InN film grown on r-plane sapphire. The absence of peaks other than the* $(11\bar{2}0)$ *InN peak reflects the single crystallinity of InN, and (b)* $(11\bar{2}0)$ *RCs for all the InN a-plane films measured along the in-plane c-axis. The FWHM of the 1000 nm thick a-plane sample is 24 arcmin.*

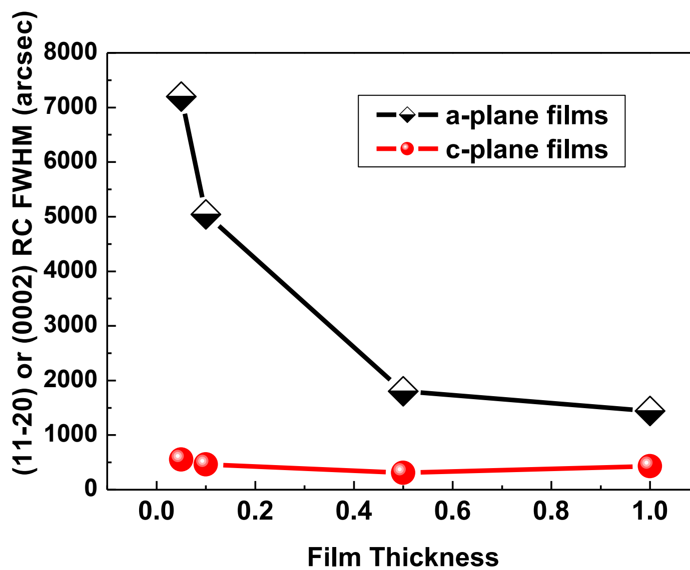

Figure 5.23 *FWHM of RCs around the* $(11\bar{2}0)$ *reflection for the a-plane InN films and FWHM of RCs around the (0002) reflection for the c-plane InN films versus the epilayer thickness. The superior crystal-quality of the c-plane InN films is clearly evident. A significant crystal quality improvement with increasing thickness is observed for the a-plane films.*

The crystalline quality of the different thickness *a*-plane InN samples was studied by HR-XRD ω-scans (rocking curves) around the $(11\bar{2}0)$ InN reflection. As shown in Fig. 5.22(b), RC FWHM values of 120, 84, 30, and 24 arcmin correspond to film thicknesses 50 nm, 100 nm, 500 nm and 1000 nm, respectively. The ω-scan line broadening due to film thickness can be estimated by the equation [50],

$$\beta = \frac{(1/t)}{|k_{hkl}|} \tag{5.1}$$

where β is the integral breadth of the line in radians, t is the sample thickness and k_{hkl} is the scattering vector. In all cases, since the FWHM values derived by Eq. (5.1) are more than an order of magnitude smaller than the experimental ones, the decreasing FWHM with thickness cannot be attributed to film thickness effects, but should rather be associated with improvement of *a*-plane InN structural quality with thickness. Similar result has been reported for *c*-plane InN grown on Al_2O_3 (0001) using buffer layer of GaN or AlN [46]. However, it is very clear from the *a*-plane InN $(11\bar{2}0)$ RC FWHM and the *c*-plane InN (0002) RC FWHM displayed in Fig. 5.23 that the crystalline quality of *a*-plane InN films is still very inferior to that of *c*-plane films. The widths for both orientations reduce with increasing film thickness from 7200 to 1440 arcsec (*a*-plane InN) and 552 to 310 arcsec (*c*-plane InN), respectively [Table 5.6]. Nevertheless, the figure highlights the improving crystal-quality of *a*-plane InN with increasing layer thickness.

5.7.4 Structural anisotropy investigation

The degree of structural anisotropy of the films was studied in a similar way to that of other *a*-plane InN films discussed in section 5.5.; by measuring the FWHM values of the $(11\bar{2}0)$ RCs along different azimuth angles of X-ray beam incidence. A negligible FWHM variation within the range of 0.01 to 0.04 degrees was determined for each one of these *a*-plane InN films by changing the azimuth of measurement. This very narrow range of variation reflects the absence of significant structural anisotropy along the orthogonal in-plane *c* and *m* axes of the samples, contrary to the significantly larger differences (comparably >1-2 order of magnitude) reported for *a*-plane InN [17,31] *m*-plane InN [26,31], *s*-plane InN [31] and *a*-plane GaN [21,23]. It again indicates that the conclusion of isotropic diffusivity of adatoms on the *a*-plane InN surface under stoichiometric III/V flux ratio conditions, based on the results of section 5.5 and Fig.5.16, is independent of film thickness.

5.7.5 Electrical properties investigation of *a*-plane and *c*-plane InN films

The thickness dependence of the electrical properties of the heteroepitaxial *a*-plane InN films was studied by single magnetic field Hall-effect measurements at 300K. Hall-effect measurements resulted to the measured electron mobility (μ_{meas}) and sheet density (N_{S_meas}) values for the films. From the N_{S_meas} values and the known thickness t of the samples, the apparent electron concentration $N_{ap} = N_{S_meas} / t$ was determined for each sample. The N_{ap} would be the actual electron concentration in the InN crystal, if the electrons were uniformly distributed and their mobility was constant throughout the entire film. However, in the case of *c*-plane InN films, it is well established that electron accumulation occurs at the surface and perhaps the interface of the InN film.

5.7.5.1 Hall-effect measurements study of the InN films

The μ_{meas}, N_{S_meas} and N_{ap} have been plotted versus the film's thickness in Fig 5.24, for both *a*-plane InN (square symbols) and *c*-plane InN (circle symbols) films of similar thicknesses. A similar dependence on thickness for both *c*- and *a*-plane InN films is evident from the plots. A rather linear increase of the N_{S_meas} with increasing thickness, consistent with a constant bulk electron concentration (N) near 10^{19} cm^{-3} is observed [5.24(b)]. The high mobility nature of the *c*-plane films; despite the as-grown electron doping concentrations degeneracy, are found to be consistent with theory [51] and are attributed to low compensation ratio and low dislocation density [52,53].

The measured electron mobility (μ_{meas}) improved monotonically with increasing InN thickness, as shown in Fig. 5.24(a). For these *a*-plane films, the μ_{meas} varied from 144 to 422 cm^2/Vs as the thickness increased from 50 nm to 1 μm, which is different from the results of Lu *et al.* [15], where no improvement of the mobility in *a*-plane InN films was observed with thickness increase from 0.5 to 3 μm. They reported the measurement of electron mobility of 270 cm^2/Vs with a corresponding N_{ap} of 6 x 10^{18} cm^{-3} for the *a*-plane films. The independence of the electrical properties of their films on thickness was attributed to the lack of significant reduction of the density of structural defects along the growth direction of the *a*-plane InN films, which is in contrast to their findings for *c*-plane InN growth. In our own study, which includes thinner InN layers down to 50 nm, we have observed the same trend for the variation of N_{S_meas}, N_{ap} and μ_{meas} versus InN thickness for both *a*- and *c*-plane InN films, as shown in Fig. 5.24.

The measured electron mobility of 422 cm^2/Vs, for the 1 μm *a*-plane film, is the highest value reported to date for *a*-plane InN films [34], although an even higher value of 630 cm^2/Vs was measured in this study for a 500 nm thick *a*-plane InN film (see section 5.3). This suggests a well optimized *a*-plane InN heteroepitaxial growth process in the experiments. However, even though the N_{S_meas} and the corresponding N_{ap} values are comparable for both *a*-plane and *c*-plane InN films [Figs. 5.24(b) and 5.24(c)], it should be pointed out that the electron mobilities of the *c*-plane InN films are more than three-times higher than that of the *a*-plane InN films, especially for thicknesses greater than 100 nm [Fig. 5.24(a)], suggesting an inferior structural quality of the *a*-plane InN. The mobility of electrons in state-of-the-art *c*-plane InN epilayers was found to be limited by charged dislocation scattering, using a combined experimental and theoretical analysis [54]. As will be discussed in section 5.10, more than one order of magnitude increase of the dislocation density of *a*-plane InN, compared with what is observed for *c*-plane InN film, could account for the reduced electron mobility typical of *a*-plane InN.

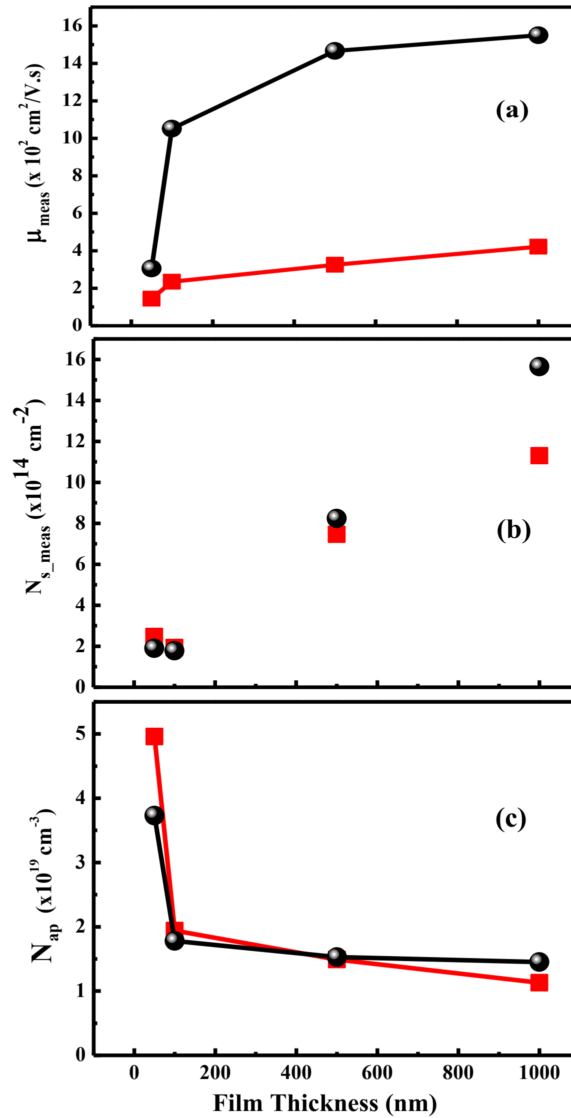

Figure 5.24 *Hall-effect results as a function of epilayer thickness for InN films of a-plane orientation grown on r-plane sapphire and c-plane InN grown on MOVPE GaN pseudo-substrates (a) measured electron mobility (μ_{meas}) (b) measured electron density (N_{S_meas}), and (c) apparent electron concentration (N_{ap}). The square and circle symbols correspond to a-plane and c-plane films, respectively.*

5.7.5.2 Modelling and analysis of the electrical properties of the InN films

The electron mobility and concentration values determined directly from the Hall-effect measurements should be treated with caution in the case of InN, due to the well known surface and interfacial electron accumulation [35,55-57]. The N_{S_meas} varied within the range of 1.7 - 15.7 x 10^{14} cm^{-2} for the *c*-plane InN samples, as film thickness increased from 100 to 1000 nm. A slightly narrower range of 1.9 - 11.3 x 10^{14} cm^{-2} was determined for *a*-plane films of same thickness range. However, careful inspection of Table 5.6 and Fig. 5.24(b) reveals an anomalous behaviour of N_{S_meas} for both *a*- and *c*-plane InN thickness below 100 nm; the minimum value of N_{S_meas} was

measured for layers of 100 nm thickness. The N_{S_meas} was increased for InN thickness t = 50 nm in comparison to t = 100 nm, contrary to the linear decrease of N_S reported by Lu *et al.* [57] for *c*-plane InN. The corresponding effect on the determined N_{ap} was a sharp decrease as t increased from 50 nm to 100 nm, followed by a slow change; N_{ap} varied from 1.9 x 10^{19} cm^{-3} for the 100 nm InN sample to 1.1 x 10^{19} cm^{-3} for the 1000 nm film.

This behavior can be understood by considering two contributions [35] to the overall film's conductivity: (1) a surface/interfacial layer electron conductivity and (2) the conductivity of the bulk of the InN film. The Hall-effect measurements were analysed qualitatively by considering the contribution of two conducting layers [35] with electron sheet density (N_S) and mobility (μ), denoted by N_{S1}, μ_1 and N_{S2}, μ_2 for the layers 1 and 2, respectively. The first conducting channel represents surface and interface contribution, while the second one corresponds to the bulk material conductivity. In this case, the measured electron density (N_{S_meas}) and mobility (μ_{meas}) are given by [58]

$$N_{S_meas} = \frac{\left(N_{S1}\mu_1 + N_{S2}\mu_2\right)^2}{N_{S1}\mu_1^{\ 2} + N_{S2}\mu_2^{\ 2}} \quad (5.2)$$

$$\mu_{meas} = \frac{N_{S1}\mu_1^{\ 2} + N_{S2}\mu_2^{\ 2}}{N_{S1}\mu_1 + N_{S2}\mu_2} \quad (5.3)$$

In order to apply this two-layer analysis in the qualitative assessment of the films' electrical characteristics' dependence on thickness, an estimate of the surface and interface contribution is needed. The best available approximation for N_{S1} and μ_{S1} are the measured ones for the 50 nm thick film case. The choice of this value is an assumption to facilitate the analysis of the Hall-effect measurements and the extraction of the most prominent electron concentration and mobility characteristics. The low mobility of the surface/interfacial electron conductivity layer may improve with increasing thickness as a result of improving structural quality of the InN layer. In the analysis, it is considered that the surface/interfacial conductivity contributes to the overall film's conductivity an electron sheet density N_{S1} = 2.5 x10^{14} cm^{-2} with μ_1 = 144 cm^2/Vs for the *a*-plane InN films and N_{S1} = 2.0 x10^{14} cm^{-2} with μ_1 = 305 cm^2/Vs for the *c*-plane InN films. The electrons in the bulk of an InN film, thicker than 50 nm, will contribute an actual electron sheet density

$$N_{S2} = N_D\,(t - 50\ \text{nm}) \quad (5.4)$$

where N_D is the actual electron concentration (assumed thickness independent) in the InN bulk and t is the thickness of the film. It is reasonable to approximate N_D with the N_{ap} value determined for the thickest samples of 1 μm InN [Table 5.6]. Then, the corresponding mobility μ_2 would be equal to the μ_{meas} value for the 1 μm films; that is, μ_2 = 422 cm^2/Vs for *a*-plane InN and 1550 cm^2/Vs for *c*-plane InN. Using the above assumed values of N_{S1}, N_{S2}, μ_1 and μ_2 in the equations (5.2) and (5.3), the expected experimental values of N_{S_meas} and μ_{meas} from the Hall-effect measurements was calculated. The expected N_{S_meas} and μ_{meas} values evaluated this way are shown by the lines in Figs. 5.25(a) and 5.25(b), respectively. The actual experimental N_{S_meas} and

μ_{meas} values (from Hall measurements) are shown by symbols. It is obvious that the assumption of the two conductivity layers explains rather quantitatively the Hall-effect measurements and the observed anomalous increase of N_{S_meas} for the 50 nm thick films.

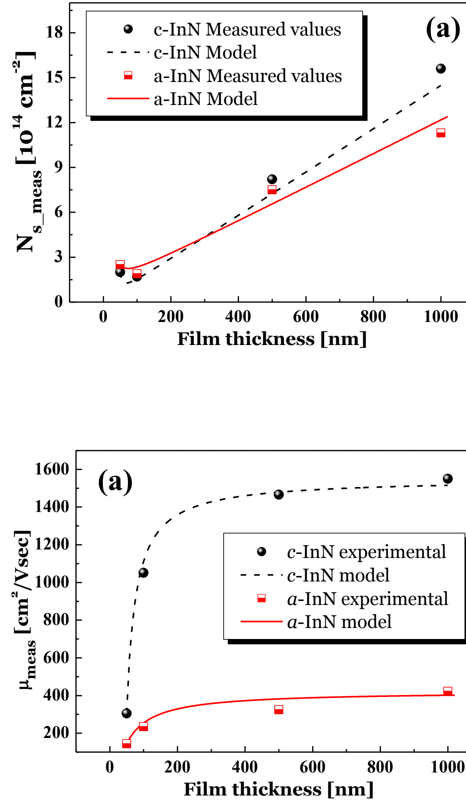

Figure 5.25 *Comparison of the measured values (symbols) of electron density (N_{S_meas}) and mobility (μ_{meas}) with the simulated values (lines) calculated according to a two conducting layers' model for both a- and c-plane InN: (a) sheet electron density and (b) mobility plotted versus the InN thickness.*

According to Fig. 5.25(b), the fast increase of μ_{meas} with increasing InN thickness (t) is mainly the effect of the weighted averaging of the two conductivity contributions in Hall-effect measurements. The differences between the modeled and measured values of μ_{meas} in Fig. 5.25(b) indicate that the actual bulk electron mobility, μ_2, also improves slightly with film thickness. For the 500 nm film, the bulk electron mobility should be less than 422 cm^2/Vs but it should be higher than 422 cm^2/Vs for the 1 μm film. This observation is attributed to the improvement of the InN crystalline quality by reduction of the defect density as the *a*-plane InN film becomes thicker, in agreement with the previously described XRD results in section 5.7.3. The slight improvement in the bulk mobility is even weaker in the case of *c*-plane InN, since the modelled μ_{meas}, assuming a constant bulk mobility, coincides with the experimental μ_{meas} values for sample thickness from 100 nm to 1000 nm.

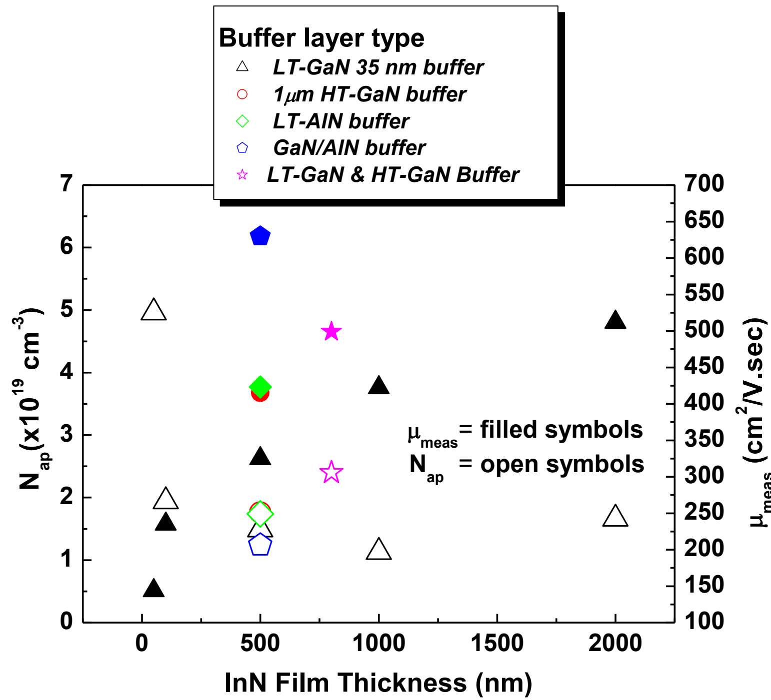

Figure 5.26 *Measured values of Hall mobility (filled symbols) and apparent electron concentration (open symbols) at 300K, for a-plane InN films of different thicknesses grown using different buffer layers on r-plane sapphire.*

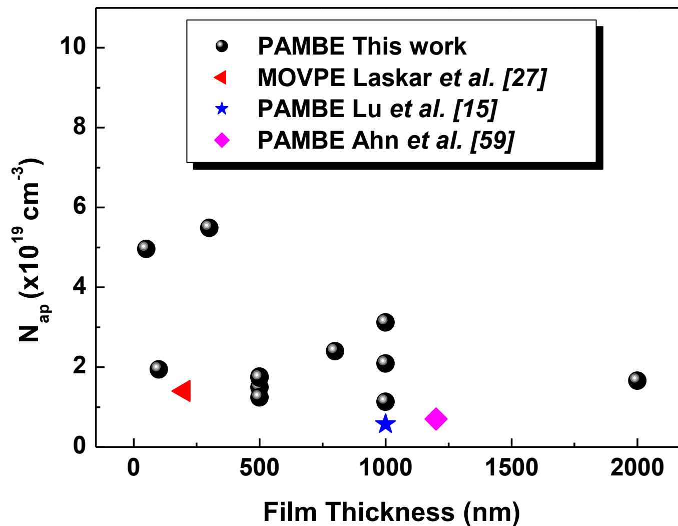

Figure 5.27 *N_{ap} extracted from Hall-effect measurements at 300K, for a-plane InN films of various thicknesses grown on r-plane sapphire, using different buffer layers and growth temperatures. Also included are values reported in the literature [15,27,59]. The a-plane samples in this work exhibited somewhat similar N_{ap} values, compared to the values reported by other authors, at 10^{19} cm^{-3}.*

Fig. 5.26 presents the Hall-effect results for a larger number of *a*-plane samples grown on *r*-plane sapphire with different buffer layers and growth conditions. The correlation between the μ_{meas} (filled symbols) and N_{ap} (open symbols) with film thickness is shown in the figure, and is similar to the general behaviour already observed for *c*-plane InN in Chapter 4 as well as in the literature [18]. The N_{ap} extracted for the *a*-plane InN films are plotted separately versus film thickness in Fig. 5.27. The best values reported by other authors [15,27,31,59] until now are also included for comparison purpose. It is obvious that the *a*-plane samples in this work exhibited electron concentration of 10^{19} cm^{-3}, which is slightly comparatively higher than reported values in the literature [15,27,59]. Similar plot for the μ_{meas}, shown in Fig. 5.28, indicates that the *a*-plane InN samples however exhibited higher electron mobility values, compared to the values reported by others [15,27,31,59], for similar film thickness.

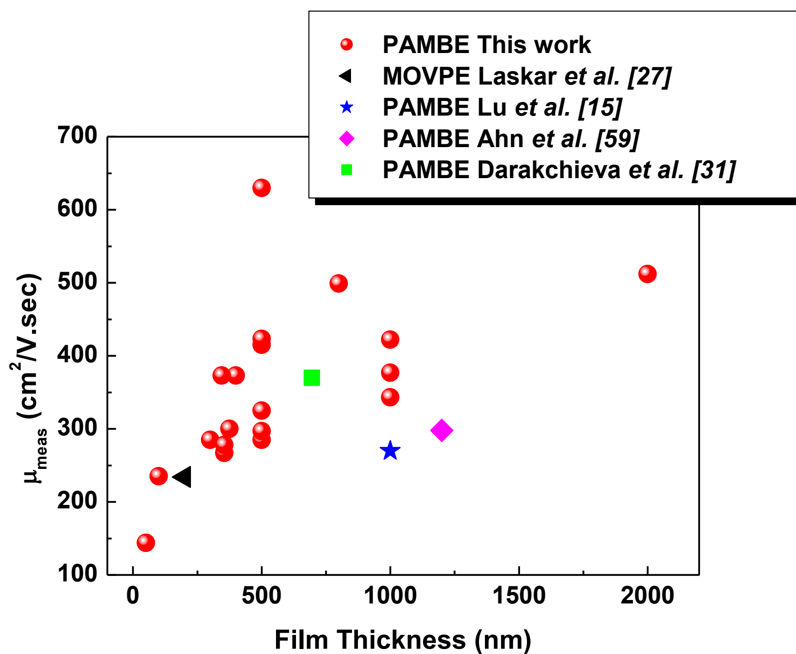

Figure 5.28 *Electron mobilities extracted from Hall-effect measurements at 300K, for a-plane InN films of various thicknesses grown on r-plane sapphire, using different buffer layers and growth temperatures. Also included are values reported in the literature [15,27,31,59]. The a-plane samples in this work, for similar film thickness, exhibited higher* μ_{meas} *values compared with the literature.*

5.7.6 Optical properties investigation of *a*-plane InN films

The thickness dependent optical properties of the *a*-plane InN films were studied by 20K PL and 300K optical transmittance (T) measurements and the results are discussed in the following.

5.7.6.1 Photoluminescence measurements of *a*-plane InN

Fig. 5.29(a) shows the 20K PL spectra of the *a*-plane InN films. From this figure, it can be observed that the PL intensity increases with increasing film thickness. Very weak PL intensity is observed for the 50 nm thick film and it is magnified by x5 for clear visibility. The improvement of the PL intensity with increasing thickness is consistent with a reduction in the density of extended defects as the InN film thickness increases, in agreement with the conclusions from the HR-XRD and Hall-effect measurements. However, it may be also related to the increase of the amount of the excited material that exhibit luminescence. The PL spectra of all samples, except of the 50 nm thick film, were dominated by emission peaks at approximately the same energy around 0.631 eV. The 50 nm thick sample exhibited very weak PL, as shown in Fig. 5.29(a). Large FWHM values of the 20K PL peaks were observed, with the lowest value of 62 meV exhibited by the 500 nm thick InN film. The lower energy peak of the *a*-plane samples was lower than that of the *c*-plane and this is also in agreement with the literature [16]. The origin of the PL peaks is discussed in the next part with the assistance of optical transmittance measurements.

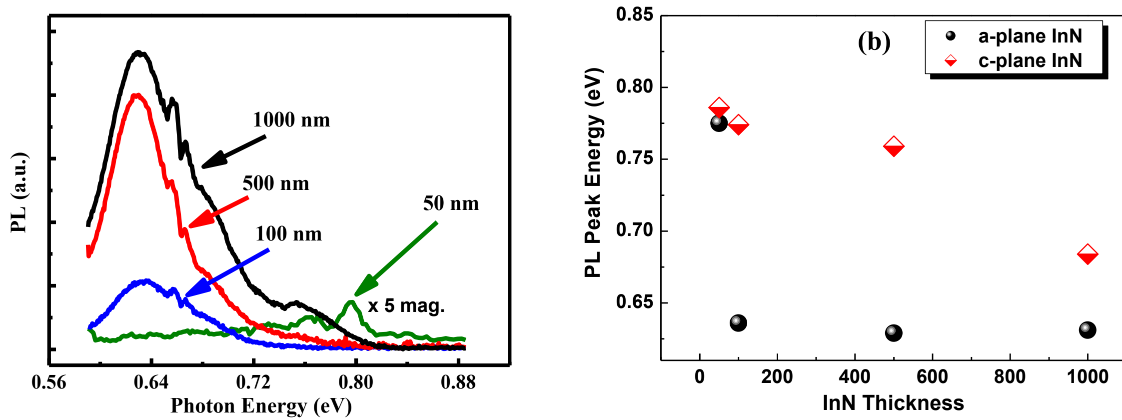

Figure 5.29 *(a) PL spectra measured at 20K for the a-plane InN films. Very weak PL intensity observed for the 50 nm thick film and it is magnified by x5 for improved visibility. (b) Energy of PL peaks for both a- and c-plane InN films as a function of film thickness.*

5.7.6.2 Transmittance measurements of *a*-plane InN

The absorption coefficient (a) is proportional to the negative of the logarithm of transmittance (*-lnT*) [60]. In Fig. 5.30, the $(lnT)^2$ at 300K and the PL intensity at 20K, are plotted versus photon energy E (eV), for the 1000 nm thick *a*-plane InN film. The red-shift of the PL energy peak from 20 to 300K is usually very small [61], in the order of about 50 meV. Therefore, physical insight for the luminescence and absorption processes could be extracted by comparing 20K PL and 300K absorption spectra of Fig. 5.30. The absorption edge was estimated equal to 0.768 eV for this sample by extrapolating the linear part of the $(lnT)^2$ versus E curve, as shown by the straight line in Fig. 5.30. Large blue-shift of the absorption edge energy from the PL energy peak is observed. It is evident that the PL peak at 0.631 eV does not coincide with the absorption edge but is shifted by 0.137 eV to lower energy. The non-

coincidence of the PL peak energy and the absorption edge has been initially reported for *c*-plane InN film [61], with the PL emission spectra considered to mainly originate from localized states in the bandtail. The determined absorption edge of 0.768 eV is consistent with the expected Burstein-Moss (*B-M*) effect due to conduction band filling with electrons.

The expected *B-M* shift (ΔE_g) of the absorption edge, using the formula of Monemar *et al.* [62],

$$\Delta E_g(n) \approx 2.2x10^{-8} n^{1/3} \qquad (5.5)$$

where n = electron concentration of the sample in question. The ΔE_g was estimated equal to 47.4 meV for $n = 1.1 \times 10^{19}$ cm^{-3}. The PL energy peak at 0.631 eV is therefore attributed to carrier recombination transitions involving defect-related localized states.

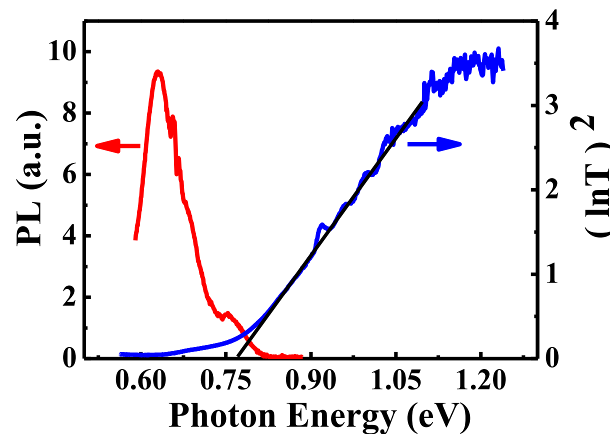

Figure 5.30 *PL at 20K and (lnT)^2 at 300K versus photon energy (eV) for the 1000 nm thick a-plane InN film. The absorption edge of 0.768 eV was extracted from the (lnT)^2 versus the photon energy plot.*

All the previously presented results, from the HR-XRD, PL and Hall-effect measurements, have created a comprehensive understanding of the thickness dependence of the structural, electrical and optical properties of *a*-plane InN films, grown on *r*-plane sapphire by PAMBE using a thin GaN nucleation layer. The properties of the *a*-plane InN films exhibited similar behaviour to that of *c*-plane InN and improved with increasing film's thickness. However, the surface morphology is consistent with nucleation and growth of three dimensional (3D) islands. Thus, unlike the *c*-plane InN films, the surface roughness of *a*-plane InN increased with increasing thickness.

For both *a*- and *c*-plane orientations, the contribution in the overall film's conductivity of a similar surface/interfacial conductivity layer, with low electron mobility, was determined in the low 10^{14} cm^{-2} range. This is in agreement with the surface electron density values determined by Darakchieva *et al.* [63] by an optical Hall-effect technique for films with high bulk electron concentrations. The carrier

concentrations of the *a*-plane films were similar to those of *c*-plane InN films, indicating that the unintentional bulk donor density does not depend on the InN orientation and crystal defect density. However, the electron mobility values of the *c*-plane InN films were more than triple the mobility values of the *a*-plane films, suggesting a significant difference in the *a*- and *c*-plane InN crystalline quality. A significant improvement with increasing film thickness, from 50 nm to 1000 nm, was observed for the electron mobility of the *a*-plane InN films, similarly to *c*-plane InN, in contrast to the earlier report of Lu *et al.* [15] who had examined a range of larger epilayer thicknesses (0.5 - 3.0 µm).

The fast increase of measured mobility with increasing thickness is due to the decreasing relative contribution of the low mobility electrons; from the surface and interface regions, to the overall conductivity. However, the mobility of the *a*-plane bulk InN electrons also improves slightly with thickness above 100 nm. The improvement of the *a*-plane InN structural quality with thickness, as evidenced by the Hall-effect measurements, was also found directly by the XRD measurements. The FWHM of $(11\bar{2}0)$ rocking curves decreased from 84 arcmin for the 100 nm film to 24 arcmin for the 1000 nm film. The reduction of the density of structural defects with increasing film thickness is also consistent with the observation of increasing PL intensity.

The general characteristics of the *a*-plane InN epilayers exhibit similarities to what has been previously observed for *c*-plane InN films grown on (0001) sapphire and reasonably confirm that the properties of *a*-plane InN are not typically different from that of *c*-plane films. Moreover, relative to other work on *a*-plane InN growth reported so far [14,15,17,64,65], a notable improvement has been achieved in the growth of single crystalline *a*-plane InN films with the achievement of an electron mobility of 650 cm^2/Vs and $(11\bar{2}0)$ RC FWHM of 24 arcmin, even when compared with the work of Ref. 17 that employed free-standing *a*-plane GaN template. Since both *a*- and *c*-plane InN films exhibited similar sheet density and electron carrier concentration, regardless of film thickness and despite the fact that the former very well consists of more structural defect than the latter, then, threading dislocations cannot be the source of the bulk donors in InN. It is important to note that impurities should be the major source of the unintentional doping.

5.8 Growth and properties of 3 µm thick *a*-plane InN grown on *r*-plane sapphire

To date, not many investigations have been carried out on thick *a*-plane InN besides the work of Lu *et al.* [15] who investigated the thickness dependence of the electrical properties of *a*-plane InN films. Most of the film thicknesses reported for *a*-plane InN are either lower or equal to 1µm. The main reason for this could be the difficulty of growing *a*-plane InN under stable conditions, in comparison to *c*-plane InN. Consequently, the properties of thick *a*-plane InN layers are not well known. This work aims to investigate the epitaxy and properties of 3 µm thick *a*-plane InN layers: G1800 and G1804, grown on nitridated *r*-plane sapphire substrates at 375°C, under stoichiometric III/V flux ratio of InN. Intermediate layers comprising of 100 nm GaN and 50 nm GaN/50nm AlN buffer layers were employed, respectively.

The FE-SEM plan-view of the films is shown in Fig. 5.31 and it confirmed the RHEED observations. Smoother surface morphology characterised with stepped features are visible on the surface of G1800 [Fig. 5.31(a)] while the surface of G1804 is very coarse [Fig. 5.31(b)]. The surface morphology of sample G1800 as represented

by the FE-SEM image seems to deviate significantly from the usual typical grainy appearance observed on thinner films, using GaN buffer layer [34]. The insets of Figs. 5.31(a) and 5.31(b) depict the final RHEED diffraction patterns observed for G1800 and G1804, respectively. The streaky and spotty patterns obtained, respectively, are in agreement with the surface morphology of the *a*-plane InN films.

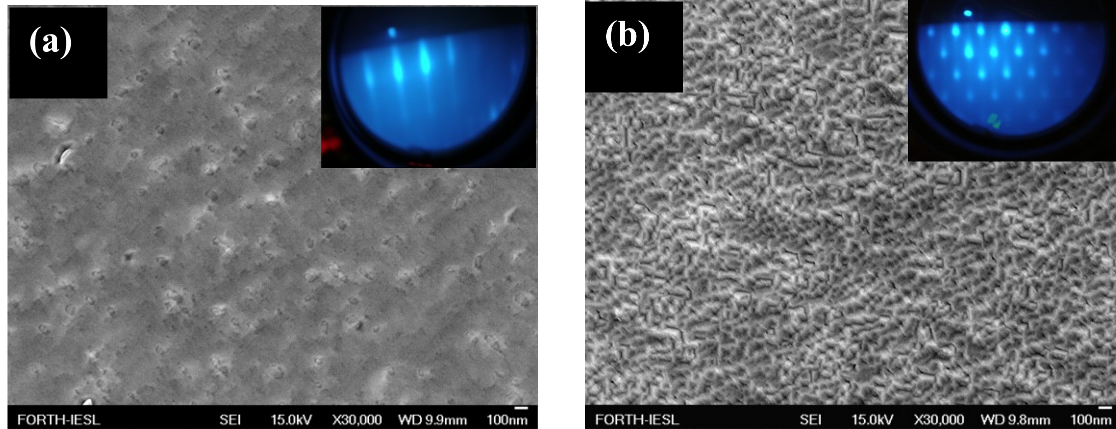

Figure 5.31 *FE-SEM micrographs of 3 μm thick a-plane InN films grown on r-plane sapphire substrates (a) G1800 with step-flow surface morphology. (b) G1804 with coarse surface morphology. The insets are the streaky and spotty pattern obtained for the a-plane films, respectively.*

Further investigation of the surface morphology of the *a*-plane films by 5x5 μm^2 AFM plan-view scans provides better understanding of their morphologies [Fig. 5.31]. A closer look at the AFM micrograph of Fig. 5.32(a), which depicts the G1800 surface morphology, indicates surface steps similar to those observed by the FE-SEM in Fig. 5.31(a). The film exhibits 2D-like surface with step arrays along the in-plane *m*-($[1\bar{1}00]$) orientation. Contrast modulations in between steps related to small InN islands that are aligned along the *c*-axis are also observed on the surface of the thick *a*-plane InN film. The profile scans on the AFM micrographs [Fig. 5.32(a)], in a direction perpendicular to the apparent step edges revealed step heights and sizes of approximately 18 nm and 5 nm, respectively, typical for step bunching [66]. The distance between these large steps, i.e the length of terraces, is in the range of 150 - 300 nm. Smaller steps are also seen on the terraces formed by the large bunched steps running in the perpendicular direction with step height of about 0.4 nm. These step sizes as determined from the AFM range are approximately 2 nm.

The investigation of the relationship between the *a*-plane InN film's large steps with the existing steps on the nitridated *r*-plane sapphire surface [Fig. 5.32(b)] indicates that the steps do not follow the sapphire surface steps and are aligned particular to those of the sapphire substrates, as clearly discernible from Fig. 5.32. The appearance of steps is related to the longer growth time (or increased layer thickness), which provides enough time for the initially nucleated islands to fully coalesce. The possibility of achieving full strain relaxation in a very thick InN epilayer is also believed to stabilize the layer-by-layer growth mode. This observation shows that under favourable growth conditions, the use of GaN buffer layer can promote step-flow growth of *a*-plane InN. The rms surface roughness of the film and the nitridated sapphire surface was determined as 5.07 nm and 0.13 nm, respectively.

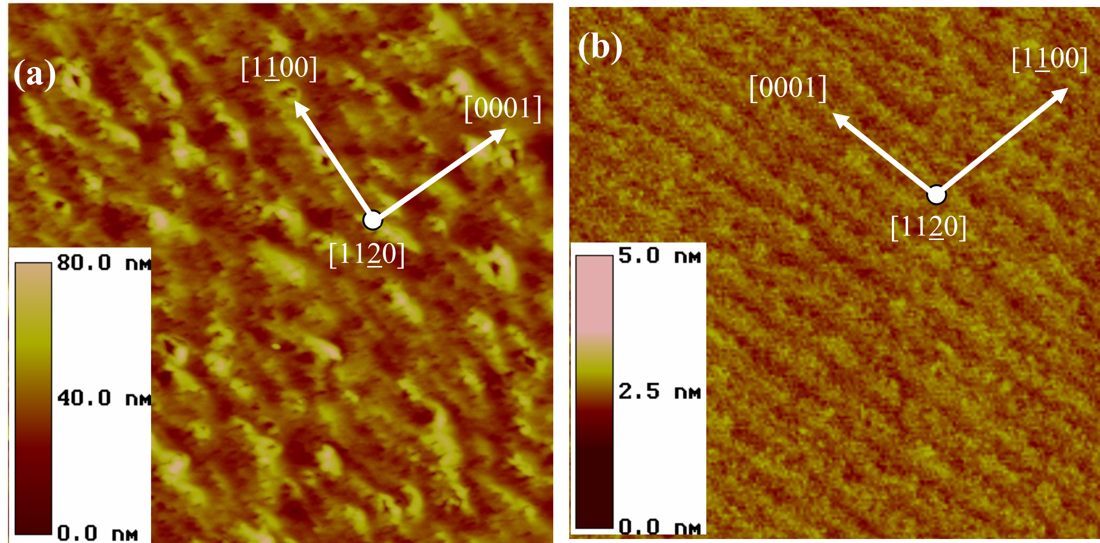

Figure 5.32 *(a) 5x5 μm² AFM micrographs of the 3 μm thick a-plane InN sample G1800 grown on r-plane sapphire, using GaN intermediate layer. A 2D-like surface with step arrays along the in-plane m-(*$[1\bar{1}00]$*) orientation and contrast modulations in between the steps relating to small InN islands aligning along the c-axis of the film are observed. (b) 5x5 μm² AFM surface morphology image of the nitridated sapphire surface with surface decorated by steps aligning along the in-plane c-axis direction. It is apparent that the observed steps on the a-plane InN film's surface do not correspond to the existing steps on the surface of nitridated r-plane sapphire substrates employed for the heteroepitaxy.*

The 5x5 μm² AFM micrograph of InN film G1804, grown with GaN/AlN buffer layer, is shown Fig. 5.33. The observed surface morphology is consistent with the rough and coarse surface depicted by FE-SEM in Fig. 5.31(b), which deviates sharply from the step-flow growth mode observed in the case of film G1800 in Fig. 5.32(a). The surface consists of very small surface roughness grains. The rms surface roughness of film G1804 was determined as 7.46 nm. In general, these results confirm that the surface morphology and roughness exhibited by the *a*-plane InN films is dependent on the nucleation layer, and the use of AlN nucleation layer promoted higher *a*-plane InN surface roughening compared to when GaN nucleation layer was used.

High resolution X-ray diffraction study of the thick InN epitaxial layers confirmed that they are both single crystalline and oriented along *a*-axis as expected. The $(11\bar{2}0)$ RC FWHM, taken with X-ray beam incidence along the two orthogonal in-plane [0001] and $[1\bar{1}01]$ directions, were determined as 0.48° and 0.58°, respectively, for G1804; indicating slight presence of structural anisotropy. This is consistent with previous observation that the use of AlN buffer layer promotes structural anisotropy, although in this case the degree of anisotropy is reduced compared to a thinner layer [see Sample 1628 in Table 5.2]. G1800 does not exhibit such anisotropy with the RC FWHM of approximately 0.69° determined for the film irrespective of the azimuth angle (Φ) employed for the $(11\bar{2}0)$ ω-scans. However, sample G1800 exhibited a higher FWHM value.

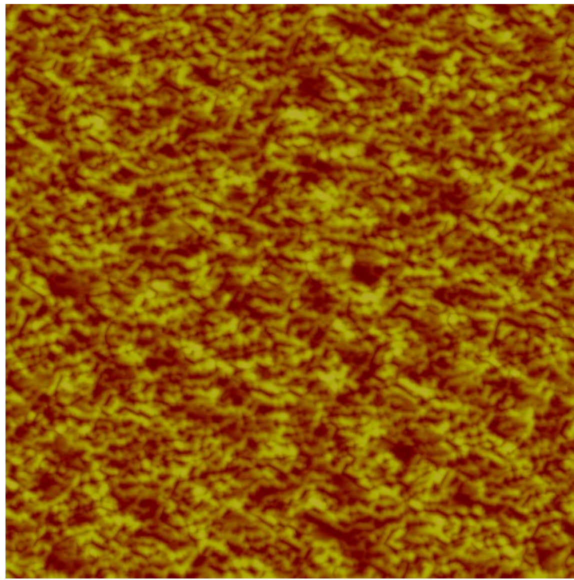

Figure 5.33 *5x5 μm^2 AFM micrographs of the 3 µm thick a-plane InN sample G1800 grown on r-plane sapphire, using GaN/AlN intermediate layer, showing rougher surface morphology with rms roughness of 7.46 nm.*

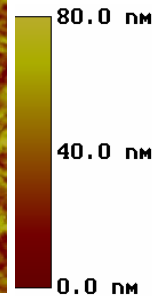

The structural anisotropy behaviour of G1800 and G1804 were investigated and compared with the results already obtained and discussed for thinner films. The measured (11-20) ω-scans widths as a function of the azimuth orientation of the diffraction plane covered the range $-45 \leq \Phi \leq 90$ and the results are shown in Fig. 5.34. The minimum and maximum RC FWHM values correspond to the RC measurements FWHM taken with the X-ray beam incidence along the c- and m-axes, respectively. The results for these 3 µm films are similar with those for thinner 1 µm a-plane InN samples in sections 5.3 and 5.5 and consistent with the previous structural anisotropy investigations, anisotropy is more pronounced in film G1804 that employed GaN/AlN buffer layer compared to G1800 that employed sole GaN buffer layer, indicating that structural anisotropy depends on the type of buffer layer and seems to be independent of epilayer thickness. The result also confirms the previous observation in Section 5.3 that the use of GaN/AlN intermediate layer for the epitaxy of InN on *r*-plane sapphire yields improved crystal quality compared with single GaN intermediate layer but also create significant structural anisotropy in *a*-plane InN.

The Hall mobility of G1800 and G1804 were measured as 333 and 348 cm^2/Vs, respectively. Similar apparent electron concentration of ~ 6.4 x $10^{19}cm^{-3}$ was determined for both films. The similar electrical behaviour indicates that the large thickness of these layers override possible effects of the used buffer layer type. The lower growth temperature employed for G1800 and G1804 is considered to also play a role in the poorer electrical behaviour compared to the results reported in section 5.3. However, these samples also exhibited a higher electron concentration, which could result from increased incorporation of unintentional donor impurities, probably as a result of a contamination source degrading the quality of vacuum of the MBE system.

It is note worthy that none of these thick *a*-plane InN samples exhibited photoluminescence even at 20K. What could be responsible for this anomaly is not yet clear, but it may be related to incorporation of contaminants. The optical properties were also investigated by using transmittance spectroscopy. The substrate backside was polished to curtail optical scattering due to surface roughness. Fig. 5.34(a) clearly shows similarity in the behaviour of the transmittance spectral obtained for both film samples. Considering the sensitivity of optical measurements to

material thickness, ellipsometry spectroscopy [67,68] was used to determine the exact thicknesses of G1800 and G1804 as 2881 nm and 2940 nm, respectively. These values were found to be close to the expected 3000 nm nominal thickness. The band gap energy of ~1.0 eV was deduced in each case from the $\alpha(E)^2$ curve in Fig. 5.34(a). The absorption edge shows a concentration dependent blue shift from the conventional 0.65eV, which results from the Burstein-Moss effect, because of the high electron carrier density of the films at mid 10^{19} cm^{-3}. This is also consistent with the already established dependence of the absorption edge on carrier density [69]. Febry-Pérot oscillations; which indicate good quality of the parallel surfaces, are clearly observed below the absorption edges of both films. The similarity of the exhibited band edges is consistent with the similar electrical and optical properties already observed for both films.

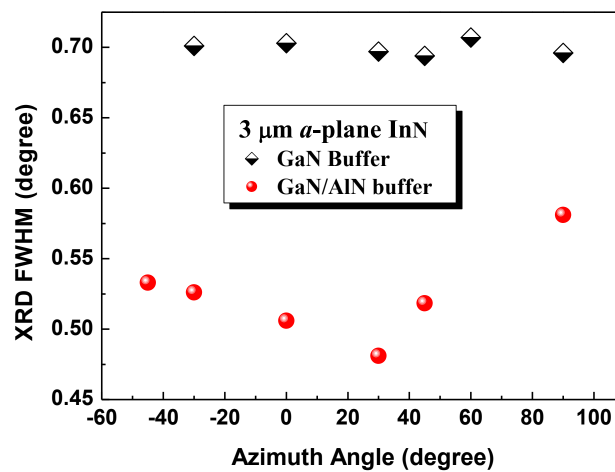

Figure 5.34 *Structural anisotropy behaviour of 3 μm thick a-plane InN films grown on r-plane sapphire using GaN (square symbol) and GaN/AlN (circle symbol) intermediate layers. The minimum and maximum RC FWHM values correspond to the FWHM along the c- and m-axes, respectively.*

In conclusion, thick *a*-plane InN layers were grown on *r*-plane sapphire. Longer time of growth permits the initially formed 3D InN islands on sapphire to achieve full coalescence; eliminating the usually observed grainy surface morphology and promoting step-flow growth with step height of about 5 nm and 2 nm, respectively for the larger and small steps that co-exists on the GaN-mediated InN layer's surface. The AlN mediated layer exhibited rougher morphology characterised with surface roughness grains but the same film exhibited smaller XRD $(11\bar{2}0)$ RC FWHM. The increased growth time caused significant reduction in the observed structural anisotropy compared to 1 μm films using a similar buffer layer. This result attests to the fact that step-flow growth could be achieved also for *a*-plane InN epitaxy. Further optimisation of growth conditions may also reduce *a*-plane InN surface roughness towards achieving the equivalent value obtainable for the state of the art rms roughness of *c*-plane InN (approximately 3 Å) [70]. Besides the distinctly different surface morphology features of the films, both exhibited the same electrical and optical characteristics. This is another evidence that high electron concentration in

the 10^{19} cm^{-3} range are not related to defects but to unintentional incorporated donor impurities.

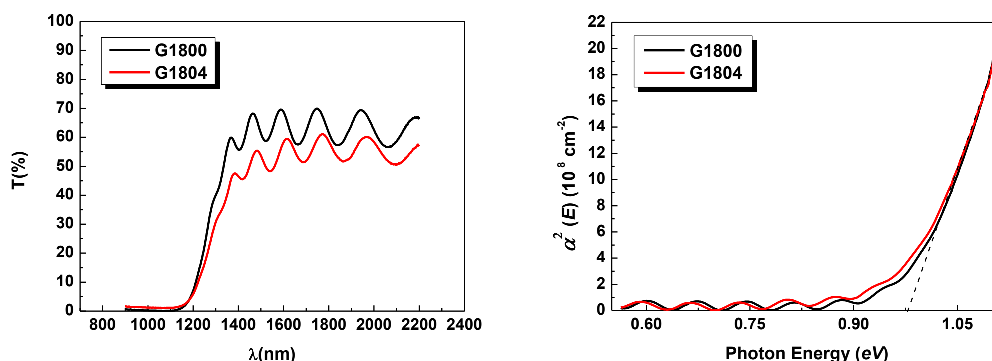

Figure 5.34 (a) Optical Transmittance spectra for samples G1800 and G1804 at 300K (b) Square of the absorption coefficient (α^2), as a function of photon energy, E, deduced from the IR transmission spectra shown in (a). The two a-plane InN samples exhibit free-electron concentrations of 6.4 x $10^{19}$$cm^{-3}$ and similar bandgap at ~ 1.0 eV.

5.10 Microstructure of *a*-plane InN films on *r*-plane sapphire substrates

Although the resilience of the III-nitride materials has been demonstrated by the possibility of fabrication of devices, in spite of the high defect density present, the presence of these defects is still detrimental to the electronic and optical properties of the devices and particularly their efficiency and lifetime [66]. Thus, understanding the film's microstructure and the defects' formation mechanisms is essential for nitrides growth optimization and defect density reduction. The microstructure of a 500 nm *a*-plane InN film G1511 has been investigated by transmission electron microscopy (TEM) techniques by collaborators (Prof. G. P. Dimitrakopulos and Prof. Th. Kehagias) from the Physics department of Aristotle University of Thessaloniki. The overall properties of this sample have been discussed in detail in section 5.3. Both conventional TEM (CTEM) and high resolution TEM (HR-TEM) were employed for the study. By CTEM analysis, the thicknesses of the GaN buffer layer and of the InN film were estimated as 30 nm and 600 nm, respectively. These values are close to the expected nominal values of the film, which were 35 nm for GaN and 500 nm for InN. The film's rms roughness was determined by TEM to be approximately 20 nm.

Fig. 5.35 is the cross-sectional two-beam dark field image of the non-polar *a*-plane epilayer, obtained off the [0001] zone axis using **g** $10\bar{1}0$. Lattice dislocations with Burgers vector components along the $[11\bar{2}0]$ and $[\bar{2}110]$ directions and partials dislocations with Burgers vector components along the $[2\bar{2}03]$ and $[02\bar{2}3]$ are the discernible defects in the film. Most of the defects are localized on the $<10\bar{1}0>$ line directions at 30° relative to the growth direction or in other words, lie on the inclined $\{1\bar{2}10\}$ prismatic planes. At the lower half of the specimen thickness, multiple interactions of defects on inclined planes are observed and threading dislocation bundles emanate from the intersection points of these defects along the growth direction.

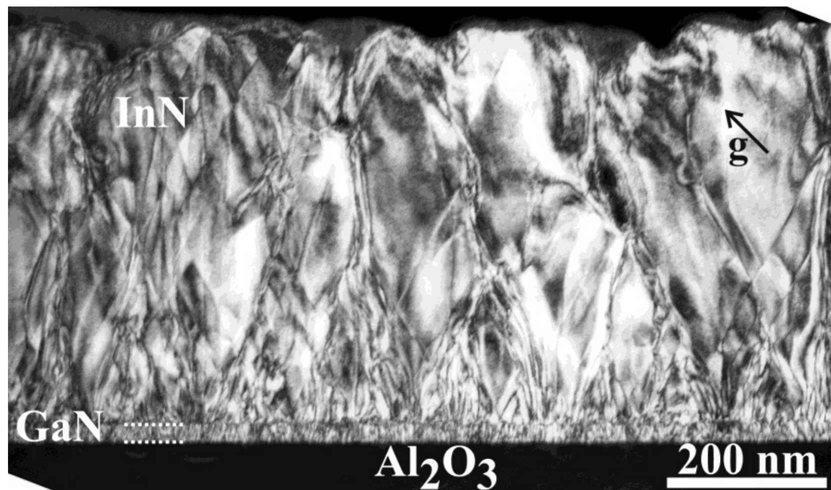

Figure 5.35 *Cross-sectional two-beam dark field image of the non-polar a-plane InN epilayer, obtained off the [0001] zone axis using* $\mathbf{g}$ $10\bar{1}0$. *A high density of inclined defects is discernible as well as defect interactions and annihilation reactions at approximately half the specimen thickness.*

The selected-area electron diffraction (SAED) patterns along the two in-plane [0001] and $[1\bar{1}00]$ directions are shown in Fig. 5.36. The main orientation of InN and GaN is identified as $(11\bar{2}0)$ as shown in the pattern and in agreement with the XRD identified orientation. The SAED patterns show the well-defined epitaxial orientation relationship between the epilayer and substrate.

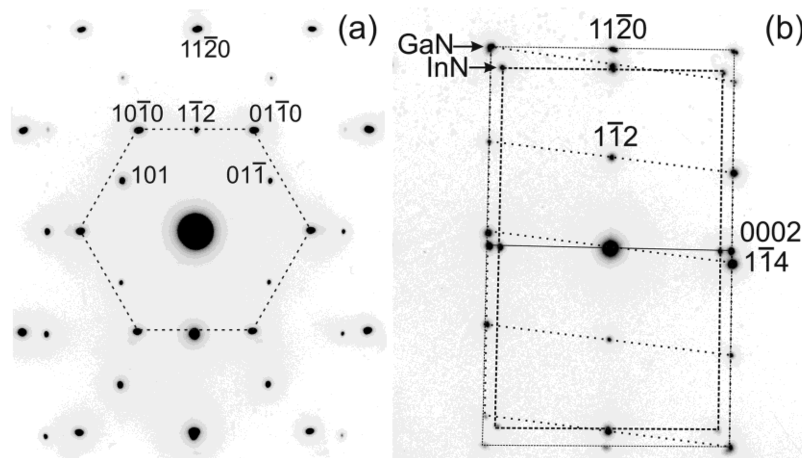

Figure 5.36 *(a) SAED pattern taken along the [0001]InN/$[1\bar{1}0\bar{1}]$$Al_2O_3$ zone axis. The InN reflections are connected by a dashed line. The reflections of sapphire are indicated in the three-axis hexagonal system (b) SAED pattern taken along $[1\bar{1}00]$InN/$[11\bar{2}0]$$Al_2O_3$ zone axis. Reflections indicated by 3-indices correspond to sapphire and 4-indices for InN. InN as well as GaN reflections from the wurtzite structure are discernible, in addition to the reflections of sapphire. In both (a) and (b) the patterns are aligned with the growth direction.*

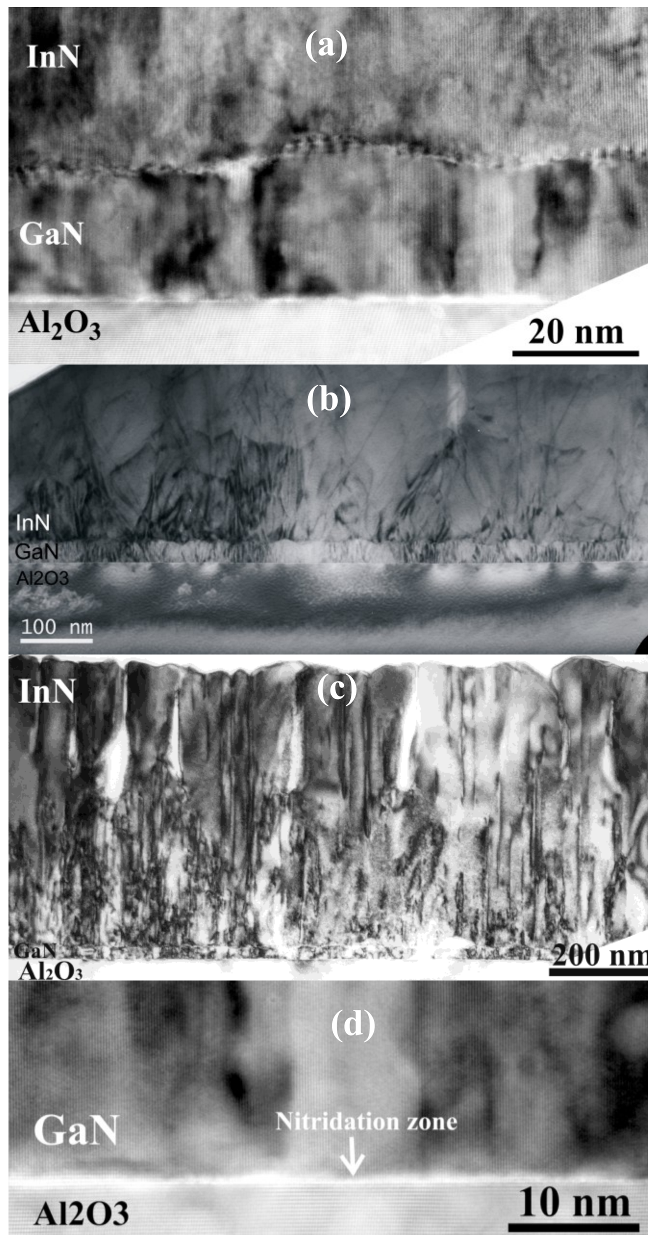

Figure 5.37 *(a) Cross sectional HRTEM image along [$1\bar{1}00$] showing the GaN buffer layer. The GaN/InN interface exhibits roughness due to the 3D growth mode of the buffer layer, which also exhibit a high defect density. (b) Cross-sectional TEM image taken along [0001] zone axis of InN. (c) Cross-sectional TEM image taken along [$1\bar{1}00$] zone axis of InN, showing multiple TD half-loops in the first ~250 nm of sample thickness. (d) Cross-sectional HRTEM image along the [$1\bar{1}00$] zone axis of InN showing the bright zone indicated at the GaN/Al_2O_3 interface, which is attributed to the nitridation pre-treatment.*

A cross-sectional HRTEM image along [$1\bar{1}00$], showing the buffer layer and the GaN/InN interface, is depicted in Fig. 5.37(a). The wavy InN/GaN interface is attributed to Volber-Weber 3D growth mode of the GaN buffer layer, which resulted to a rough GaN surface. A larger area (lower magnification) image of the structure is provided in Fig. 5.37(b), which is the cross-sectional TEM image taken along [0001]

zone axis of InN. When viewed along $[1\bar{1}00]$ zone axis (z.a) of InN, the interface of the *a*-plane InN seems relatively sharper [Fig. 5.37(c)] than the interface when viewed along [0001] z.a of InN [Fig. 5.37(b)], where the interface is clearly more distorted. Large density of threading dislocations (TDs) originates from the GaN/Al_2O_3 interface. The dislocation behavior within the *a*-plane InN layer is very similar to that observed in *c*-plane InN [19], being mostly annihilated or bent and revealing a significant TD network with many closed loops within the first ~250 nm thickness [Figs. 5.35, 5.37(b) and 5.37(c)], leading to improvement of crystal quality with increasing film thickness.

The density of α-type and partials dislocations in the InN layer is 1.4×10^{11} cm^{-2}. Although this value may be comparable with that obtained by Wang *et al*. at a distance of 200 nm away from the MBE grown *c*-plane InN/GaN interface [71], it is still one order higher than that of the state of the art *c*-plane InN with comparable thickness of 600 nm [19]. A strong correlation between the structural and transport properties of the as-grown InN layers has been identified, with charged dislocation scattering consequently proposed as the dominant transport scattering mechanism in *c*-plane InN layers [54]. Since the *a*-plane InN exhibits higher density of TDs compared to *c*-plane, the weaker electron transport properties generally observed in the *a*-plane InN films [34] can therefore be conveniently attributed to the increased density of dislocations present in the former.

Fig. 5.37(d) illustrates in detail the GaN/Al_2O_3 interface, which exhibits a characteristic bright zone attributed to AlN and oxynitride formation due to the nitridation pre-treatment. The lattice parameters of the *a*-plane InN film were measured from diffractogrammes obtained by fast fourier transform (FFT) of the cross sectional HRTEM images along the $[1\bar{1}00]$ and [0001] projections. The obtained lattice parameters $a_{InN} = 0.3527 \pm 0.0008$ nm and $c_{InN} = 0.5704 \pm 0.0030$ nm, indicate that the epilayer exhibits the relaxed InN lattice parameters. The misfit between (0002) GaN and (0002) InN planes was estimated as 9.6%.

5.11 Concluding remarks

In summary, using different buffer schemes, consisting of GaN and AlN nucleation/buffer layers, we have been able to optimise the conditions for the growth of high quality *a*-plane InN films on *r*-plane sapphire substrates. Similar to *c*-plane InN, *a*-plane InN structural and electrical properties improve with increase in growth temperature. A growth window of about 370°C – 420°C is proposed for the epitaxy of high crystalline quality *a*-plane InN without surface decomposition.

Even though all the GaN and AlN nucleation/buffer layers resulted to InN of pure *a*-plane $(11\bar{2}0)$ orientation, we observed that the InN material properties depend sensitively on the buffer layer type employed. Moreover, the initial spotty RHEED pattern observed during the growth of *a*-plane InN always improves towards becoming streaky with prolonged growth duration. GaN buffered *a*-plane InN grown under stoichiometric III/V flux ratio conditions on *r*-plane sapphire does not exhibit morphological and structural anisotropy. Structural anisotropy was always observed on the surface of *a*-plane InN film grown by using AlN nucleation layer. Despite generating structurally anisotropic in *a*-plane InN epilayer, AlN consistently demonstrates better wetting layer on Sapphire compared to GaN, leading to narrower

$(11\bar{2}0)$ RC FWHM. A GaN/AlN buffer layer resulted to a 500 nm thick *a*-plane InN film with the highest electron mobility of 630 $cm^2V^{-1}s^{-1}$, to date.

The main defects observed by cross-sectional TEM in the *a*-plane InN film are dislocations. Although the TDs originated from the GaN/sapphire interface, the density was reduced as it crosses the InN/GaN interface. Many dislocation half-loops in the GaN buffer layer and the InN region close to the interface. The density of these dislocations decreases with increasing epilayer thickness. A 500 nm thick *a*-plane InN film exhibited *a*-type dislocation density of 1.4 x 10^{11} cm^{-2}. The misfit at the InN/GaN interface was relaxed by misfit dislocation between (0002) GaN and (0002) InN planes was estimated as 9.6%.

The surface morphology, structural and electrical properties of *c*- and *a*-plane InN thin films, as a function of thickness, were also investigated and compared. All samples were grown under same conditions on *c*- and *r*-plane Al_2O_3 substrates by PA-MBE, respectively, using GaN buffer layers. The epitaxial growth of *a*-plane InN proceeded through the nucleation, growth and coalescence of 3D islands, resulting to increased surface roughness with increasing film thickness. Step-flow growth mode was maintained during the growth of c-plane films. The rms roughness determined for 2x2μm^2 AFM scans was 0.3nm and 5.9nm for 500nm thick *c*- and *a*-plane films, respectively. However, the a-plane InN films did not exhibit any structural or surface morphology anisotropy, which is typical for *a*-plane GaN. The lowest to date XRD (11-20) rocking curve (RC) FWHM of 1440 arcsec was determined for a 1000 nm *a*-plane InN film. The sheet electron density (N_s) and mobility were determined by single magnetic field Hall-effect measurements and exhibited a similar dependence on thickness for both *c*- and *a*-plane InN films. The measured N_s exhibited a minimum of ~2.10^{14} cm^{-2} for 100 nm thickness. It increased linearly with increasing thickness above 100 nm but it also increased with decreasing thickness below 100 nm. Analysis of the peculiar behaviour of the Hall data by considering the contribution of two conducting layers indicates a similar accumulation of low mobility electrons with N_s > 10^{14} cm^{-2} at the films' surface/interfacial region for InN films of both orientations. The fast increase of measured mobility with increasing InN thickness is mainly the effect of the weighted averaging of the two conductivity contributions in Hall-effect measurements. The actual electron mobility of the InN bulk increases only slightly with thickness for both orientations, as a result of improving structural quality. The mobilities of the *c*-plane films were more than three times those of the *a*-plane InN films. At the more than one order of magnitude higher dislocation density level observed for *a*-plane InN film, compared to *c*-plane InN film, the exhibition of similar sheet electron density and electron concentrations in the films of both orientation, regardless of thickness, indicates that charged dislocations are not the major source of surface electron accumulation in InN.

With the progress achieved in the heteroepitaxial growth of *a*-plane InN on sapphire substrate in this work, we may therefore conclude the growth of device quality *a*-plane InN could be possible by further optimization of the nucleation and growth on *r*-plane sapphire substrates.

References

1. P. Waltereit, O. Brandt, A. Trampert, H. T. Grahn, J. Menniger, M. Ramsteiner, M. Reiche and K. H. Ploog, *Nature* **406**, 865-868 (2000)
2. F. Bernardini and V. Fiorentino, *Phys. Rev. B*, vol. 56, pp. R10024–R10027, (1997)
3. H. Song, J. S. Kim, E. K. Kim, Y. G. Seo and S-M. Hwang, *Nanotechnology* **21**, 134026 (2010)
4. S-C Ling, T-C Wang, J-R Chen, P-C Liu, T-S Ko, B-Y Chang, T-C Lu, H-C Kuo, S-C Wang, and J-D Tsay *IEEE Photonics Technology Letters*, **21(16)**, 1130 (2009)
5. A. G. Bhuiyan, A. Hashimoto, A. Yamamoto, *J. Appl. Phys*. **94**, 2780 (2003)
6. C.-L. Wu, H.-M. Lee, C.-T. Kuo, C.-H. Chen, and S. Gwo, *Phys. Rev. Lett*. **101**, 106803 (2008)
7. D. Segev and C. G. Van de Walle, *Europhys. Lett*. **76**, 305 (2006)
8. C. G. Van de Walle and D. Segev, *J. Appl. Phys*. 101, 081704 (2007)
9. E. Dimakis, E. Iliopoulos, K. Tsagaraki, and A. Georgakilas, *Phys. Status Solidi (a)* **203**, 1686 (2006)
10. C. S. Gallinat, G. Koblmüller, Feng Wu, and J. S. Speck, *J. Appl. Phys.* **107**, 053517 (2010)
11. V. Cimalla, U. Kaiser, I. Cimalla, G. Ecke, J. Pezoldt, L. Spiess, O. Ambacher, H. Lu, W. Schaff, *Superlattices and Microstruct.* **36**, 487–495 (2004)
12. S. Watanabe, Y. Kumagai, A. Tsuyuguchi, H. Na, H. Naoi, T. Araki, and Y. Nanishi, *Phys. Status Solidi (c)* **4**, 2556– 2559 (2007)
13. F. Bechstedt, J. Furthmüller, M. Ferhat, L.K. Teles, L.M.R. Scolfaro, J.R. Leite, V.Yu. Davydov, O. Ambacher, R. Goldhahn, *Phys. Status Solidi (a)* **195**, 628 (2002)
14. X.L. Zhu, L.W. Guo, M.Z. Peng, B.H. Ge, J. Zhang, G.J. Ding, H.Q. Jia, H. Chen, J.M. Zhou, *J. Cryst. Growth* **310**, 3726–3729 (2008)
15. H. Lu, W. J. Schaff, L. F. Eastman, J. Wu, W. Walukiewicz, V. Cimalla, and O. Ambacher, *Appl. Phys. Lett*. **83**, 1136 (2003)
16. G. Shikata, S. Hirano, T. Inoue, M. Orihara, Y. Hijikata, H. Yaguchi, S. Yoshida, *J. Cryst. Growth* **301–302**, 517–520 (2007)
17. G. Koblmüller, G. D. Metcalfe, M. Wraback, F. Wu, C. S. Gallinat, and J. S. Speck, *Appl. Phys. Lett*. **94**, 091905 (2009)
18. H. Lu, W.J. Schaff, L.F. Eastman, J. Wu, W. Walukiewicz, D. Look, R.J. Molnar, *Mater. Res. Soc. Symp. Proc*. **743**, L4.10.1(2003)
19. E. Dimakis, J. Domagala, A. Delimitis, Ph. Komninou, A. Adikimenakis, E. Iliopoulos, and A. Georgakilas, *Superlattices and Microstruct*. **40**, 246 (2006)
20. L. Lymperakis and J. Neugebauer, *Phys. Rev. B* **79**, 241308(R) (2009)
21. D.S. Li, H. Chen, H.B. Yu, X.H. Zheng, Q. Huang, J.M. Zhou, *J. Cryst. Growth* **265**, 107–110 (2004)
22. T. Paskova, V. Darakchieva, P.P. Paskov, J. Birch, E. Valcheva, P.O.A. Persson, B. Arnaudov, S. Tungasmitta, B. Monemar, *J. Cryst. Growth* **281**, 55–61 (2005)
23. X. Ni, Y. Fu, Y.T. Moon, N. Biyikli and H. Morkoc, *J. Cryst. Growth* **290**, 166–170 (2006)
24. J. L. Hollander, M. J. Kappers, C. McAleese, and C. J. Humphreys, *Appl. Phys. Lett*. **92**, 101104 (2008)

25. B. Ma, W. Hu, H. Miyake, and K. Hiramatsu, *Appl. Phys. Lett*. **95**, 121910 (2009)
26. G. Koblmüller, A. Hirai, F. Wu, C. S. Gallinat, G. D. Metcalfe, H. Shen, M. Wraback, and J. S. Speck, *Appl. Phys. Lett.* **93**, 171902 (2008)
27. M. R. Laskar, A. Kadir, A.A. Rahman, A.P. Shah, N. Hatui, M.R. Gokhale and A. Bhattacharya, *J. Cryst. Growth*, **312**, 2033 (2010)
28. B. Zhang, H. Song, J. Wang, C. Jia, J. Liu, X. Xu, X. Liu, S. Yang, Q. Zhu, Z. Wang, *J. Cryst. Growth* **319**, 114 (2011)
29. J. Smalc-Koziorowska, G. Tsiakatouras, A. Lotsari, A. Georgakilas, and G. P. Dimitrakopulos, *J. Appl. Phys.* **107**, 073525 (2010)
30. J. Smalc-Koziorowska, G. P. Dimitrakopulos, S.-L. Sahonta, G. Tsiakatouras, A. Georgakilas, and Ph. Komninou, *Appl. Phys. Lett*. **93**, 021910 (2008)
31. V. Darakchieva, M.-Y. Xie, N. Franco, F. Giuliani, B. Nunes, E. Alves, C. L. Hsiao, L. C. Chen, T. Yamaguchi, Y. Takagi, K. Kawashima, and Y. Nanishi, *J. Appl. Phys.* **108**, 073529 (2010)
32. M. Moret, S. Ruffenach, O. Briot, and B. Gil, *Phys. Status Solidi A* **207**, 24 (2010)
33. K. Wang, T. Yamaguchi, A. Takeda, T. Kimura, K. Kawashima, T. Araki, and Y. Nanishi, *Phys. Status Solidi A* **207**, 1356 (2010)
34. A. O. Ajagunna, E. Iliopoulos, G. Tsakatouras, K. Tsagaraki, M. Androulidaki, and A. Georgakilas, *J. Appl. Phys*. **107**, 024506 (2010)
35. C.H. Swartz, R.P. Tompkins, N.C. Giles, T.H. Myers, H. Lu, W.J. Schaff, L.F. Eastman, *J. Crystal Growth* **269**, 29 (2004)
36. E. Dimakis, E. Iliopoulos, K. Tsagaraki, Th. Kehagias, Ph. Komninou, A. Georgakilas, *J. Appl. Phys.* **97**, 113520 (2005)
37. X. Wang and A. Yoshikawa, *Prog. Cryst. Growth Charact. Mater*. **48/49**, 42 (2004)
38. C.S. Gallinat, G. Koblmuller, J.S. Brown, S. Bernardis, J.S. Speck, *Appl.Phys.Lett*. **89**, 032109 (2006)
39. X. Wang, S. B. Che, Y. Ishitani, A. Yoshikawa, *J. Appl. Phys*. **99**, 073512 (2006)
40. G. Koblmuller, C. S. Gallinat, S. Bernardis, J. S. Speck, G. D. Chern, E. D. Readinger, H. Shen, M. Wraback, *Appl. Phys. Lett*. **89**, 071902 (2006)
41. H. Lu, W. J. Schaff, J. Hwang, H. Wu, W. Yeo, A. Pharkya, and L. Eastman, *Appl. Phys. Lett*. **77**, 2548 (2000)
42. X. Wang, S.-B. Che, Y. Ishitani, and A. Yoshikawa, Appl. Phys. Lett. **90**, 151901 (2007)
43. M. Losurdo, M. M. Giangregorio, G. Bruno, T.-H. Kim, P. Wu, S. Choi, A. Brown, F. Masia, M. Capizzi, and A. Polimeni, *Appl. Phys. Lett.* **90**, 011910 (2007)

44. E. Dimakis, E. Iliopoulos, K. Tsagaraki, and A. Georgakilas, *Appl. Phys. Lett.* **86**, 133104 (2005)
45. C. S. Gallinat, G. Koblmüller, J. S. Brown, and J. S. Speck, *J. Appl. Phys.* **102**, 064907 (2007)
46. S. Yamaguchi, M. Kariya, S. Nitta, T. Takeuchi, C. Wetzel, H. Amano, and I. Akasaki, *J. Appl. Phys*. **85**, 7682 (1999)
47. M. Higashiwaki and T. Matsui, *Jpn. J. Appl. Phys.*, Part 2 41, L540 (2002)
48. W. Liu, R. J. N. Tan, C. B. Soh, and S. J. Chua, *Appl. Phys. Lett*. **97**, 042110 (2010)
49. Th. Kehagias, A. Delimitis, and Ph. Komninou, E. Iliopoulos, E. Dimakis, and A. Georgakilas, G. Nouet, *Appl. Phys. Lett*. **86**, 151905 (2005)
50. M. A. Moram and M. E. Vickers, *Rep. Prog. Phys*. **72**, 036502 (2009)
51. B. R. Nag, *J. Cryst. Growth* **269**, 35-40 (2004)
52. V.W. L. Chin, T.L. Tansley and T. Osotchan, *J. Appl. Phys*. **75**, 7365-7372,(1994)
53. S. Vitanov, M. Nedjalkon and V. Palankovski, *NMA 2006, LNCS* **4310**, 197-204 (2007)
54. K. A. Wang, Y. Cao, J. Simon, J. Zhang, A. Mintairov, J. Merz, D. Hall, T. Kosel, and D. Jena, *Appl. Phys. Lett*. **89**, 162110 (2006)
55. I. Mahboob, T. D. Veal, L. F. J. Piper, and C. F. McConville, Hai Lu and W. J. Schaff, J. Furthmüller and F. Bechstedt, *Phys. Rev. B* **69**, 201307(R) (2004)
56. P. D. C. King, T. D. Veal, C. F. McConville, F. Fuchs, J. Furthmüller, F. Bechstedt, P. Schley, R. Goldhahn, J. Schörmann, D. J. As, K. Lischka, D. Muto, H. Naoi, Y. Nanishi, Hai Lu and W. J. Schaff, *Appl. Phys. Lett.* **91**, 092101 (2007)
57. H. Lu, W. J. Schaff, L. F. Eastman, and C. E. Stutz, *Appl. Phys. Lett*. **82**, 1736 (2003)
58. D. K. Schroder, *Semiconductor Material and Devices Characterization*, John Wiley & Sons, Inc., New Jersey, Chap.8, p. 474. (2006)
59. H. Ahn, Y.-P. Ku, C.-H. Chuang, C.-L. Pan, H.-W. Lin, Y.-L. Hong, and S. Gwo, *Appl. Phys. Lett*. **92**, 102103 (2008)
60. T. Yang , Z. Zhang, Y. Li, M. Lv, S. Song, Z. Wu, J. Yan, S. Han, *Applied Surface Science* **255**, 3544 (2009)
61. J. Wu, W. Walukiewicz, W. Shan, K. M. Yu, J. W. Ager III, S. X. Li, E. E. Haller, H. Lu and W. J. Schaff, *J. Appl. Phys*. **94**, 4457 (2003)
62. B. Monemar, P. P. Paskov and A. Kasic, *Superlattices and Microstruct*. **38,** 38 (2005)

63. V. Darakchieva, T. Hofmann, M. Schubert, B. E. Sernelius, B. Monemar, P. O. Å. Persson, F. Giuliani, E. Alves, H. Lu, and W. J. Schaff, *Appl. Phys. Lett*. **94**, 022109 (2009)

64. Y. Kumagai, A. Tsuyuguchi, H. Naoi, T. Araki, H. Na, and Y. Nanishi, *Phys. Status Solidi (b)* **243**, 1468 (2006)

65. G. Shikata, S. Hirano, T. Inoue, M. Orihara, Y. Hijikata, H. Yaguchi, and S. Yoshida, *Phys. Stat. Sol. (c)* **5**, 1808 (2008)

66. T. Kimoto, A. Itoh, and H. Matsunami, *Appl. Phys. Lett*. **66**, 3645 (1995)

67. E. Sakalauskas, H. Behmenburg, C. Hums, P Schley, G. Rossbach, C. Giesen, M. Heuken, H. Kalisch, R. H. Jansen, J. Bl¨asing, A. Dadgar, A. Krost and R. Goldhahn, *J. Phys. D: Appl. Phys*. **43**, 365102 (2010)

68. E. Sakalauskas, P. Schley, J. Räthel, T. A. Klar, R. Müller, J. Pezoldt, K. Tonisch, J. Grandal, M. A. Sánchez-García, E. Calleja, A. Vilalta-Clemente, P Ruterana, and R. Goldhahn, *Phys. Status Solidi (a)*, **207**, 1066 (2010)

69. J. Wu, W. Walukiewicz, S. X. Li, R. Armitage, J. C. Ho, E. R. Weber, E. E. Haller, H. Lu, W. J. Schaff, A. Barcz, and R. Jakiela, *Appl. Phys. Lett.* **84**, 2805 (2004)

70. E. Dimakis, E. Iliopoulos, M. Kayambaki, K. Tsagaraki, A. Kostopoulos, G. Konstantinidis, and A. Georgakilas, *J. Electron. Mater.* **36**, 373 (2007)

71. K. A. Wang, T. Kosel, and D. Jena, *Phys. Status Solidi (c)* **5**, 1811 (2008)

6 Epitaxy of cubic (002) InN, polar (0001) InN and semipolar $(10\bar{1}1)$ InN on *r*-plane $(1\bar{1}02)$ sapphire substrates

6.1 Background knowledge and importance of semipolar InN

6.2 Experimental descriptions

6.3 *In-situ* reflection high electron energy diffraction investigation

6.4 Investigation of the surface morphology

6.5 X-ray diffraction Analyses

6.6 Structural Anisotropy Behaviour Investigations

6.7 Transmission electron microscopy investigations

6.7.1 Microstructures of the *c*-plane InN layer on *r*-plane sapphire substrate

6.7.2 Microstructures of the *s*-plane InN layer on *r*-plane sapphire substrate

6.8 Investigation of the electrical properties of the films

6.9 Investigation of the optical properties of the films

7.0 Concluding remarks

6.1 Background knowledge and importance of semipolar InN

Nonpolar planes are those which are orthogonal to the (0001) *c*-plane [Fig. 3.1]. Since the polarization vector is within the growth plane, polarization effects in the growth direction are eliminated entirely [1]. On the contrary, semi-polar planes {*hkil*} have at least one of the *h,k* or *i* Miller–Bravais indices being non-zero with the *l* index also non-zero and the polarization vectors are inclined with respect to the growth direction; resulting to reduction in the strength of the vertical polarization field [Fig. 3.1]. Hence, the effects of polarization induced electric fields could also be significantly reduced also by growing III-nitrides along the semi-polar directions for optoelectronic device applications. Even though weaker polarization field may still exist in semipolar structures, which can also result to band bending, the red-shift of PL emission is expected to be much less pronounced compared to what *c*-plane oriented structures exhibit. Growth and characterisation of semipolar AlN [2-4], GaN [5-7] or even III-nitride alloys have been widely reported [8-11] as well as some applications of such semipolar materials for optoelectronic devices fabrication [12]. Various substrates, such as Si (11*h*) [13], *m*-plane sapphire [2,7], *r*-plane sapphire [3], *s*-plane ZnO [14,15] have also been employed for semipolar nitrides' growth.

Authors have reported semipolar InN of $(10\bar{1}\bar{3})$ [16] and $(11\bar{2}2)$ [17] InN orientations grown on *m*-plane sapphire by MOVPE. The synthesis of $(10\bar{1}3)$ InN on (112) $LaAlO_3$ by MOMBE, and $(10\bar{1}3)$ InN on undoped semi-insulating (110) GaAs [18] have also been published in the literatures. Fujii *et al.* have also demonstrated various PLD grown semipolar InN epilayers with orientations $(1\bar{1}03)$, $(2\bar{2}05)$, $(1\bar{1}01)$ and $(1\bar{1}05)$ InN on (113), (110), (001), and (112) YSZ (Yttria-Stabilized Zirconia) substrates, respectively [19]. However, no direct PAMBE growth of semipolar *s*-plane $(10\bar{1}1)$ InN on *r*-plane sapphire has been reported to date, except of the recent work of Hsiao *et al*. [20].

Meanwhile, no single crystal polar (0002) or cubic (002) InN growth has also been reported. Most reports described the *c*-plane InN growth on *r*-plane sapphire with mixed cubic or other wurzite InN domains [21,22]. In this chapter, the epitaxial growth of pure crystalline *s*-plane InN and *c*-plane InN on $(1\bar{1}02)$ *r*-plane sapphire by nitrogen plasma source molecular beam epitaxy (PAMBE) are examined. The role of sapphire surface nitridation and InN nucleation layer were investigated to understand the critical conditions necessary for achieving single crystalline cubic InN, semipolar *s*-plane InN and polar *c*-plane InN films.

6.2 Experimental description

Several samples consisting of approximately 500 nm thick InN films were grown by PAMBE [23] on $(1\bar{1}02)$ *r*-plane sapphire substrates. The substrates' *ex-situ* wet cleaning procedure and *in-situ* surface thermal preparation have been previously discussed in section 3.3. Where applicable, nitridation of sapphire was carried out for 15 minutes at 900°C. A two-step growth process was generally employed by growing first an InN nucleation layer at 225°C (LT-InN) prior to the main InN epilayer deposition at an average growth temperature of 440°C, except in the case of G1756 (Sample A) that employed single step growth and the InN epilayer was grown

immediately after the sapphire surface nitridation step. The sapphire surface treatment and other growth conditions of the LT-InN nucleation layers are given in Table 6.1. The method of determining the III/V flux ratio has been previously described in section 3.4. The LT-InN layers were grown either under N-rich condition, using a III/V flux ratio of 0.2 or under stoichiometric III/V flux ratio. For all samples, the main InN epilayers were grown under stoichiometric III/V flux ratio conditions. The InN growth was monitored *in-situ* by RHEED and *ex-situ* by AFM, HR-XRD, conventional cross-sectional and high resolution TEM (CTEM and HR-TEM) as well as Hall-effect measurements.

6.3 ***In-situ*** reflection high electron energy diffraction investigation

Typical RHEED patterns observed during the growth experiments are shown in Fig. 6.1. Fig. 6.1(a) is a RHEED pattern observed for the *r*-plane sapphire surface after 15 minutes of nitridation. The RHEED patterns of the final InN epilayers shown in Figs. 6.1 (b), 6.1 (d) and 6.1 (f) confirm the growth of single crystalline InN layers. Film A that was grown directly on a nitridated *r*-plane sapphire substrate, without the use of LT-InN nucleation layer (NL), manifested spotty RHEED patterns as shown in Fig. 6.1(b).

Table 6.1 *Growth conditions of the InN on r-plane sapphire samples, grown with or without the use of low temperature InN (LT-InN) nucleation layer (NL) prior to the main InN epilayer deposition under stoichiometric III/V flux ratio condition. The LT-InN layers were grown at 225°C.*

Sample Identification	***Substrate treatment***	***Nucleation layer (NL)***	***III/V flux ratio of NL***	***Epilayer T_{sub} (^{o}C)***	***Epilayer RHEED***
G1756 = A	Nitridation	-	-	450	Spotty
G1500 = B	-	20 nm LT-InN	0.20	440	Streaky
G1501 = C	Nitridation	20 nm LT-InN	0.20	440	Streaky
G1758 = D	Nitridation	20 nm LT-InN	0.20	450	Streaky
G1502 = E	Nitridation	20 nm LT-InN	~ 1.0	440	Streaky
G1508 = F	-	20 nm LT-InN	~ 1.0	440	Streaky
G1817 = G	-	25 nm LT-InN	0.70	450	Streaky

Fig. 6.1(c) shows a typical spotty RHEED pattern observed for a 20 nm thick LT-InN nucleation layer grown under N-rich conditions, such nucleation layers (NLs) were employed for the growth of samples B, C, and D [Table 6.1]. The streaky RHEED pattern of the original thermally cleaned *r*-plane sapphire surface transformed to a spotty pattern by the deposition of the LT-InN nucleation layer. It should be noted that the effective annealing of the nucleation layer that occurred while ramping up the T_{sub} to the final epilayer's growth temperature resulted to elongation of the spots and appearance of modulated streaks, indicating a smoothening of the surface. The RHEED pattern of the final InN epilayer, grown on

such a LT-InN layer is shown in Fig. 6.1(d). The streaky character of the RHEED patterns improved with the time of growth of the main epilayer. Same RHEED pattern evolution was observed in all cases for samples B, C, and D, irrespective of whether sapphire nitridation step was taken or skipped prior to the InN nucleation layer deposition.

When stoichiometric or near stoichiometric III/V flux ratio was used to grow the LT-InN nucleation layer, as for the case of samples E, F and G (Table 6.1), a spotty RHEED pattern shown in Fig. 6.1(e) evolved only after initial formation of a ring pattern. The initially formed ring pattern was observed within the first 10 seconds of the nucleation layer growth initiation, which corresponds to the deposition of approximately 4 monolayers (ML) of InN, indicating the formation of polycrystalline material. The quick change of the RHEED pattern from ring to spotty is attributed to the fast transformation (or overgrowth) of the non-oriented nuclei to (by) oriented InN islands with increasing growth time. The spotty RHEED patterns transformed rapidly to streaky ones at the growth initiation of the main InN epilayer [Fig. 6.1(f)] without any evidence of streak distortion in any of the azimuths, except in the case of sample F where nitrogen surface treatment of sapphire was skipped.

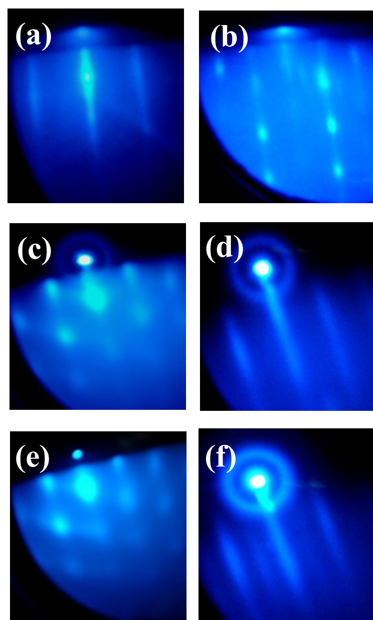

Figure 6.1 *Typical RHEED patterns, observed in the experiments of InN growth on r-plane sapphire substrates for, (a) the r-plane sapphire surface after 15 minutes nitridation, (b) the final surface of sample A: InN directly grown on r-plane sapphire under stoichiometric III/V flux ratio but without LT-InN nucleation layer, (c) a LT-InN nucleation layer grown under N-rich conditions, (d) the final InN epilayer grown on a LT-InN nucleation layer grown under N-rich conditions (Samples B, C & D). (e) a LT-InN nucleation layer grown under stoichiometric III/V flux ratio. (f) the final InN epilayer grown on a LT-InN nucleation layer grown under stoichiometric III/V flux ratio (Samples E, F & G).*

It is also crucial to mention that the RHEED patterns of the final InN epilayers, whenever LT-InN was employed, were streaky and deviated from the commonly observed spotty pattern for InN grown on *r*-plane sapphire. The two-step growth method employed using LT-InN with $F_{In}/F_N \leq 1$ seems to accommodate effectively the lattice mismatch and provide high density of nucleation centers that promote lateral growth of the main epilayer.

6.4 X-ray diffraction Analyses

The crystallinity and orientation of the InN epilayers were investigated by using HR-XRD *θ-2θ* scans. Different crystallographic orientations were determined, depending on the conditions of the InN nucleation on *r*-plane sapphire. For the sample A, consisting of InN grown at T_{sub} = 450°C, directly on nitridated sapphire, the HR-XRD *θ-2θ* scans exhibited only the (002) and (004) peaks of the zincblende structure together with the $(01\bar{1}2)$,$(02\bar{2}4)$ and $(03\bar{3}6)$ peaks of *r*-plane sapphire, as shown in Fig. 6.2. This result is similar to the reported cubic (200) InN growth by Cimalla *et al.* with a similar growth process, except of not using sapphire nitridation [21]. Nitridation of sapphire surface for 20 and 10 minutes prior to high temperature InN growth has been reported by Kumagai *et al.* to yield single crystal *a*-plane InN$(11\bar{2}0)$ and InN with mixed hexagonal $(11\bar{2}0)$ and cubic (002) domains [24], respectively. However, the X-ray diffraction investigation of sample A did not exhibit any trace of hexagonal InN domains [Fig. 6.2], making this the first realization of a single crystal cubic InN film on *r*-plane sapphire substrate.

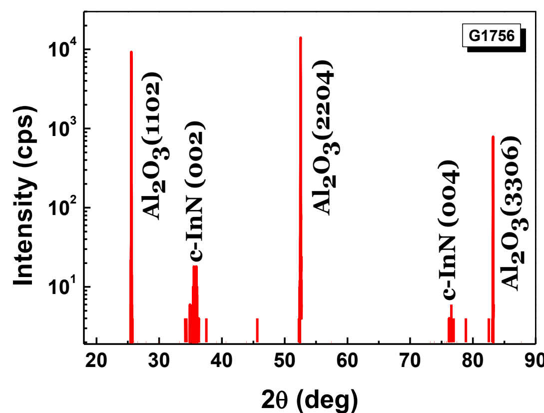

Figure 6.2 *HR-XRD (θ-2θ) scan of InN layer grown at 450°C directly on nitridated r-plane sapphire substrate (sample A). Only the cubic (002) InN and (004) InN reflections were observed aside from the peaks corresponding to the sapphire substrate.*

Samples B and C exhibited similar HR-XRD (*θ-2θ*) results, as shown in Fig. 6.3(a), indicating the mixture of domains of polar (0001) and non-polar $(10\bar{1}1)$ orientation, with preferred orientation being the (0001). The *c*-axis of the predominant hexagonal InN structure is perpendicular to the substrate's surface. The reflection observed at 38.23 degree is attributed to the Aluminium sample holder of the diffractometer. It was observed that sapphire surface nitridation prior to InN nucleation did not play a significant role in the determination of the preferred orientation of the films. For sample D that shares similar LT-InN nucleation growth conditions with B and C [see Table 6.1], single crystalline polar *c*-plane InN film was grown according to the XRD *θ-2θ* scan profile shown in Fig. 6.3(b). This is attributed to the higher T_{sub} (450°C) employed for the growth of the main epilayer, indicating that the higher growth temperature should favour the expansion of (0001) islands and overgrowth of any $(10\bar{1}1)$ islands that may occurred at the early stages of growth. This confirmed that under favourable conditions, single-crystal (0001) InN that seems to be more stable on *c*-plane sapphire substrate, can also be deposited on *r*-plane sapphire.

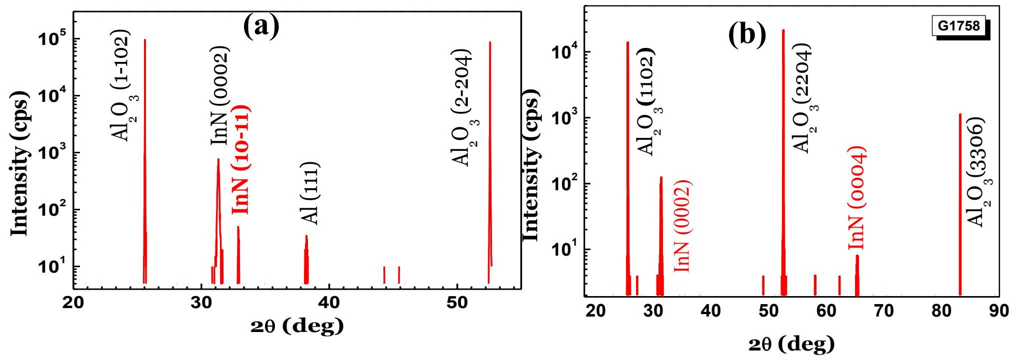

Figure 6.3 *HR-XRD (θ-2θ) scan for InN samples grown, using LT-InN NLs deposited under N-rich conditions (III/V flux ratio of 0.2) (a) Sample B that exhibited a dominant polar (0002) InN orientation with weak hexagonal semipolar* $(10\bar{1}1)$ *InN. A similar result was also obtained for sample C. The reflection at 38.23 degree is attributed to the Aluminium sample holder of the diffractometer (b) Sample D grown with a similar LT-InN NL , but at higher epilayer growth temperature of* $450^{o}C$*.*

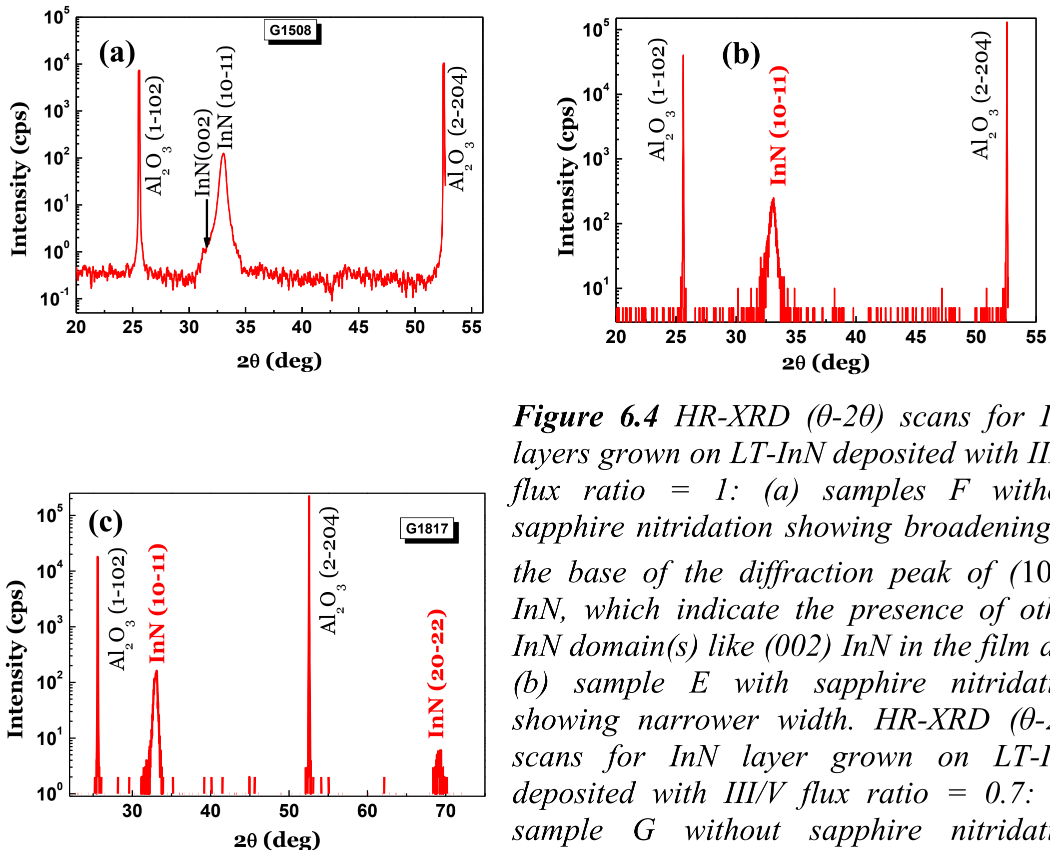

Figure 6.4 *HR-XRD (θ-2θ) scans for InN layers grown on LT-InN deposited with III/V flux ratio = 1: (a) samples F without sapphire nitridation showing broadening at the base of the diffraction peak of* $(10\bar{1}1)$ *InN, which indicate the presence of other InN domain(s) like (002) InN in the film and (b) sample E with sapphire nitridation showing narrower width. HR-XRD (θ-2θ) scans for InN layer grown on LT-InN deposited with III/V flux ratio = 0.7: (c) sample G without sapphire nitridation showing a profile similar to that shown in (b) for sample E, indicating that both sample E and G consist of pure semipolar* $(10\bar{1}1)$ *InN.*

Samples E and F, which employed LT-InN nucleation layers grown under stoichiometric III/V flux ratio conditions [see Table 6.1], also exhibited similar HR-XRD (θ-2θ) results [Figs. 6.4(a) and 6.4(b)], except of the increased broadening of the $(10\bar{1}1)$ InN peak for sample F [Fig. 6.4(a)]. The broadening in (θ-2θ) scan mode is well known to be mainly caused by lattice constant non-uniformity or strain. In this particular case, the broadening extends over the region of cubic (002) InN reflection [identified by black arrow in Fig 6.4(a)], indicating the mixing of some cubic domains in the bulk of the sample F. The narrower width of sample E [Fig. 6.4(b)] indicates that the use of sapphire nitridation [see Table 6.1] assists in homogeneous nucleation of $(10\bar{1}1)$ InN crystallites. Although sample G was grown on an unnitridated sapphire surface (in a similar way to sample F) and used a LT-InN nucleation layer grown under slightly N-rich conditions (III/V = 0.7) [see Table 6.1], it surprisingly exhibited slightly improved $(10\bar{1}1)$ InN peak compared to sample E [Fig. 6.4(b)] that employed nitridated sapphire without the broadening observed for sample F [Fig. 6.4 (a)], as shown in Fig. 6.4(c). Despite the fact that film sample G did not employ sapphire surface nitridation, the InN nucleation at slightly N-rich growth conditions apparently assists the domination of the $(10\bar{1}1)$ InN orientation. In conclusion, the X-ray diffraction investigations indicate that hexagonal semipolar $(10\bar{1}1)$ InN can be grown on *r*-plane sapphire by employing a LT-InN nucleation layer grown under stoichiometric or slightly N-rich III/V flux ratio conditions.

Table 6.2 *Overall results from the investigated cubic InN and hexagonal c- and s-plane InN films grown on r-plane sapphire. "InN orientation" is the film orientation(s) identified by the HRXRD θ-2θ measurements, "Roughness" is the 5 x 5 μm² AFM scans rms surface roughness while "n_d" and "μ" are the apparent electron concentration and mobility determined from the Hall-effect measurements of the InN films, respectively.*

Sample Identity	InN Film orientation	5x5 rms Roughness (nm)	n_d (x 10^{19}cm^{-3})	μ (cm^2/V.s)
A	(002)	8.30	1.90	539
B	(0002), $(10\bar{1}1)$	3.13	3.58	382
C	(0002), $(10\bar{1}1)$	1.83	2.86	469
D	(0002)	4.52	1.67	868
E	$(10\bar{1}1)$	2.59	3.26	364
F	$(10\bar{1}1)$, (002)	3.34	3.56	359
G	$(10\bar{1}1)$	8.73	7.28	358

Even though some other groups have reported the growth of single crystalline *a*-plane $(11\bar{2}0)$ InN directly on $(1\bar{1}02)$ *r*-plane Al_2O_3 by using a nitridation step to suppress growth along other orientation(s) [17,24,25], neither the direct growth of InN on nitridated *r*-plane sapphire surface [Fig. 6.2] nor the use of LT-InN nucleation layer prior to InN epilayer growth [Figs. 6.3 and 6.4] produced *a*-plane InN in this

work. Nevertheless, our results show that single crystal cubic (002) InN could be successfully grown on *r*-plane sapphire by using a one step growth process while polar (0001) or semipolar $(10\bar{1}1)$ InN could be realized on the same substrate by using a two-step growth process comprising of the use of N-rich or near stoichiometric LT-InN nucleation layer, respectively, prior to the main InN epilayer growth.

For the *c*-InN layer, the (002) RC FWHM was evaluated as 102 arcmin. The $(10\bar{1}1)$ rocking curve FWHM of the *s*-plane InN was 70 arcmin while a FWHM of 84 arcmin was obtained for the (0002) RC of the *c*-plane InN sample. The large HR-XRD RC FWHM values correspond to high crystalline mosaicity in the InN epilayers.

6.5 Investigation of the surface morphology

The surface morphologies of the InN films were investigated by both FE-SEM and AFM. Before the observations, all samples were dipped in a HCl solution to ensure that their surfaces were free of any metallic In accumulation. The SEM plan view micrographs of the samples are shown in Fig. 6.5. Quite distinctive and growth condition dependent surface morphology features are revealed for all the InN samples. Sample A shown in Fig. 6.5(a) appears to consist of domains separated by deep trenches aligned mainly along two perpendicular directions. The samples grown using similar LT-InN growth conditions exhibited similar surface morphology, irrespective of whether the sapphire surface was nitrogen treated or not. Hence, only a representative FE-SEM image for each set is shown in Figs. 6.5(b) - (c). A uniform surface morphology was obtained for samples with LT-InN grown under N-rich conditions, as in the cases of samples B, C, and D [Fig. 6.5(b)] while few micro-holes characterised the surface morphology of samples E and F [Fig. 6.5(c)] that employed LT-InN nucleation layer grown under stoichiometric III/V flux ratio. The obtained FE-SEM image of Sample G, with nucleation layer grown with III/V = 0.7 differs significantly in morphology, compared to other samples, exhibiting a very rough surface characteristic of 3D islands growth and coalescence [Fig. 6.5(d)].

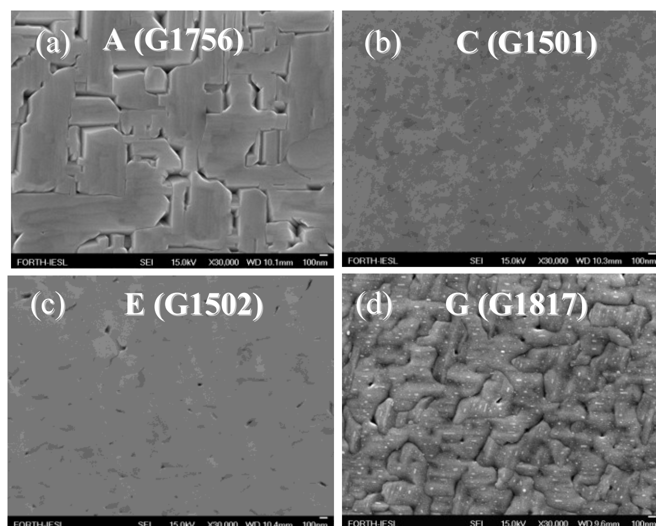

Figure 6.5 *Representative plan-view FE-SEM micrographs of InN layers grown on r-plane sapphire substrates with different nucleation layers: (a) without LT-InN nucleation layers – single step growth as in the case of sample A (b) with LT-InN grown under III/V flux ratio of 0.2 as in the case of samples B, C and D (c) with LT-InN grown under stoichiometric III/V flux ratio as in the case of samples E and F (d) with LT-InN grown under III/V flux ratio of 0.7 as in the case of sample G.*

The 5 x 5 μm^2 AFM micrographs, showing the surface topography of the films at high resolution, are shown in Fig. 6.6. Somewhat distinctive features were observed

even in cases where FE-SEM revealed similar features. All the films exhibited rough surface morphology and it is obvious that the typical step-flow growth commonly observed for InN on MOVPE GaN (0001) pseudo-substrates is not manifested by any of the films despite the streaky RHEED patterns observed for most of them. The rms surface roughness was significantly higher compared to *c*-plane InN grown on GaN/sapphire (0001) pseudo-substrates, which exhibited rms surface roughness less than 1 nm [Section 4.3]. Similar surface morphology was observed by both FE-SEM and AFM for sample A as shown in Figs. 6.5(a) and 6.6(a), respectively. In the case of samples B and C, grown without and with sapphire surface nitridation [Table 6.1], the AFM revealed same surface morphology as shown in Figs. 6.6(b) and 6.6(c); indicating that the nitridation of the sapphire substrate has no significant effect at least when growth is initiated by the deposition of a LT-InN nucleation layer at extremely N-rich conditions. However, sample D [Figs. 6.6(d)] did not exhibit a surface morphology similar to that of samples B and C [Figs. 6.6(b) and 6.6(c)]. The main difference in the growth of sample D, compared to samples C and D, is the higher growth temperature used for sample D [Table 6.1]. This indicates that the higher growth temperature significantly influenced the growth evolution of sample D; leading to the exhibition of larger surface grains [Fig. 6.6(d)].

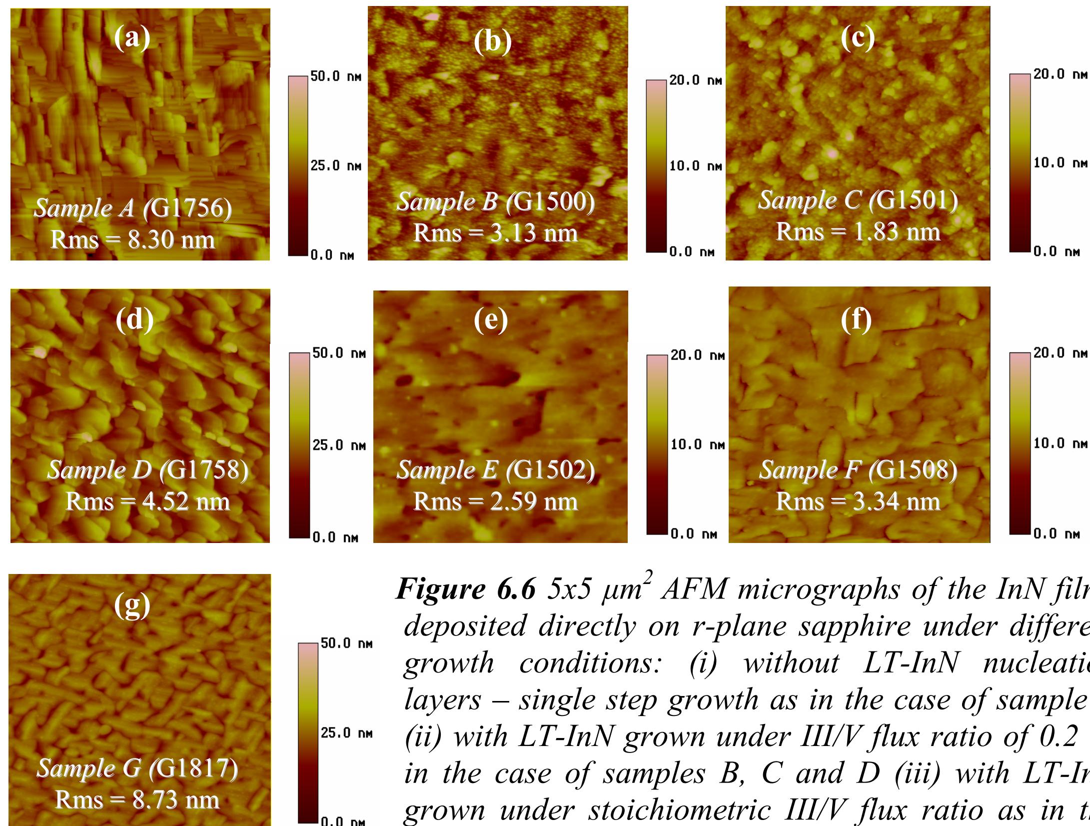

Figure 6.6 *5x5 μm² AFM micrographs of the InN films deposited directly on r-plane sapphire under different growth conditions: (i) without LT-InN nucleation layers – single step growth as in the case of sample A (ii) with LT-InN grown under III/V flux ratio of 0.2 as in the case of samples B, C and D (iii) with LT-InN grown under stoichiometric III/V flux ratio as in the case of samples E and F (iv) with LT-InN grown under III/V flux ratio of 0.7 as in the case of sample G. All samples manifested distinctive surface morphologies.*

Figs. 6.6(e) and 6.6(f) show the surface morphology of samples E and F, respectively. The only difference in these samples is the absence of sapphire nitridation in the case of sample F [Fig. 6.6(f)]. The observed difference in the surface morphology of the two samples indicates that sapphire nitridation affects the growth when the LT-InN nucleation layer is grown under stoichiometric conditions. Sample

G, with LT-InN nucleation layer grown under slightly N-rich conditions, exhibited significant roughness and features characteristic of 3D islands growth.

According to the determined 5 x 5 μm^2 AFM rms surface roughness of the InN films given in Table 6.2, the higher rms roughness of sample A is expected because of its spotty RHEED pattern [Fig. 6.1(b)]. However, in spite of the streaky RHEED pattern obtained for sample G, it exhibited the highest rms roughness of 8.73 nm, which is attributed to the higher growth temperature employed for the epilayer, especially in comparison to samples E and F grown under similar conditions. The same higher growth temperature is responsible for the observed high rms surface roughness evaluated for sample D, compared to samples B and C [Table 6.1]. In general, the AFM and FE-SEM characterisation results indicate that the surface morphology of the InN layer directly grown on *r*-plane sapphire is dependent on the nucleation growth conditions and both III/V flux ratio and growth temperature play more important role than the effect of sapphire substrate surface nitridation.

6.6 Transmission electron microscopy investigations

6.6.1 Microstructure of the *c*-plane InN layer on *r*-plane sapphire substrate

Further investigation of the 500 nm thick film samples C and F were carried out by collaborators (Prof. G. P. Dimitrakopulos and Prof. Th. Kehagias) from the Physics department of Aristotle University of Thessaloniki, using CTEM and HR-TEM to study their microstructure. For sample C, the SAED pattern along the $[11\bar{2}0]$ zone axis of sapphire as obtained from the region of the film/substrate interface is shown in Fig. 6.7(a). The SAED pattern is aligned with the growth direction. It is clear from the SAED pattern that the film exhibits significantly more distortion close to the interface with multiple weaker reflections appearing. As already inferred from the XRD, the figure also confirmed (0002) as the predominant InN phase in the film. A second phase close to the interface is cubic InN, possibly due to cubic pockets of $(\bar{1}\bar{1}\bar{1})$ sphalerite InN viewed along $[01\bar{1}]$, as shown by the magenta three indices in Fig. 6.7(a). Measurements of the lattice parameters from SAED by using sapphire as reference revealed that close to the interface, the hexagonal InN lattice parameters are a = 0.3579 nm and c = 0.5719 nm while 0.5106 nm was determined for a in the cubic InN. Only InN material with (0002) orientation was found towards the top of the film and the lattice constants a and c were estimated as 0.3603 nm and 0.5791 nm, respectively.

The bright-field cross-sectional TEM image along the $[11\bar{2}0]$ zone axis of sapphire is shown in Fig. 6.7(b). The CTEM image clearly shows the film's dislocation structure. The improvement in the crystal quality of the (0002) InN as growth thickness increases is attributed to the overgrowth of different orientation crystalline domains. The dislocation density was estimated in the order of ~ 10^{11} cm^{-2}, which is higher, compared to (0001) InN films grown on GaN pseudo-template [26].

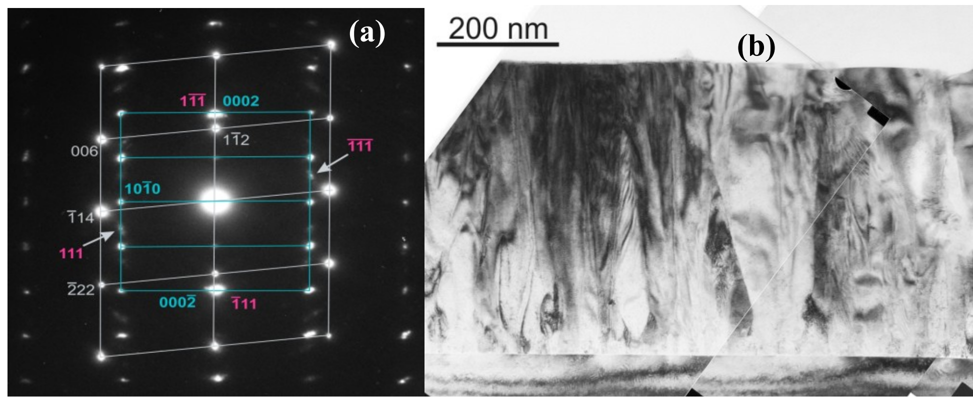

Fig. 6.7 *(a) SAED pattern obtained from the region of the film/substrate interface along the $[11\bar{2}0]$ zone axis of sapphire. The SAED pattern is aligned with the growth direction. White lines and three indices denote sapphire. Blue lines and Miller-Bravais indices denote (0002) wurtzite InN viewed along $[1\bar{2}10]$. Magenta three indices denote $(1\bar{1}\bar{1})$ zincblende InN viewed along $[01\bar{1}]$. (b) Bright-field cross-sectional TEM image along the $[11\bar{2}0]$ zone axis of sapphire, showing the film's dislocation structure.*

6.6.2 Microstructure of the *s*-plane InN layer on *r*-plane sapphire substrate

Fig. 6.8(a) is a HRTEM image for the 500 nm *s*-plane InN film F taken along the $[20\bar{2}\bar{1}]_{sapph.}$ zone axis, and with InN viewed along $[\bar{1}\bar{1}20]_{InN}$. The angle 61° the *c*-axis forms with the interface confirms the $(1\bar{1}01)$ orientation of the epilayer. However, the epilayer is too heavily faulted, making the Fast Fourier Transform (FFT) to give a very streaky pattern (inset). The spacing between the streaks in the FFT gives the *d*-spacing of $(1\bar{1}00)$ planes as 0.301 nm which is equal to $\frac{a\sqrt{3}}{2}$, where α is the lattice constant of InN and was measured as 0.348 nm. The SFs introduce local transformations from the …ABAB… stacking towards …ABC… stacking, suggesting the presence of wurtzite hexagonal and zincblende cubic mixtures in the epilayer. The arrows indicate sapphire protrusions inside the InN epilayer. The protrusion is more clearly shown in Fig. 6.8(b).

Fig. 6.9(a) is a HRTEM image along $[0\bar{2}2\bar{1}]_{sap}$ zone axis. Sapphire protrusions are also denoted near the InN-sapphire interface. Two semipolar variants are present in the sample. The two variants exhibit distinct contrast. One variant is projected along $[\bar{1}\bar{1}20]_{InN}$ and the other along $[\bar{2}113]_{InN}$. The two variants give distinct contrast since along the $[\bar{1}\bar{1}20]_{InN}$ projection the *c*-axis is edge-on and the region is manifested by multiple stacking faults (SFs). SFs exist along two orientations at ~70.5^{o} angle. This could be possible if the SFs were on two crystallographically equivalent {111} planes of cubic InN viewed along $[110]_{InN}$. This is further confirmed from angle measurement on the FFT [Fig. 6.9(b)], where the 3-indices correspond to cubic InN and 4-indices denote sapphire. Similar *s*-plane InN structure and image have been reported by Darakchieva *et al.* [27]. In Fig. 6.9(c) a

large nanocrystal is denoted with dotted line and a sapphire island is also indicated at its base.

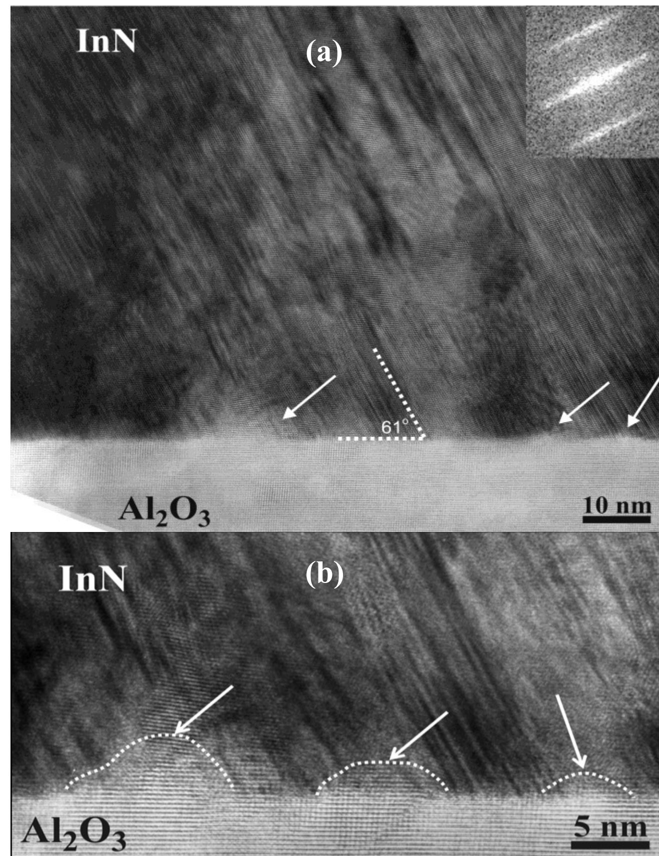

Figure 6.8 *HRTEM image along the* $[20\bar{2}\bar{1}]_{sapph.}$ */* $[\bar{1}\bar{1}20]_{InN}$ *zone axis. The angle between the interface and the c-axis is 61°, indicating that the InN is* $(1\bar{1}01)$ *semipolar. The inset is an FFT diffractogram of the InN layer. The high density of SFs results to a streaky FFT. The white arrows denote sapphire protrusions inside the InN epilayer. (b) The enlarged image of the interface showing the sapphire protrusions more clearly.*

Figure 6.10(a) is a HRTEM image of the InN/sapphire interface. The InN is hexagonal viewed along $[\bar{1}\bar{1}20]$. Figure 6.10(b) is the corresponding lattice strain map obtained by geometrical phase analysis using the $\boldsymbol{g}$ $10\bar{1}4_{sapph.}/0002_{InN}$ spatial periodicities. From this, the strain of the *s*-plane InN film was measured as 12.6% ± 1.5% and the *c* lattice parameter of InN was determined as 0.574 nm ± 0.008 nm from the measured lattice strain.

It has been reported that the preferred orientation is determined by a competition between two thermodynamical parameters; the surface free energy and the strain energy. Rauschenbach and J. W. Gerlach [28] argued for film materials that an orientation corresponding to that with the lowest surface energy is the preferred at small thicknesses. On the other hand, strain energy becomes larger than the surface energy at larger film thicknesses due to the fact that strain energy in the film increases with the thickness while surface energy does not vary with the film thickness. Due to the foregoing, it is reasonable that the mixtures of cubic and hexagonal InN domains characterised all the interfaces of the respective films, irrespective of the nucleation condition, since surface energy of InN and sapphire is expected to be same and dominate in all cases during the initial growth period. The InN different nucleation growth conditions or method employed; whether one step or two steps, should affect the amount of inherent strain in the epilayer. These different conditions are therefore believed to lead to different strain energies that principally determine the epilayer preferred orientation as InN thickness increases.

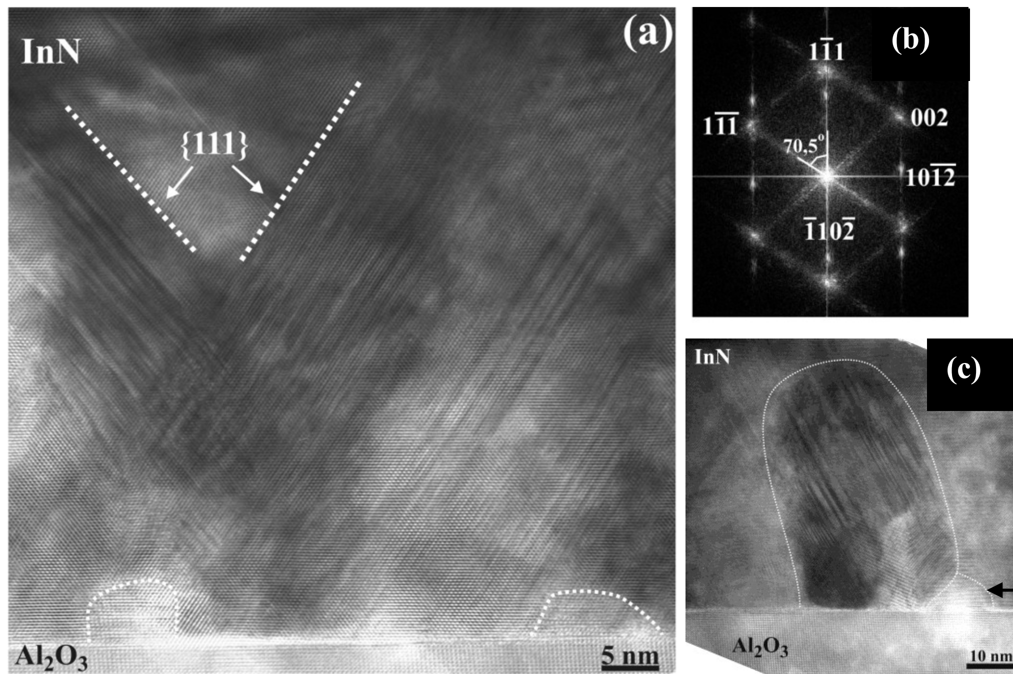

Figure 6.9 *(a) HRTEM image of a cubic region of the InN epilayer existing in-between the two variants of semipolar domain. The {111} planes are denoted. Sapphire protrusions are also denoted. (b) FFT diffractogram of (a) where three-indices denote cubic InN and 4-index system is used for the sapphire. (c) HRTEM image of an InN nanocrystal containing both hexagonal and cubic InN as well as a sapphire protrusion denoted by an arrow in the base of the nanocrystal.*

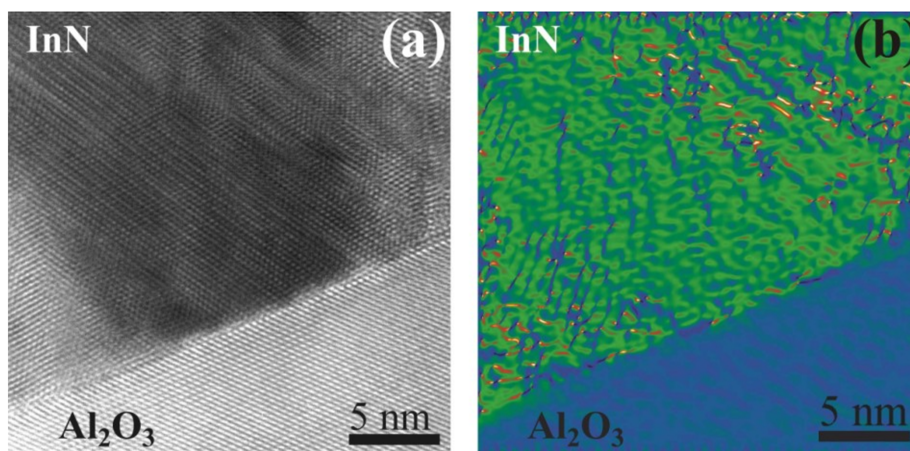

Figure 6.10 *(a) HRTEM image along* $[20\bar{2}\bar{1}]_{sap}$ *zone axis from the InN/sapphire interface. (b) Corresponding* $(10\bar{1}4)_{sapph.}/(0002)_{InN}$ *lattice strain map obtain by GPA using a g/2 mask size.*

Evidence obtained from the RHEED and TEM studies of these InN films has confirmed that the degree of InN deposit orientations on *r*-plane sapphire improve as deposition proceeds. Since growth process is often associated with the development of a preferred orientation or crystalline texture [29], we also believe that the observed improvement in the *c*- and *s*-plane samples could be attributed to the possible rotation

of individual nuclei by several degrees as nuclei size increases and gradual increase in the overall alignment of the nuclei as coalescence occurs [30,31]. However, Jacobs *et al.* have reported that such coalescence of nuclei may cause the grain boundary formed at the junction to migrate out of the composite island and consequently convert the orientation of one of the islands to that of the other [32], which may explain, for example, why two semipolar variants co-exist in the *s*-plane film.

Besides grain boundaries that mainly show up at the InN/sapphire interface, BSFs are the dominant defects observed in the *s*-plane InN films. Study of the energetic and electronic structure of stacking faults in AlN, GaN and InN has led to the discovery that BSFs electrically and optically affect non-polar nitride films and detrimental to their optoelectronic device applications [33-35]. Luminescence has already been observed to originate from stacking faults in gallium nitride [36]. BSFs results in conductivity anisotropy in the directions parallel and perpendicular to the *c*-axis [37]. Bernardini *et al.* have also attributed internal electric field to SF-terminated internal polarization along the [0001] axis, which creates a charge accumulation at the SF interfaces, and consequently establishes an electric field in highly polar material [38]. For terahertz (THz) applications, however, the SF-related internal electric fields can be beneficial since it enhances THz generation in nonpolar or semipolar semiconductors where all or a projection of the [0001] axis lays in-plane and such enhanced THz generation due to SF-related in-plane electric fields has recently been observed in *m*-plane GaN [39], indicating that the existence of high density SFs in the *s*-plane InN film may find applications in THz emission.

6.7 Investigation of the electrical properties of the films

The electrical properties of the different orientation films were investigated by Hall-effect measurements at 300K and the results are given in Table 6.2. All the InN on *r*-plane sapphire films exhibited electron degeneracy typical of InN. The *s*-plane films generally exhibited the lowest electron mobility and highest carrier density, compared to the cubic and polar *c*-plane films, which are attributed to the very high density of SFs in the films, as previously observed for sample F by TEM. However, the measured Hall mobilities for the semipolar films are comparable to *a*-plane InN film of similar thickness grown on *r*-plane sapphire, using GaN nucleation layer [40]. In spite of the inferior crystalline quality of Film D, which was determined to be pure (0002) InN by X-ray diffraction, it exhibited high Hall mobility of 868 cm^2/Vs and the lowest electron density of 1.67×10^{19} cm^{-3}. The mobility was however drastically reduced to half when InN with preferred (0002) growth orientation co-exist with weak semipolar $(10\bar{1}1)$ domain as cases of samples B and C [Table 6.2]. The single crystalline cubic (002) InN film A demonstrated the second best transport properties as shown in Table 6.2.

6.8 Investigation of the optical properties of the films

The results of low temperature (20K) PL measurements on the samples are shown in Fig. 6.11. Single PL peaks were exhibited by all the films except the *s*-plane InN sample with two peaks at 0.621 and 0.689 eV. This may be related to the presence of high density of stacking fault in the hexagonal *s*-plane film [Fig. 6.8(a)]. The *c*-InN photon energy peak occurred at 0.689 eV. The films with single-crystal (0001) orientations or preferred (0001) orientation, exhibited single PL peaks at 0.673 and 0.661 eV, respectively.

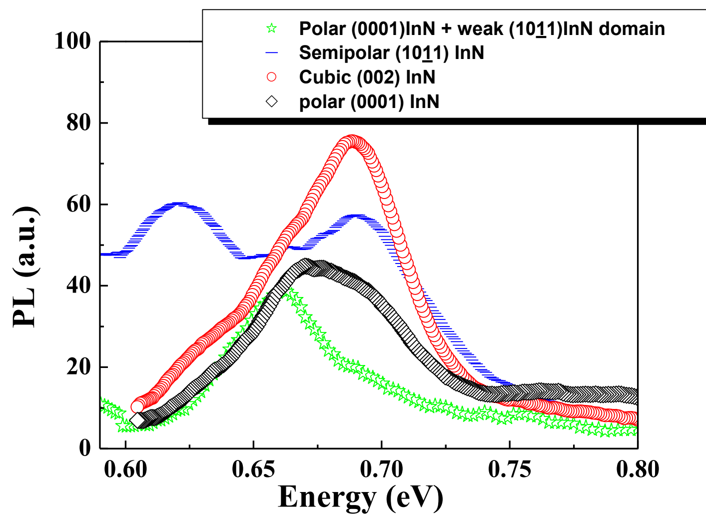

Figure 6.11 *PL spectra of the InN films of different orientations grown on r-plane sapphire. The PL was performed at 20K.*

6.9 Concluding remarks

The direct heteroepitaxial growth by plasma-assisted molecular beam epitaxy (PAMBE) and the properties of InN films on *r*-plane $(1\bar{1}02)$ Al_2O_3 substrates have been investigated. The possibility of nucleating cubic InN and hexagonal InN of *s*- and *c*-plane orientations on *r*-plane Al_2O_3 is demonstrated. X-ray diffraction studies revealed that the crystallographic orientation of InN epilayers on *r*-plane sapphire depends strongly on the used III/V flux ratio and substrate temperature for InN nucleation. Single crystal cubic (002) InN could be grown on *r*-plane sapphire by using a one step growth process, while polar (0001) or semipolar $(10\bar{1}1)$ InN could be realized on the same substrate by using a two-step growth process comprising of the use of an InN layer grown at low temperature under N-rich or near stoichiometric III/V flux ratio conditions, respectively, prior to the main InN epilayer growth. None of the InN nucleation growth conditions resulted to *a*-plane InN on *r*-plane sapphire. Neither did the sapphire substrates' surface nitridation treatment for 15 minute, prior to InN deposition, yielded *a*-plane InN. The microstructure of the *r*-plane sapphire surface (microfacets, roughness) may be also affected by the growth conditions and alter the preferential orientation of nucleated InN 3D islands. Moreover, none of the investigated films exhibited the typical atomically smooth step-flow surface morphology observed for InN (0001) grown on GaN/sapphire (0001) pseudo-substrates. Rough surface morphologies generally characterised the films due to the 3D growth mode, which was followed at least at the early stages of growth. Evidence obtained from the RHEED and TEM studies of the InN films confirmed that the degree of orientations of InN on *r*-plane sapphire improves as growth proceeds. The *s*-plane layers exhibit high density of SFs that resulted to poorer electrical properties compared to *c*-plane films. The cubic InN and the hexagonal *c*-plane and *s*-plane films exhibited Hall mobility of 539, 868 and 364 cm^2/Vs with corresponding electron carrier density of 1.90×10^{19}, 1.67×10^{19} and 3.26×10^{19} cm^{-3}, respectively.

References

1. L. Zhou, R. Chandrasekaran, T.D. Moustakas, and D.J. Smith, *J. Cryst. Growth* **310**, 2981 (2008)
2. L. Lahourcade, E. Bellet-Amalric, E. Monroy, M. Abouzaid and P. Ruterana, *Appl. Phys. Lett.* **90**, 131909 (2007)
3. R. Chandrasekaran, A. S. Ozcan, D. Deniz, K. F. Ludwig, and T. D. Moustakas, *Phys. Status Solidi (c)* **4**, 5 (2007)
4. K. Ueno, A. Kobayashi, J. Ohta, H. Fujioka, H. Amanai, S. Nagao, and H. Horie, *Phys. Status Solidi RRL* **3**, 58 (2009)
5. R. Ravash, J. Blaesing, A. Dadgar, and A. Krost, *Appl. Phys. Lett*. **97**, 142102 (2010)
6. N. Sawaki, T. Hikosaka, N. Koide, S. Tanaka, Y. Honda, and M. Yamaguchi, *J. Cryst. Growth* **311**, 2867 (2009)
7. P. Vennéguès, Z. Bougrioua, and T. Guehne, *Jpn. J. Appl. Phys*., 46,7A (2007)
8. K. Ueno, A. Kobayashi, J. Ohta, and H. Fujioka, *Phys. Status Solidi (a)* **207**, 2149 (2010)
9. S. Kamiyama, A. Honshio, T. Kitano, M. Iwaya, H. Amano, I. Akasaki, H. Kinoshita, and H. Shiomi, *Phys. Status Solidi (c)* **2**, 2121 (2005)
10. A. Chakraborty, T. J. Baker, B. A. Haskell, F. Wu, J. S. Speck, S. P. DenBaars, S. Nakamura, and U. K. Mishra, *Jpn. J. Appl. Phys., Part 2* **44**, L154 (2005)
11. M. Funato, M. Ueda, Y. Kawakami, Y. Narukawa, T. Kosugi, M. Takahashi, and T. Mukai, *Jpn. J. Appl. Phys*., Part 2 **45**, L659 (2006)
12. Guhne, T. DeMierry, P. Nemoz, M. Beraudo, E. Chenot, S. Nataf, G., *Electronics Letters*, **44**, 231 (2008)
13. R. Ravash, J. Blaesing, A. Dadgar, and A. Krost, *Appl. Phys. Lett.* **97**, 142102 (2010)
14. K. Ueno, A. Kobayashi, J. Ohta, H. Fujioka, H. Amanai, S. Nagao, and H. Horie, *Phys. Status Solidi RRL* **3**, 58 (2009)
15. K. Ueno, A. Kobayashi, J. Ohta, and H. Fujioka, *Phys. Status Solidi (a)* **207**, 2149 (2010)
16. Dinh, D. V., Pristovsek, M., Kremzow, R. and Kneissl, M, *Phys. Status Solidi RRL*, **4**, 127 (2010)
17. M. Moret, S. Ruffenach, O. Briot and B. Gil, *Phys. Status Solidi (a)* **207**, 24 (2010)
18. H. Murakami, H.C. Cho, M. Suematsu, R. Togashi, Y. Kumagai, R. Toba, A. Koukitu, *J. Cryst. Growth*, doi:10.1016/j.jcrysgro.2010.10.027
19. T. Fujii, A. Kobayashi, K. Shimomoto, J. Ohta, M. Oshima, and H. Fujioka, *Jpn. J. Appl. Phys*. **49**, 080204 (2010)
20. C. L. Hsiao, T. W. Liu, C. T. Wu, H. C. Hsu, G. M. Hsu, L. C. Chen, W. Y. Shiao, C. C. Yang, A. Gällström, P. O. Holtz, C. C. Chen, and K. H. Chen, *Appl. Phys. Lett*. **92**, 111914 (2008)
21. V. Cimalla, U. Kaiser, I. Cimalla, G. Ecke, J. Pezoldt, L. Spiess, O. Ambacher, H. Lub, W. Schaff, *Superlattices and Microstruct*. **36**, 487 (2004)
22. S. Watanabe, Y. Kumagai, A. Tsuyuguchi, H. Na, H. Naoi, T. Araki, and Y. Nanishi, *Phys. Status Solidi (c)* **4**, 2556 (2007).
23. E. Iliopoulos, A. Adikimenakis, E. Dimakis, K. Tsagaraki, G. Konstantinidis, A. Georgakilas, J. Crystal Growth **278,** 426 (2005).

24. Y. Kumagai, A. Tsuyuguchi, H. Naoi, T. Araki, H. Na, and Y. Nanishi, *Phys. Status Solidi (b)* **243**, 1468 (2006)
25. X.L. Zhu, L.W. Guo, M.Z. Peng, B.H. Ge, J. Zhang, G.J. Ding, H.Q. Jia, H. Chen, J.M. Zhou, *J. Cryst. Growth* **310**, 3726 (2008).
26. A. Georgakilas in "CAS 2008 PROCEEDINGS" pp 43 (IEEE, 2008).
27. V. Darakchieva, M.-Y. Xie, N. Franco, F. Giuliani, B. Nunes, E. Alves, C. L. Hsiao, L. C. Chen, T. Yamaguchi, Y. Takagi, K. Kawashima, and Y. Nanishi, *J. Appl. Phys.* **108**, 073529 (2010)
28. B. Rauschenbach and J. W. Gerlach, *Cryst. Res. Technol*. **35**, 6 (2000)
29. B. Rauschenbach and J. W. Gerlach, *Cryst. Res. Technol.* **35**, 675 (2000)
30. G. A. Bassett, *Proc. Eur. Reg. Conf. Electron Micros., Delft*, p.270 (1961)
31. D.W. Pashley, M.J. Stowell, M.H. Jacobs and T.J. Law, *Phil. Mag*. **10**, 127 (1964)
32. M.H. Jacobs, D.W. Pashley and M.J. Stowell, *Phil. Mag*. **13**, 129 (1966)
33. C. Stampfl and C. G.Van de Walle, *Phys. Rev. B* **57**, R15052, (1998)
34. Y. T. Rebane, Y. G. Shreter, and M. Albrecht, *Phys. Status Solidi (a)* **164**, 141 (1997)
35. P. Corfdir, P. Lefebvre, J. Ristic´, J.-D. Ganière, and B. Deveaud-Plédran, *Phys. Rev. B* **80**, 153309 (2009)
36. R. Liu, A. Bell, F. A. Ponce, C. Q. Chen, J. W. Yang, and M. A. Khan, *Appl. Phys. Lett.* **86**, 021908 (2005)
37. M. McLaurin and J. S. Speck, *Phys. Stat. Sol. (RRL)* **1**, 110 (2007)
38. F. Bernardini, V. Fiorentini, and D. Vanderbilt, *Phys. Rev. B* **56**, R10024 (1997)
39. G. D. Metcalfe, H. Shen, M. Wraback, A. Hirai, F. Wu, and J. S. Speck, *Appl. Phys. Lett.* **92**, 241106 (2008)
40. A. O. Ajagunna, E. Iliopoulos, G. Tsiakatouras, K. Tsagaraki, M. Androulidaki and A. Georgakilas, *J. Appl. Phys.* **107**, 024506 (2010)

7 Nucleation and buffer layers for InN on Si (111) heteroepitaxy

7.1 Si surface properties and review of earlier work on InN on Si (111) epitaxy

7.2 Investigation of direct InN epitaxy on Si (111): The role of III/V flux ratio

7.3 Study of the role of intermediate layer in the growth of InN on Si (111)

7.4 TEM Study of InN film grown on Si (111) using GaN/AlN buffer layer

7.5 Investigation of the role of thick GaN layer on the properties of InN film grown on Si (111) using GaN/AlN double buffer layer

7.6 Concluding remarks

7.1 Review of earlier work on InN/Si (111) epitaxy and Si surface properties

This chapter discusses the work aimed at investigating the PAMBE growth and properties of InN on Si (111) substrates. The Si (111) substrate orientation is the optimum for growth of *c*-plane III-nitrides due to its crystal symmetry and our discussion will therefore be limited to this orientation. For the heteroepitaxial growth of InN on Si (111) substrates, the lattice mismatch of ~8% in comparison to ~11% for the heteroepitaxial growth on GaN/sapphire (0001) pseudo-substrates is an important advantage. The additional advantages of using Si substrates are its low-cost, availability in large surface area/diameter and the potential of integrating III-V devices with the established Si-technology.

In spite of these advantages, limited research efforts have focused on the growth and properties of InN on Si [1-4]. Grandal *et al.* [1] reported the effect of growth temperature on the morphology of InN grown by nitrogen radio frequency plasma source molecular beam epitaxy (PAMBE). They also compared the use of high temperature (HT) AlN and low temperature (LT) InN buffer layers on Si and reported the improvement of the InN crystal quality when HT-AlN buffer was used. Wu *et al.* [2] studied the PAMBE growth of InN using an intermediate ultrathin β-Si_3N_4 buffer layer on Si and found that it serves as an effective diffusion barrier that prevents Si outdiffusion and auto-doping of the InN epilayer. Maleyre *et al.* [3] compared the metalorganic vapour phase epitaxy (MOVPE) of InN on Al_2O_3 and Si (111) substrates. They reported that InN exhibits better wetting behaviour on the nitridated Al_2O_3 surface than on Si (111). Finally, Chang *et al.* [4] employed a two-step growth process, with initial deposition of a GaN/AlN buffer layer on the Si (111) substrate and the initiation of InN growth after deposition of In layer, to improve the quality of their MOVPE grown InN overlayer. Although significant progress has been made, more work is needed to improve the understanding and optimize the heteroepitaxy of InN on Si.

The atomically clean surfaces of semiconductors are usually reconstructed [5]. Silicon (111) surfaces exhibits reconstructions, which are basically dependent on temperature, misorientation, method of sample cleaning or surface preparation and type of impurity that is significantly entrenched on the surface. The surface reconstructions usually occur at low-index surfaces and play an important role in determining the structural phase of Si by stabilizing the low-index surface and inducing changes in the average step height by changing the relative free energy of the steps [6]. The fundamental driving force for this complicated reconstruction is the removal of dangling bonds [7]. The temperature at which 7x7 reconstruction appears on Si (111) surface is around 800°C [2]. On ramping down the temperature, 7x7 changes to 2x1 under a temperature lower than 200°C [8]. However, the 7x7 is much more stable than the 2x1 reconstructions [9].

The cooling rate, after the *in-situ* thermal cleaning process of Si, plays a strong role in the formation of defects and boundary regions [10] and large defect regions has been reported to exist on Si (111) surfaces when the temperature is ramped down abruptly even to 600°C [11,12] due to instantaneous freezing of such regions on the surface [10]. 7x7 reconstructions produced by abrupt heat treatment and subsequent rapid cooling to RT therefore could promote defect and unwanted multifaceted-steps as a result of improper atomic arrangement. A slow annealing treatment should allows sufficient atomic mobility that permits the atoms in the disordered regions to diffuse and build up more ordered structures, thereby reducing the boundaries and defect regions on the surface significantly.

In general, the quality of epitaxial growth critically depends on the preparation of an atomically clean substrate surface [13,14]. Hence, developing a good cleaning procedure for Si substrate surface is of high importance for high quality thin film growth. Realizing a pristine 7x7 surface reconstruction RHEED patterns during thermal cleaning of Si is very critical for III-nitrides growth by MBE. The formation of this reconstruction also requires a careful *ex-situ* chemical cleaning. Consequently, extra care was taken in this work to ensure that the Si chemical cleaning follows the optimised process previously discussed in Section 3.3 and the thermal annealing and cooling process in the MBE were carried out at a slow rate to ensure that the surface structure are well ordered. In all experiments, the 7x7 reconstruction was always observed after *in-situ* thermal cleaning of the used Si(111) substrate's surfaces. In the following, the effects of N/In flux ratio, growth temperature and buffer layers comprising of InN, GaN, AlN and GaN/AlN on the properties of InN heteroepitaxial layers on Si (111) are investigated.

7.2 Investigation of single-step growth of InN on Si (111): Role of III/V flux ratio

The first experiments aimed to identify whether the heteroepitaxy of InN on Si (111) follows the self-regulated growth mechanism determined for the growth of InN on GaN (0001) [15,16]; at high substrate temperature, the substrate surface coverage is proportional to the In/N flux ratio and the growth rate along the *c*-axis of the three-dimensional (3D) InN islands is limited by the flux of reactive nitrogen species (F_N) and not by the lower In flux (F_{In}). Full coverage of the GaN(0001) substrate surface and layer-by-layer (step-flow) growth mode for InN are achieved only for stoichiometric In/N flux ratio [15-17]. Si(111) substrates of 330±15 μm thickness, Boron-doped, with resistivity > 10,000 Ωcm and misorientation of ± 0.5°, were employed for this study.

***Table 7.1** Epitaxial structures and conditions of PAMBE growth of InN on Si (111). T_{sub} is the substrate temperature. Compact InN films were grown using N/In flux ratio equivalent to 1 ($F_N/F_{In} \approx 1$), while nanopillar structures were grown for $F_N/F_{In} \geq 2$ with constant $F_{In} \approx 120$ nm/h.*

Sample Identity	Structure	F_N/F_{In}	T_{sub} (°C)	Thickness (nm)	Growth rate along *c*-axis (nm/h)
G983	InN Film/Si	~ 0.9	450	700	350
G1160	InN Film/Si	1	425	2000	500
				Height along *c*-axis (nm)	
G1262	InN NPs / Si	2	500	760	190
G1263	InN NPs / Si	4	500	1470	368
G1264	InN NPs / Si	6	500	2290	572

The performed InN on Si growth experiments are described in Table 7.1. The methods of controlling the substrate temperature (T_{sub}), the fluxes of the In atoms (F_{In}) and the reactive nitrogen species (F_N) have been described in Chapter 3. The flux ratio F_N/F_{In} was varied from ~ 0.9 to 6. In the first case, Sample G983 was grown by direct deposition of InN on Si (111), using $F_N/F_{In} \approx 0.9$ (slightly In-rich condition) at a

substrate temperature (T_{sub}) of 450°C. In the case of $F_N/F_{In} \approx 1$, Sample G1160 was grown at a T_{sub} of 425°C. Under such growth conditions, a step-flow growth mechanism is followed for InN growth on GaN (0001) [15,17]. In the case of $F_N/F_{In} \geq 2$, the samples G1262, G1263 and G1264 were realized by growing InN directly on Si (111) at T_{sub} = 500°C using F_N/F_{In} equal to 2, 4 and 6, respectively (Table 7.1). For samples G1262-1264, F_{In} was kept constant at approximately 120 nm/h (equivalent InN growth rate) and the F_N/F_{In} ratio was varied by changing only the F_N. Similar growth duration of 4 hours was kept for each InN sample, except G983 that was grown for only 2 hours. Prior to characterization, all film samples were dipped in HCl solution to remove any metallic In that may have been formed on the surface during growth.

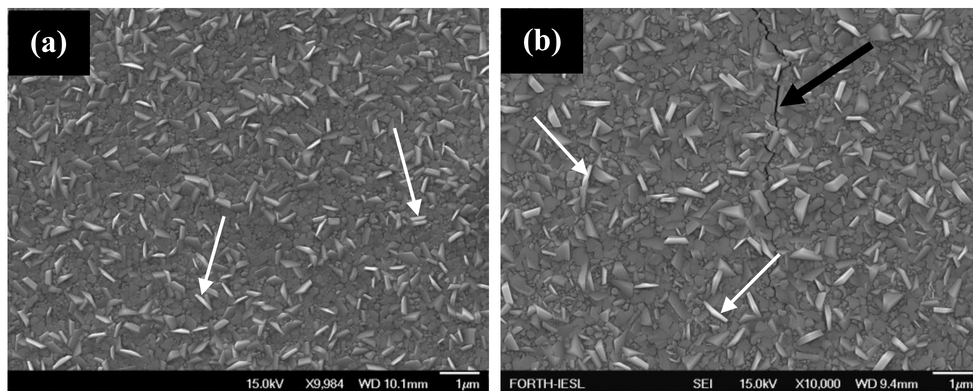

Figure 7.1 *SEM micrographs showing the surface morphology of (a) 700 nm thick sample G983 and (b) 2000 nm thick G1160 compact InN film samples grown on Si (111). The arrow in (b) points to one of the existing microcracks on the surface of G1160.*

The FE-SEM micrographs of Figs. 7.1(a) and 7.1(b) show the morphology of samples G983 and G1160, respectively. The SEM micrographs of Figs. 7.2(a)-(c) reveal the morphology and structure of the InN samples G1262, G1263 and G1264 grown at T_{sub} = 500°C, with F_N/F_{In} equal to 2, 4 and 6, respectively (N-rich conditions). It is evident that samples G983 and G1160 consisted of compact InN films, while samples G1262-G1264 consisted of InN nanopillars. The film samples G983 and G1160 are first discussed.

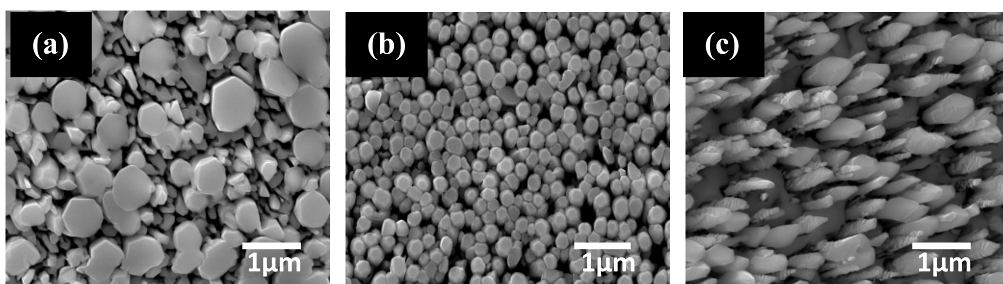

Figure 7.2 *SEM micrographs showing the surface morphology of the InN on Si (111) samples (a) G1262, (b) G1263 and (c) G1264, which evolved as InN nanopillars.*

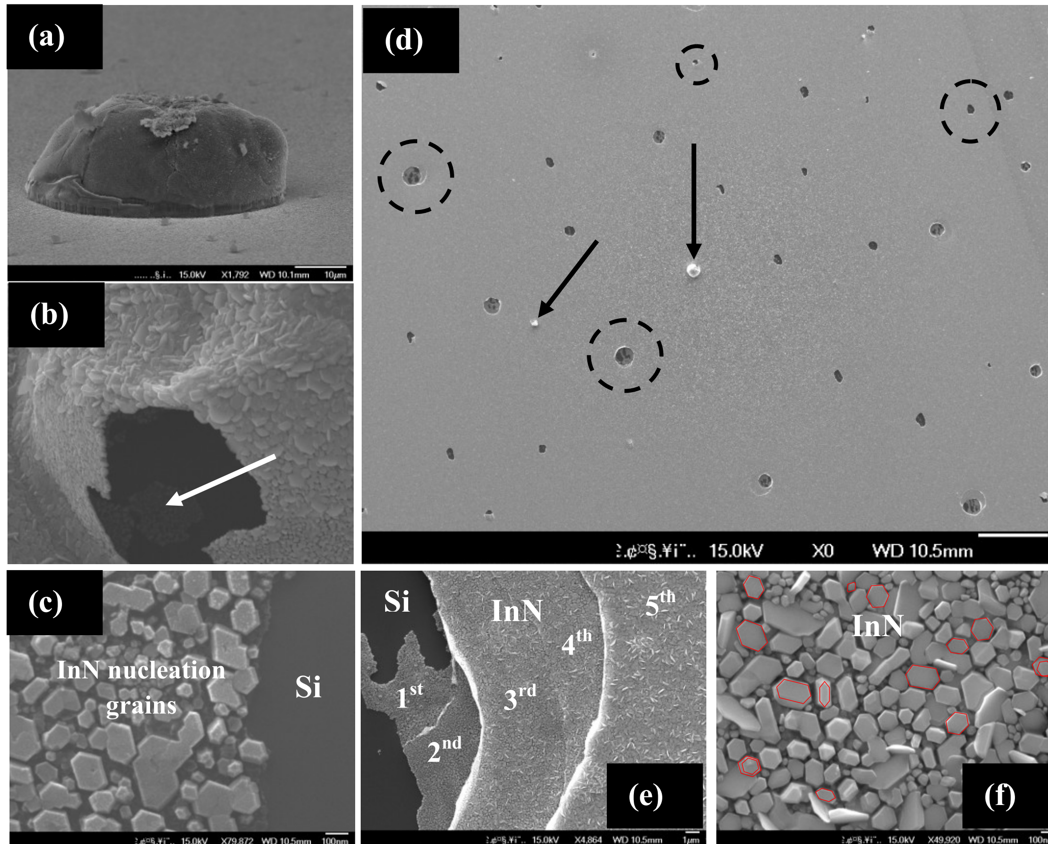

Figure 7.3 *FE-SEM micrographs of InN sample G983 showing (a) bird-view image of one of the micro-domes (covered with InN flakes) observed on the surface, (b) enlarged image of a micro-dome with a broken side, (c) image of the micro-dome interior taken through the broken side of the dome shown in (c), (d) Low magnification plan-view showing a larger surface area of sample G983, which consist of micro-domes (arrows) and micro-holes (enclosed in broken circles), (e) image of one of the micro-holes enclosed with broken rings in (d) showing the sub-levels of the initially grown InN (labelled 1st to 5th) formerly enclosed by a micro-dome, (f) enlarged image of one of the initial nucleation layer that indicated that the InN growth proceeded with the nucleation and coalescence of hexagonally shaped InN islands (depicted).*

Sample G983 and G1160 exhibited similar granular surface morphology that corresponds to high surface roughness of the films as shown in Fig. 7.1. Some of the grains formed InN outshoots on the films' surfaces, like the ones identified by white arrows. Microcracks (identified by arrow in Fig. 7.1(b)) were observed on the surface of sample G1160 only. The observation of such microcracks for GaN on Si (111) film has been attributed to tensile strain build-up within the epilayer due to thermal mismatch [18,19], which is also believed to be the case for InN on Si since Si has similar thermal expansion coefficient, perpendicular to *c*-axis, with both InN (3.59 x 10^{-6} K^{-1}) and GaN (5.59 x 10^{-6} K^{-1}) [20]. The absence of such microcracks on the surface of sample G983, in spite of its higher growth temperature, is attributed to the film's lower thickness (700 nm) compared to G1160 that is 2000 nm. Although both samples have been grown directly on Si (111), using the ideal conditions for step-flow growth of InN [15-17], the surface morphology differs significantly compared to the smooth surface with monolayer height steps of InN grown on GaN/Al_2O_3 (0001)

[17]. AFM observations were also in agreement with the FE-SEM results. The rms roughness of the InN surface, determined from the 2 x 2μm^2 AFM scans, was about 24 nm for both films. It is therefore evident that the optimum growth conditions for layer-by-layer growth of InN films on GaN (0001) cannot be used for direct growth on Si (111) and this should be related to the different chemical bonds at the InN/Si interface.

Some dome-like features, similar to the one shown in Fig. 7.3(a), were found on the surface of sample G983. Microanalysis of the top of the micro-domes by EDX revealed the presence of In, N and Si with higher Si composition in the domes' matrices, confirming also that the features were not In droplets but defective regions on the InN film's surface. A larger magnification image of the dome with a broken side is shown in Fig. 7.3(b). The broken side acts as a see-through window from which the image of Fig. 7.3(c) was taken, indicating that the dome was formed on top of both InN nucleation layer and bare Si surface. It is evident also, from the image, that continuous growth of InN cannot be sustained on Si within these domes. A lower magnification image shown in Fig. 7.3(d) indicate that some of the micro-domes might have been removed from the surface during HCl etching of the sample, creating micro-holes of different sizes (identified by broken circles) while the surviving micro-domes are also visible on the film's surface (identified by arrows). The plan-view image of one of the micro-holes is shown in Fig. 7.3(e), where the different growth levels along the vertical distance of the InN are apparent and are labeled according to their closeness to the InN/Si interface from 1st to the 5th level. One interesting observation from this figure is that the sizes of the grains present on each level's surface reduce from the top (labeled 5th) to the bottom level (labeled 1st) and the bottom layer exhibits smoother surface morphology, indicating that the surface roughness of InN, when grown directly on Si, increases with growth time (or thickness). These defective regions were only observed on the surface of the sample G983 grown under In-rich condition and not on sample G1160 grown under stoichiometric flux ratio. Since EDX indicated a larger amount of Si in the matrix, it is believed that Si-outdiffusion or inter-mixing with In atoms was enhanced under the nitrogen limited growth condition employed and this is responsible for the initial inhibition of InN growth in some regions of the Si surface and the eventual formation of this domes to cover these regions up through a kind of epitaxial lateral overgrowth process. This anomaly was not observed in the case of sample G1160, grown under stoichiometric III/V flux ratio, as a result of equal supply of reactive nitrogen species and In adatoms for In-N bonding during growth, which prevents In-Si interaction.

Moreover, the magnified image of the initial InN nucleation layer of Fig. 7.3(c), clearly show that the growth of InN proceeded with formation and coalescence of hexagonal-shaped InN islands (3D growth mode), also depicted by red in Fig. 7.3(f). The enlarged view of the image revealed that all the islands/grains are hexagonal, indicating that wurzite InN and not cubic was nucleated on Si (111), supporting the well know fact that hexagonal InN structure is the preferential growth orientation of III-nitride semiconductors on Si (111).

The cross-sectional FE-SEM micrograph of the thicker InN film G1160 is shown in Fig. 7.4. The arrows point to the network of microcracks existing in the bulk of the film [Fig. 7.4(a)], indicating that the microcracks are not limited to its surface as previously shown in Fig. 7.1(b) but are also entrenched in the bulk structure. The formation of microcracks is unlikely to result from thermal tensile strain alone, as in the case of GaN-on-Si [18,19], but it should also be related to an intrinsic tensile strain induced by the 3D growth mechanism [21]. Moreover,

microcracks may also result from the adhesion problems that exist at the InN/Si interface of the film (see arrow in Fig. 7.4(b)).

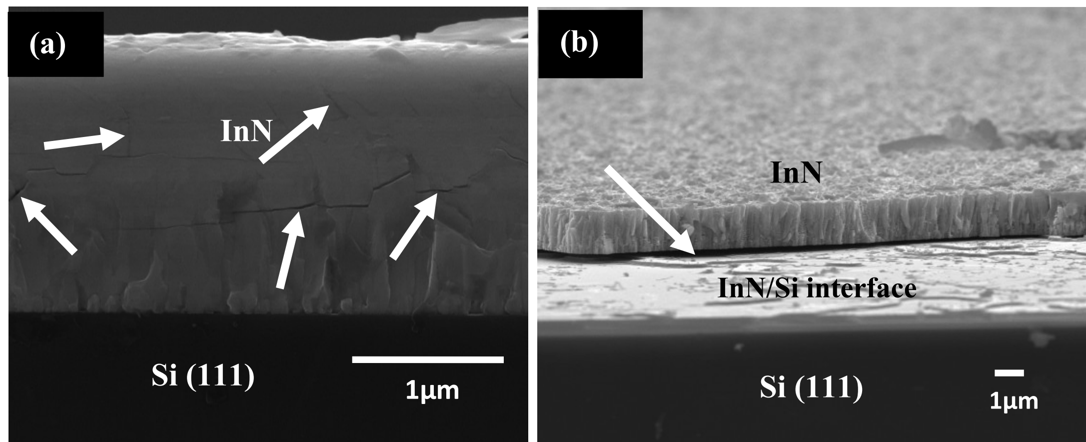

Figure 7.4 *FE-SEM cross-sectional micrographs of the 2 µm thick InN film G1160 directly grown on Si(111) showing (a) the existence of microcracks in the bulk of the 2000 nm thick film G1160 (see arrows), (b) poor adhesion in some regions along the InN/Si interface of G1160 (see arrow).*

HR-XRD rocking curves (RC) around the (0002) InN reflection for samples G983 and G1160 exhibited FWHM values of 1.7^{o} and 7.0^{o}, respectively. The structural results are in correspondence to the SEM observations. The larger mosaicity exhibited by sample G1160, compared with G983, should be related to the existence of microcracks in the bulk. The lattice parameters, *a* and *c* of sample G983 that did not exhibited micro-cracks were determined as 0.3538 nm and 0.5696 nm, respectively, using the extended Bond method [21]. These values almost coincide with the stress free lattice parameters of InN [21] and indicate the presence of negligible tensile strain in the InN epilayer.

TEM analysis of the G983 was carried out by collaborators (Prof. Th. Kehagias and Prof. Ph. Komninou) at the Physics department of Aristotle University of Thessaloniki to further understand the microstructure of the InN film sample. The cross-sectional TEM (CTEM) image taken with **g** = 110 tilted by 5 degrees from the Si [001] axis is shown in Fig. 7.5(a). It is apparent that G983 is a columnar film and it also exhibits a large range of grain sizes. The slightly In-rich growth condition employed could not prevent the formation of amorphous Si_xN_y layer at the InN/Si interface, as depicted by arrow in the HRTEM of Fig. 7.5(b).

TEM plan view image of sample G983 is shown in Fig. 7.6. InN grains ranging in lateral dimensions of between 20 nm (for the smallest crystallites) to 500 nm (for the larger coalesced grains) are visible in Fig. 7.6(a). Fig. 7.6(b) depicts the hexagonal morphology of the observed InN columns, in agreement with FE-SEM observations in Fig. 7.3(f). Each column possesses the same general epitaxial orientation relationship of [110] Si // $[11\bar{2}0]$ InN, although most InN grains are twisted by a few degrees from this orientation.

It is therefore evident from both plan-view and cross-sectional images of sample G983, which is also representative of sample G1160, that columnar film of InN consisting of different grain sizes will result from the direct growth of InN on Si (111), whenever the conventional growth conditions that should produce high quality

InN film on GaN (0001) templates are employed. This makes the direct growth of high quality InN on Si (111) a great challenge.

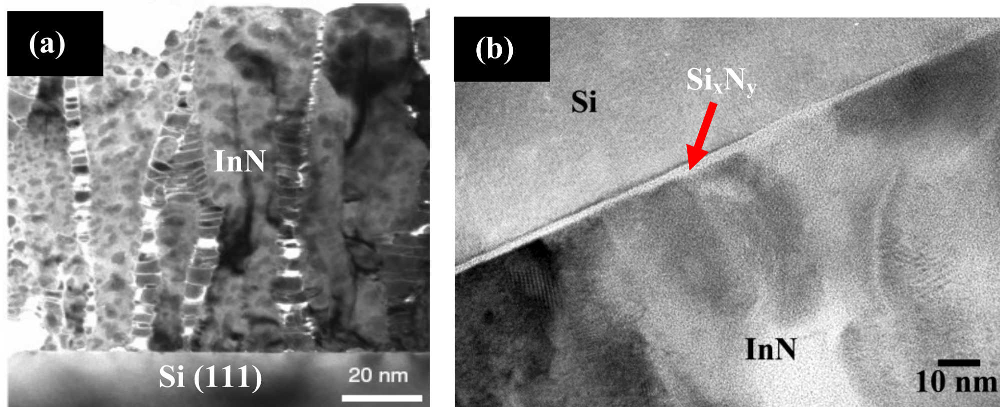

Figure 7.5 *(a) CTEM image taken with g = 110 tilted by 5 degrees from the Si [001] axis, showing a columnar film that also exhibits a large range of grain sizes, (b) HRTEM image of the InN/Si interface showing the formation of amorphous* Si_xN_y *(red arrow).*

Hall-effect measurements revealed better electrical properties for sample G983 compared to G1160. The measured room temperature (RT) electron mobility (μ) and carrier concentration (N) of the films were 127 cm^2 / Vs and 7.3 x 10^{20} cm^{-3} for G1160 and 640 cm^2 / Vs and 4.66 x 10^{19} cm^{-3} for G983, respectively. The apparent very poor electrical properties of G1160 are attributed to the high density of microcracks in the film. Hall-effect measurements should not reveal the actual properties of sample G1160 due to the measurement of a non-homogenous layer (due to cracks).

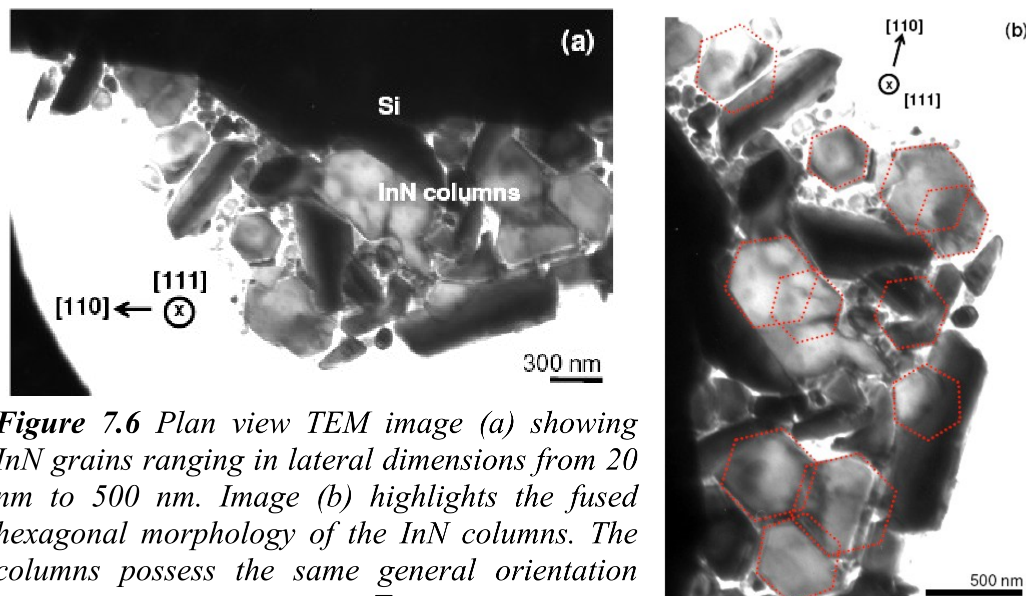

Figure 7.6 *Plan view TEM image (a) showing InN grains ranging in lateral dimensions from 20 nm to 500 nm. Image (b) highlights the fused hexagonal morphology of the InN columns. The columns possess the same general orientation relationship of [110] Si // [11*$\bar{2}$*0] InN.*

Fig. 7.7 shows the PL measurements at 20K of the InN film samples G983 and G1160. Both samples exhibited main PL peak at ~0.78 eV, which is reasonable considering their similar carrier concentration.

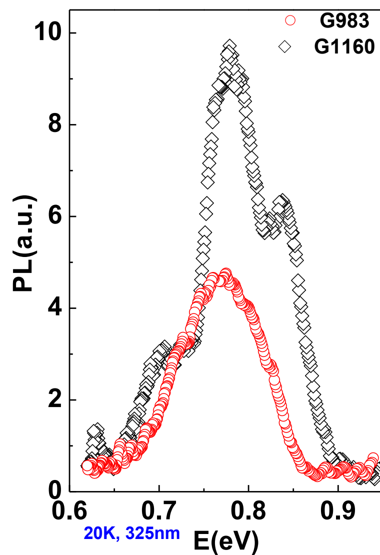

Figure 7.7 *20K PL spectra of film samples G983 and G1160.*

The FE-SEM plan-view micrographs of Figs. 7.2(a) - 7.2(c) show the different morphologies of the nanopillar samples G1262, G1263 and G1264, grown with F_N/F_{In} equal to 2, 4 and 6, respectively. Large diameter nanopillars dominated the structure of sample G1262 (F_N/F_{In} = 2), as it is also shown in the cross-sectional SEM micrograph of Fig. 7.8(a). The overall density of nanopillars in sample G1262 was ~5.8 x 10^8 cm^{-2} and their diameter varied from 100 to 400nm [Fig. 7.2(a)]. Sample G1263 (F_N/F_{In} = 4) consisted of ~1.4 x 10^9 cm^{-2} nanopillars with diameter between 100 and 200nm [Fig. 7.2(b)]. Sample G1264 (F_N/F_{In} = 6) demonstrated the lowest density of nanopillars of ~4.6 x 10^8 cm^{-2} [Fig. 7.1(c)]. Their shape almost resembles a cone with varying diameter from top to bottom as shown in Fig. 7.2(c) and schematically drawn in Fig. 7.8(b).

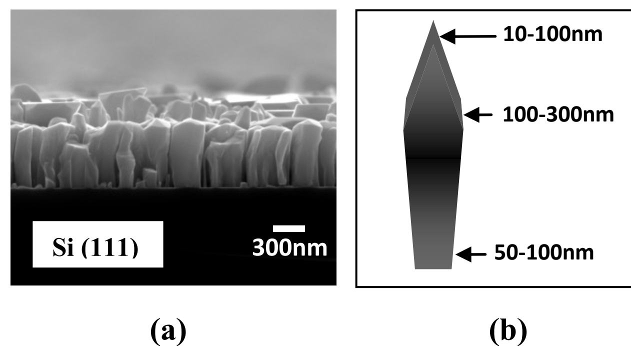

Figure 7.8 *(a) SEM micrograph showing the cross-sectional view of G1262. (b) A schematic image depicting the typical thickness variation along the c-axis of the nanopillars sample G1264.*

The measured average height and the corresponding growth rate along the *c*-axis for the nanopillars of samples G1262-G1264 are given in Table 7.1. A linear dependence of both quantities on the F_N/F_{In} value was found. The nanopillars' heights were 760 nm, 1470 nm and 2290 nm in samples, G1262, G1263 and G1264, respectively, which correspond to growth rates of 190 nm/h, 368 nm/h and 572 nm/h

(Table 7.1). These growth rates are equal to approximately 80% of the F_N used in each sample. They are much higher than the incident flux of In atoms (F_{In}) of ~120 nm/h and are thus limited by the incident flux of reactive nitrogen species (F_N), in very good agreement with the self-regulated growth mechanism identified for the growth of InN on GaN (0001) [15,16].

The 3D growth mode of InN (0001) is induced by the lattice mismatch strain energy and the high surface energy of the N-stabilized InN (0001) surface under N-rich growth conditions (F_N/F_{In} >1). The formation of InN nanopillar structures is then related to the short surface diffusion length (and residence time) of N adatoms under N-rich conditions, while the In adatoms exhibit very large diffusion lengths on the substrate surface and the nonpolar facets of the 3D InN islands-nanopillars. The desorption of In adatoms from the surface is also negligible for T_{sub} up to ~600°C. Thus, mobile In adatoms are transferred from the uncovered substrate areas to the initially nucleated 3D InN islands and nanopillars are grown with self-regulated dimensions so that a stoichiometric supply of In and N adatoms occurs on the top InN (0001) surface [15,16].

From the XRD analyses of the crystal quality, the (002) RC FWHM values of 2.44^o, 4.71^o and 1.20^o were estimated for G1262, G1263 and G1264, respectively, showing that the condition of growth of G1264 led to a significant improvement of the crystallinity of the InN NPs.

20K PL measurements carried out on the nanopillar samples G1262-G1264 showed that the PL intensity increased with increasing F_N/F_{In}. As shown in Fig. 7.9, no PL peak was recorded for sample G1262, while sample G1264 exhibited the highest PL intensity measured for the three samples, signifying the higher crystalline quality of G1264 in agreement with the XRD results. The absence of PL emission in G1262 is attributed to the large diameter of the nanopillars, which would increase the density of crystal defects induced by the lattice mismatched growth.

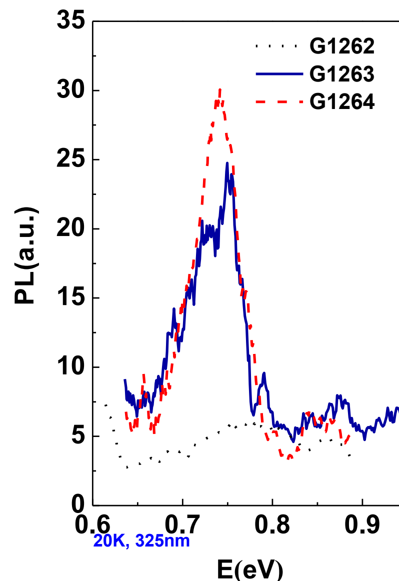

Figure 7.9 *20K PL spectra for NPs samples G1262, G1263 and G1264. Sample G1264 exhibited higher emission intensity and narrower FWHM; indicating superior crystal quality in agreement with the XRD measurements.*

7.3 Study of two-step growth of InN on Si (111): Role of intermediate layer

To overcome the problems of the single-step growth of InN on Si(111), different two-step growth processes were investigated. This study was aimed at understanding the role of an initial buffer layer on the properties of InN epilayers grown on Si (111) substrates. In this study, four different ways of initiating the growth of InN on Si (111) were investigated, using intermediate layers comprising of low temperature InN (LT-InN), low temperature GaN (LT-InN), AlN, and a GaN/AlN bilayer. The details of the growth conditions of these samples are listed in Table 7.2. The main InN epilayers were grown at T_{sub} of 425 - 440°C with $F_N/F_{In} \geq 1$, using an In-flux (F_{In}) equivalent to an In-limited InN growth rate of 500 nm/h. This condition is required to avoid metallic In accumulation on the surfaces.

Table 7.2 *Description of the epitaxial structures and growth conditions employed for InN films heteroepitaxy on Si (111), using different buffer layers.* F_N/F_{In} *is the Nitrogen to Indium flux ratio and* T_{sub} *is the substrate temperature.*

Sample	Buffer layer Structure	Buffer layer T_{sub} (°C)	InN F_N/F_{In}	InN T_{sub} (°C)
G1161	50nm GaN/30nm AlN/Si	800/900	1	425
G1162	30nm LT-InN/Si	300	1	425
G1343	130nm GaN/100nm AlN/Si	810/900	1.1	440
G1352	100nm AlN/Si	900	1.1	440
G1397	100nm GaN/20nm LT-GaN/Si	825/350	1.1	440

The FE-SEM micrographs of Fig. 7.10 show the morphology of the InN samples G1161, G1162, G1343, G1352 and G1397. A comparison with Fig. 7.2 suggests that growth conditions employed resulted to compact InN films. Compared to G1160 [Fig. 7.1(b)], the InN surface morphology improved when a LT-InN buffer layer was used prior to the growth of the main InN epilayer under optimum conditions, as in the case of sample G1162 [Fig. 7.10(b)]. However, sample G1162 exhibited also trenches on the surface, aligned along the major in-plane directions of the hexagonal crystal on the *c*-plane surface. These trenches should correspond to the boundaries of coalesced InN islands/grains. The significantly larger size of these apparent grains, compared to G1160 grown directly on Si [Fig. 7.1(b)], indicates the improved nucleation of InN on Si (111) at lower T_{sub} (300°C).

The smoothest surface morphology was obtained for sample G1161 that employed a thin GaN/AlN buffer layer and was grown under stoichiometric F_N/F_{In} as shown in Fig. 7.10(a). The surface morphology manifested by G1343, G1352 and G1397, which are depicted in Figs. 7.10(c), 7.10(d) and 7.10(e), respectively, is similar to that observed for InN grown on Ga-polarity GaN/Al_2O_3 (0001) templates [15,16] with F_N/F_{In} slightly higher than 1 (slightly N-rich conditions). Of all the buffer layers employed, the deposition of a low temperature GaN nucleation layer followed by a high temperature GaN buffer layer produced the worst surface morphology, as in the case of G1397 in Fig. 7.10(e). Despite the lower epilayer thickness in comparison to others, the surface of the G1397 is characterised by cracks (arrows) and InN grain clusters, in additions to the roughening caused by the slightly N-rich condition employed for the InN layer growth at high temperature [Table 7.2]. The formation of microcracks, which were not exhibited in the other samples using

different nucleation schemes in the experiment, is attributed to tensile strain build-ups within the film's heterostructure. Table 7.3 describes the deduced rms values of surface roughness from 2x2μm^2 AFM scans for each film sample. A very high rms surface roughness of 39 nm was exhibited by G1397. Sample G1343, which used intermediate layers similar to G1161, exhibited a higher rms surface roughness compared to the latter. The higher surface roughness of G1343 and G1352 in comparison to G1161 should be related to the higher growth temperature and slightly N-rich growth conditions employed [Table 7.2]. It is known that N-rich growth conditions result to 3D growth mode in PAMBE of InN (0001) [15].

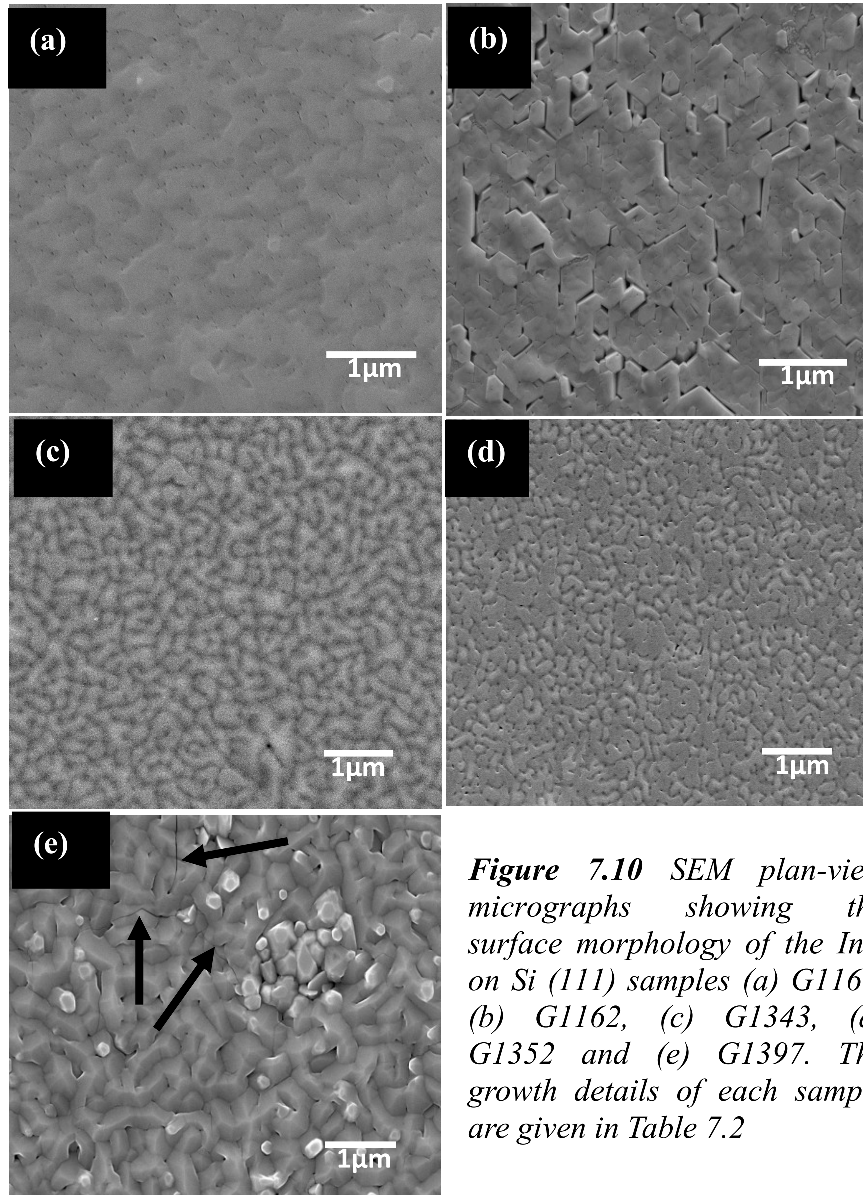

***Figure 7.10** SEM plan-view micrographs showing the surface morphology of the InN on Si (111) samples (a) G1161, (b) G1162, (c) G1343, (d) G1352 and (e) G1397. The growth details of each sample are given in Table 7.2*

HR-XRD θ-2θ scans confirmed the single crystallinity of the entire InN films, indicating that they are all oriented along the *c*-axis. The measured FWHM values of the XRD rocking curves (RC) around the (0002) and $(10\bar{1}5)$ reflections are given in Table 7.3. The structural results are in correspondence to the surface morphological observations and samples G1161, G1343 and G1352 with AlN nucleation/buffer

layers demonstrated superior crystal quality over the rest of the InN samples. The crystal-quality of G1343 with (0002) RC FWHM of 0.33^o showed a noticeable improvement over that of G1161, which may be related to the higher growth temperature, even though the thicker GaN/AlN buffer layer employed for G1343 [Table 7.3] could also have played a role. The thicker GaN/AlN buffer layer should more effectively accommodate and prevent defects caused by the high lattice mismatch of the AlN/sapphire interface from propagating into the InN epilayer. The use of LT-InN nucleation layer yielded film sample G1162 with the poorest crystal-quality, although it exhibited a significantly reduce mosaicity in comparison with the 7.0^o obtained for the similar thickness InN film G1160 grown directly on Si without buffer layer. Although sample G1397 exhibits very high surface roughness and crystal mosaicity [Fig. 7.10(e)], yet it manifested superior crystal quality compared to G1162, indicating that GaN may also behave as a better nucleation layer on Si compared to InN. The superior structural quality of samples G1343 and G1352 indicates that AlN nucleates more efficiently than InN or GaN on Si (111) substrate's surface. This is also confirmed by the similar and narrower $(10\bar{1}5)$ RC FWHM measured for all the InN films that employed AlN buffer/nucleation layer [Table 7.3], compared with samples G1162 and G1397 that used LT-InN and LT-GaN buffer layers, respectively. The (0002) RC FWHM values measured for samples G1343 and G1352 are however larger than the value of 0.1^o obtained for InN grown on GaN/Al_2O_3 substrate [22]. The lattice parameters *a* and *c* of film G1161 were determined equal to 0.3545 nm and 0.5698 nm, respectively, using the extended Bond method [21], which almost coincide with the stress free lattice parameters of InN [23].

Table 7.3 *Summary of the overall characterisation result data obtained for the InN films grown on Si (111) substrates, by a two-step process, using different buffer layers. Compact InN films were grown on the respective intermediate layers. t is the InN epilayer thickness,* AFM_{rms} *is the rms surface roughness values determined from the 2x2* μm^2 *AFM scans, (0002)* RC_{FWHM} *and* $(10\bar{1}5)$ RC_{FWHM} *are the full width at half maximum values obtained from the measurements of the HRXRD rocking curves of the InN film samples around the (0002) and* $(10\bar{1}5)$ *reflections, respectively,* N_d *and* μ *are the films' respective apparent concentrations and mobility of electrons determined from Hall-effect measurements at 300K.*

Sample	Buffer layer	*t* (nm)	AFM_{rms} (nm)	(0002) RC_{FWHM}	$(10\bar{1}5)$ RC_{FWHM}	N_d (x 10^{19} cm^{-3})	μ (cm^2/V.s)
G1161	GaN/AlN/Si	2000	2.8	0.44^o	0.20^o	1.35	1208
G1162	LT-InN/Si	2000	8.5	2.62^o	2.13^o	7.0	860
G1343	GaN/AlN/Si	2000	11.3	0.33^o	0.20^o	2.30	1155
G1352	AlN/Si	2000	9.48	0.35^o	0.19^o	2.36	1106
G1397	GaN/LT-GaN/Si	1000	39.0	1.17^o	0.77^o	1.85	819

The InN/Si interfacial adhesion was improved for sample G1162, using a LT-InN nucleation layer, compared to sample G1160 with InN grown directly on Si at 425°C [Fig. 7.4(b)], although some voids could still be observed at the InN/Si interface of G1162. On the contrary, excellent interfacial adhesion was observed by FE-SEM for the InN film sample G1161, as shown in Fig. 7.11(b). The observed differences in the adhesion of InN/Si and AlN/Si heterostructures should be related to

weaker bonds at the InN/Si interface, and the less dense nucleation of InN islands compared to AlN. The results confirm the superiority of GaN/AlN as an intermediate layer for high quality InN growth on Si (111) and the excellent wetting property of AlN on Si (111) substrates.

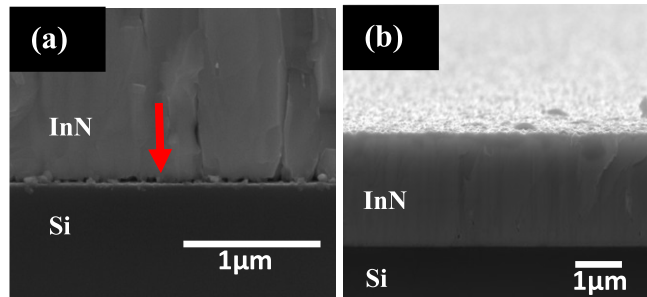

Figure 7.11 *FE-SEM image showing the cross-section of samples (a) G1162 and (b) G1161. Adhesion difficulty and voids occurred at the InN/Si interface of sample G1162 (see arrows).*

Hall-effect measurements revealed better electrical properties for samples G1161, G1343 and G1352 that employed AlN nucleation layer, in comparison with samples G1162 and G1397 that employed LT-InN and LT-GaN nucleation layers, respectively. The room temperature (RT) electron mobility (μ) and apparent concentration (N_d) for these InN films are given in Table 7.3. The higher defect density of sample G1162 should have enhanced Si atoms out-diffusion along the vertically propagating defects/boundaries, leading to extremely high carrier concentration of 7.0 x 10^{19} cm^{-3}, in comparison to the other InN samples. In the case of sample G1397, the presence of microcracks is believed to be responsible for the exhibited poorest Hall mobility, in spite of its lower carrier density compared to G1162 and even G1343 and G1352 that employed AlN nucleation layer.

Samples G1161 and G1162 exhibited high mobility values for electron concentrations in the 10^{19} cm^{-3} range, in comparison to results from other groups [24-27]. High mobility values for high carrier concentrations are usual for the InN films grown in our MBE system [16,28], and are attributed to low compensation of the unintentional donors by acceptor impurities or defects [29]. Specifically, Hall-effect measurements on a reference InN film grown on GaN/Al_2O_3 (0001) resulted to electron mobility of 1900 cm^2/Vs and carrier concentration of 1.1x10^{19} /cm^3. The lower electron mobility of sample G1161 (1208 cm^2/Vs) indicates the superior structural quality of InN grown on MOCVD GaN/Al_2O_3 template compared to Si. The electron mobility of sample G1162, though unusually high, is still within the theoretical predictions of B. R. Nag, where a value of $\mu \approx 880$ cm^2 / Vs can be estimated for N = 7.0 x 10^{19} cm^{-3}, in the case of negligible compensation of donors by acceptor impurities or defects [29].

Figure 7.12 shows the PL measurements at 20K of the InN film samples G1161, G1162, G1343, G1352, and G1397. Only samples G1162 and G1397 exhibited single emission peaks at 0.68 eV and 0.77 eV, respectively. Double photon energy peaks were observed for InN films G1161 at 0.69 eV (main peak) and 0.78 eV (weaker peak) and G1352 at 0.75 eV (main peak) and 0.82 eV (weaker peak). No PL

peak could be recorded for sample G1343, although the same film exhibits the overall highest crystal quality according to HRXRD [Table 7.4].

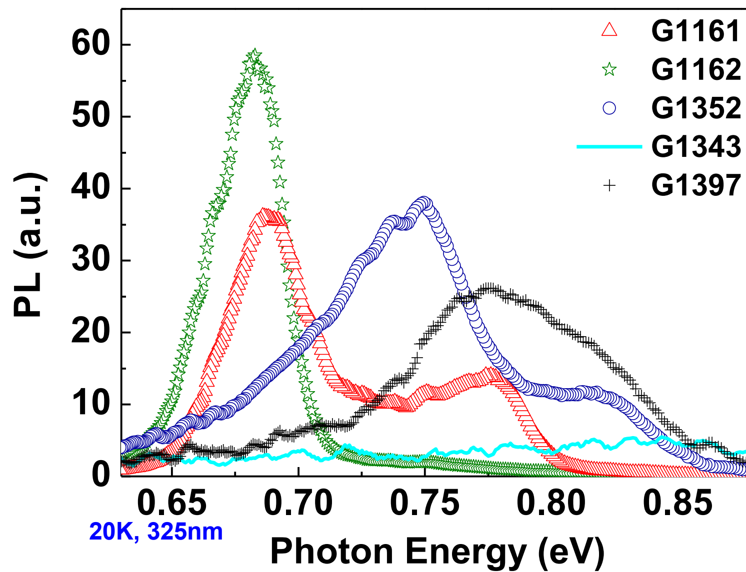

Figure 7.12 *20K PL spectra of InN films G1161, G1162, G1343, G1352 and G1397 grown on Si (111), using different buffer layer schemes. The growth structures are described in Table 7.2.*

Optical transmittance measurements were carried out only on samples G1161 and G1162 at 300K. The absorption coefficient (α) was calculated from the measurements and the absorption edge of the samples was determined from the plots of α^2 as a function of photon energy (hν) (plots not shown) as 0.78 eV and 0.85 eV, respectively, under the assumption of parabolic direct band-edge of InN [28]. Only the weaker PL energy peak of sample G1161 out of the two samples (G1161 and G1162) on which transmittance measurements were taken coincides with the band edge value extracted from the absorption curve at 0.78 eV. This suggests that the weaker emission peak of G1161 corresponds to band-to-band electron-hole recombination.

7.4 TEM Study of InN film grown on Si (111) using GaN/AlN buffer layer

Up to date, only few efforts have focused on investigating the microstructure of InN grown on silicon substrates, either by MBE or MOVPE [4,30,31]. Despite the lattice strain and thermal coefficient mismatch increase from 8% and 53% between InN and Si, to 19% and 62% between AlN and Si, respectively, AlN remains a better wetting layer for wurtzite growth on Si. The transmission microscopy investigation, carried out by collaborators (Prof. Th. Kehagias and Prof. Ph. Komninou) at the Physics department of Aristotle University of Thessaloniki, is focused on understanding the effects of a buffer layer, consisting of a GaN/AlN bilayer on the microstructure of the InN epilayer. This buffer layer resulted to the superior InN properties, according to the previous presented results. Sample G1161 of Table 7.3 is employed for this study.

Fig. 7.13(a) is a bright-field XTEM image along the $[11\bar{2}0]_{III\text{-}N}/[1\bar{1}0]_{Si}$ zone axis showing the film morphology and defect structure. A smooth and compact InN film is observed with no de-cohesion from the substrate surface or other interfaces in the structure in agreement with FE-SEM observations shown in Fig. 7.11(b). The higher bond strength of AlN, in comparison to SiNx, naturally deprives Si access to N-species and inhibits the formation of SiNx. Threading dislocations (TDs) constitute the predominant structural defects. A significant reduction of the threading dislocation density is observed after the first ~200 nm of film thickness, owing to dislocation annihilation interactions. Such interactions are more common between threading dislocations with *a*-type Burgers vector components and lead to the formation of dislocation loops as can be observed in Fig. 7.13(a). V-defects are observed at the points of the threading dislocations' emergence on the film's surface, signifying that many dislocations reaching the surface comprise of *c*-type Burgers vector components [32]. The film was found to have N-polarity as determined by comparing experimental convergent beam electron diffraction (CBED) patterns [Fig. 7.13(b)] with simulated ones obtained by using the EMS software [33] shown in Fig. 7.13(c). The selected-area electron diffraction (SAED) pattern obtained along the $[11\bar{2}0]_{III\text{-}N}/[1\bar{1}0]_{Si}$ zone axis of G1161 is also shown in Fig. 7.13(d). The determined epitaxial relationship in-between InN/GaN/AlN/Si are $(0001)_{III\text{-}N}/(111)_{Si}$, and $[11\bar{2}0]_{III\text{-}N}/[1\bar{1}0]_{Si}$.

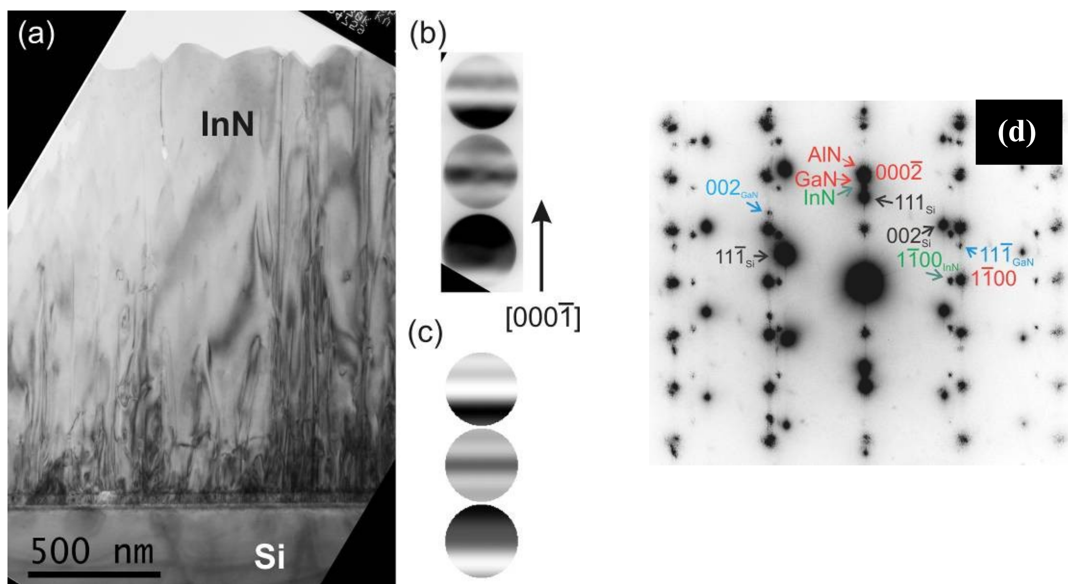

Figure 7.13 *(a) Bright-field XTEM image of the whole heterostructure viewed along the $[11\bar{2}0]$ zone axis. (b) and (c) Experimental and simulated CBED patterns obtained along the $[10\bar{1}0]$ zone axis. (d) SAED pattern along the $[11\bar{2}0]_{III\text{-}N}/[1\bar{1}0]_{Si}$ zone axis. Reflections in black letters are from Si, reflections in red letters are from wurtzite GaN and AlN, and in green letters from InN. Reflections in blue letters are from sphalerite GaN.*

Fig. 7.14(a) and 7.14(b) are dark-field XTEM images recorded under two-beam diffraction conditions with **g** 0002 and **g**$1\bar{1}00$ respectively. In Fig. 7.14(a), only the TDs with *c*-type Burgers vector components are visible, in accordance with the **g.b** ≠ 0 visibility criterion, whereas two thirds of the population with *a*-type Burgers vector components are the only visible TDs in Fig. 7.14(b). Mixed-type TDs with *a*+*c* Burgers vector component are visible in both images and are arrowed. It is

observed that in the middle and top of the film the density of *a*+*c* and *c*-type TDs is larger than that of *a*-type ones. In addition to loops, *a*-type TDs are also terminated by basal stacking faults. Dislocation density measurements were performed at 400 nm and 800 nm film thickness taking into account the 3/2 correction factor for *a*-type Burgers vector components, as well as the variation of the thickness of the TEM foil from the substrate up to the surface. The results are indicated in Table 7.4. A significant reduction in the density of *a*-type threading (ETDs) dislocations with increasing thickness is observed. However, the *a*+*c* dislocations (Mixed TDs) and *c*-type dislocations (STDs) are relatively unaffected. The overall threading dislocation density at 800 nm is 2.6×10^{10} cm^{-2}. At 100 nm from the buffer layer the overall threading dislocation density is significantly higher, i.e. ~ 5×10^{10} cm^{-2}.

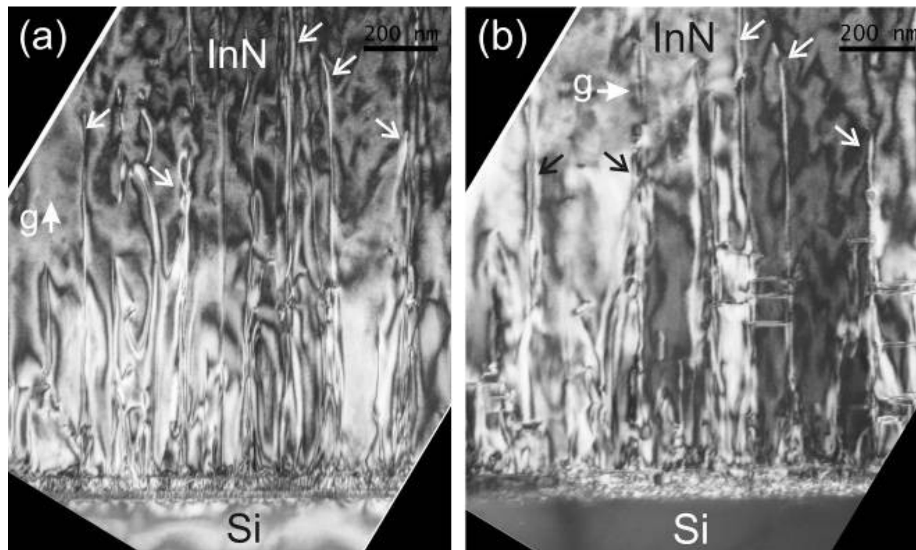

Figure 7.14 *(a) XTEM two-beam dark-field image, off the* $[11\bar{2}0]$ *zone axis with* **g** *0002. (b) Two-beam dark-field image with* **g** $1\bar{1}00$. *Mixed-type threading dislocations are arrowed.*

Table 7.4 *Threading dislocation density measurements in the InN epilayer.*

Distance from buffer layer	*a*-type edge ($\times 10^{10}$ cm^{-2})	*c*-type screw ($\times 10^{10}$ cm^{-2})	*a*+*c* type mixed ($\times 10^{10}$ cm^{-2})
400 nm	1.54 (±0.26)	1.55 (±0.25)	1.03 (±0.18)
800 nm	0.53 (±0.07)	1.30 (±0.20)	0.85 (±0.15)

The effect of the buffer layer interfaces in reducing the threading dislocation density is illustrated in Figs. 7.15(a) and 7.15(b), which were taken under two-beam conditions with **g** 0002, so that the interfaces are viewed edge-on. It is observed that the AlN buffer is heavily faulted whereas GaN exhibits threading dislocations with a density of the order of 10^{11} cm^{-2}, as well as inversion domain boundaries (IDBs). However, most defects terminate at the heteroepitaxial interfaces. No IDBs are observed in the InN epilayer.

The nanostructure of the epilayer and GaN/AlN buffer layer was studied by HRTEM. Fig. 7.16(a) is HRTEM image showing the structure of the AlN/Si and GaN/AlN interfaces. It is seen that the AlN/Si interface is crystalline with no intermediate amorphous SiN_x layer. However, the first monolayers of AlN up to a thickness of ~10 nm are heavily faulted, containing a large density of stacking faults. The GaN/AlN interface exhibits roughness probably as a result of coalescence of islands from the initial 3D growth mode. The reflections in blue letters in Fig. 7.13(d) are from sphalerite GaN, which are due to pyramidal-shaped nanocrystals inside the GaN buffer layer, with height of ~20 nm and diameter of ~100 nm. Such a nanocrystal is shown in Fig. 7.16(b), where all other periodicities have been filtered out for clarity, using masking in Fourier space. These large cubic 'pockets' abut on the GaN/AlN interface and hence their nucleation has to be attributed to the interfacial roughness that causes excessive local stacking disorder.

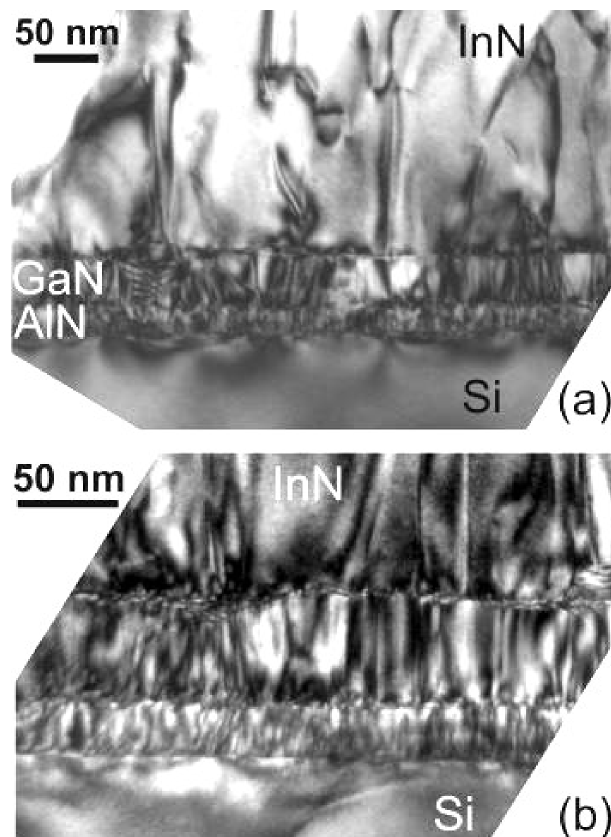

Figure 7.15 *(a) XTEM two-beam bright-field image of the buffer layers taken off the* $[11\bar{2}0]$ *zone axis with* ***g*** *0002. (b) XTEM two-beam dark-field image off the* $[11\bar{2}0]$ *zone axis with* ***g*** *0002.*

However, in this heterostructure the structural imperfection of the InN/GaN interface is further promoted by the large threading dislocation density in the GaN buffer layer. Threading dislocations terminating at the InN/GaN interface introduces depressions that are then overgrown in a faulted manner. Such a rather large depression is illustrated in the HRTEM image of Fig. 7.18(d). Such areas act as sources of threading dislocation with *c*-type Burgers vector components due to height differences during nuclei coalescence and could be responsible for the high density of screw dislocation found in this InN epilayer on Si.

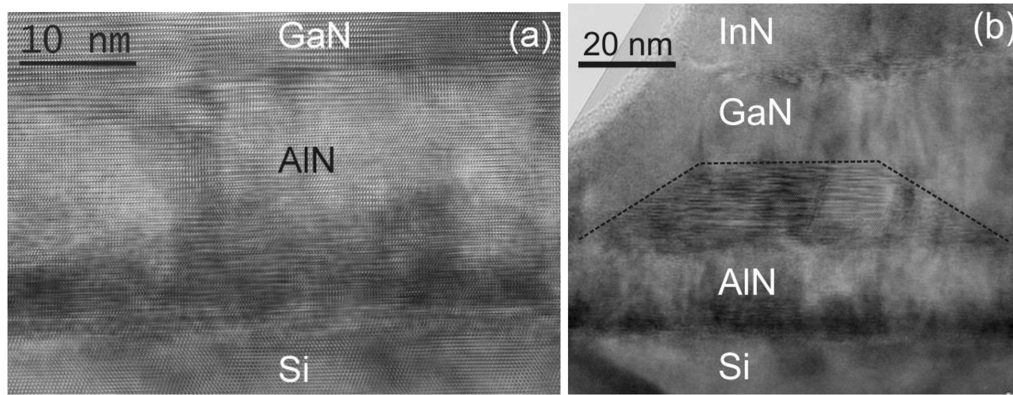

Figure 7.16 *Cross-sectional HRTEM filtered images along the* $[11\bar{2}0]$ *zone axis, showing the buffer layer heterostructure. In (a) the AlN buffer layer is shown. The AlN/Si interfacial region is crystalline but exhibits a large stacking fault density. The GaN/AlN interface is rough. In (b) a nanocrystal of sphalerite GaN grown on AlN is indicated by a dotted line. All other periodicities have been filtered out.*

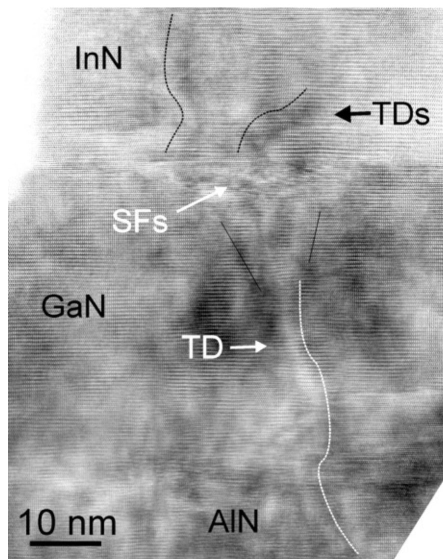

Figure 7.17 *Cross-sectional HRTEM filtered image along the* $[11\bar{2}0]$ *zone axis showing a threading dislocation from the buffer layers introduce a depression at the InN/GaN interface. The distortion is a source of threading dislocations that emanate into the InN epilayer.*

7.5 Investigation of the role of thick GaN layer on the properties of InN film grown on Si (111) using a GaN/AlN buffer layer

In spite of the superb AlN wetting nature on Si, buffer layers consisting of a GaN/AlN bilayer must be used with caution during InN epitaxy. For example Fig. 7.18 shows the FE-SEM cross-sectional image of InN Film G1343 of Table 7.3. It is very clear that the GaN/AlN and AlN/Si interfaces exhibit good adhesion as expected but problem exists with the InN/GaN interface, which is characterized by voids as shown by the arrow in Fig. 7.18(a). Further observation of this InN heterostructure showed that the voids originated from the high surface roughness of the underlying GaN film, as depicted in Fig. 7.18(b). This means that interfacial adhesion's difficulty cannot be attributed only to mismatch strain build up in the heterostructure, since the surface roughness of the underlying material also plays a very important role, underscoring the importance of ensuring smooth surfaces and interfaces during InN heteroepitaxy on Si. Several investigations [1,2,34,35] have shown the difficulty of

growing a smooth-surface III-N semiconductor layer with step flow growth mechanism on Si (111), contrary to what has been experienced on (0001) sapphire.

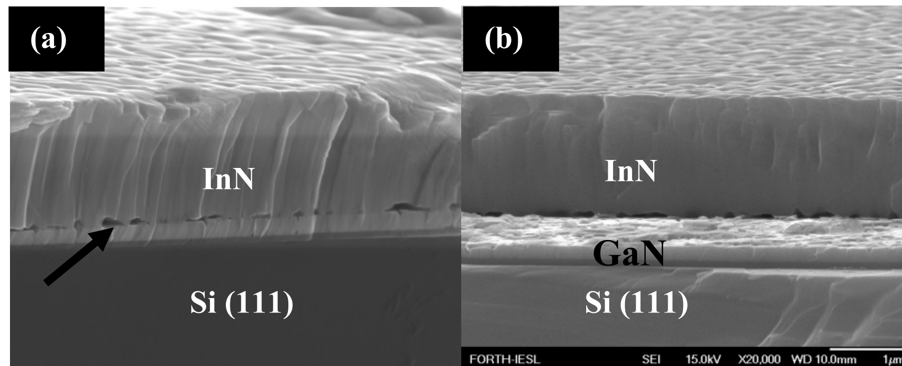

Figure 7.18 *FE-SEM micrographs of the (a) cross-sectional view of the interfacial regions of InN/GaN, GaN/AlN and AlN/Si heterojunctions of the 2μm thick InN film sample G1343. The interface of the InN/GaN is characterised by voids; indicating poor adhesion. (b) Image showing the high surface roughness of the GaN underlayer of the InN film sample G1343; suggesting that the adhesion difficulty originated from high surface defect of the GaN layer.*

In this section, the effect of thick GaN buffer layer on the growth and properties of InN on Si is investigated. Previous TEM/HR-TEM studies on sample G1161 (Section 7.4) have shown that the overgrown InN epilayer was free of inversion domain boundaries (IDBs) observed in the 50 nm GaN buffer layer. Growing a 1 μm thick GaN buffer layer prior to the InN overlayer deposition could assist our understanding of the factors that may be responsible for the propagation of IDBs in the GaN layer and their subsequent termination at the InN/GaN interface.

A 1μm thick GaN layer (G1787) was grown on Si (after the deposition of a 60 nm AlN nucleation layer), using similar conditions employed for the 50 nm GaN buffer layer of sample G1161. The growth process was optimized to obtained layer-by-layer growth of GaN. The step-flow surface morphology of the GaN sample G1787 is shown in Fig. 7.19(a). The XRD theta-2theta measurements of the GaN layer shown in Fig. 7.20(a) indicated that it is pure crystalline wurzite *c*-plane oriented layer. The XRD symmetric (0002) RC and asymmetric $(10\bar{1}5)$ RC FWHM values for the GaN epilayer were 0.31^{o} and 0.12^{o}, respectively [Table 7.4].

Table 7.4 *The structure and HRXRD symmetric (0002) and asymmetric* $(10\bar{1}5)$ *rocking curve FWHM of the optimized GaN layer G1787 and the InN film G1811 growth on such GaN layer.*

Sample	Layer Structure	*XRD (0002) RC FWHM*	*XRD* $(10\bar{1}5)$ *RC FWHM*
G1787	Optimised 1000 nm GaN/AlN/Si	0.31^{o}	0.12^{o}
G1811	Optimised 600 nm InN/GaN/AlN/Si	0.31^{o}	0.24^{o}
1μm thick GaN underlayer of G1811		0.24^{o}	0.14^{o}

A 600 nm thick InN film sample G1811 was heteroepitaxially grown on such 1μm GaN layer grown with conditions similar to sample G1787. The InN properties

were significantly improved when this thicker buffer layer was used. ‘Very sharp’ InN/GaN, GaN/AlN and AlN/Si interfaces were observed by SEM without voids and adhesion problems, as shown in Fig. 7.19(c). This result shows that obtaining smooth surfaces for the GaN and/or AlN buffer or nucleation layers grown initially on Si, is crucial for the overgrown InN structure. Moreover, the growth of a thick GaN buffer layer undoubtedly assists in smoothening the GaN surface and consequently led to more homogeneous InN nucleation and elimination of voids at the InN/GaN interface.

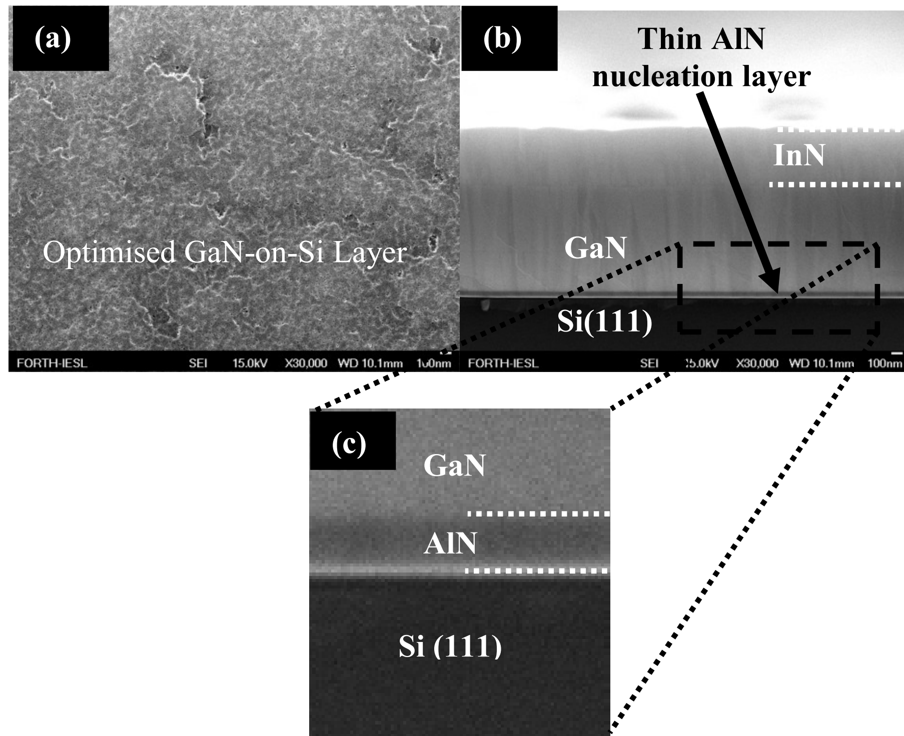

Figure 7.19 *FE-SEM micrographs showing (a) plan-view of the 1 μm thick GaN layer G1787 grown on Si, using 60 nm AlN buffer layer, showing that step-flow growth mode was followed, (b) cross-sectional view of the InN/GaN, GaN/AlN and AlN/Si interfaces that resulted from growing InN on a 1 μm thick GaN buffer layer similar to G1787 shown in (a),and (c) magnified image of the interfaces enclosed in the red box of (b).*

The theta-2theta scans shown in Fig. 7.20(b) revealed that the InN film is single crystalline and is oriented along the growth direction (*c*-axis). Despite the lower thickness of this InN film (600 nm), the obtained HRXRD (0002) RC and $(10\bar{1}5)$ RC FWHM values were 0.31^{o} and 0.24^{o}, respectively, which similar to the best value measured for the 2 μm thick InN films of Table 7.2. It also exhibited RC FWHMs that are almost the same with the optimized 1μm GaN underlayer [Table 7.4]. These results suggest that the improvement of InN film’s crystal quality depends also on the surface morphology and interfacial sharpness of the underlying buffer layer of the heterostructure on Si.

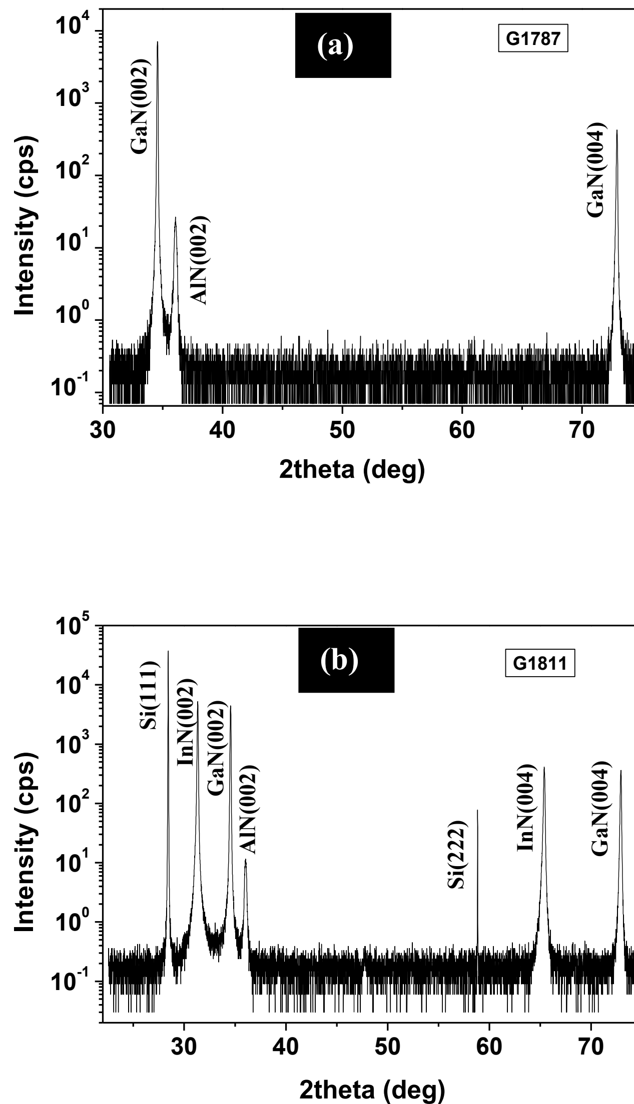

Figure 7.20 *HR-XRD theta-2theta measurements for (a) sample G1787, consisting of 1μm GaN/60 nm AlN/Si(111) and (b) sample G1811, consisting of 600 nm InN-on 1μm GaN-on-Si(111), grown with the GaN/AlN buffer layer grown under similar conditions as in sample G1787.*

The microstructure of the InN film G1811 was investigated by TEM and HRTEM. Fig. 7.21(a) shows a cross-sectional bright field TEM image taken under two-beam conditions off the $[11\bar{2}0]$GaN axis. Threading dislocations (TDs) with *c*-type Burgers vector component are visible in the image. The TD density reduces with thickness in the GaN buffer layer and in the InN epilayer, while the thin AlN nucleation layer is very defective. Fig. 7.21(b) is the corresponding dark-field image of the same region of the film. The different interfaces of the G1811 heterostructure are very sharp, in agreement with the lower magnification imaging by FE-SEM [Figs. 7.19(b) and 7.19(c)].

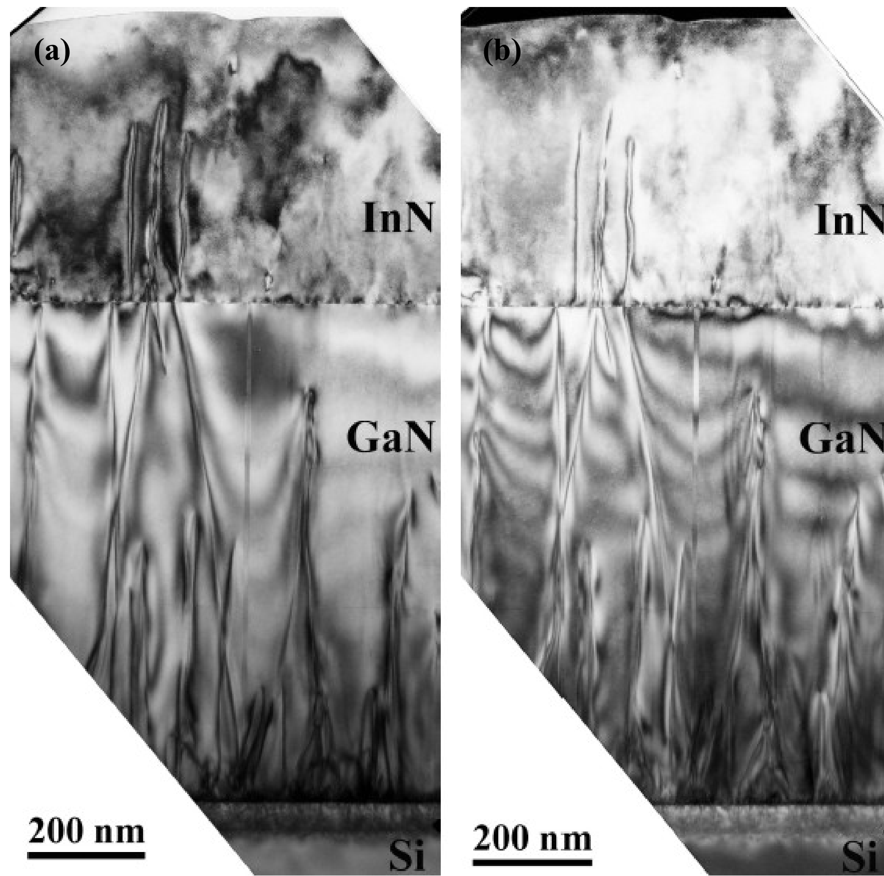

Figure 7.21 *TEM results for sample G1811: (a)Cross-sectional bright-field TEM image, taken under two-beam conditions off the [1120]GaN/[110] Si axis, with* ***g*** *0002 GaN/InN (b) Cross-sectional dark-field TEM image, taken under two-beam conditions off the [1120]GaN/[110] Si axis, with* ***g*** *0002 GaN/InN.*

Fig. 7.22 (a) is a two beam bright-field image of the film showing threading dislocations with an *a*-type Burgers vector component. The GaN layer seems to contain a higher defect density in comparison to the InN layer. The density of TDs with a *c*-type component in the InN layer is $8.5x10^9$ cm^{-2}, while it is slightly increased in the GaN layer to $3.5x10^{10}$ cm^{-2}. The density of TDs with an *a*-type component in the InN layer is $4x10^{10}$ cm^{-2} while in the GaN buffer layer is $8x10^{10}$ cm^{-2}. These results indicate that the use of a thick (1μm) GaN buffer layer slightly reduced the STD density in the InN layer from $1.5x10^{10}$ cm^{-2} to $8.5x10^9$ cm^{-2}, when compared with sample G1161, which employed thin (50 nm) GaN buffer layer [Table 7.4]. On the contrary, the ETD density exhibited a slight increase from $1.5x10^{10}$ cm^{-2} (for sample G1161 with thin GaN buffer layer) to $4x10^{10}$ cm^{-2} (for 1 μm thick GaN buffer layer sample G1811).

Figs. 7.22 (b) and 7.22 (c) show the InN/GaN interface. The GaN/InN interface appears to be rather sharp, even though inversion domain boundaries (IDBs) were observed in the GaN layer and they propagate across the entire layer up to the GaN/InN interface where they were terminated. IDBs have also been observed in the thin GaN buffer layer of G1161 [Fig. 7.15] but no IDBs were observed in the overgrown InN epilayer. The thicker nature of the GaN buffer layer of G1811 allows the IDB density to be estimated as $4x10^7$ cm^{-2}.

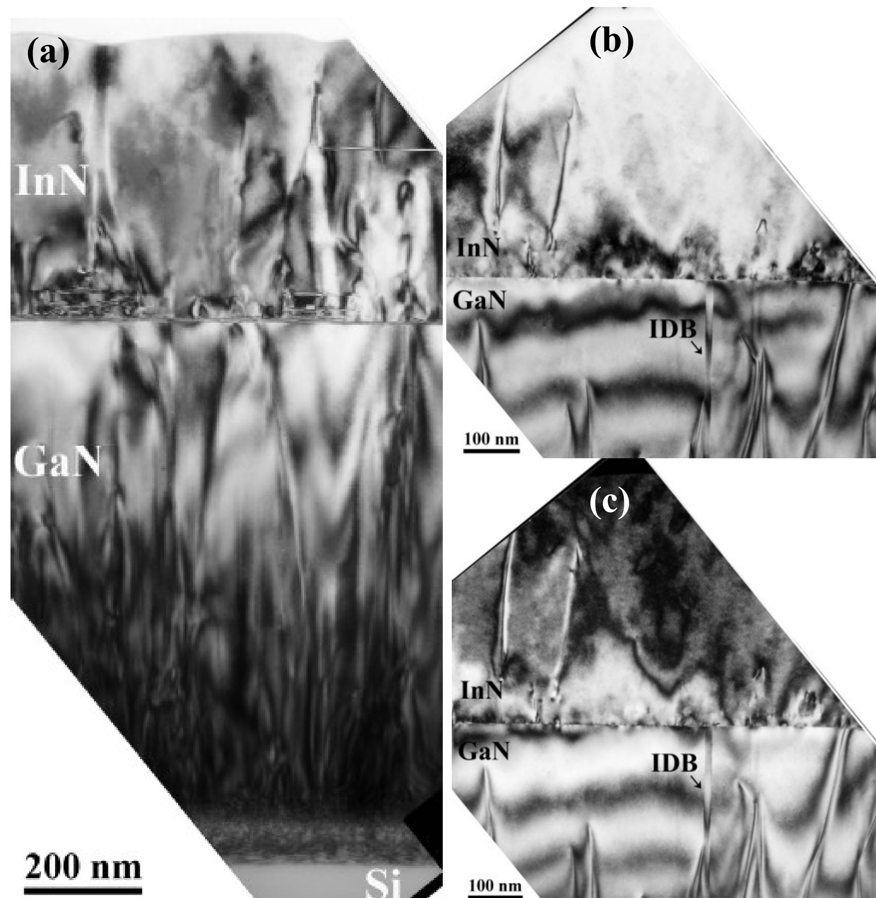

***Figure** 7.22 TEM study of sample G1811: (a) Cross-sectional bright-field TEM image, taken under two-beam conditions off the [1120]GaN /[110] Si axis, with **g** 1010 GaN/InN, showing TDs with an a-type Burgers vector component (b) Cross-sectional bright-field TEM image, taken under two-beam conditions off the [1120]GaN /[110] Si axis, with **g** 0002 GaN/InN, showing the GaN/InN interface. (c) Cross-sectional dark-field TEM image, taken under two-beam conditions off the [1120]GaN/[110] Si axis, with **g** 0002 GaN/InN, showing the GaN/InN interface.*

7.6 Concluding remarks

The heteroepitaxy of InN on Si (111) has been investigated. Direct InN growth on Si, using the optimised growth conditions applicable to the molecular beam epitaxy of InN on MOVPE grown (0001) GaN/Al_2O_3 pseudo-substrates, did not result to step-flow growth mode on the Si (111) surface. Rather, the growth proceeded with columnar InN growth, characterised with coarse, granular surface morphology and poor interface adhesion, with microcracks observed in the bulk of 2 μm thick InN epilayers. Moreover, direct nucleation of InN on Si (111) always results to the formation of unintentional amorphous Si_xN_y layer at the InN/Si interface independent of the III/V flux ratio conditions employed. In order to optimise the growth of InN films on Si, different intermediate layers comprising of InN, GaN, GaN/AlN and AlN were investigated. A thin nucleation layer grown at low temperature (LT-InN) allows the overgrowth of a 2 μm thick InN film with improved surface morphology and without microcracks, compared to InN growth directly on Si

at high temperature. The initiation of growth on Si by an AlN nucleation layer and a possible GaN buffer layer, prior to the growth of the InN epilayer, resulted to high structural quality films with excellent interfacial adhesion. Moreover, the growth of a thick 1 μm GaN buffer layer on the AlN nucleation layer undoubtedly assists in achieving smooth surface morphology on the GaN surface, typical of step-flow growth. The homogeneous nucleation of InN on the smooth GaN surface led to a higher crystal quality InN epilayer and elimination of voids at the InN/GaN interface.

Transmission electron microscopy revealed that chemically and structurally sharp InN/GaN interface was achieved on Si, using a buffer layer consisting of a GaN/AlN bilayer. TEM also confirmed the relaxation of lattice mismatch strain of the InN epilayer through misfit dislocation arrays. The buffer layer interfaces were effective in reducing the threading dislocation density in the heterostructure through dislocation annihilation interactions. The GaN buffer layer always contained a higher defect density in comparison to the overgrown InN epilayer. When a 1 μm thick GaN buffer layer was employed, the density of TDs with a *c*-type component and *a*-type component in the InN layer was $8.5x10^{9}$ cm^{-2} and $4x10^{10}$ cm^{-2}, respectively, while both TD densities were slightly increased in the GaN buffer layer to $3.5x10^{10}$ cm^{-2} and $8x10^{10}$ cm^{-2}, respectively. This 0.48 μm thick InN-on-Si (111) film compares favourably with InN layers grown on GaN/(0001) sapphire pseudo-substrates. In these layers, the densities of TDs with a *c*-type component have been reported as $3.5x10^{10}$ cm^{-2} [36], $1.1x10^{9}$ cm^{-2} [37], $0.5x10^{8}$ cm^{-2} [38] for thicknesses of 0.5 μm, 1.5 μm and 10 μm, respectively, whilst the reported densities of *a*-type component TDs are $2.2x10^{10}$ cm^{-2} [39], 35 $x10^{10}$ cm^{-2} [37], 4.4 $x10^{9}$ cm^{-2} [38] for InN layer thicknesses of 0.75 μm, 1.5 μm and 10 μm, respectively. A striking difference between the use of thin (50 nm) and thick (1 μm) GaN buffer layer for InN growth on Si is that with the thicker GaN buffer layer the InN exhibits TD density approximately 10^{10} cm^{-2} that is about one order less than what was obtained in the case of the thinner GaN buffer layer. Although IDBs were always observed in the GaN buffer layer, independently of its thickness, none of the InN epilayers exhibited these defects, since IDBs propagating through the GaN buffer layer were always terminated at the InN/GaN interface.

In general, even though direct growth on Si is a required step for InN integration with the Si technology, the difficulties commonly encountered with the direct growth on Si are potential setbacks to make this a reality. This investigation has shown that the optimum growth conditions for layer-by-layer growth of InN films on GaN (0001) cannot be used for direct growth on Si (111). InN growth on Si (111) thus requires its own nucleation and growth procedure, different from the one commonly used for growth on GaN-on-sapphire templates, for high quality InN heteroepitaxy on Si (111).

References

1. J. Grandal, M.A. Sánchez-García, *J. Cryst. Growth* **278**, 373 (2005)
2. C.-L. Wu, C.-H. Shen, H.-Y. Chen, S.-J. Tsai, H.-W. Lin, H.-M. Lee, S. Gwo, T.-F. Chuang, H.-S. Chang, T.M. Hsu, *J. Cryst. Growth* **288**, 247 (2006)
3. B. Maleyre, S. Ruffenach, O. Briot, B. Gil, A. Van der Lee, *Superlattices and Microstruct.* **36**, 517 (2004)
4. K.J. Chang, J.Y. Chang, M.C. Chen, S.M. Lahn, C.J. Kao, Z.Y. Li, W.Y. Uen, G.C. Chi, *J. Vac. Sci. Technol. A* **25**, 701 (2007)
5. H.-J Gossmann and L.C Feldman, *Appl. Phys. A* **38**, 171 (1985)
6. H. Hibino, T. Fukuda, M. Suzuki, Y. Homma, T. Sato, M. Iwatsuki, K. Miki and H. Tokumoto, *Phys. Rev. B* **47**, 13027 (1993).
7. S. D. Solares, S. Dasgupta, P. A. Schultz,Y-H Kim, C. B. Musgrave, and W. A. Goddard III, *Langmuir* **21**, 12404 (2005)
8. P. P. Auer and W. Mönch, *Surf. Sci.* **80**, 45 (1979)
9. D. J. Chadi, R. S. Bauer, R. H. Williams, G. V. Hansson, R. Z. Bachrach, J. C. Mikkelsen Jr., F. Houzay, G. M. Guichar, R. Pinchaux, and Y. Pétroff *Phy. Rev. Lett.* **44**, 799 (1980)
10. Y. Zhou, C. Zhou, H. Zhan, Q. Wu, J. Kang, *Materials Science in semiconductor Processing* **9**, 279 (2006)
11. T. Hoshino, K. Kumamoto, K. Kokubun, T. Ishimaru, I. Ohdomari *Phys. Rev. B* **51**, 14594 (1995)
12. M. Hoshino, Y. Shigeta, K. Ogawa, and Y. Homma, *Surf. Sci.* **365**, 29 (1996)
13. F. Peiro, A. Cornet, A. Herms, J.R. Morante, A. Georgakilas, G. Halkias, *J. Vac. Sci. Technol. B* **10**, 2148 (1992)
14. G. O. Krause, *Phys. Status Solidi (a)* **3**, 899 (1970)
15. E. Dimakis, E. Iliopoulos, K. Tsagaraki, A. Georgakilas, *Appl. Phys. Lett*. **86**, 133104 (2005)
16. E. Dimakis, E. Iliopoulos, K. Tsagaraki, A. Georgakilas, *Phys. Status Solidi (a)* **203**, 1686 (2006)
17. E. Dimakis, E. Iliopoulos, M. Kayambaki, K. Tsagaraki, A. Kostopoulos, G. Konstantinidis, A. Georgakilas, *J. Elect. Mater.* **36**, 373 (2007)
18. A. Krost and A. Dadgar, *Proceedings of 12th International Conference on Semiconducting & Insulating Materials, IEEE*, p. 41 (2002)
19. N. Chaaben, T. Boufaden, A. Fouzri, M.S. Bergaoui, B. El Jani, *Applied Surface Science* **253**, 241–245 (2006)
20. O Ambacher, *J. Phys. D: Appl. Phys*. **31**, 2653 (1998)
21. E. Dimakis, E. Iliopoulos, K. Tsagaraki, A. Adikimenakis, A. Georgakilas, *Appl. Phys. Lett.* **88**, 191918 (2006)
22. E. Dimakis, E. Iliopoulos, K. Tsagaraki, Th. Kehagias, Ph. Komninou, A. Georgakilas, *J. Appl. Phys.* **97**, 113520 (2005)
23. M A Moram and M E Vickers *Rep. Prog. Phys*. **72**, 036502 (2009)
24. X. Wang, S-B. Che, Y. Ishitani, A. Yoshikawa, *Appl. Phys. Lett*. **90**, 151901 (2007)
25. H. Lu, W.J. Schaff and L.F. Eastman, J. Wu, W. Walukiewicz, D. Look, R.J. Molnar, *Mat. Res. Soc. Symp. Proc.* **743**, L4.10.1 (2003)
26. W. Walukiewicz, J.W. Ager III, K.M. Yu, Z. Liliental-Weber, J. Wu, S.X. Li, R.E. Jones, J.D. Denlinger, *J. Phys. D: Appl. Phys.* **39**, R83–R99 (2006)
27. Y. Nanishi, Y. Saito, T. Yamaguchi, M. Hori, F. Matsuda, T. Araki, A. Suzuki, T. Miyajima, *Phys. Status Solidi (a)* **200**, 202 (2003)

28. A. Georgakilas, in "*CAS 2008 Proceedings*" (IEEE, 2008) 43
29. B. R. Nag, *J. Cryst. Growth* **269**, 35 (2004)
30. Z. Y. Li, S. M. Lan, W. Y. Uena, Y. R. Chen, M. C. Chen, Y. H. Huang, C. T. Ku, S. M. Liao, T. N. Yang, S. C. Wang, and G. C. Chi, *J. Vac. Sci. Technol. A* **26**, 588 (2008)
31. M. A. Sánchez-García, J. Grandal, E. Calleja, S. Lazic, J. M. Calleja, and A. Trampert, *Phys. Status Solidi (b)* **243**, 1490 (2006)
32. P. Vennégùes, B. Beaumont, M. Vaille, and P. Gibart, *Appl. Phys. Lett.* **70**, 2434 (1997)
33. P. A. Stadelmann, *Ultramicroscopy* **74**, 131 (1987)
34. N. Chaaben, J. Yahyaoui, M. Christophersen, T. Boufaden, B. El Jani, *Superlattices and Microstruct*. **40**, 483 (2006)
35. Y-H Wang and W-L Chen, *Physica E* **41**, 848 (2009)
36. K. A. Wang, T. Kosel, and D. Jena, *Phys. Status Solidi (c)* **5**, 1811 (2008)
37. C. S. Gallinat, G. Koblmüller, Feng Wu, and J. S. Speck, *J. Appl. Phys*. **107**, 053517 (2010)
38. E. Dimakis, J. Domagala, A. Delimitis, Ph. Komninou, A. Adikimenakis, E. Iliopoulos, A. Georgakilas, *Superlattices and Microstruct*. **40**, 246 (2006)
39. C. J. Lu, L. A. Bendersky, Hai Lu, and William J. Schaff, *Appl. Phys. Lett*. **83**, 2817 (2003)

8 Optimisation of InN nucleation for direct heteroepitaxy on Si

8.1 Introduction to direct InN epitaxy on Silicon substrates

8.2 Study of InN nucleation on Si (111) substrates

8.3 Heteroepitaxy of InN on Si (111) using different nucleation layers (NLs)

8.4 Epitaxy of InN film on Si (111) using an optimised InN NL

8.5 Investigation of the microstructure of InN-on-Si (111) films

8.6 Concluding remarks

8.1 Introduction to direct InN epitaxy on Silicon substrates

Heteroepitaxy of high-quality group-III-nitrides is very attractive for optoelectronic and electronic devices and growing the III-nitrides on silicon should provide an added advantage of low cost production and/or monolithic integration with Si integrated circuits (ICs). InN is a promising material for sub-THz electronic devices due to its very high electron mobility and maximum electron drift velocity [1-4]. The growth of high-quality InN or InN-rich InGaN or InAlN on Si may allow the monolithic integration of optoelectronic devices with Si ICs. This heteroepitaxial material technology will also permit the harnessing of the InN potential for the development of high-efficiency and low-cost solar cells, by forming InN-based/Si tandem structures [5,6], where layers of varying III-N alloy composition can be stacked to maximize absorption of the solar spectrum with the remarkable range of band gap tuning made possible by changing the In concentration within the material system.

Various researchers have investigated the influence of growth parameters, like buffer layers [7,8] and substrate temperature [7,9], on the crystalline quality of InN epilayers on Si. In most cases, an AlN intermediate layer is initially grown on Si to provide a III-nitride surface for the nucleation of InN [7-13]. Although the direct growth of InN on Si presents the advantage of lower lattice mismatch, compared to InN growth on GaN or AlN and AlN growth on Si, previous studies of direct deposition of InN films on Si showed that such films are usually polycrystalline [14] and/or characterised by grain boundaries, micro-cracks (in thicker layers), granular surface morphology and poor interfacial adhesion [10,12,15,16] while those grown with the use of an intermediate layer of GaN/AlN or AlN did not exhibit such defects [10,11,13]. The observed differences in InN growth on Si, when compared with its growth on GaN, should be related to weaker bonds at the InN/Si interface compared to the InN/GaN interface, which would change the favourable growth mode and affects the extent of unintentional nitridation of the Si surface from the incoming nitrogen beam at the initiation of growth, leading to extensive amorphous silicon nitride (Si_xN_y) layer formation at the InN/Si interface [13,14,16], and consequently poor morphology and structural quality of the overgrown InN film [10,14,16]. The formation of such interfacial unintentionally deposited Si_xN_y has also been acknowledged for GaN growth on Si [17,18].

For these reasons, we have emphasised in the previous Chapter that the optimum growth conditions for layer-by-layer growth of InN films on GaN (0001) pseudo-substrate cannot be used to directly grow a high crystal quality InN film, with step-flow surface morphology, on Si (111). This means that direct InN nucleation on Si (111) should require growth conditions typically different from those commonly used for InN nucleation on GaN pseudo-substrates. However, the direct epitaxy of InN on Si and the formation of InN/Si heterojunctions may be very important for some device applications like vertical conduction light-emitting diodes and solar cells, with Si backside contact and InN/Si solar cell devices with active role of the InN/Si heterojunction. To date, there have been no reports on the optimization of direct InN nucleation on Si, underscoring the importance of developing a successful nucleation procedure for high quality InN heteroepitaxy on Si (111). In this study, the possibility of eliminating growth deficiencies like microcracks, weak InN-Si interfacial adhesion, columnar InN structure, and granular surface morphology, which are obtainable

whenever InN is grown directly on Si (111), has been targeted. The success of this optimisation study will enable taking advantage of the smaller lattice mismatch of 8% for InN heteroepitaxy on Si, eliminating the intermediate wide-band gap barriers for vertical conduction InN devices on Si and realizing InN/Si heterojunction devices.

As a first step, the effects of growth temperature (T_{sub}) and III/V flux ratio on the nucleation of InN on Si (111) substrates by PAMBE, was studied. The samples consisted of 70 monolayers (ML) InN deposited on high resistivity (>1000 Ω.cm) boron-doped Si (111) substrates. All samples were grown after the substrates' thermal cleaning in the growth chamber produced a 7x7 surface reconstruction. The N-flux was fixed for an equivalent N-limited growth rate of 450 nm/h, which corresponds to operation of the plasma source with gas flow and RF power conditions of 0.36 sccm and 300 W, respectively. When necessary, only the In flux was changed to vary the III/V flux ratio. Different substrate temperatures (T_{sub}) from 225°C to 550°C were employed in the study. The effects of T_{sub} and III/V flux ratio on the surface morphology and structural quality of the nucleation layers were basically investigated using *in-situ* RHEED and *ex-situ* SEM, EDX and AFM.

In the second step, selected nucleation layers' growth conditions were engaged for the epitaxial growth of thicker InN films on Si (111) and the effects of these nucleation conditions on the surface morphology, crystal mosaicity, microstructure, and the electrical and optical properties of the InN films were studied using FE-SEM, AFM, HR-XRD, TEM/HRTEM, Hall-effect, photoluminescence and transmittance measurements.

8.2 Study of InN nucleation on Si (111) substrates

In this section, the effect of growth temperature (T_{sub}) and III/V flux ratio on 70 ML InN films that were directly nucleated on Si (111) is discussed. The growth experiments were divided into three groups. In the first group (G_1), the role of T_{sub} was investigated by keeping the flux of N fixed at 450 nm/h and using a III/V flux ratio of 0.8 (slightly nitrogen rich conditions) to avoid In accumulation on the InN thin film surface for T_{sub} in the range from 225 to 550°C. Eight samples labelled A to H (as given in Table 8.1) were grown for the investigation. The second group (G_2) consisting of four samples, labelled I to L, were grown on Si using T_{sub} from 225 to 400°C but under a very low III/V flux ratio of 0.2 instead of the almost stoichiometric conditions used for the G_1 set. For the third group (G_3), the effect of III/V flux ratio on the properties of InN thin film deposited on Si (111) was investigated by varying the ratio of the In to N beam equivalent pressure from 0.2 to 0.8 at a fixed substrate temperature of 225°C. The RHEED was used to monitor the InN crystallinity and surface morphology during the growth process. The details of the different growth conditions employed for the InN samples of each group and the RHEED diffraction patterns are given in Table 8.1.

For set G_1, the RHEED patterns were generally characterised by diffused light and rings, suggesting the presence of significant crystal disorder in the surface layer that diffracts the electron beam. Diffraction spots indicative of a rough surface crystalline InN film were also apparent at the end of 70 ML deposition. A spotty RHEED pattern was visible during the entire InN deposition only for the high T_{sub} of 470°C (sample F), suggesting the presence of large 3D islands on the surface from the initial stages of growth. A dark RHEED screen was observed for the highest T_{sub} =

550°C (sample H), indicating that InN could not be synthesized at this temperature due to fast thermal decomposition.

Table 8.1 *Growth conditions, RHEED patterns and AFM rms surface roughness of 70 ML InN thin films directly grown on Si (111) substrates. The experiments are divided into three groups; (i) G_1 = 8 samples labelled A to H: the T_{sub} was varied from 225 to 550°C while the III/V flux ratio was kept constant at 0.8, (ii) G_2 = 4 samples labelled I to L: the T_{sub} was varied from 225 to 400°C while the III/V flux ratio was kept constant at 0.2 and (iii) G_3 = 4 samples labelled M to P: III/V flux ratio was varied from 0.2 to 0.8 while T_{sub} was kept constant at 225°C. In all experiments, the N-flux was 450 nm/h.*

Group	Sample	T_{sub} (°C)	III/V flux ratio	Initial RHEED Pattern	Final RHEED pattern	10x10 µm² rms roughness (nm)
G_1 III/V = 0.8 T_{sub} varied	A ≡ G1180	225	0.8	Diffused rings	Diffused rings and spots	0.6
	B ≡ G1176	250	0.8	Diffused rings	Diffused rings and spots	2.7
	C ≡ G1195	300	0.8	Rings	Rings and spots	2.2
	D ≡ G1177	400	0.8	Rings	Rings and spots	3.4
	E ≡ G1260	440	0.8	Rings	Rings and spots	4.6
	F ≡ G1258	470	0.8	Dark and spotty	Spotty and darker	20
	G ≡ G1178	500	0.8	Dark and rings	Very dark	43.9
	H ≡ G1194	550	0.8	Turned dark immediately	Very dark and unobservable	90
G_2 III/V = 0.2 T_{sub} varied	I ≡ G1196	225	0.2	Diffused	Elongated spots	0.4
	J ≡ G1315	250	0.2	Diffused rings and spots	Diffused elongated spots	1
	K≡ G1312	300	0.2	Rings	Brighter and rings	3
	L≡ G1317	400	0.2	Spots	Rings	4.7
G_3 III/V varied T_{sub} = 225°C	M≡ I ≡ G1196	225	0.2	Diffused	Elongated spots	0.4
	N≡ G1319	225	0.4	Diffused and rings	Spots and rings	0.46
	O ≡ G1318	225	0.6	Rings	Rings	0.5
	P ≡ A ≡ G1180	225	0.8	Diffused rings	Diffused rings and spots	0.6

The SEM plan-view images shown in Fig. 8.1 give comprehensive information about the nucleation and morphology of the 70 ML InN layers grown at different T_{sub}. It is noticeable from the micrographs that InN maintains a fairly smooth surface with good InN coverage for T_{sub} from 225 to 300°C [Figs. 8.1(a) – 8.1(c)]. Above this temperature, uniformly distributed InN grains with similar grain sizes are observed up to 440°C [Figs. 8.1(d) and 8.1(e)], corresponding to significantly increased surface roughness. Beyond 440°C, Si substrate's surface coverage with InN became unsustainable [Figs. 8.1(f)-1(h)]; leading to the formation of a non-uniform

distribution of islands/grains. The Si surface is visible in between the islands/grains. EDX examinations confirmed the non-existence of InN but only Si in the open regions in-between islands/grains [Figs. 8.2 to 8.4].

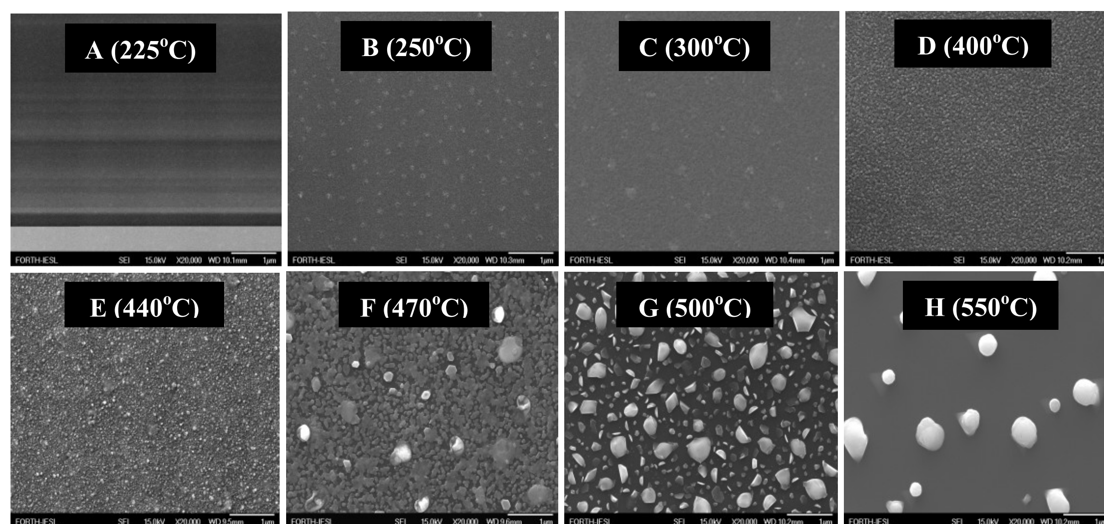

Figure 8.1 *SEM micrographs showing the surface of 70 ML InN films grown on Si (111) under the same In/N flux ratio of 0.8 and In flux of 360 nm/h but different substrate temperatures: (A) 225°C, (B) 250°C, (C) 300°C, (D) 400°C, (E) 440°C, (F) 470°C, (G) 500°C, (H) 550°C.*

At 470°C [Fig. 8.1(f)], the spotty RHEED pattern observed for G1258 was increasingly darker with growth time; suggesting the initiation of decomposition of InN. EDX analyses of the white grains observed on the surface of G1258 are showed in the regions enclosed in the black dotted circle of the SEM micrograph of Fig. 8.2. The quantitative analyses indicate that the clusters contain equal percentage of In (10%) and N (10%), suggesting a stoichiometric representation of In and N in the clusters and thus, confirm that the clusters are InN. The 80% of Si detected are from the Si substrate. The measurements of the islands enclosed in the white dotted circle in Fig. 8.2 suggest only a small amount of In (2%) and N (4%). These islands could be stoichiometric InN as the error of the measurement is high due to the small amount of these materials. Moreover, metallic In clusters are indeed not favourable under the slightly N-rich growth conditions employed and the short growth duration required for 70 ML of InN film to be deposited.

On increasing the T_{sub} to 500°C, the RHEED became very dark and well separated InN Islands of various sizes were formed on the Si surface, as shown in Fig. 8.1(g). Increase of the temperature from 470°C to 500°C appeared to enhance the decomposition and only few large clusters (flakes) appear on the surface. An almost similar percentage of In (55%) and N (45%) was detected in the flakes, according to the EDX spectra of Fig. 8.3. Since the deviation from stoichiometric In and N composition in the flakes is within the error margin, we can reasonably conclude that these islands are InN.

At 550°C, the RHEED was completely dark, indicating the presence of a metallic In layer on the surface. The darkening of the RHEED with no pattern observable agrees with the findings of Dimakis *et al*. for InN deposition on

GaN(0001) pseudo-substrate at temperature higher than 500°C, where InN decomposition rate rapidly increases [19]. EDX investigation [Fig. 8.4] revealed that the composition of the clusters observed on the substrate's surface [Fig. 8.1(h)], consisted of 22% In, 11% N and 67% Si. The wide divergence of In and N values indicates a non-stoichiometric amount of In and N in the cluster. Moreover, these clusters did not exhibit either hexagonal or cubical shape and are therefore believed to be an amorphous mixture of In-N-Si. Only Si was detected in the region enclosed with the white dotted ring in Fig. 8.4.

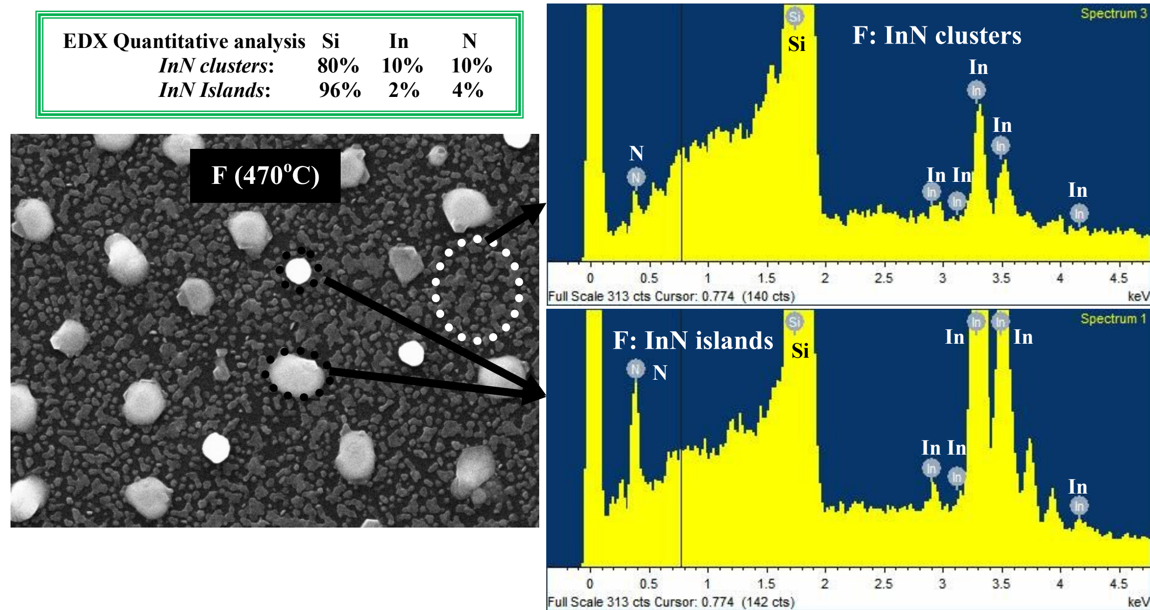

Figure 8.2 *EDX quantitative analyses and spectra for InN sample F (G1258) grown on Si (111) under In/N flux ratio of 0.8 and substrate temperature of 470°C, showing that the clusters (black rings) and islands (white ring) from the FE-SEM micrograph are InN.*

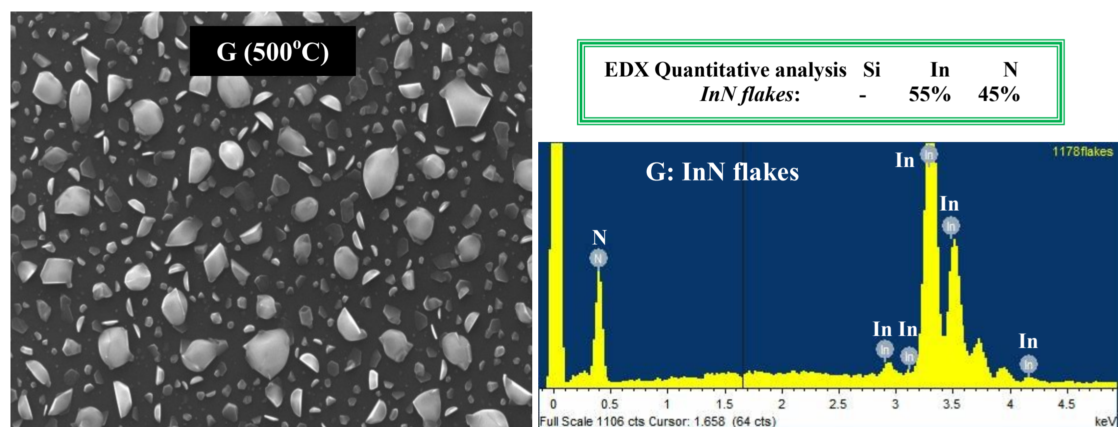

Figure 8.3 *EDX quantitative analyses and spectra taken from the apparent clusters (or flakes) in the FE-SEM micrograph of InN sample G (G1178), showing that the clusters are InN. The InN sample was grown on Si (111) under In/N flux ratio of 0.8 and substrate temperature of 500°C.*

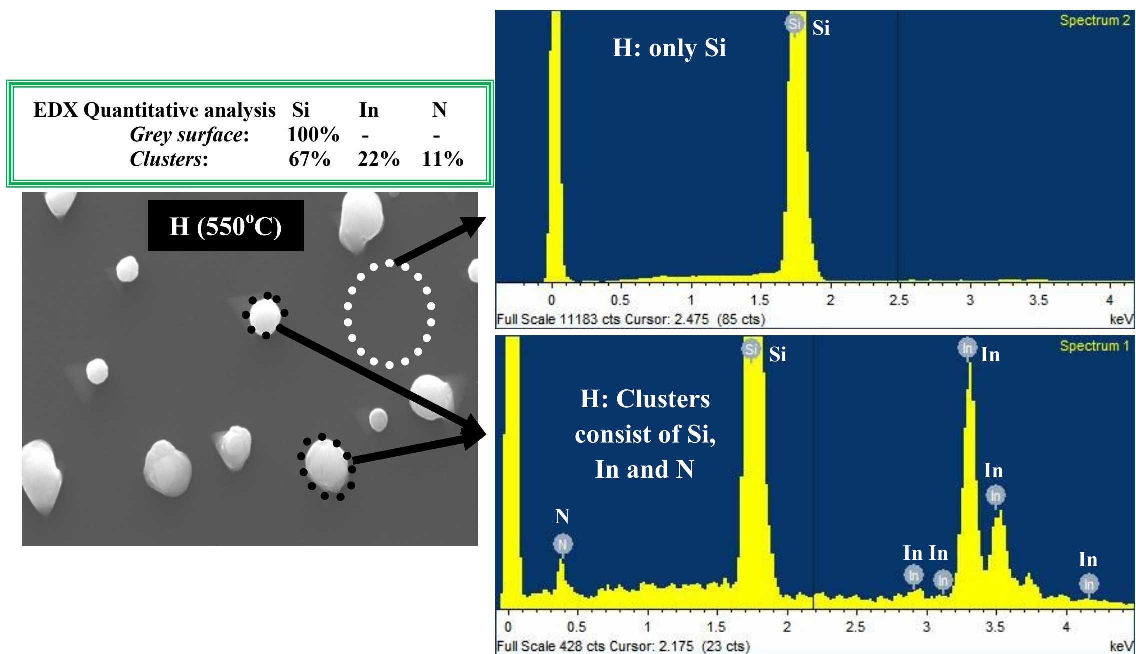

Figure 8.4 *EDX quantitative analyses and spectra for InN sample H (G1194) grown on Si (111) under In/N flux ratio of 0.8 and substrate temperature of 550°C, showing that the terrace (white ring) is bare Si while In, Si, and N co-exist in a non-stoichiometric proportion in the clusters (black rings).*

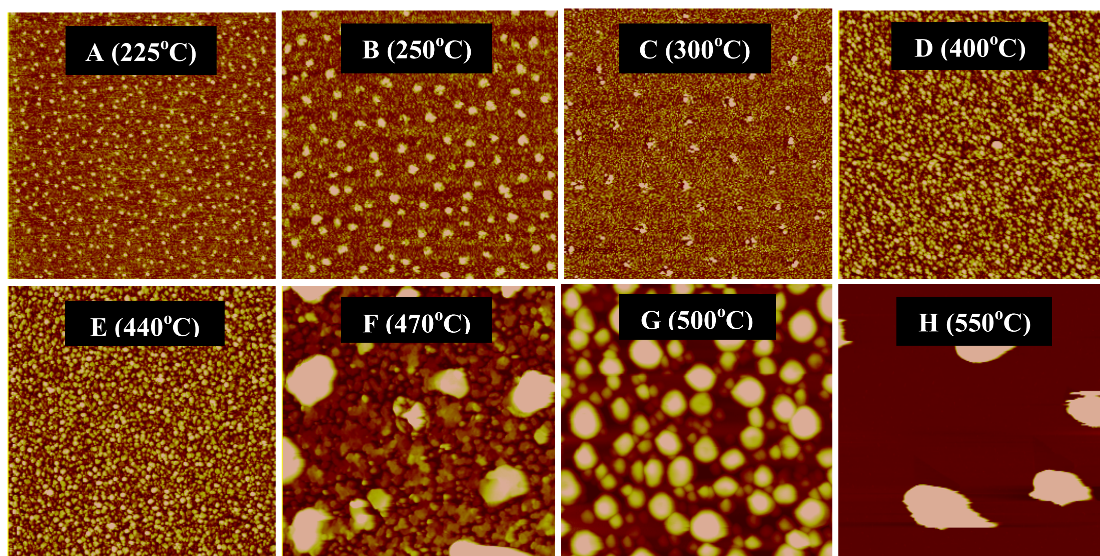

Figure 8.5 *5x5μm^2 AFM micrographs of the 70 ML InN thin films grown on Si (111) under constant In/N flux ratio of 0.8 and In flux of 360 nm/h but different substrate temperature: (A) 225°C, (B) 250°C, (C) 300°C, (D) 400°C, (E) 440°C, (F) 470°C, (G) 500°C, (H) 550°C. The z-axis full scale is 5.18 nm, 15.65 nm, 17.51 nm, 20.29 nm, 21.92 nm, 122.17 nm, 141.96 nm, and 394.73 nm, respectively.*

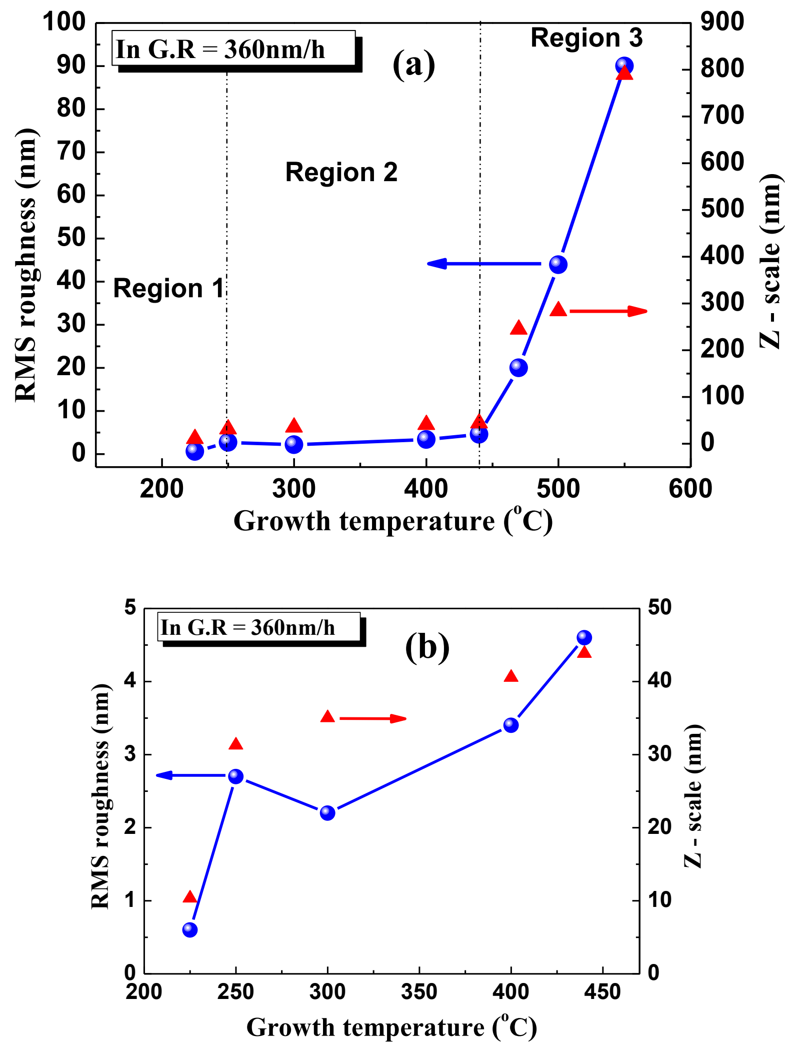

Figure 8.6 *The rms roughness, determined from 10x10 μm² AFM scans, for the surface of 70 ML InN films grown on Si (111) at different growth temperatures. The InN films were grown using a constant III/V flux ratio of 0.8. (a) Plots of rms surface roughness (circle symbol) and corresponding z-axis full scale (triangle symbol) as functions of* T_{sub}. *Different regions of sharp increase in surface roughness are identified by Region 1 to 3. (b) A zoomed image of Regions 1 and 2 showing a clear view of the relationship between* T_{sub} *and the surface roughness of the InN films.*

The corresponding 5 x 5 μm² AFM micrographs of these samples are shown in Fig. 8.5, and appear to be consistent with the FE-SEM images of Fig. 8.1. High degradation in the surface morphology is observed at growth temperatures above 440°C. The estimated rms surface roughness from the 10 x 10 μm² AFM micrographs and the corresponding *z*-axis full scale are plotted as functions of the growth temperature in Fig. 8.6. According to Fig. 8.6(a), the rms roughness (line with circle symbol) appears to increase monotonically with substrate temperature from 0.6 nm to 90.0 nm. Regions of sharp increase in surface roughness are identified as Regions 1 to 3. A very slow, almost linear increase of the surface roughness occurs from 225°C to

440°C [see a zoomed image of this region in Fig. 8.6(b)] while an abrupt increase, supposedly promoted by InN decomposition, occurs for temperatures above 440°C. Similar trend is observed in the figure for the *z*-axis full scale of each image (depicted by triangle symbols) with respect to the growth temperatures. The InN thin film A grown at the lowest T_{sub} of 225°C manifested the smoothest surface morphology with rms surface roughness of 0.62 nm [Fig. 8.1(a) and Table 8.1].

The growth temperatures employed for the deposition of InN thin film samples D, E and F (400, 440 and 470°C, respectively) are within the range of the optimum T_{sub} for the growth by PAMBE of high crystal quality In-polar InN (0001) [9,20-22]. For T_{sub} in the range of 400-450°C, InN can be grown by step-flow growth mode directly on a GaN (0001) pseudo-substrate. However, polycrystalline [7] or columnar [11] InN layers always result in the case of direct InN growth on Si (111). In the present experiment, ring patterns were observed during the InN thin films' deposition at 400 and 440°C, from growth initiation to completion [Table 8.1]. Exhibition of ring patterns suggests the nucleation of polycrystalline InN films. However, when 470°C was employed, spotty diffraction pattern and the darkening of the screen as growth time prolongs were observed.

Figs. 8.7(a), 8.7(b) and 8.7(c) give the 2x2 μm^{2} AFM micrographs of samples D, E and F, respectively, for a clearer observation of the InN surface morphology. A columnar structure that depends on the T_{sub} is evident for these three samples. The area density of the columns reduces while their lateral dimensions increase with increasing substrate temperature. The columnar structure of the samples is indicative of the 3D growth mode of InN on Si (111) and the increasing diffusion lengths of the atoms on the surface with increasing T_{sub}. The formation of an amorphous silicon nitride layer between the initially nucleated InN 3D islands may also influence the InN nucleation and stabilize the columnar InN growth on Si (111), under conditions that result to compact InN films on GaN (0001) surfaces.

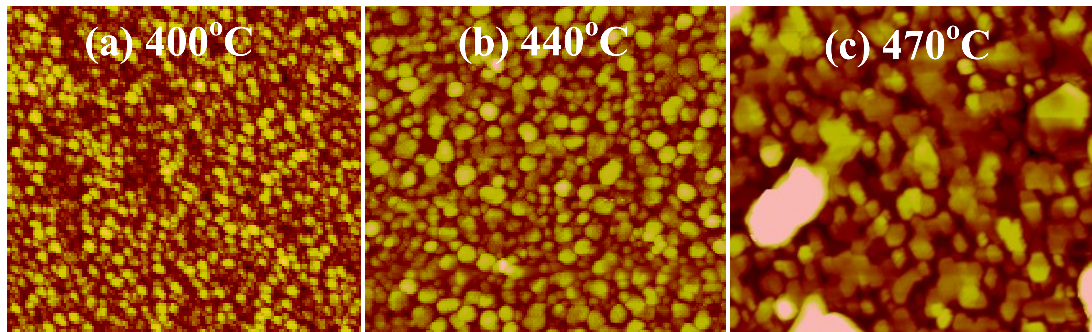

Figure 8.7 *2x2 μm^{2} AFM micrographs showing the surface morphology of 70 ML InN films for (a) sample D, (b) sample E and (c) sample F, grown directly on Si (111) substrate at 400°C, 440°C and 470°C, respectively. The evolution of grainy/columnar morphology in the InN thin film samples, which were grown within the range of growth temperatures at which step-flow growth of InN film on GaN(0001) pseudo-substrate is obtainable, reveals why grainy surface morphology and columnar InN structure are inevitable at these temperatures for direct growth on Si.*

The conclusion from G_1 experiments is that InN nucleation on Si at the lowest T_{sub} = 225°C is preferable, since it could result to a high density of islands forming a

compact 70 ML InN film with reasonable rms roughness of 0.6 nm, through coalescence of the 3D InN islands. However, a significant crystal disorder appears in this layer according to the mixture of rings and spots that was observed by RHEED.

The second set of experiments involved group G_2 from Table 8.1, which consists of samples I to L. The 70 ML InN samples were grown at T_{sub} ranging from 225-400°C directly on Si (111) under an extremely N-rich growth conditions (III/V flux ratio = 0.2) rather than the III/V flux ratio of 0.8 employed in the previous G_1 experiments. The RHEED patterns of these InN thin films exhibited a trend toward ring diffraction patterns, with increasing growth temperature, under the highly N-rich growth condition employed. Only the sample I (grown at the lowest T_{sub} = 225°C) exhibited elongated-spotty pattern. As shown in Fig. 8.8, the 5x5 μm^2 AFM micrographs of the surface of the four thin film samples also revealed different degrees of smoothness. It should be pointed out that the z-scale increases from 5.48 nm (T_{sub} = 225°C) in Fig. 8.5(a) to 28.41 nm (T_{sub} = 400°C) in Fig. 8.5(d). The 3D growth evolution becomes evident as the growth temperature increases.

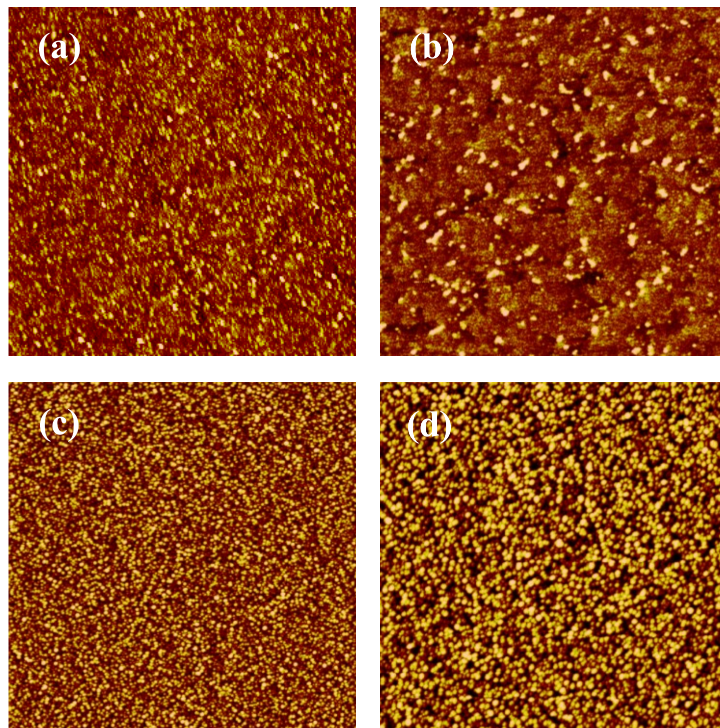

Figure 8.8 *5x5μm^2 AFM micrographs showing the surface morphology of 70 ML InN thin film samples grown on Si (111) at different temperatures with the use of constant III/V flux ratio = 0.2 (a) sample I at 225°C. (b) sample J at 250°C (c) sample K at 300°C and (d) sample L at 400°C. The z-axis full scale is 5.48 nm, 6.36 nm, 13.38 and 28.41 nm, respectively.*

The rms values of surface roughness, determined from the 10x10 μm^2 AFM micrographs, are plotted in Fig. 8.9 against the used T_{sub}. Similarly to the trend obtained in Fig. 8.6(b), the rms surface roughness of these InN thin films monotonically increases with increasing growth temperature. The lowest rms surface roughness was exhibited again by the thin film grown at the lowest T_{sub} of 225°C. These results indicate that the use of a very low T_{sub} is a key requirement for nucleating InN with good surface morphology on Si (111). Moreover, a slight

reduction in the rms value to 0.4 nm is observed for when In/N flux ratio of 0.2 was used (sample I), in comparison to the 0.6 obtained for an In/N flux ratio of 0.8 (sample A) [Table 8.1].

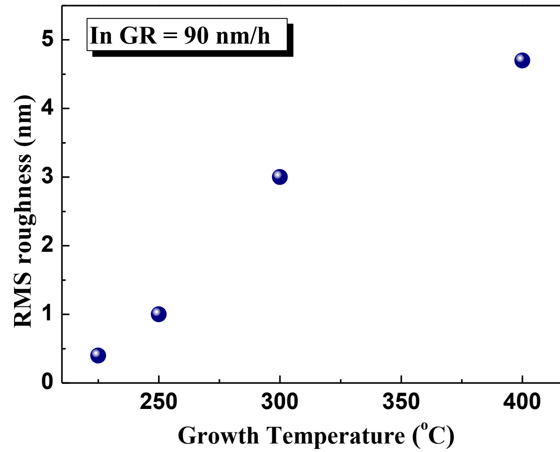

Figure 8.9 *Dependence of the 10x10 μm^2 AFM rms surface roughness on growth temperature for InN thin films grown on Si using a constant III/V flux ratio = 0.2.*

Having established the requirement of a very low T_{sub} (225°C) as key to the reduction of the surface roughness of InN thin film grown on Si (111), the next step was to study the effect of III/V flux ratio in the range from 0.2 to 0.8 by keeping the optimised T_{sub} = 225°C constant. Stoichiometric In to N flux ratio growth condition was continually avoided in the investigation to ensure that metallic In accumulation will not occur on the deposited thin film's surface. This third set of experiments produced samples M to P of G_3 in Table 8.1.

All the investigated III/V flux ratios resulted to ring RHEED patterns at InN growth initiation, except sample M (or I) grown with III/V flux ratio of 0.2. The transformation of the initial RHEED pattern of sample M from diffused to elongated spots after deposition of ~ 9 ML InN indicates the nucleation of well-ordered 3D islands with fast coalescence into a continuous film exhibiting significantly reduced crystal disorder and surface roughness in comparison to samples N, O, and P grown at higher III/V flux ratio, as shown in Table 8.1.

The rms roughness of the surface of these samples, estimated from the 10 x 10 μm^2 AFM micrographs, is plotted against the III/V flux ratio in Fig. 8.10. It is evident that the lowest rms surface roughness of 0.4 nm was obtained for sample M, which was deposited by using the lowest III/V flux ratio. This result is in agreement with the RHEED observations, since this was the only film that exhibited elongated spotty pattern [Table 8.1]. An almost linear dependence of the InN rms surface roughness on III/V flux ratio is observed in Fig. 8.10. The roughness increased with increasing In flux, with the nitrogen flux kept constant at 450 nm/h. In general, all the films investigated exhibited rms surface roughness that is $\leq$ 0.6 nm, indicating that improved surface smoothness could be achieved for InN thin films when deposited on Si at low substrate temperature, irrespective of the III/V flux ratio.

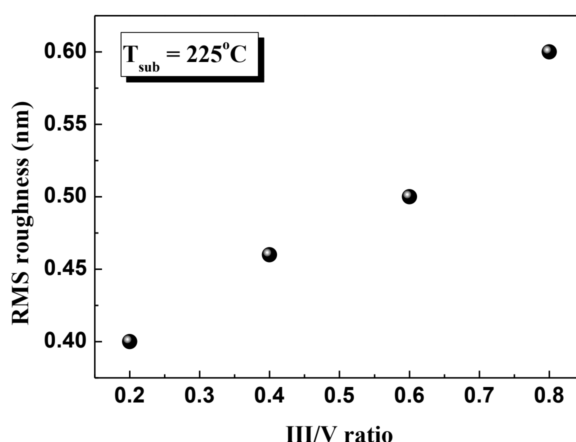

Figure 8.10 *Plot of the 10x10 μm^2 AFM rms roughness determined for the 70 ML InN films grown on Si (111) at 225°C versus III/V flux ratio.*

In general, these results underscore the fact that the surface morphology of InN thin films grown directly on Si substrates is highly sensitive to the growth temperature while exhibiting weaker dependence on the III/V flux ratio. The rms roughness values increase at a rate approximately equal to 2 nm for every 100°C increase in T_{sub} from 225°C (0.4 nm) to 450°C (4.7 nm), as shown in Figs. 8.6 and 8.9. On the other hand, when the T_{sub} is fixed at a low value of 225°C, the rms surface roughness mildly increased from 0.4 nm to 0.6 nm as the In/N flux ratio increased from 0.2 to almost stoichiometric flux ratio [Fig. 8.10].

The high N-flux is known to limit the diffusion length of III-atoms on the substrate surfaces (fast bonding of III atoms). Thus, the combination of high N-flux and very low T_{sub} would increase the density of nucleated 3D InN islands on Si. The coalescence of a high density of small 3D islands into a continuous film occurs at an earlier stage compared to nucleation of lower density 3D islands with larger individual size. This leads to a smoother surface of the continuous film that results from the 3D island's coalescence. It also protects the Si surface from extensive nitridation due to its fast full coverage by InN material. In fact, the cross-sectional TEM (which shall be discussed in Section 8.4 of this Chapter), gives clear confirmation of the discussed growth mechanism.

Using the results of this investigation, we propose that the simultaneous engagement of low T_{sub} and highly N-rich growth conditions for InN nucleation on Si could provide an adequate smooth InN surface on Si, which can be used as template for the continuation of InN growth at the optimum growth conditions ($T_{sub} \approx 450^o$C, III/V flux ratio ≈ 1).

8.3 Heteroepitaxy of InN on Si (111) using different nucleation layers (NLs)

The conclusions of the previous section were also confirmed by actual growth of 0.5 μm thick InN films on different 70 ML nucleation layers following a two-step growth process [Fig. 8.11]. The aim was to identify the effect of each NL on the final InN overlayer. The selected NLs growth conditions are similar to those employed for the growth of InN samples M, L, P and D of Table 8.1 and the films grown on these

NLs shall be referred to as films FM, FL, FP and FD, respectively. Table 8.2 gives a brief description of the grown samples. The expected nominal thickness of each of the InN epilayers is 500 nm. All the films were grown at 440°C under slightly N-rich (III/V flux ratio = 0.93) to avoid metallic In accumulation on the surfaces during growth. Such In accumulation on the surface can inhibit the growth process.

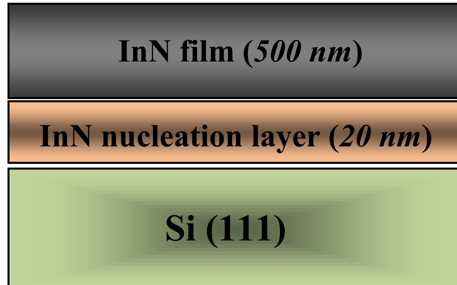

Figure 8.11 *Typical structure of the InN films grown by a two-step process on Si (111) substrates. The different growth conditions of the InN NLs are given in Table 8.2.*

As expected, no In droplets were observed on any of the InN epilayers' surfaces by optical microscopy. FE-SEM cross-sectional micrographs revealed distinctively different cross-sectional morphologies for the films grown on the various NLs [Fig. 8.12]. In the case of sample FM, the use of N-rich LT-InN NL resulted to a continuous InN film with flat surface and an excellent InN/Si interfacial adhesion [Fig. 8.12(a)], comparable to that of the InN/GaN interface on sapphire (0001) [23] or the InN/AlN on Si (111) and AlN/Si interfaces [10]. On the contrary, it is evident from Fig. 8.12(b) that sample FL could not achieve full coalescence of the initially formed crystallites/islands from the high T_{sub} of InN NL. Samples FP [Fig. 8.12(c)] and FD [Fig. 8.12(d)] that employed InN NLs grown at low T_{sub} [Fig. 8.11(b)] and high T_{sub} [Fig. 8.11(d)], respectively, exhibited improved coalescence of the initially formed islands compared to sample FL [Fig. 8.12(b)]. However, Fig. 8.12(d) indicates that sample FD also exhibited a porous columnar film structure.

Table 8.2 *Growth conditions for the 20 nm InN nucleation layers (NLs) employed for the two-step growth of 500 nm InN epilayers on Si (111) substrates at 440°C and under slightly N-rich growth conditions (III/V flux ratio = 0.93).*

Sample	NL T_{sub} (°C)	NL III/V flux ratio	NL initial RHEED Pattern	NL final RHEED pattern
FM = G1716	225	0.2	Diffused	Elongated spots
FL = G1717	400	0.2	Spots	Rings
FP = G1718	225	0.8	Diffused rings	Diffused rings and spots
FD = G1719	400	0.8	Rings	Rings and spots

The FE-SEM plan-view micrographs of these InN samples are shown in Fig. 8.13. The surface morphology of the samples also shows different features, although the surfaces were generally characterised by rough, 3D facetted surface morphology. Sample FM evidently exhibited the smoothest surface.

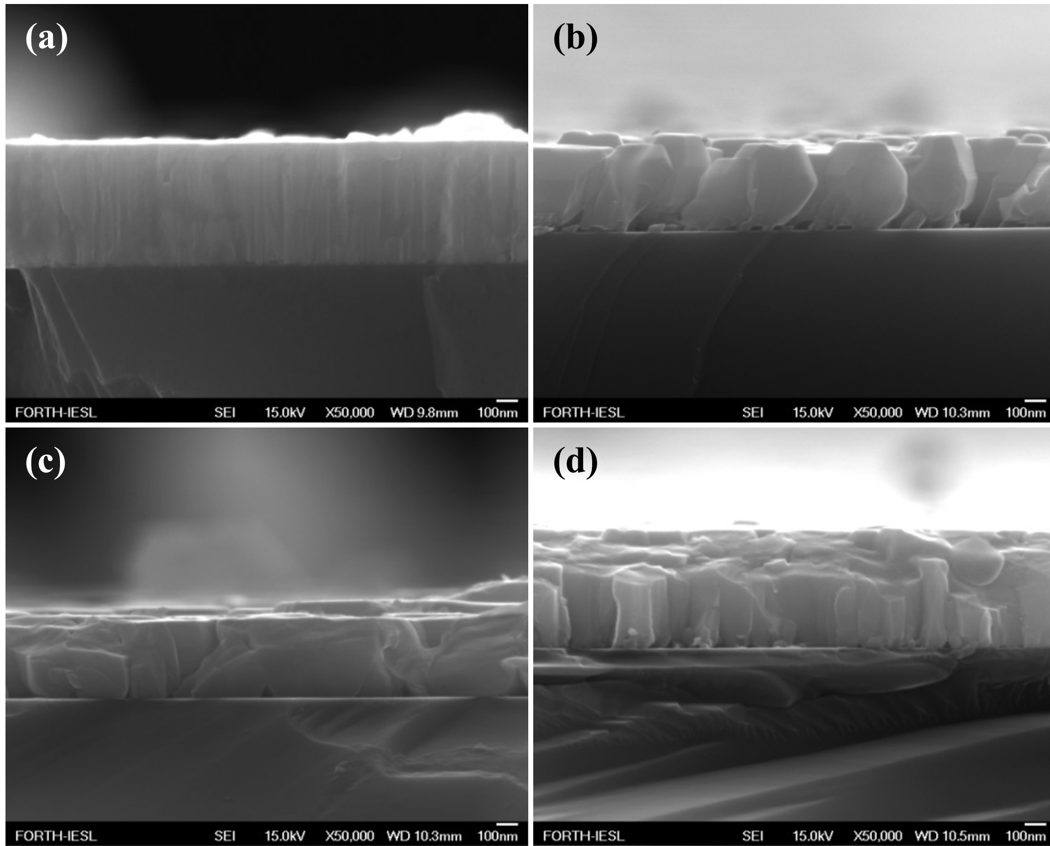

Figure 8.12 *(a) FE-SEM images showing the cross-sectional view of the InN epilayers grown on Si (111) at 440°C, using different InN nucleation layers described in Table 8.2: (a) sample FM, (b) sample FL, (c) sample FP and (d) sample FD.*

The 2x2 μm^2 AFM micrographs of the InN samples shown in Fig. 8.14 give higher resolution images of the surfaces and are in agreement with the FE-SEM observations. The appearance of steps equivalent to approximately 1 ML step height on sample FM's surface [Fig. 8.14(a)], indicates that the used NL provided an efficient template for InN (0001) overgrowth by 2D growth mode. The high rms roughness of 2.18 is mainly attributed to the slightly N-rich growth conditions employed for the main InN film growth. It is believed that a more uniform and smoother surface morphology would have been achieved under a stoichiometric [22,24] or slightly In-rich In/N flux ratio [20,21]. On the contrary, samples FL, FP and FD generally evolved with 3D growth mode and trenches corresponding to the boundaries of large 3D InN islands/columns are observed on their surfaces. The 2 x 2 μm^2 AFM rms surface roughness was 9.96 nm, 12.60 nm and 4.68 nm, respectively, in comparison to 2.81nm for sample FM [Table 8.3]. These results indicate that a LT-InN NL deposited under highly N-rich growth conditions resulted to optimum template for layer-by-layer growth of the final InN layer (sample FM).

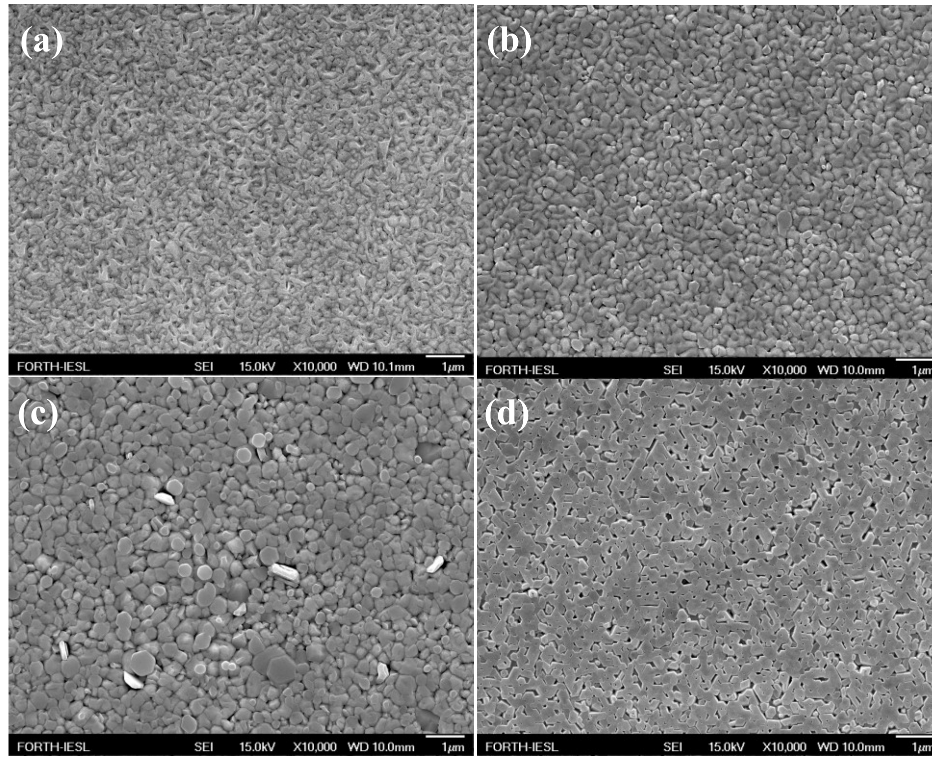

Figure 8.13 *FE-SEM plan-view micrographs of the InN epilayers grown on Si (111) at 440^oC, using different InN nucleation layers described in Table 8.2: (a) sample FM, (b) sample FL, (c) sample FP and (d) sample FD.*

Table 8.3 *Characterisation results obtained for InN films deposited on Si (111) at 440^oC, using InN nucleation layers grown under different III/V flux ratios and substrate temperatures described hereunder. AFM_{rms} is the rms surface roughness values from the 2x2 μm^2 AFM scans, RC_{FWHM} is the FWHM values of the HR-XRD rocking curves around the symmetric (0002) and asymmetric ($10\bar{1}5$) reflections of InN, N_d and μ are the apparent electron concentration and mobility determined from the Hall-effect measurements of the films, respectively.*

Sample	Nucleation Layer		AFM_{rms}	*XRD RC_{FWHM}*		N_d (x 10^{19} cm^{-3})	μ (cm^2/V.s)
	III/V ratio	T_{sub} (^oC)		(0002)	($10\bar{1}5$)		
FM	0.2	225	2.18 nm	0.98^o	0.56^o	0.85	784
FL	0.2	400	9.96 nm	2.56^o	2.20^o	1.53	773
FP	1	225	12.60 nm	3.04^o	2.70^o	1.12	730
FD	1	400	4.68 nm	3.76^o	2.20^o	1.65	528

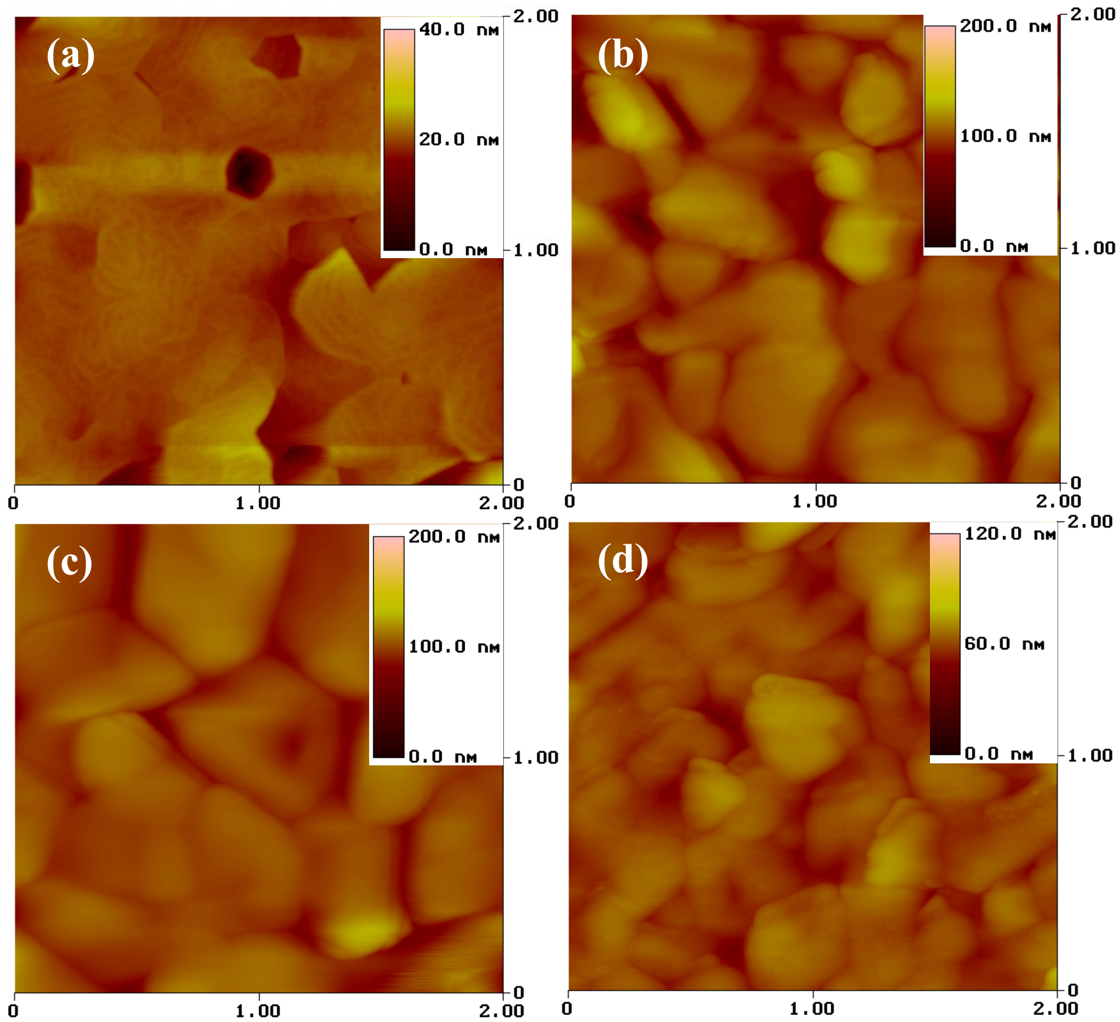

Figure 8.14 *(a) AFM micrographs of InN epilayers grown on Si (111) at 440°C, under slightly N-rich growth conditions (III/V flux ratio = 0.93), by two-step growth. The description of the growth conditions of the InN NLs employed prior to the main InN growth are given in Table 8.2: (a) sample FM, (b) sample FL, (c) sample FP and (d) sample FD with corresponding AFM rms surface roughness of 2.18 nm, 9.96 nm, 12.60 nm and 4.68 nm, respectively.*

HR-XRD θ-2θ scans confirmed that all the films were single crystalline and oriented along the *c*-axis, unlike the polycrystalline layers reported for direct InN growth on Si (111) in the literature [7,25,26]. The different nucleation conditions play a more significant role in the degree of mosaicity exhibited by the InN epilayers, which are represented by the respective rocking curves (RC) full-width at half-maximum (FWHM) values around the (0002) and $(10\bar{1}5)$ InN reflections, given in Table 8.3. Each of the nucleation layers apparently resulted to epilayer with significantly different crystal quality. Sample FM exhibits the highest crystalline quality with (0002) RC and $(10\bar{1}5)$ RC FWHM values of 0.98° and 0.56°, respectively. On the contrary, the RC FWHM values obtained for FL, FP and FD around either reflection always exceed 2° and the broadest (0002) RC FWHM was realized for FD that was nucleated on Si at high temperature, using stoichiometric III/V flux ratio. Despite the step-flow surface morphology manifested by FM, the

symmetric and asymmetric FWHM values are still very high compared to 0.31^o and 0.24^o, respectively, already achieved for InN of similar thickness grown on Si (111) using a thin GaN/AlN buffer layer (Section 7.3) or 0.08^o and 0.13^o, respectively, measured on a GaN (0001) pseudo-substrate (Section 4.4). Nonetheless, the LT-InN nucleation layer employed for the growth of FM has been able to effectively and significantly reduce the FWHM values below those reported to date for direct MBE or MOVPE InN growth on Si (111) [10,25-27].

The room temperature (RT) Hall-effect measurements data, given in Table 8.3, are consistent with the previously discussed characterisation results. The nucleation conditions employed for the epitaxy of sample FM also resulted to the best electrical properties; leading to a Hall mobility of 784 $cm^2/V.s$ and a corresponding apparent electron concentration of 8.53 x 10^{18} cm^{-3}. Sample FD, which was nucleated at high temperature and under stoichiometric III/V flux ratio, apparently demonstrated the poorest electrical properties with the mobility and carrier concentration values estimated as 528 $cm^2/V.s$ and 1.65 x 10^{19} cm^{-3}, respectively. It is important to note that the Hall mobility and apparent electron concentration values measured for the films did not show any significant difference, especially for samples FM, FL and FP, despite the notable differences in their crystal mosaicity.

InN exhibits surface electron accumulation that makes Schottky contact difficult to fabricate. Since conventional Capacitance-voltage (C-V) profiling is difficult on InN, use of electrochemical capacitance-voltage (ECV) measurement is a possible way to maneuver around this difficulty. The ECV measurements were performed by using the method previously described in Chapter 2 to further investigate the electrical properties of the InN-on-Si films FM to FD. Fig. 8.15 is the plot of the electron concentration as a function of profiling depth for the InN sample FD and is representative of those obtained for FM to FP. The results were found to be consistent with the observation of Lu *et al.*, who revealed an intrinsic surface-electron accumulation layer in the *n*-type InN samples by C-V profiling with an electron carrier concentration gradient ranging from 10^{20} to 10^{18} cm^{-3} within the depth of 6 nm from the surface of the InN [28].

Table 8.4 *Comparative results of the electrochemical capacitance-voltage (ECV) and Hall-effect measurements obtained for InN directly grown on Si (111) at 440°C, using InN nucleation layers deposited under different T_{sub} and III/V flux ratio conditions. For the nucleation layers, $L_{III/V}$ and $H_{III/V}$ indicate low and high In-flux, respectively, while LT and HT represent low and high temperature, respectively.*

Sample	InN nucleation layer growth conditions	Hall measurements		Electrochemical C-V measurements	
		N(cm^{-3})	N_s(cm^{-2})	N_{bulk} (cm^{-3})	N_s (cm^{-2})
FM	$L_{III/V}$, LT	8.53x10^{18}	3.84x10^{14}	4.5x10^{17}	2x10^{14}
FL	$L_{III/V}$, HT	1.53x10^{19}	5.52x10^{14}	$< 10^{17}$	2.8x10^{13}
FP	$H_{III/V}$, LT	1.12x10^{19}	4.47x10^{14}	3x10^{15}	1.9x10^{12}
FD	$H_{III/V}$, HT	1.65x10^{19}	7.25x10^{14}	9-10 x10^{17}	5x10^{14}

The ECV results were compared with those of the Hall-effect measurements in Table 8.4. The sheet carrier density (N_s) was determined from the ECV measurement by integrating the curves of the electron concentration (N_d) versus depletion (μm) for each sample. The calculated N_s For samples FM and FD, which is greater than 10^{14} cm^{-2}, is consistent with the Hall-effect measurements, and correlates also with the intrinsic surface accumulation density existing in *a*- and *c*-plane InN grown on *r*- and *c*-plane sapphire substrates, respectively [29]. Moreover, both FM and FD exhibit bulk electron carrier concentrations of 4.5 x 10^{17} cm^{-3} and 9.0 x 10^{17} cm^{-3}, respectively. The high discrepancy between the Hall and the ECV data for sample FL and FD, as given in Table 8.4, is attributed to the morphology and high surface roughness of both films [Fig. 8.12 and Table 8.3], since surface roughness plays a very important role in ECV measurement technique.

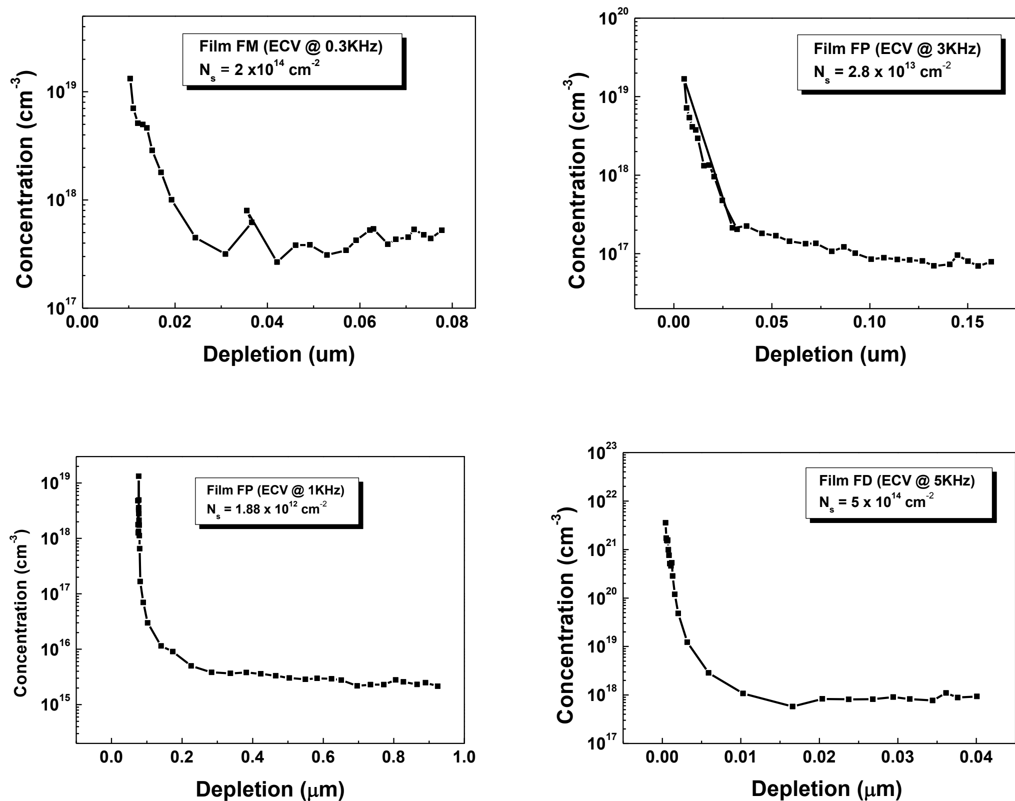

***Figure 8.15** Electron concentration versus depth determined by electrochemical C-V measurements from the surface of InN/Si (111) samples. The ECV plot for each sample is labelled accordingly. The sheet carrier density was estimated by integrating the ECV plot and the value obtained for each sample is given in Table 8.4.*

Fig. 8.16 shows the PL measurements at 20K on the InN film samples FM, FL, FP and FD. It is evident that the III/V flux ratio employed for the respective nucleation layer has a more significant effect on the emission intensity than the growth temperature. The PL emission intensity is higher for InN films FP and FD nucleated under stoichiometric III/V flux ratio and lower for FM and FL nucleated under highly N-rich growth condition. The T_{sub} of the nucleation layer plays a role only when the same III/V flux ratio is used for the deposition of the nucleation layer;

leading to higher PL emission with increased nucleation temperature. The PL emission peaks for the InN film samples are all within the range of 0.666 to 0.692 eV, which is typical of InN [Fig. 8.16 and Table 8.5].

Table 8.5 *Optical characterisation results obtained for InN on Si (111) film samples grown with different nucleation layers. For the nucleation layers, $L_{III/V}$ and $H_{III/V}$ indicate low and high In-flux, while LT and HT represent low and high temperature, respectively. N_d is the apparent electron concentration determined from the Hall-effect measurements of the films, E_{gap} is the absorption edge estimated from the transmittance measurements; E_{PL} is the 20K PL energy peak, PL_{FWHM} is the full width at half maximum evaluated from the respective InN PL spectra.*

Sample	InN nucleation layer growth conditions	N_d (x10^{19} cm^{-3})	E_{gap} (eV)	E_{PL} (eV)	PL_{FWHM} (meV)
FM	$L_{III/V}$, LT	0.85	0.715	0.692	49
FL	$L_{III/V}$, HT	1.53	0.757	0.676	49
FP	$H_{III/V}$, LT	1.12	0.746	0.686	58
FD	$H_{III/V}$, HT	1.65	0.774	0.666	51

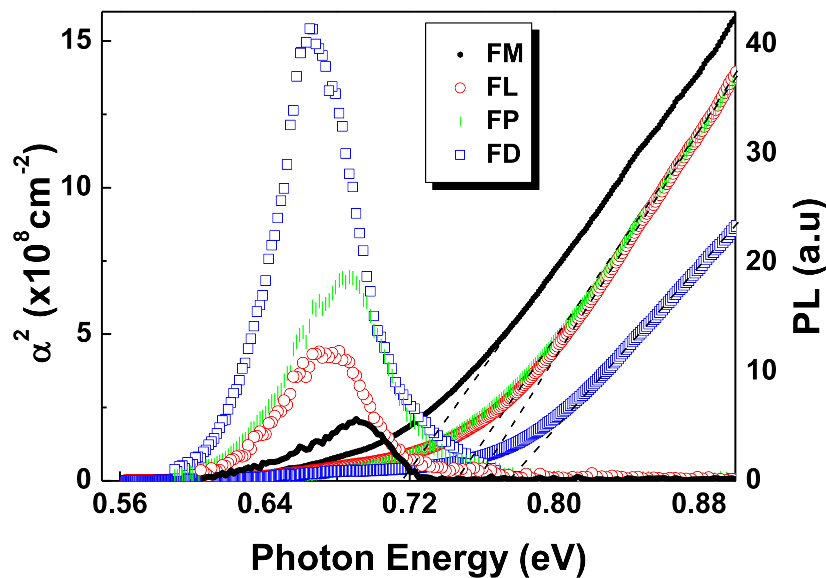

Figure 8.16 *Plots of the low temperature PL spectra at 20K and the square of absorption coefficient determined from transmittance measurements at 300K versus photon energy (eV), for InN films grown on Si (111) at 440°C, using different InN nucleation layers. The main PL peak (FWHM) of samples FM, FL, FP and FD are 0.692 eV (49 meV), 0.676 eV (49 meV), 0.686 eV (58 meV) and 0.666 eV (51 meV), respectively, while the estimated bandgap is 0.715 eV, 0.757 eV, 0.746 eV and 0.774 eV, respectively.*

The PL FWHM could also give an insight into the crystal quality and purity of the InN films; in general, the narrower the FWHM, the better the crystal quality expected. The determined PL FWHM values did not show any significant differences in the four samples but a tendency for larger FWHM values appears for InN nucleation at stoichiometric III/V flux ratio, as shown in Table 8.5. The PL intensity and FWHM exhibited opposite trends. PL measurements can be affected by point defects, impurities and the morphology of the samples (columns versus compact films). Thus, no conclusions can be safely drawn for the correlation with the dislocation density of the samples.

From the 300K optical transmittance measurements, the square of the absorption coefficient (α^2) was calculated and plotted as a function of photon energy (eV) for each sample, as shown in Fig. 8.16. The absorption edge of the films was estimated in the range 0.715 to 0.774 eV, as given in Table 8.5. However, none of the exhibited absorption edges coincides with the energy of the PL peak for any of the investigated films, indicating that the PL peaks do not correspond to band-to-band recombination transitions and must have emanated from defect centres in the films.

The previous sections described a comprehensive study that concluded to optimum nucleation of InN on Si at 225°C under N-rich conditions. To fully evaluate the capabilities of the optimized two-step growth approach, an additional 650 nm thick InN overlayer (sample G1378) was grown on the optimum nucleation layer, using stoichiometric III/V flux ratio. The typical 7x7 reconstruction pattern observed for the thermally cleaned Si (111) substrate surface is shown in Fig. 8.17(a). The initial diffused RHEED pattern and the final elongated-spotty diffraction pattern observed at the initiation and end of the LT-InN NL growth are shown in Figs 8.17(b) and 8.17(c), respectively. It should be noted that no ring pattern was observed during the deposition of the LT-InN NL. Fig. 8.17(d) is the RHEED pattern observed from the surface of the overgrown 650 nm InN layer. The streakiness of the pattern indicates that the growth of InN proceeded in 2D mode and the film exhibited smooth surface morphology.

The plan-view FE-SEM micrograph, depicting the smooth step-flow surface morphology of sample G1378, is shown in Fig. 8.18(a). The characteristic sharp InN/Si interface obtainable whenever the optimised LT-InN NL is used is shown in Fig. 8.18(b). The 1x1 μm^2 AFM image of sample G1378, shown in Fig. 8.18(c), clearly indicates that step-flow growth is achieved for this film, in a similar way to InN growth on GaN (0001) pseudo-substrates under stoichiometric In/N flux ratio [21,22,24]. The increased diffusion lengths of adatoms for the In-stabilized surface resulted to smooth surface morphology with steps of approximately 1 ML step height [Fig. 8.18(c)]. The rms surface roughness was determined as 0.68 nm; which indicates improved surface morphology compared to sample FM grown with similar LT-InN NL but under slightly N-rich condition (III/V flux ratio = 0.93), which exhibited an rms roughness of 2.18 nm [Fig. 8.14(a) and Table 8.3].

HR-XRD rocking curves were measured for the symmetric (0002) and asymmetric $(10\bar{1}5)$ reflections and resulted to FWHM of 0.81^{o} and 0.60^{o}, respectively. The apparent electron concentration and mobility determined from Hall-effect measurements was 2.8 x 10^{19} cm^{-3} and 710 cm^{2}V^{-1}s^{-1}, respectively. The sample exhibited 20K PL at 0.657 eV with PL FWHM of 30 meV.

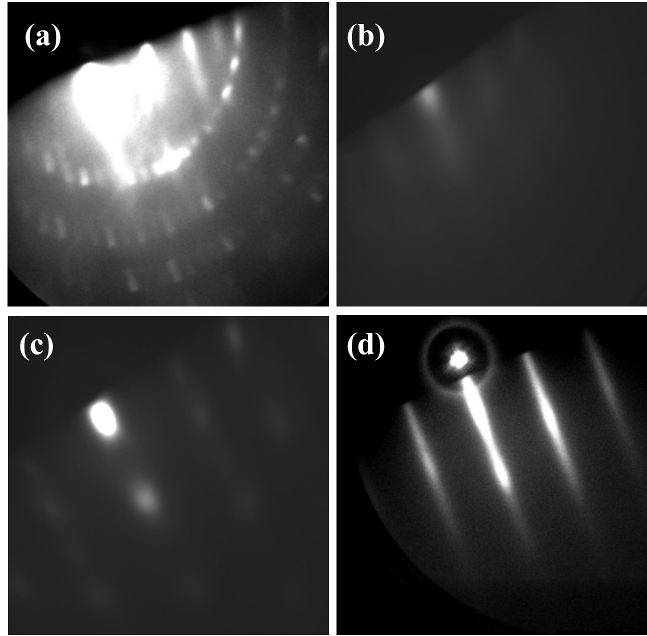

Figure 8.17 *Heteroepitaxial growth of InN on Si(111) using an optimised InN NL: (a) Typical 7x7 reconstruction RHEED pattern observed from the surface of the thermally cleaned Si (111) substrate, (b) Initial diffused pattern observed at the onset of the 20 nm LT-InN NL growth, (c) Elongated-spotty pattern observed at the completion of the 20 nm LT-InN NL and (d) Diffraction pattern obtained from the final 650 nm InN layer.*

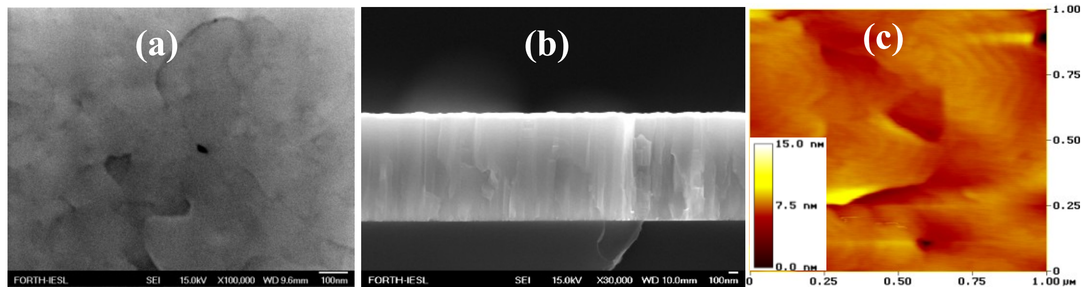

Figure 8.18 *InN film sample G1378 grown on Si (111) under stoichiometric In/N flux ratio, using an optimised LT-InN nucleation layer: (a) SEM plan-view, (b) SEM cross-sectional view and (c) 1x1 μm^2 AFM micrograph showing that the film exhibits step-flow surface morphology. The rms surface roughness was determined as 0.68 nm.*

8.5 Transmission electron microscopy study of InN-on-Si (111) heterostructures

(a) Single step InN growth on Si (111)

Sample G1719 (FD) consisted of InN grown directly on Si at the high T_{sub} = 440°C with III/V flux ratio ~1. The cross-sectional TEM (XTEM) [Fig. 8.19(a)] revealed that the growth is mainly achieved through the formation of irregularly-shaped highly defective InN columns. The thickness of the deposition varies from 350 to 520 nm. An unintentional amorphous Si_xN_y layer with thickness ranging from 2 to

15 nm is observed across the interface and it is attributed to excessive interaction of the active N species with the top Si monolayers due to the low coverage of Si surface by InN islands, resulting to irregular Si_xN_y thickness that consequently created a non-oriented columnar InN with non-uniform film thickness. Disorientations of the InN columns along the *c*-axis are observed with respect to Si, as shown in the SAED pattern of Fig. 8.19(b).

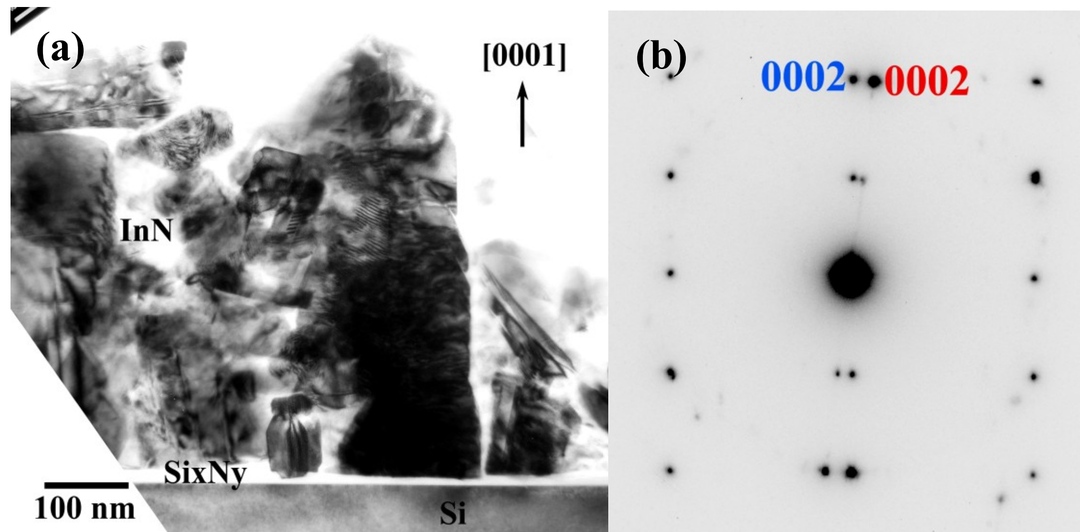

Figure 8.19 *InN film FD grown directly on Si (111) at 440°C: (a) Cross-sectional TEM showing various-shaped highly defected columns,(b) SAED pattern showing two adjacent InN columns with disorientation of 7° along the c-axis relative to one another.*

(b) Optimized 20 nm InN growth on Si (111)

Sample M (G1196) consisted of 20 nm LT-InN nucleation layer (NL) grown at 225°C with III/V flux ratio of 0.2 [Table 8.1]. The HRTEM (shown in Fig. 8.20(a)) revealed columnar features that indicates that the growth of the LT-InN layer must have proceeded with the nucleation and coalescence of 3D islands on Si. A well defined nanocrystal is denoted by a black arrow in Fig. 8.20(a). The visible Moire fringes are believed to arise from the overlapping of the InN nanocrystals. The average nanocrystal height and width was measured as 22.4 (±0.6) nm and 8 (±1) nm, respectively. The measured average height is in a good agreement with the expected 20 nm thickness of the thin film. The rms roughness of the NL was measured equal to 1.25 nm or 1.2 ± 0.2 nm on the average. An unintentional layer of amorphous silicon nitride (Si_xN_y) of 1.25 ± 0.13 nm measured thickness is also formed at the InN/Si interface, indicated by a white arrow in Fig. 8.19(a), and it is attributed to the partial coverage of the Si surface by InN 3D islands, during InN nucleation and the N-rich growth condition employed [Table 8.1]. This amorphous Si_xN_y layer exhibits a more uniform thickness along the InN/Si interface compared to what was observed for sample FD (G1719) [Fig. 8.19(a)].

Fig. 8.20(b) is the Fast Fourier Transform (FFT) digital diffractogram common to both substrate and the film and it shows the epitaxial orientation of InN on

Si. The 0002 InN spot is elongated (arc-shaped) due to small deviations of the [0001] axis of the columnar InN nanocrystals from the <111> growth direction. This is only an out-of-plane deviation, since no arc-shaped contrast was observed from the 10-10 (in-plane) reflections in selected area electron diffraction (SAED) patterns and FFT diffractogram.

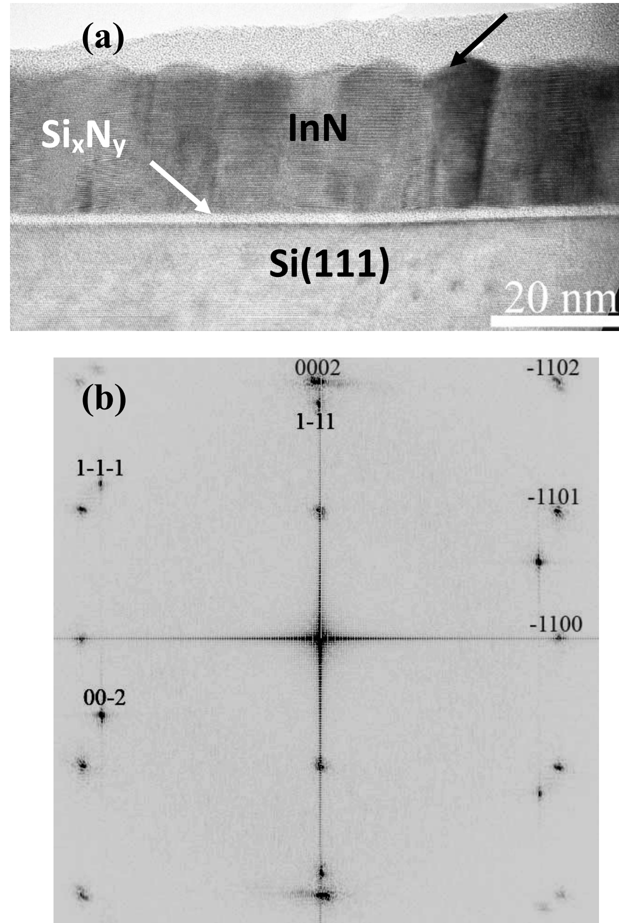

Figure 8.20 *HRTEM investigation of the 20 nm LT-InN NL (sample M): (a) Cross-sectional HRTEM image, taken along [11-20]InN/[110]Si, showing a thin uniform amorphous Si_xN_y layer (white arrow) of 1.25 (±0.13) nm thickness at the InN/Si interface. The InN consist of columnar structure made up of InN nanocrystals like that shown by the black arrow (b) FFT image, for both Si (three indices) and the LT-InN (four indices).*

(c) 650 nm InN grown by the optimised two-step growth process

Sample G1378 consisted of a 650 nm InN film grown on Si (111) under stoichiometric III/V flux ratio at 440°C, using an optimized 20 nm InN NL (grown at 225°C with III/V flux ratio of 0.2). The XTEM image of the InN overlayer taken with g = 0002 off the $[1\bar{1}0]$Si/$[11\bar{2}0]$InN axis and depicted in Fig. 8.21(a) gives an overall view of this sample. The estimated average thickness of 645 (± 3) nm for the InN layer is in a good agreement with the nominal thickness of 650 nm. The dotted line indicates the height of the LT-InN NL. SAED analysis [Fig. 8.21(b)] established the (0001)InN/(111)Si, $[11\bar{2}0]$InN/$[1\bar{1}0]$Si heteroepitaxial orientation relation between

the two lattices. Relatively high densities of threading dislocations (TDs) were observed emanating from the InN/Si interface. Frequent looping of groups of these TDs observed at the first 100-200 nm of InN growth resulted to highly reduced TD density. Furthermore, TDs occasionally terminate in basal SFs responsible for the formation of the observed cube-like formations (with dark contrast) close to the interface (identified by black arrows in Fig. 8.21(a)). These basal SFs act as TDs annihilation centres that further reduce the TD density.

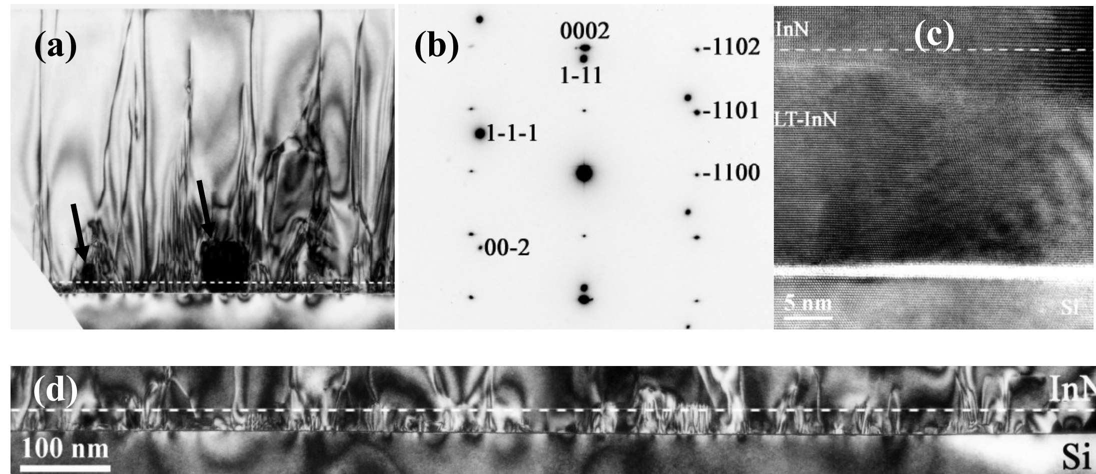

Figure 8.21 *Transmission electron microscopy investigation of the microstructure of InN sample G1378 grown on Si (111), using an optimised LT-InN nucleation layer (the height of which is indicated by dotted line): (a) Cross-sectional bright-field (BF) TEM image along* $[11\bar{2}0]$*InN/*$[1\bar{1}0]$*Si with* ***g*** *0002 InN. Cube-like defect formations identified by black arrows are observed at the interface. TD looping and basal SFs observed within the first 200 nm of InN layer result to substantially reduced TD density, (b) Common SAED pattern of the heterostructure, taken along the [11-20] InN / [1-10] Si zone axis, where 3- and 4-index notations denote reflections of the Si substrate and InN epilayer, respectively. The 0002 reflection of InN is slightly elongated normal to the [0001] direction, suggesting the presence of domains within InN misoriented along this direction, (c) Cross-sectional HRTEM image illustrating the coalesced and/or overlapping nanocrystals within the LT-InN NL and the existence of thin 1.25 (±0.13) nm amorphous* Si_xN_y *layer at the LT-InN/Si interface and (d) Cross-sectional DF TEM image, along [11-20] InN / [1-10] Si with g 0002 InN, showing that the majority of the observed defect occurred within the LT-InN layer.*

The thin uniform Si_xN_y layer of 1.63 (±0.17) nm formed at the InN/Si interface of the unannealed LT-InN NL [Fig. 8.20(a)] is also visible in Fig. 8.21(c). The sharpness of the InN/Si_xN_y/Si (111) interfaces shows that the nucleation scheme assists to completely eliminate adhesion problems at the interface [Figs. 8.21(c) and 8.21(d)]. The epitaxial relationship of the InN epilayer and Si substrate also suggests that dominant InN crystallites/islands were nucleated directly on Si through nanopores of this thin Si_xN_y layer and then expanded laterally over the formed Si_xN_y layer. The small and homogeneous Si_xN_y thickness indicates a high density and homogeneous nucleation of InN crystallites and they coalescence to fully cover the Si substrate at a very early stage of the growth process.

Table 8.6 *TEM estimated TD densities for the InN film G1378 directly grown on Si (111), using an optimised InN NL. The values of the TD density reported in the literature for InN layers grown on Si using AlN nucleation layers [9,11] as well as InN films deposited on MOVPE GaN(0001) pseudo-substrates or $Al_2O_3(0001)$ substrates [30-34] are given for comparison.*

InN Layer Thickness and Growth Structure	Screw type TDs ($x10^9$ cm^{-2})	Edge type TDs ($x10^9$ cm^{-2})
650 nm InN/Si (111) [This work]	1.7	4.0
500 nm InN/AlN/Si (111) [9]	2.0	22.7
2000 nm InN/GaN/AlN/Si (111) [11] TD estimated at 800 nm from interface	13.0	5.3
10000 nm InN on Al_2O_3 (0001) substrate [30]	0.5	4.4
1500 nm InN on GaN(0001) pseudo-substrate [31]	1.1	35.0
500 nm InN on GaN(0001) pseudo-substrate [32] TD estimated at 200 nm from interface	35.0	-
InN on GaN(0001) pseudo-substrate [33]	0.3	21.0
750 nm InN on Al_2O_3(0001) substrate [34]	-	22.0

Due to the mechanisms that reduce the TD density in sample G1378, the total density of the TDs varies from the interface to the surface of the InN film. The measured density of TDs with a *c*-type Burgers vector component (screw component) is $4.6x10^9$ cm^{-2} in the lower InN region and $1.7x10^9$ cm^{-2} at the upper part. The density of TDs with *a*-type Burgers vector component (edge component) in the lower InN region is $6.31x10^9$ cm^{-2} and at the upper part is $4.0x10^9$ cm^{-2}. Due to scarcity of reports on transmission electron microscopy of InN layers grown either directly on Si or with the use of buffer layers, the published results for InN films grown on GaN pseudo-template are also given in Table 8.6 for comparison. It is very apparent from the table that the used NL did effectively reduce the edge-type TD density in sample G1378 to values comparable with those published to date even for InN on MOVPE $GaN/Al_2O_3(0001)$ pseudo-substrate or Al_2O_3 (0001) substrates [30-34]. The optimised LT-InN layer also results to improved structural quality compared to InN films grown on Si using AlN buffer layer [9,11].

The XTEM image of the interfacial layer in Fig. 8.21(d) shows that the majority of the observed defects occurred within the LT-InN layer, indicating that the NL growth conditions confined the defects close to the InN/Si interface, leading to InN film with comparable crystal quality to those grown on MOCVD GaN (0001) template. The high crystal quality InN layer, obtained in this case, suggests that the unintentional amorphous Si_xN_y interfacial layer plays a non-detrimental role in the growth process.

It is well known that the TD structure of InN on GaN/Al_2O_3 (0001) templates is usually dominated by edge-type TDs [34], whereas the screw-type TD density is usually about 1 to 2 orders of magnitude lower [30,31,33]. In the case of sample G1378, approximately similar edge- and screw-type TD densities of 10^9 cm^{-2} have been observed. This may be attributed to the different nucleation of 3D islands on Si (111) and the formation of amorphous Si_xN_y layer that increased the tilt mosaicity.

8.5 Concluding remarks

The nucleation of InN on Si (111) by plasma assisted molecular beam epitaxy (PA-MBE) has been investigated, in order to identify the optimum nucleation layer conditions for the epitaxy of high crystalline quality InN heterostructures on Si. The effects of substrate temperature and III-V flux ratio were comprehensively studied and both are found to be critical parameters for controlling the InN heteroepitaxy on Si.

Columnar InN growth and a highly disordered crystal structure, related to extensive and inhomogeneous nitridation of the Si surface, are always favoured for high temperature direct growth of InN on Si, even under stoichiometric III/V flux ratio conditions.

Direct growth of high crystalline quality InN films on Si has been achieved only by using a two-step growth process, consisting of nucleating a thin InN layer on Si at low temperature and under N-rich growth conditions, prior to the main epilayer growth at the optimum high temperature with stoichiometric III/V flux ratio. The low substrate temperature and excessive N-flux increase the InN nucleation density on the Si surface and full coverage of the substrate surface by coalescence of the InN 3D islands can be achieved at the very early stages of growth, which also limits the extent of unintentional nitridation of the Si surface and formation of an amorphous Si_xN_y interfacial layer. The surface of such a LT nucleation layer exhibits the lowest roughness and it can be used as template for overgrowth of the main InN film at the optimum conditions, i.e. $T_{sub} \sim 450^oC$ and III/V flux ratio =1. This growth approach resulted to step-flow growth of the main InN epilayer exhibiting an atomically smooth surface morphology. The fast coalescence of the InN islands also enhanced defect annihilation processes at the interfacial region of the InN epilayer and facilitated the reduction of the InN threading dislocation (TD) density to $4.0x10^9$ cm^{-2} for the edge-type and $1.7x10^9$ cm^{-2} for the screw-type TDs.

References

1. V. Yu. Davydov, A.A. Klochikhin, R.P. Seisyan, V.V. Emtsev, S.V. Ivanov, F. Bechstedt, J. Furthmüller, H. Harima, A.V. Mudryi, J. Aderhold, O. Semchinova, J. Graul, *Phys. Status Solidi (b)* **229**, R1 (2002)
2. J. Wu, W. Walukiewicz, K. M. Yu, J. W. Ager III, E. E. Haller, H. Lu, W. Schaff, Y. Saito, Y. Nanishi, *Appl. Phys. Lett.* **80**, 3967 (2002)
3. S.K. O'leary, B.E. Foutz, M.S. Shur, U.V. Bhapkar, L.F. Eastman, *J. Appl. Phys*. **83**, 826 (1998)
4. B. R. Nag, *J. Cryst. Growth* **269**, 35 (2004)
5. A. Yamamoto, M. Tsujino, M. Ohkubo, A. Hashimoto, *J. Cryst. Growth* **137**, 415 (1994)
6. A. Yamamoto, M. Tsujino, M. Ohkubo, A. Hashimoto, *Sol. Energy Mater. Sol. Cells* **35**, 53 (1994)
7. J. Grandal, M.A. Sánchez-García, *J. Cryst. Growth* **278**, 373–377 (2005)
8. C.C. Huang, R.W. Chuang, S.J. Chang, J.C. Lin, Y.C. Cheng, and W.J. Lin, *J. Elect. Mater*, **37**, (2008)
9. Y-H. Wang, W-L. Chen, M-F. Chen, *Physica E* **41**, 1746–1751 (2009)
10. A. O. Ajagunna, A. Adikimenakis, E. Iliopoulos, K. Tsagaraki, M. Androulidaki and A. Georgakilas, *J. Cryst. Growth* **311,** 2058 (2009)
11. G. P. Dimitrakopulos, Th. Kehagias, A. Ajagunna, J. Kioseoglou, I. Kerasiotis, G. Nouet, A. P. Vajpeyi, Ph. Komninou, and Th. Karakostas, *Phys. Status Solidi (a)* **207**, 1074 (2010)
12. C.-L. Hsiao, L.-W. Tu, M. Chen, Z.-W. Jiang, N.-W. Fan, Y.-J. Tu and K.-R. Wang, *Jpn. J. Appl. Phys*., **44**, 34 (2005)
13. S. Gwo, C.-L. Wu, C.-H. Shen, W.-H. Chang, T.M. Hsu, J.-S. Wang, J.-T. Hsu, *Appl. Phys. Lett*. **84**, 3765 (2004)
14. A. G. Bhuiyan, A. Hashimoto, A. Yamamoto, *J. Appl. Phys*. **94**, 2790 (2003).
15. Q. Guo, M. Ogata, Y. Ding, T. Tanaka, M. Nishio, *J. Cryst. Growth* **311**, 2783 (2009)
16. X.H. Ji, S.P. Lau, H.Y. Yang, Q.Y. Zhang, *Thin Solid Films* **515**, 4619 (2007)
17. S.A. Nikishin, N.N. Faleev, V.G. Antipov, S. Francoeur, L. Grave de Peralta, G.A. Seryogin, H. Temkin, T.I. Prokofyeva, M. Holtz, S.N.G. Chu, Appl. Phys. Lett. 75 (1999) 2073.
18. A. Krost and A. Dagar, *Mat. Sci. and Eng. B.* **93**, 77 (2002)
19. E. Dimakis, G. Konstantinidis, K. Tsagaraki, A. Adikimenakis, E. Iliopoulos and A. Georgakilas, *Superlattices and Microstruct.* **36**, 497 (2004)
20. C. S. Gallinat, G. Koblmüller, J. S. Brown, and J. S. Speck, *J. Appl. Phys.* **102**, 064907 (2007)
21. E. Dimakis, E. Iliopoulos, K. Tsagaraki, A. Adikimenakis, A. Georgakilas, *Appl. Phys. Lett*. **88**, 191918 (2006)
22. E. Dimakis, E. Iliopoulos, M. Kayambaki, K. Tsagaraki, A. Kostopoulos, G. Konstantinidis, A. Georgakilas, *J. Elect. Mater.* **36**, 373 (2007)
23. E. Dimakis, K. Tsagaraki, E. Iliopoulos, Ph. Komninou, Th. Kehagias, A. Delimitis, A. Georgakilas, *J. Cryst. Growth* **278**, 367 (2005)
24. E. Dimakis, E. Iliopoulos, K. Tsagaraki, A. Georgakilas, *Appl. Phys. Lett*. **86**,133104 (2005)
25. T. Yodo, H. Ando, D. Nosei, and Y. Harada, *Phys. Status Solidi (b)* **228**, 21 (2001)

26. T. Yodo, H. Yona, H. Ando, D. Nosei, Y. Harada, *Appl. Phys. Lett.*, **80**, 968, (2002)
27. Y. Nanishi, Y. Saito, T. Yamaguchi, T. Araki, T. Miyajima, and H. Naoi, *Phys. Status Solidi (c)* **1**, 1487 (2004)
28. H. Lu, W. J. Schaff, L. F. Eastman and C. E. Stutz, *Appl. Phys. Lett*. **82**, 17 (2003)
29. A. O. Ajagunna, E. Iliopoulos, G. Tsiakatouras, K. Tsagaraki, M. Androulidaki, and A. Georgakilas, *J. Appl. Phys*. **107**, 024506 (2010)
30. E. Dimakis, J. Domagala, A. Delimitis, Ph. Komninou, A. Adikimenakis, E. Iliopoulos, A. Georgakilas, *Superlattices and Microstruct*. **40**, 246 (2006)
31. C. S. Gallinat, G. Koblmüller, Feng Wu, and J. S. Speck, *J. Appl. Phys*. **107**, 053517 (2010)
32. K. (Albert) Wang, T. Kosel, and D. Jena, *Phys. Status Solidi (c)* **5**, 1811 (2008)
33. X. Wang, S.-B. Che, Y. Ishitani, and A. Yoshikawa, *Appl. Phys. Lett*. **90**, 151901 (2007)
34. C. J. Lu, L. A. Bendersky, Hai Lu, and William J. Schaff, *Appl. Phys. Lett*. **83**, 2817 (2003)

9 Growth of InN Nanopillars on Si (111) and *r*-plane Al_2O_3 substrates

9.0 Introduction to InN Nanostructures

9.1 Initial experiment on the spontaneous growth of InN NPs on Si (111)

9.2 Investigation of the role of III/V flux ratio on InN NPs properties (N-flux constant)

9.3 Investigation of the role of III/V flux ratio on InN NPs properties (In-flux constant)

9.4 The role of AlN nucleation layer on InN NPs properties (In-flux constant)

9.5 Conclusions for PAMBE growth of InN NPs on Si (111)

9.6 Growth of InN nanopillars on *r*-plane sapphire substrates

9.7 Concluding remarks

9.0 Introduction to InN Nanostructures

Growth and properties of nanostructures has recently attracted the interest of the scientific community, because of their potential applications to novel devices, such as light emitters, solar cells, transistors and sensors. The understanding of the behaviour of nanostructures is very important to the optimization of their growth and control of their properties. Nanostructures mainly consist of low dimensional structures of quantum dots (QDs), and nanowires, such as nanobelts, nanotubes and nanopillars.

Heteroepitaxial growth of III–V semiconductors on silicon has been very interesting for the monolithic integration of III–V optoelectronic and microwave devices with Si digital circuits [1] to increase the functionality of the Si chips, to increase their speed by using optical interconnections and to enable innovative opto-electro-mechanical micro- and nano-systems. However, a major problem of the heteroepitaxial growth of III-nitride materials on Si is the formation of a high density of threading dislocations, of the order of 10^9-10^{11} cm^{-2} [2,3], which adversely affects device performance [4]. Hence, III-nitride nanostructures, such as nanowires (NWs) in the form of nanopillars (NPs) are promising, not only for the fabrication of nanodevices with device scaled down dimensions but also for the overgrowth of stress-free films, since the small lateral length of NPs is expected to allow InN heteroepitaxial growth without the formation of threading dislocations. The ability to grow or fabricate high quality InN-based nanostructures will allow the maximisation of the high potentials of InN and its ternary (InGaN and InAlN) or quaternary (InAlGaN) alloys, which consist of a unique semiconductor material system covering from the near infrared through the visible wavelength to the UV region of the electromagnetic spectrum, with significant applications in LEDs and LDs [5,6].

Many methods of nucleating and growing NPs have been employed over the years. The most commonly applied are catalyst assisted growth, spontaneous or self-assembly growth and mask-assisted growth processes. The major contrast in these different approaches is that catalyst-assisted NPs accommodate many stacking faults and impurities but also grow faster while the self-assembly or mask-assisted NPs are largely free of defects with sharper and more intense photoluminescence [7,8]. A lot of work already done on NPs employed different techniques, such as metal-organic vapor phase epitaxy [9,10], molecular beam epitaxy [11,12], chemical beam epitaxy [13], and laser ablation [14,15], to grow GaN and InN on several substrates like sapphire [16-18] and Si [19-21]. In all cases, the major difficulty is how to control the growth process to achieve the required dimensions and positioning. MBE is still a very suitable technique, offering the ability to precisely control the growth process and dimensions of the NPs. The heteroepitaxial growth of NPs by MBE usually follows either the 3D growth mode (Volmer–Weber) or 2D to 3D growth mode (Stranski–Krastanov).

Up till now, even though many attempts have been made to grow InN NPs, achieving high quality InN NPs with desired surface to volume aspect ratio is still a challenge. In the present work, the spontaneous growth of InN Nanopillars (NPs) by MBE was investigated. Numerous growth conditions were employed and optimised to identify the most suitable ones for the spontaneous growth of InN NPs on Si (111) substrates. Different characterisation techniques were also employed to study the

growth and properties of the resulting NPs. The results of an attempt to grow InN NPs on *r*-plane sapphire substrates shall also be treated. Nitrogen rich growth conditions were always employed to nucleate InN nanopillars, in accordance with the findings described in Chapters 7 and 8. RHEED was employed for *in-situ* monitoring of the growth processes. The InN samples were entirely grown by PA-MBE on 330±15 μm thick, boron-doped, 3-inch diameter *p*-type Si (111) wafers with resistivity >100 Ωcm and crystallographic plane misorientation of ± 0.5^{o}. Although the substrates were Epi-ready, the surfaces were always cleaned using the previously discussed method in Chapter 3. 7x7 reconstruction typical of the clean Si (111) surface was always observed by RHEED after the substrate's *in-situ* surface preparation. The morphology and dimensions of the InN structures were determined by FE-SEM. HR-XRD measurements were performed to characterize the orientations of the InN NPs. The microstructure of some of the InN NPs was also studied by conventional TEM and HRTEM observations by the group of Prof. Komninou and Prof. Kehagias at the Physics department of the Aristotle University of Thessaloniki. The optical properties of the NPs were investigated by low temperature PL measurements.

9.1 Initial experiment on the spontaneous growth of InN NPs on Si (111)

For the initial work, InN was deposited directly on Si (111) substrate's surface for 2 hr, using an effective In/N flux ratio of ~ 0.2. The growth rate of the N-flux was 516 nm/hr. The In K-cell was maintained at a temperature of 748°C, which corresponded to a growth rate of 97.5 nm/hr. No intermediate buffer layer was employed. The substrate temperature used in the experiment was 450°C. During the initial stage of the growth, the RHEED showed ring pattern within the first two minutes of growth initiation, indicating the formation of polycrystalline InN and possibly silicon nitride layer on the major part of the substrate's surface. The formation of amorphous silicon nitride layer has been previously reported by Kim *et al.* for GaN NPs [11] and Grandal *et al.* for InN NPs [19]. The observed ring patterns later changed to arc-like diffraction spots on the RHEED; which is indicative of the formation of (0001) oriented NPs and this form of pattern remained until the end of the growth. The properties of the resulting InN sample G984 were investigated.

Fig. 9.1 shows the plan-view and cross-sectional FE-SEM images of the InN NPs grown spontaneously on Si (111) substrates without metal catalyst. The NPs are believed to have been generated from the lattice mismatch strain of the InN material on Si and the high surface energy of their nitrogen stabilized surfaces. The average height and average diameter of the NPs are 600 nm and 60-80nm, respectively, indicating that the growth rate along the *c*-axis of the three-dimensional (3D) InN islands was limited by the flux of reactive nitrogen species (F_N), which was 516 nm/hr and not by that of the In flux (F_{In}) that should be less than 200 nm/hr within the 2 hr growth duration of the NPs.

The crystallographic orientation of the NPs was investigated by HR-XRD. According to the theta-2theta scan shown in Fig. 9.2, only two peaks consisting of (0002) InN and (0004) InN were identified, indicating that single crystalline wurtzite InN NPs were grown parallel to the *c*-axis. No traces of polycrystallinity were detected.

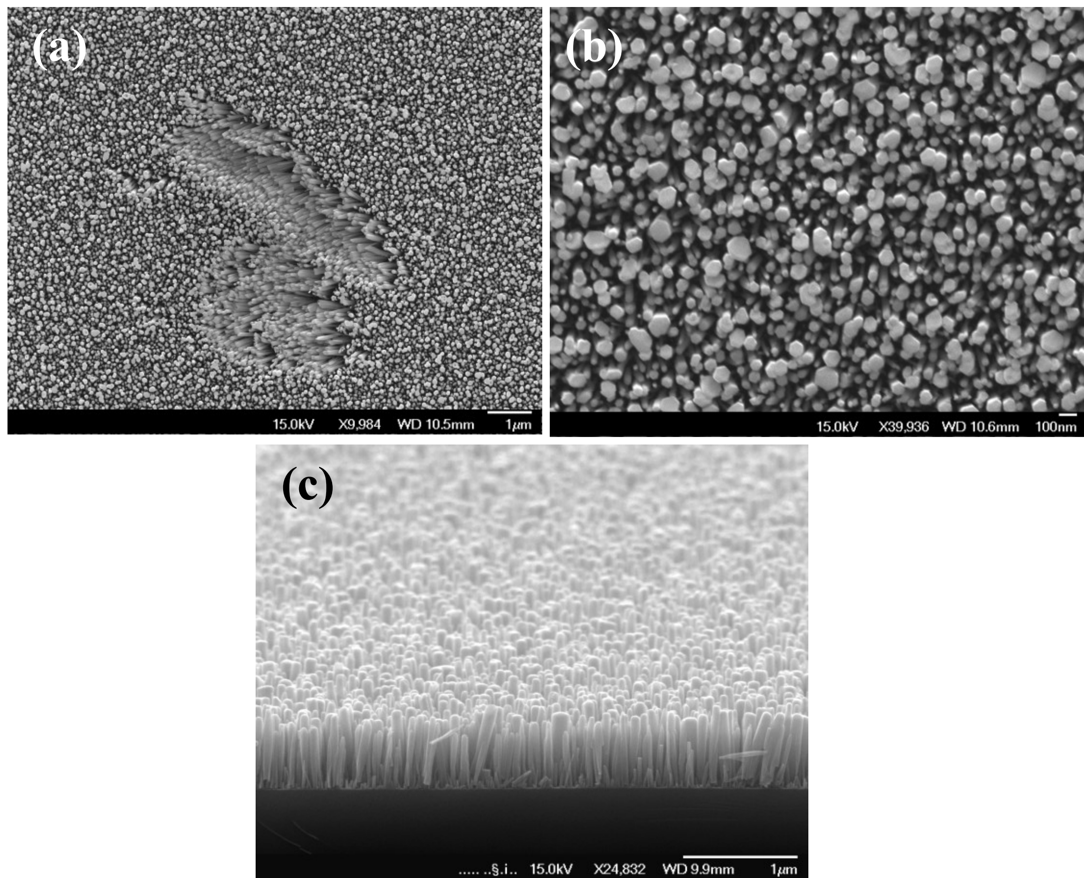

Figure 9.1 *FESEM micrographs of InN sample G984 grown on Si (111): (a) and (b) are plan-view images in different magnifications while (c) is the bird-view image. InN was grown for 2 hr using In flux of 97.5 nm/hr and N-flux of 516 nm/hr.*

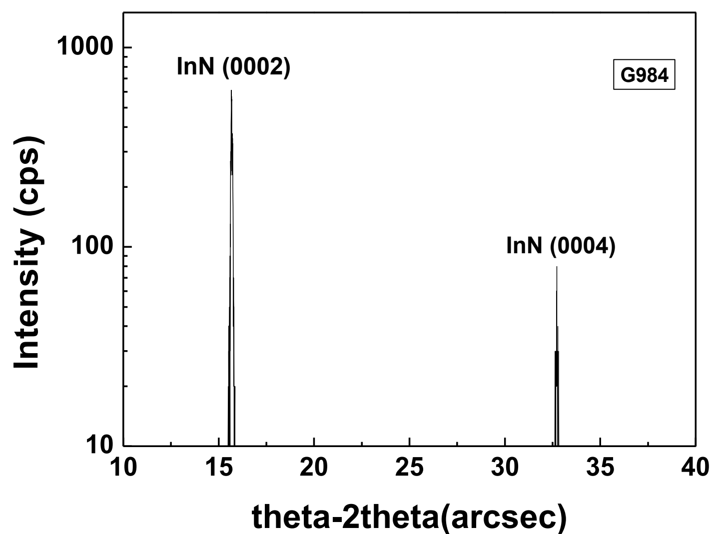

Figure 9.2 *HR-XRD theta-2theta scans profile of InN NPs G984 spontaneously grown on Si (111) at 450°C showing only InN peaks, which indicates that the NPs are oriented along the c-axis.*

The microstructure of the NPs was studied by transmission electron microscopy. The XTEM image of nanocolumns taken along the Si [110] zone axis and Si [$1\bar{1}0$] zone axis are shown in Fig. 9.3(a) and Fig. 9.3(b), respectively. The NPs are aligned closely with [111] and exhibited a tapered morphology. Increase in NPs diameter from approximately 20 nm at the substrate interface to 80 nm at the tip was observed with an average height of approximately 600 nm, which is in agreement with the SEM estimation of the dimensions of the NPs. Basal plane stacking faults were visible in some nanocolumns. The diffraction pattern of the NPs shows that most nanocolumns have the orientation relationship (0001)InN//(111)Si, [$1\bar{2}10$]InN//[110]Si [Fig. 9.3(b)]. Arc-shaped 0002 spots indicate deviation of the columns from the [0001] direction by a few degrees.

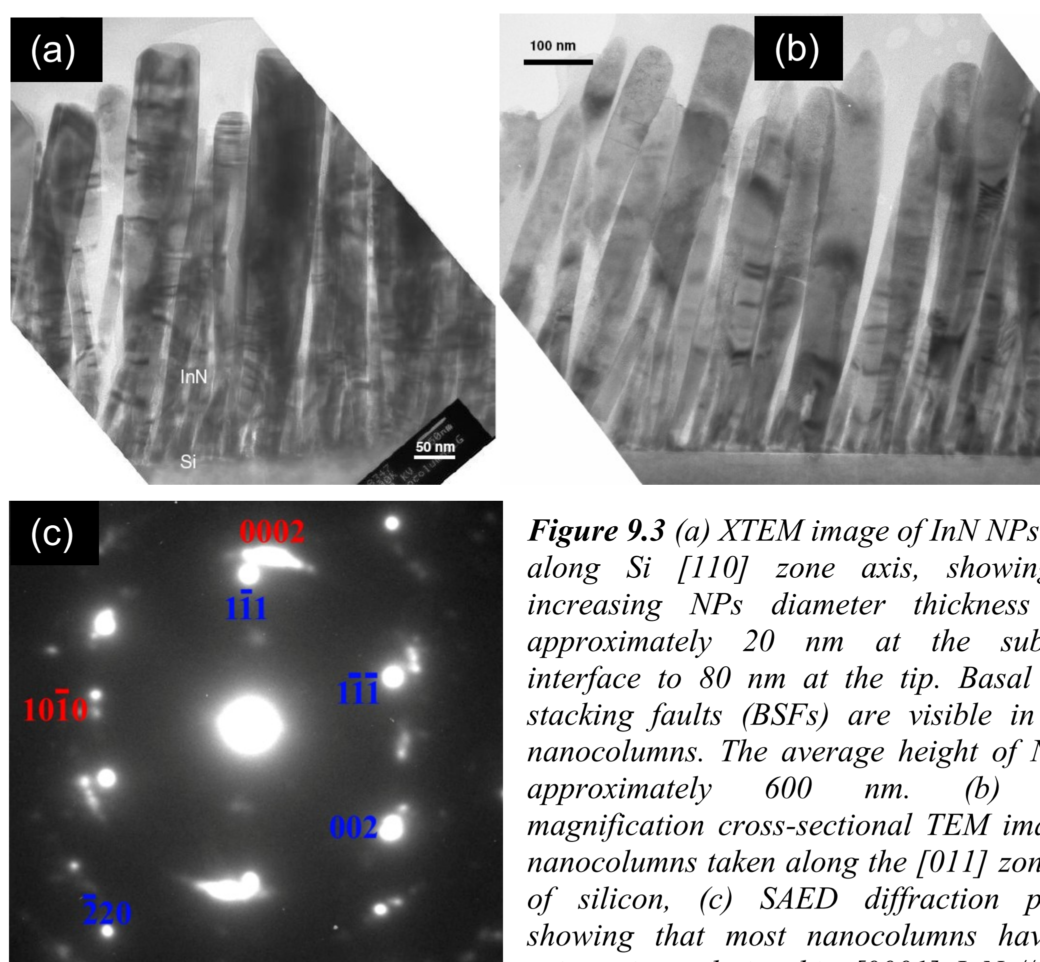

Figure 9.3 *(a) XTEM image of InN NPs G984 along Si [110] zone axis, showing the increasing NPs diameter thickness from approximately 20 nm at the substrate interface to 80 nm at the tip. Basal plane stacking faults (BSFs) are visible in some nanocolumns. The average height of NPs is approximately 600 nm. (b) Low-magnification cross-sectional TEM image of nanocolumns taken along the [011] zone axis of silicon, (c) SAED diffraction pattern showing that most nanocolumns have the orientation relationship [0001] InN // [111] Si, [$1\bar{2}10$] InN // [110] Si. The arc-shaped 0002 spots indicate deviation of the columns from the [0001] direction by a few degrees.*

HRTEM image of Fig. 9.4(a) shows a nanocolumn with no column twists (i.e. [$11\bar{2}0$]//Si[$1\bar{1}0$]), allowing the observed strong contrast from both the Si and InN atomic columns. Almost all NPs possess a small twist about the Si [111] axis. A 10° tilt of the pillar is apparent in Fig. 9.4(a) The observed strong atomic contrast in the

InN nanocolumns is an indication that epitaxy seems to be maintained from the Si substrate to the InN, despite the formation of a thin Si_xN_y layer at the InN/Si interface. The thickness of the layer varies between 3 nm and 7 nm throughout the specimen and the non-uniform thickness of the Si_xN_y is believed to be responsible for the exhibited 10° misorientation of the columns.

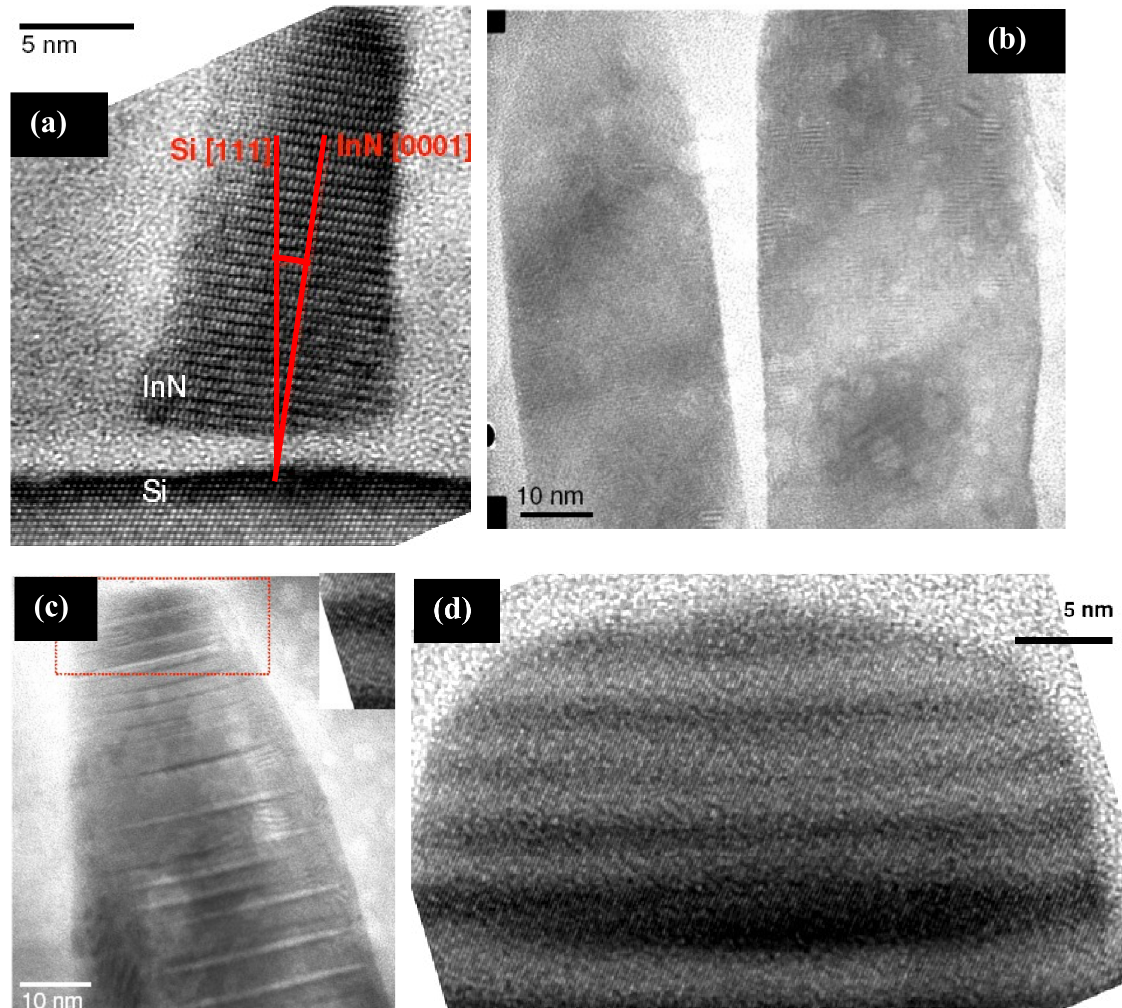

Figure 9.4 *(a) HRTEM image of G984 showing a nanocolumn with no column twist (i.e. InN [1120]//Si [110]) such that strong contrast from both the Si and InN atomic columns are visible. A 10° tilt of the column from [111] is represented in the image. (b) HRTEM lattice image taken with the specimen tilted slightly about Si [111]. The upper regions of two nanowires are visible, with respective lateral dimensions of 30 nm and 50 nm as well as rounded top facets (c) HRTEM image showing nanocolumn tip facet morphology with basal plane stacking faults (d) Image of the boxed region in (c) showing more clearly the alternating light and dark contrast in the nanocolumn tip, which indicates a change in thickness at the column tip.*

Fig. 9.4(b) is the HRTEM lattice image taken with the specimen tilted slightly about Si [111] showing the upper regions of two nanowires with respective lateral dimensions of 30 nm and 50 nm as well as rounded top facets. Fig. 9.4(c) shows the image of a nanocolumn tip. The column exhibits a flat top facet with rounded edges. Many basal plane stacking faults, shown by dark and bright line contrast, are present

at the top of the column. Contrast reversal of the stacking faults is attributed to the changes in thickness of the column along its width. The magnified view of the boxed region in Fig. 9.4(c) is shown in Fig. 9.4(d) and the alternating light and dark contrast in the nanocolumn tip, which indicates a change in thickness at the column tip are clearly visible.

It is noteworthy to state that the NPs did not exhibit PL emission and this may be related to the density of SFs present in the NPs. Nonetheless, the result obtained for sample G984 indicates that although stress free InN NPs may be spontaneously grow on Si (111), growing InN NPs free of SFs and also well aligned along the growth direction on Si will need further optimization of the growth conditions. In the following sections, different parameters, mainly the III/V flux ratio and the substrate temperature, were investigated in order to be able to realize the optimum growth conditions for high crystalline quality oriented InN nanopillars. The structural and morphological properties of the InN NPs are also investigated.

9.2 Investigation of the role of III/V flux ratio on InN NP properties (N-flux constant)

The role of the III/V flux ratio was first investigated by using a constant flux of active nitrogen species (F_N) of 783 nm/hr, operating the RF plasma source with RF power of 300W and N_2 flow rate of 1.35 sccm. The In-flux (F_{In}) was varied to obtain In/N flux ratios of 0.1, 0.15, 0.2 and 0.25 and the InN samples grown under these conditions are G1430, G1429, G1428 and G1427, respectively. Each of the samples was grown at 440°C for 1 hr and 30 min. The growth conditions are described in Table 9.1.

Table 9.1 *Growth conditions and properties of InN NPs grown on Si (111) under different In/N flux ratio with nitrogen flux kept constant at 783 nm/hr by using RF power and N_2 flow rate of 300W and 1.35 sccm, respectively. All NP samples were grown at T_{sub} of 440°C for 1:30 hr. % F_N and % F_{In} are the percentage of the incident N-flux and In-flux incorporated into the area of the NPs, respectively.*

Sample Identity	F_{In} (nm/hr)	F_{In}/F_N	Height along *c*-axis (nm)	G.R./ F_{In}	% F_N	% F_{In}
G1430	78.21 nm/h	0.1	130 nm/h	1.1	11	100
G1429	98.01 nm/h	0.15	160 nm/h	1.1	14	100
G1428	146.52 nm/h	0.20	250 nm/h	1.1	21	100
G1427	195.03 nm/h	0.25	330 nm/h	1.1	28	100

The FE-SEM images of Fig. 9.5 show the morphology of the samples. All samples evolved with a very dense structure of merged NPs and exhibited growth heights of 130 nm, 160 nm and 250 nm and 330 nm, which correspond to growth rate (G.R) along the *c*-axis of 86 nm/hr, 107 nm/hr, 167 nm/hr and 220 nm/hr, respectively [Table 9.1]. This means that the differences in the III/V flux ratio had negligible effect on the as-grown height of the InN NPs, which was limited mainly by the In-flux. The NPs only demonstrated 10 to 25 nm/hr increment above the In growth rate [Table 9.1]. The low growth temperature of 440°C employed resulted to negligible transfer of

In atoms to the NPs and consequently a dense NPs structure that tends to forming porous structure as the F_{In}/F_N increases from 0.1 to 0.25.

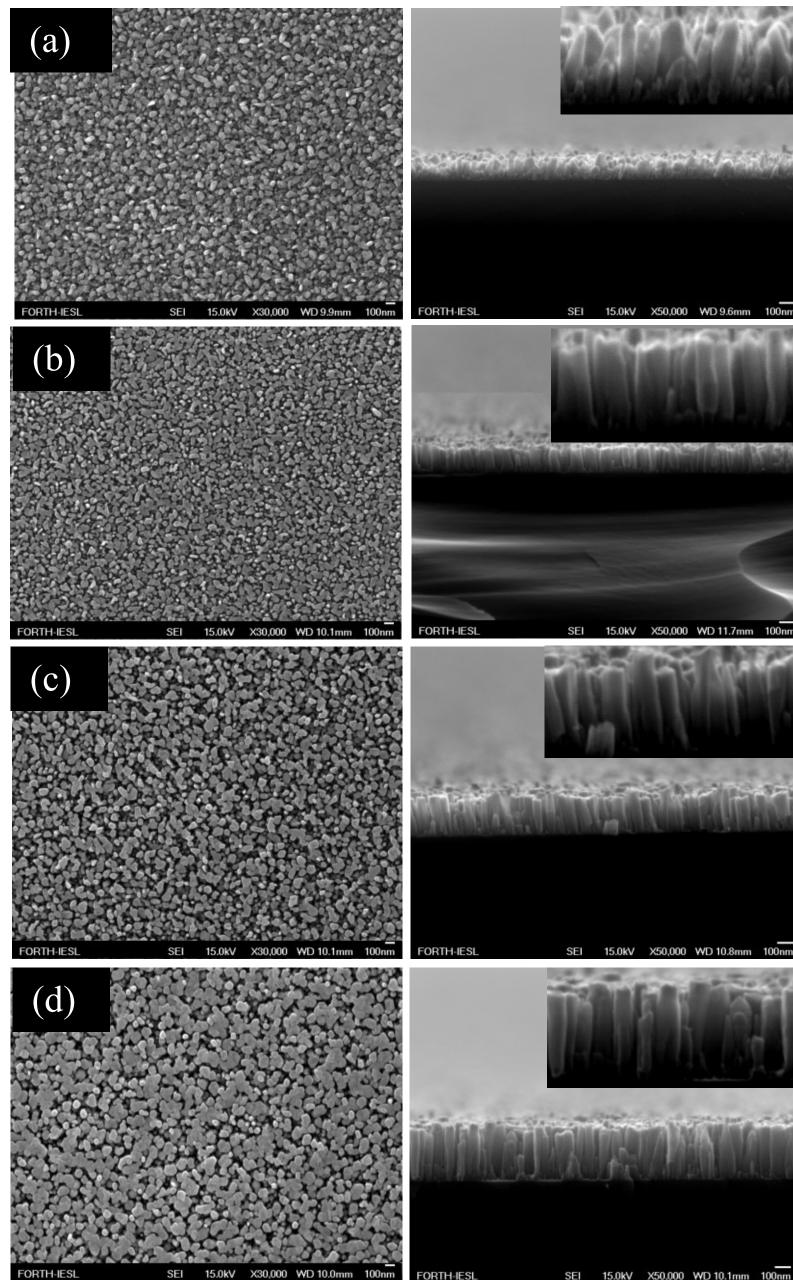

Figure 9.5 *SEM micrographs of InN NPs spontaneously grown on Si (111) for 1:30 hr each at 440°C under constant N- flux of 783 nm/hr, using different In/N flux ratios of (a) 0.1 (b) 0.15 (c) 0.2 and (d) 0.25. The inset images reveal the NPs structure more clearly.*

9.3 Investigation of the role of III/V flux ratio on InN NPs properties (In-flux constant)

Unlike the preceding section investigation on the role of III/V flux ratio under constant N-flux, this section employs the variation of the III/V flux ratio keeping the

In-flux constant at 120 nm/hr (equivalent beam pressure of 1.8 x 10^{-7} Torr). The RF power was fixed at 300 W while the nitrogen flow was varied. NPs samples G1304 (0.26 sccm), G1305 (0.47 sccm), and G1306 (1.12 sccm) resulted from the use of In/N flux ratio of 0.36, 0.22, and 0.16, respectively. The growth duration of each sample was 2 hr and the substrate temperature employed was 470°C. Table 9.2 gives a comprehensive description of the growth conditions.

Table 9.2 *Growth conditions and properties of InN NPs grown on Si (111) under different In/N flux ratios with In-flux (F_{In}) kept constant at 120 nm/hr. The RF power was constant at 300W and the N-flux (F_N) was varied by changing the N_2 flow rate. All the NP samples were grown at T_{sub} of 470°C for 2 hr each. % F_N is the percentage of the incident N-flux incorporated into the area of the NPs.*

Sample Identity	N_2 flow rate	F_N	F_{In}/F_N	Height along *c*-axis	G.R./ F_{In}	% F_N
G1304	0.26 sccm	365 nm/h	0.33	415 nm	1.73	56%
G1305	0.47 sccm	540 nm/h	0.22	585 nm	2.44	54%
G1306	1.12 sccm	770 nm/h	0.16	815 nm	3.40	53%

The FE-SEM micrographs of Fig. 9.6 revealed that all samples exhibited InN NP structures. The coalescence of the NPs was found to be a function of the used III/V flux ratio and the degree of coalescence increases with increasing In/N flux ratio. The inset of each image presents a better look at the form of the resulting pillars. The InN NP samples exhibited linear increase in height from 415 to 815 nm as the N-flow increased (with other growth parameters kept constant) from 0.26 to 1.12 sccm, which correspond to N-flux increase from 365 nm/hr to 770 nm/hr [Table 9.2]. Sample G1306, grown with III/V flux ratio of 0.16 [Fig. 9.6(c)], evolved with the best NP morphology and demonstrated a more uniform pillar dimension among the used flux ratio. It is very discernible that when the N-flow was increased, the NPs growth rate also increased to values multiples of the In-flux (120 nm/hr) [Table 9.2]. Moreover, over 50% of the incident N atoms at the area of NPs are incorporated under the moderate substrate temperature employed. For higher temperature (500°C), N incorporation of approximately 80% has been determined [21]. The results for the growth rate of NPs in samples G1304-1306 are inconsistent with those of samples G1427-1430; the growth rate of NPs along the *c*-axis is a much higher fraction of F_N in the case of samples G1304-1306 compared to G1427-1430. These results may be attributed to differences in the growth conditions (III/V flux ratio and growth temperature). Lower substrate temperature increased the nucleation density of NPs samples G1427-1430. The higher growth temperature, as in the case of samples G1304-G1306, undoubtedly increased the surface diffusion length of In atoms on the substrate surface and enhanced their migration from the uncovered substrate regions to the top of the nucleated 3D InN, thereby accelerating the growth of the nanopillars along the growth direction (*c*-axis) to permit stoichiometric supply of In and N atoms on the top surfaces, in accordance to the mechanism of N-limited growth condition discovered for InN NPs [22-24]. However, the results also indicate that under different III/V flux ratio, whichever flux is varied among In-flux and the N-flux sets

the limit of the growth rate. In this case, the effect of F_N is significantly stronger than F_{In} due to the variation of the N-flux.

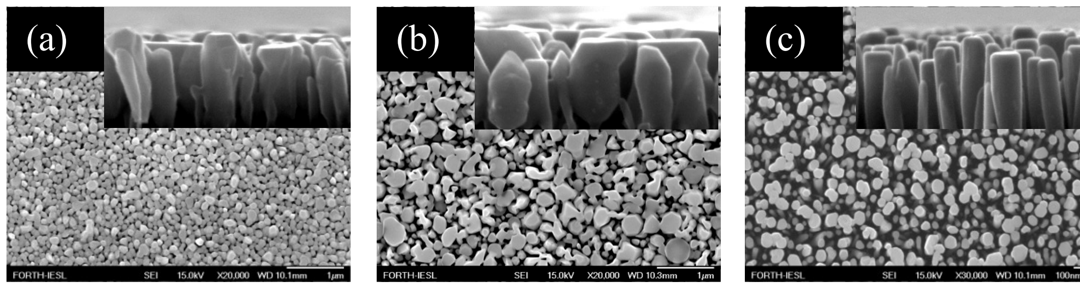

Figure 9.6 *FE-SEM micrographs of InN NPs spontaneously grown on Si (111) for 2 hr each at 370°C, using different N-flow rates of 0.26, 0.47, and 1.12 sccm which correspond to In/N flux ratio of (a).0.33, (b) 0.22 and (c) 0.16 for NPs samples G1304, G1305 and G1306, respectively.*

None of the samples G1304-1306 exhibited low temperature PL emission. An EDX study confirmed the existence of stoichiometric concentrations of In and N in all the InN NPs samples. Further investigation should be carried out to understand what is responsible for the non-observation of PL emission in the InN NPs.

In a study to further optimise the InN NPs growth conditions, a new set of NPs was grown by using a higher substrate temperature of 500°C. The III/V flux ratios of samples G1304, G1305 and G1306 in Table 9.2 were re-employed for the new samples G1611, G1612 and G1613, respectively, but the growth duration was reduced to 1hr. The FE-SEM micrographs of Fig. 9.7 revealed the plan-view and the cross-sectional morphologies of the InN nanopillars of samples G1611, G1612 and G1613. The samples exhibited less density of NPs, thus improved NP separation, compared to the previous samples. Every NP is aligned parallel to the growth direction and manifested conical tips with hexagonal base typical of wurzite structure. All the previously grown NPs in this Chapter exhibited flat tips. Moreover, unlike the typical non-uniform NP width observed in the previous set of NP samples, G1611 to G1613 maintain similar diameter for each pillar from bottom to top.

Table 9.3 *Growth conditions and properties of InN NPs grown on Si (111) under different In/N flux ratios with In-flux (F_{In}) constant at 120 nm/hr. The RF power was 300W and the N_2 flow rate was varied to vary the F_N, respectively. All the NP samples were grown at T_{sub} = 500°C for 1 hr. % F_N is the percentage of the incident N-flux incorporated into the area of the NPs.*

Sample Identity	N_2 flow rate	F_N	F_{In}/F_N	Height along *c*-axis	G.R./ F_{In}	% F_N
G1611	0.26 sccm	365 nm/h	0.33	220 nm	1.83	60%
G1612	0.47 sccm	540 nm/h	0.22	330 nm	2.75	61%
G1613	1.12 sccm	770 nm/h	0.16	340 nm	2.83	44%

The obtained differences in the density, dimensions and morphology of NPs at different growth temperatures underscore the importance of optimising the substrate temperature for InN nucleation and NPs growth. The FE-SEM micrographs of Fig. 9.7 revealed a reduction of the height and separation of NPs and an increasing merging of the NPs with increasing III/V flux ratio from G1613 to G1611 [Table 9.3]. Among all the NP samples, G1613 demonstrates the best pillar morphology by exhibiting NPs with uniform diameter and good inter-pillar spacing [Fig. 9.7(a)].

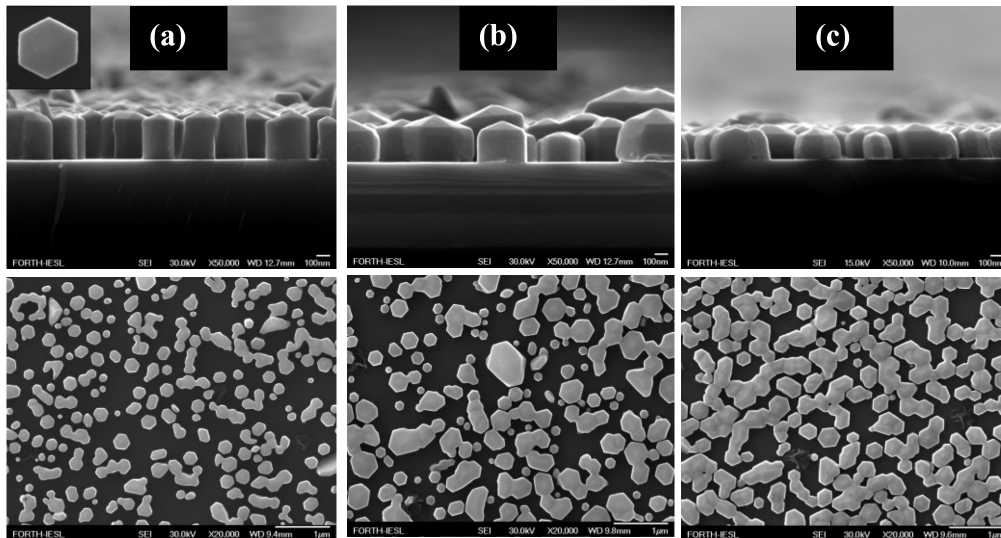

Figure 9.7 *FE-SEM micrographs of InN NPs (a) G1613, (b) G1612 and (c) G1611 spontaneously grown on Si (111) for 1hr each at 500°C, using different In/N flux ratio of 0.16, 0.22 and 0.33, respectively.*

The plot of the different NP growth rates obtained at growth temperatures of 470°C and 500°C versus N-flux (with In-flux = 120 nm/hr) is shown in Fig. 9.8. It is apparent that the growth rates increases with increasing N-flux. It is also evident that the height of the nanopillars increased as the growth temperature increased from 470°C to 500°C and the difference observed in the NPs growth rate becomes increasingly pronounced towards the regions of higher incident N-flux while the effect of growth temperature is almost negligible when low N-flux was employed.

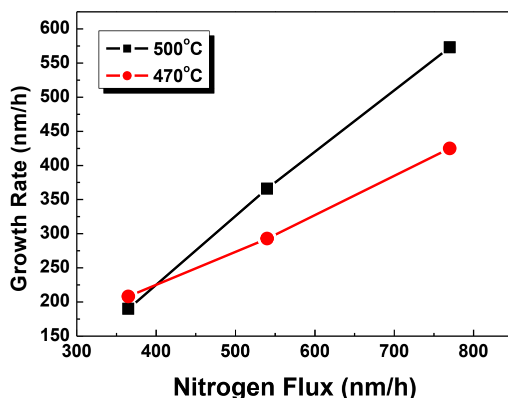

Figure 9.8 *Dependence of the growth rate of InN NPs on nitrogen flux for two different substrate temperatures of 470°C and 500°C.*

An XTEM micrograph of sample G1613 that evolved with the best NPs morphology [Fig. 9.7(a)] is presented in Fig. 9.9. The measured heights of the NPs were 330 ± 15 nm, which agrees very well with the value estimated by FE-SEM [Table 9.3]. Thin and wide NPs with diameters of 80 ± 15 nm and 235 ± 45 nm are shown in Figs. 9.9(a) and 9.9(b), respectively. A "roof-like" morphology of the NP tips was observed for G1613 [Figs. 9.9], similar to the FE-SEM observations of Fig. 9.7(a), in contrast to the typically round tip of G984 [Figs. 9.1(c) and 9.3(a)]. The rounded tips observed in some of the G1613 NPs are primarily attributed to the ion-milling process during preparation of the samples rather than the growth process. HRTEM image of the NPs top (not shown) revealed that the (0001) planes are bounded by facets ($\{10\bar{1}4\}$ facets) inclined by ~ 23°-26°. The NPs areal density was ~ 8 x 10^8 cm^{-2} , which is almost two orders of magnitude lower than the $1.7x10^{10}$ cm^{-2} obtained for G984 [Fig. 9.3].

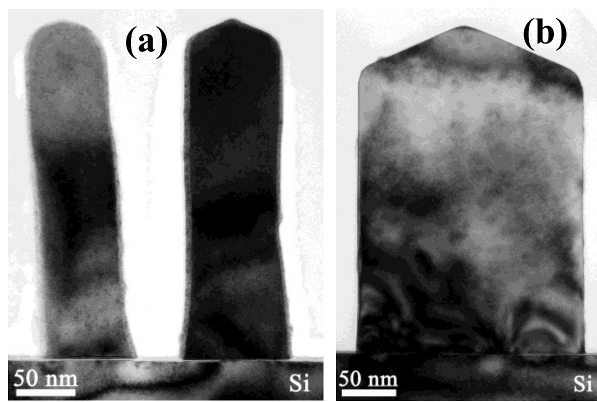

Figure 9.9 *XTEM micrograph of G1613, taken along* $[11\bar{2}0]_{GaN}//[1\bar{1}0]_{Si}$ *zone axis, showing the morphology of the (a) thin NPs with diameters 80±15 nm and (b) wide NPs with diameters 235±45 nm.*

Fig. 9.10 is the cross-sectional HRTEM image that depicts well the Si/InN NPs interface. Crystalline formations with cubic lattice-stacking sequence were observed in the amorphous SiN layer (see arrows), owing to the nitridation of Si substrate surface during the NPs growth. These crystalline formations are probably Si, which was left intact by the Si nitridation process due to the nucleation of InN islands at these sites, which masked the Si surface from the N-beam thus preventing the local nitridation. These crystalline regions operated as "seeds" for the epitaxial growth of InN NPs on Si.

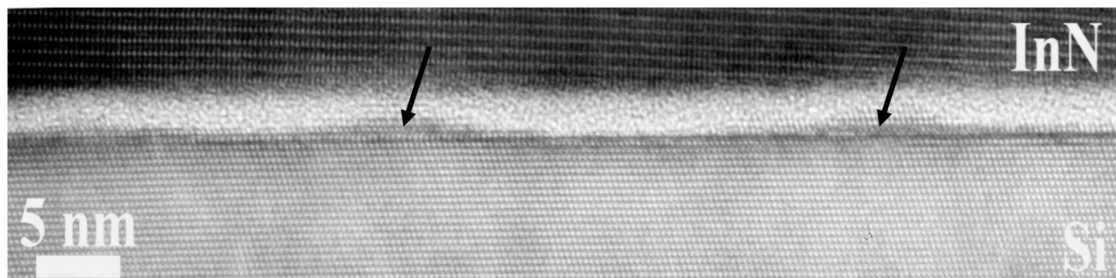

Figure 9.10 *Cross-sectional HRTEM images taken along* $[11\bar{2}0]_{GaN}//[1\bar{1}0]_{Si}$ *zone axis, representing the Si/InN NPs interface and showing the existence of interfacial* Si_xN_y*. The arrows identify crystalline formations in the* Si_xN_y *layer.*

It is well known that the onset of InN film decomposition starts at about 450°C [25]. However, the growth of InN NPs is sustainable at higher T_{sub} without the observation of metallic In accumulation due to the nitrogen rich growth conditions employed [22,26]. The In atoms from InN decomposition will re-bond to the excess nitrogen atoms on the substrate's surface and thus, will be fully incorporated in InN growth.

The low temperature PL spectra of samples G1611 to G1613 are shown in Fig. 9.11. Only sample G1613 with the thinnest, most separated and most uniform NPs exhibited PL peak. The FWHM of the PL peak was 100 meV. It is reasonable to attribute the observation of PL only in sample G1613 to a superior structural quality of these NPs compared to the other samples. A higher density of defects is expected in the wider NPs of samples G1611 and G1612.

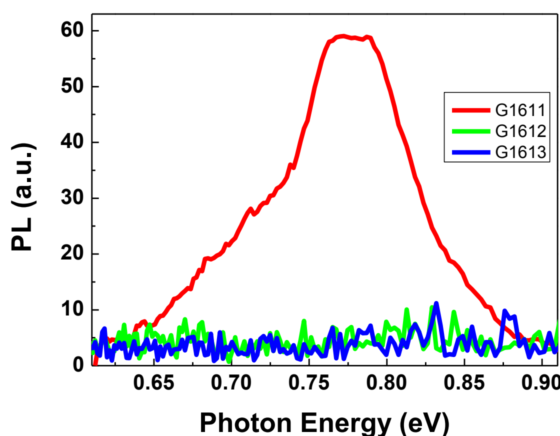

Figure 9.11 *20K PL spectra for InN NPs of samples G1611 to G1613. Only sample G1613 yielded photoluminescence.*

9.4 The role of AlN nucleation layer on InN NPs properties (In-flux constant)

The effect of using a thin AlN nucleation layer as an intermediate material prior to growing InN NPs on Si (111) was also investigated. AlN is known to exhibit good wetting behaviour on Si. The thickness of the AlN NL employed was always 10 nm and the growth temperature was 900°C. Three samples were grown by depositing InN on the AlN NLs at 370°C for 2hrs under similar growth conditions to the set of samples G1304, G1305 and G1306, where InN was grown directly on Si [Fig. 9.6 and Table 9.2]: Different In/N flux ratios were used with the In-flux kept constant at 120 nm/hr. The growth conditions are described in Table 9.4. The surface morphology of the resulting InN samples G1307, G1308 and G1309 are shown in Figs. 9.12(a), 9.12(b) and 9.12(c), respectively.

Interestingly, in contrast to the InN NP structures of samples G1304 - G1306 that resulted from the same growth conditions on bare Si surface [Fig. 9.6], the use of an AlN NL on Si led to nanoporous InN structures, as shown in Fig. 9.12, and the degree of porosity depends on the used III/V flux ratio. The thickness of the nanoporous layers of samples G1307, G1308 and G1309 was 435 nm, 285 nm and 460 nm, respectively, which corresponds to a growth rate that is multiple of the F_{In}. In fact, the growth rate of the nanoporous samples was slightly higher than what was

obtained for the InN NPs set of Fig.9.6 that were grown without AlN nucleation layer [Fig. 9.13]. In both cases, the growth rate similarly reduces with the lowering of the N-flux, under the constant In-flux employed [Table 9.4]. The consistently higher growth rate obtained, compared with that of the constant In-flux employed (120 nm/hr), confirmed that the growth is N-flux limited and not In-flux limited for both nanoporous InN and InN NPs.

Table 9.4 *Growth conditions and properties of InN NPs grown on Si (111), after the initial growth of a 10 nm ALN NL. Different N-fluxes (F_N) were employed with the In-flux (F_{In}) kept constant at 120 nm/hr. The RF power was constant at 300W and the N_2 flow rate was varied. The samples were grown at T_{sub} of 470^oC for 2 hr similar to the set of samples G1304, G1305 and G1306 described in Fig. 9.6 and Table 9.2.*

Sample Identity	N_2 flow rate	F_N	F_{In}/F_N	Measured thickness	G.R./ F_N	G.R./ F_{In}
G1307	0.26 sccm	365 nm/h	0.33	435 nm	0.60	1.82
G1308	0.47 sccm	540 nm/h	0.22	600 nm	0.56	2.5
G1309	1.12 sccm	770 nm/h	0.16	920 nm	0.60	3.83

In a similar vein, an attempt to grow InN NPs on Si under the optimum growth conditions like that of G1306 after the initial deposition of a thin LT-InN nucleation layer, also yielded a porous InN layer as shown in Fig. 9.14 (sample G1316). This sample exhibited lower porosity compared to the samples of Fig. 9.12. Similar results were also obtained when the LT-InN NL was annealed at 500^oC. These results indicate that the nucleation and growth of InN NPs on Si is driven by the lattice mismatch strain and chemical differences of InN and Si that favour the 3D growth mode, as well as the formation of amorphous Si_xN_y on the Si surface between the InN nuclei, which is an unfavourable surface for InN nucleation.

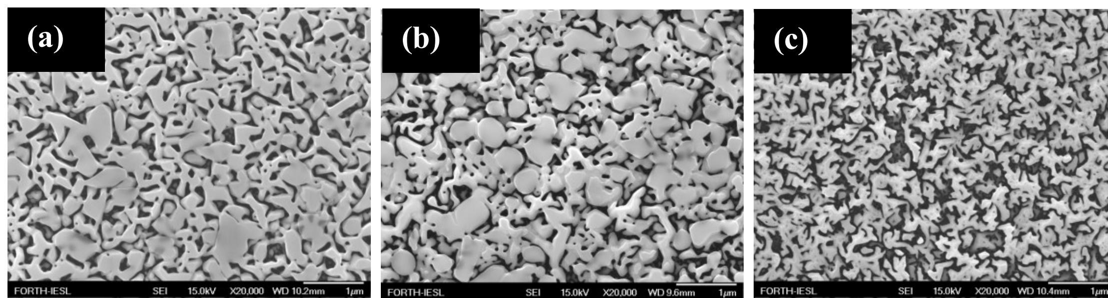

Figure 9.12 *FE-SEM plan-view micrographs showing the surface of the InN nanoporous samples (a) G1307, (b) G1308, and (c) G1309 that resulted from InN growth on Si (111) using a 10 nm HT-AlN nucleation layer and the growth conditions listed in Table 9.4. These conditions resulted to InN NPs structures on bare Si surface (without AlN nucleation), as shown in Fig. 9.6.*

Hence, further investigations to find the appropriate growth conditions for AlN mediated InN NPs growth on Si were carried out. The best growth conditions obtained so far resulted to the NPs sample G1619 shown in the FE-SEM micrograph of Fig. 9.15. G1619 was grown only for 1 hr at 370^oC by increasing the N-flow rate to 1.35 sccm instead of the initial rates [Table 9.4] and the RF power to 400W while the

In flux was kept constant at 120 nm/hr. Fig. 9.15 shows that sample G1619 indeed exhibited InN NPs with well aligned axis along the growth direction (*c*-axis). The NPs are basically of a narrow "V" shape configuration. Within the 1 hr of the NPs' growth at 370°C, the growth rate attained 560 nm/hr, which is 4.7 times the incident F_{In}.

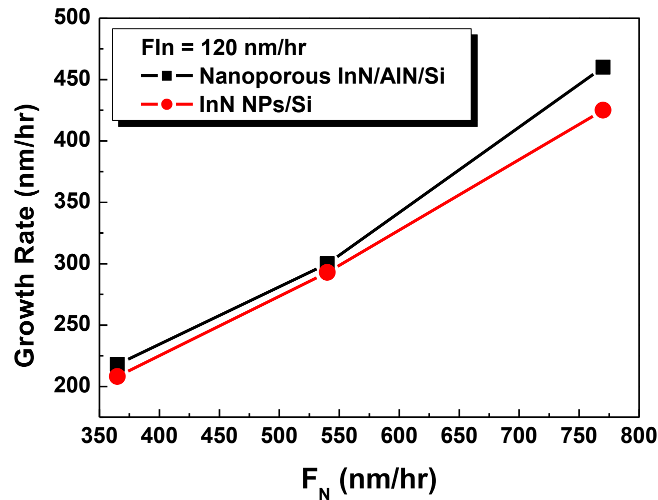

Figure 9.13 *Similar dependence of the growth rate on the N-flux (F_N) for the nanoporous InN and InN NP samples grown at 470°C with constant In-flux (F_{In} = 120 nm/hr). The growth rate has been limited by the N-flux instead of In-flux.*

In general, these experiments suggest that much higher flux of reactive nitrogen species is needed to successfully nucleate and grow a well defined structure of InN NPs parallel to *c*-axis on AlN surfaces, compared to the growth on bare Si surfaces.

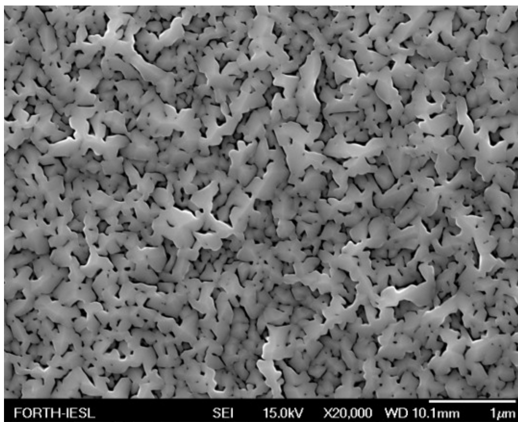

Figure 9.14 *FE-SEM plan-view micrographs of the InN nanoporous sample G1316 obtained by InN growth on Si (111) at 470°C, using a III/V flux ratio of 0.16 (similar to that of G1306 listed in Table 9.2) after the initial deposition of a 10 nm LT-InN nucleation layer.*

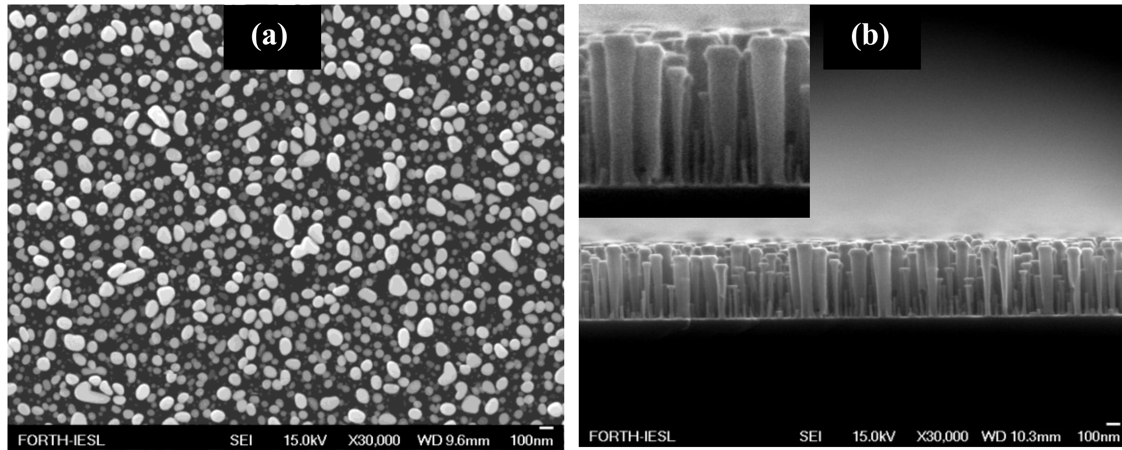

Figure 9.15 *FE-SEM images of the (a) plan-view and (b) cross-section of InN NPs G1619 grown on AlN/Si surface. InN NPs structures were successfully nucleated on the AlN wetting layer on Si substrate using higher N-flow rate of 1.35 sccm and rf-power of 400W than required to nucleate and grow InN NPs on bare Si (111) surface.*

9.5 Conclusions for PAMBE growth of InN NPs on Si (111)

The previous sections described a series of experiments for the PAMBE growth of InN nanopillars on Si (111) substrates. Influences of III/V flux ratio, substrate temperature and intermediate layer on the morphology of the NPs were investigated to understand the NPs growth mechanism on Si (111). The substrate temperature range favourable for obtaining InN NPs was in-between 450 and 500°C, using In/N flux ratio range of 0.15 to 0.2. However, the density of the InN NPs was reduced when T_{sub} was increased from 450 [Fig. 9.2] to 500°C [Fig. 9.7], leading to well separated InN NPs. Diameter widening of the NPs top was almost always observed at the expense of the bottom region. This phenomenon may be understood considering the following: As growth time increases and the NPs height increases, the base of each NP may have slightly higher temperature than the top region, leading to the decomposition of InN at the base region. The In atoms from the dissociation process diffuse along the side wall of the NP to the top surface, which has a lower temperature and there can be bonded to incident N-atoms. Due to the geometrical shape of the NPs, direct incidence of nitrogen species on the walls, and especially near the base of the NPs, should be negligible. It is also known that N-atoms have a very short residence time on the substrate surface and essentially cannot diffuse but only bond to available In unbonded atoms. Thus, decomposed material at the base of NPs cannot be re-synthesized due to lack of incident N atoms. However, N atoms are continuously supplied by the plasma source at the top region of the NPs. This results to thickening of the top region of the NPs (tapering effect) at the expense of the base region. The tapered morphology is not favoured in InN NPs with low growth duration and low areal density, since the temperature and N-flux gradients are negligible or reduced, along the vertical distance of the NPs and hence the mechanisms responsible for the tapering phenomenon could not be fully activated.

Although high growth temperature plays a very important role in the activation of tapering effect in spontaneously grown InN NPs on Si (111), the solution does not lie in the reduction of the temperature, which should promote coalescence of

individual pillars and structural defect incorporation in the NPs. While InN NPs with uniform diameter can be easily realised by growing NPs of low height, a method of maintaining similar temperature (avoiding temperature gradient) along the vertical distance for spontaneously grown InN NPs is ideally needed for NPs with higher heights. The low areal density or large spacing of NPs, together with inclined incidence of the N-beam to the substrate surface and rotation of the substrate can also assist to preserve a uniform diameter along the axis of the InN NPs, by supplied N-atoms uniformly to the NP walls.

9.6 Growth of InN nanopillars on *r*-plane sapphire substrates

Even though a lot of reports exist for the growth of polar *c*-plane InN NPs on different substrate materials, only one has been published so far on non-polar *a*-plane InN NPs [27], which were grown by plasma-assisted molecular beam epitaxy on *a*-plane GaN/*r*-plane sapphire templates. We have also studied the growth of InN NPs on *r*-plane sapphire and the work is presented in this section. The optimised conditions (F_{In} = 120 nm/hr and F_N = 770 nm/hr) for InN NPs growth on Si (111) were employed with the intention of growing InN NPs on *r*-plane sapphire. Four samples were grown to investigate the role of T_{sub}, sapphire surface nitridation and *a*-plane GaN buffer layer. Table 9.5 described the growth conditions and some of the properties of the deposited InN. For the samples that include sapphire nitridation in the growth procedure, the nitridation step was carried out *in-situ* for 15 min at 900°C under a N-flux of 635 nm/hr (N_2 flow rate of 0.56 sccm and RF power of 300W). All of the samples were characterised by FE-SEM, HR-XRD and low temperature PL to investigate their morphology, crystallographic orientation and optical properties, respectively.

Table 9.5 *Samples of InN grow on r-plane Al_2O_3 substrates, using the optimized growth conditions for InN NPs growth on Si (111). N-flux of 783 nm/h (RF power of 300W and N_2 flow rate of 1.12 sccm) and In-flux of 120 nm/hr were employed. The growth rate and its relation to F_{In} and F_N are given.*

Sample Identity	*r*-Al_2O_3 surface treatment	F_{In}/F_N	T_{sub} (^{o}C)	Height along *c*-axis	Growth rate along *c*-axis	G.R./ F_N	G.R./ F_{In}
G1376	Nitridation	0.16	470	650 nm	480 nm/hr	0.61	4.00
G1493	Nitridation	0.16	430	200 nm	160 nm/hr	0.20	1.33
G1495	No Nitridation	0.16	430	130 nm	104 nm/hr	0.13	0.87
G1494	20 nm GaN	0.16	430	-	120 nm/hr	0.15	1.00

The FE-SEM micrographs of Fig. 9.16 indicate that InN NPs were formed for InN growth directly on the *r*-plane sapphire, as shown in Figs. 9.16(a)-(c) (samples G1376, G1493 and G1495, respectively). However, an intermediate 20 nm GaN layer resulted to a compact InN film, as shown in Fig. 9.16(d). The inset images of Figs. 9.16(a)-(d) provide a clearer view of the InN structures. The pillars were all apparently aligned along the growth direction.

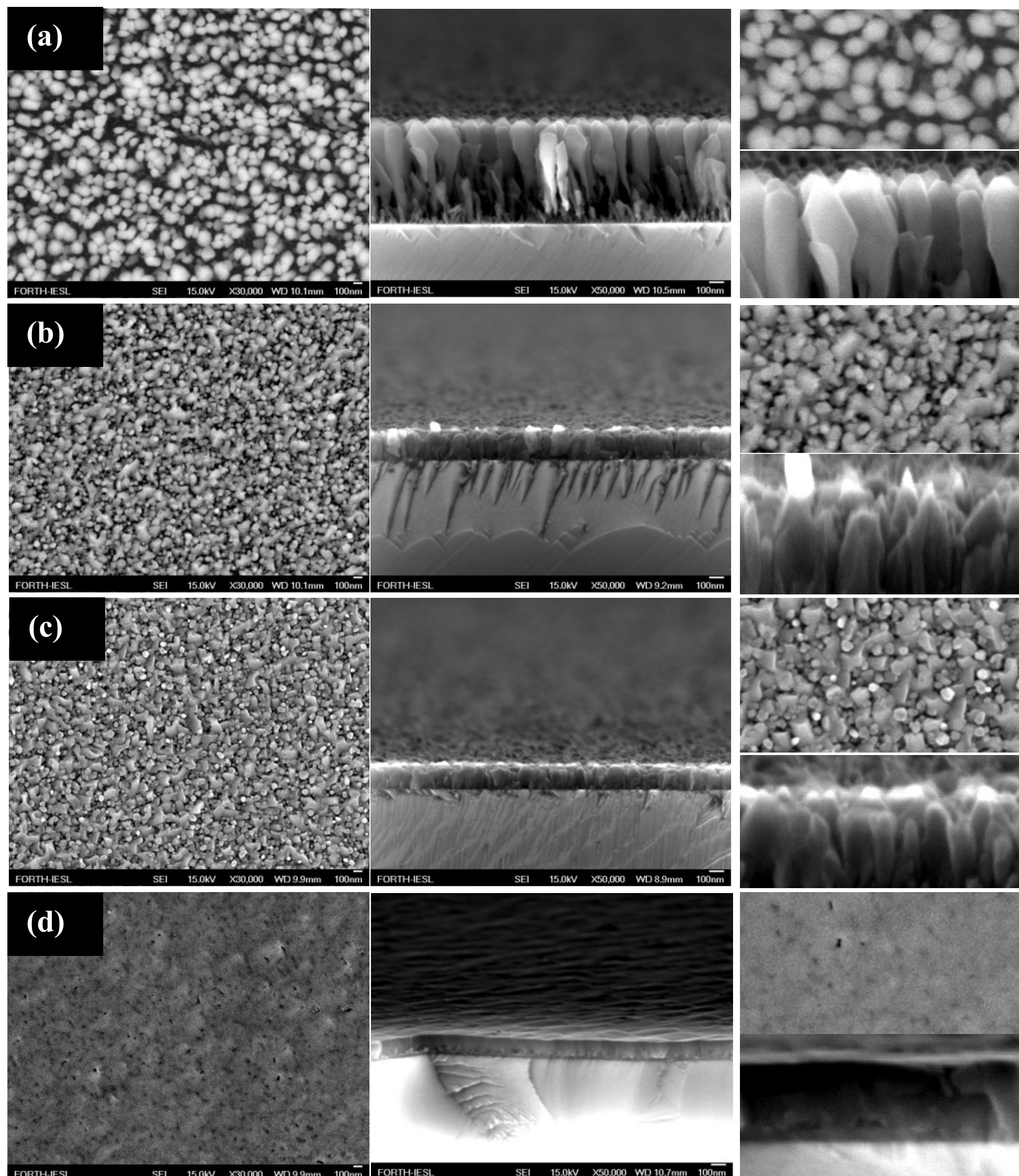

Figure 9.16 *FE-SEM plan-view and cross-sectional view of InN grown on r-plane sapphire substrates, using the already optimized III/V and T_{sub} growth conditions for InN NPs growth on Si (111): (a) sample G1376 showing a well separated NPs structure (b) sample G1493 showing NPs structure (b) sample G1495 showing NPs structure and (d) sample G1494 showing InN film structure. The insets present a clearer image of the InN morphology.*

Sample G1376 grown at 470°C exhibited arrow-like top with faceted sides [Fig. 9.16(a)] in contrast to InN NP sample G1306 grown under similar conditions on Si (111) substrate that exhibited a flat surface [Fig. 9.6(c)]. The faceting of these NPs is typically different also from the InN NPs reported by Liliental-Weber *et al*. [28], which were grown on *a*- and *r*-plane sapphire by MOVPE and the NPs reported by Grandal *et al.* [27], which were grown on *a*-plane GaN template by PAMBE. The sample G1376 also exhibited thinning of the NPs' bottom, with the average bottom

and top diameters estimated as 30 nm and 100 nm, respectively. There is no significant dispersion in the NPs heights as shown in Fig. 9.16(a).

The NPs of sample G1493 grown at 430°C, were basically merged, which is attributed to higher density of nucleated NPs at the reduce T_{sub} , due to the reduced In adatoms' diffusion at the surface. The nitridation of the *r*-plane sapphire surface did not changed essentially the morphology of the deposited InN NPs [Fig. 9.16(c)], and only a significant change in the NP height was observed, as shown in Table 9.5, suggesting increased coalescence of the NP in sample G1495. The significantly higher growth rate and increased spatial distance from one another for NPs grown at the higher T_{sub} of 470°C (sample G1376) are consistent with what has been previously observed for InN NPs grown Si (111) in Section 9.3. The percentage of N atoms incorporated into the InN NPs G1376 grown at 470°C was approximately 61%, and dropped to ~20% for growth at 430°C (sample G1493). However, within the accuracy of the flux control, the nitridation of the sapphire surface (sample G1495) reduced even more the InN layer growth rate and approached the In-flux limited value that was also observed for compact film of G1494. The growth rate of G1494 strikingly conforms to that of the In flux (120 nm/hr) employed for the experiment [Table 9.5]. The inability of G1494 to yield NPs structure is partly attributed to the reduced lattice mismatch strain by the used GaN wetting layer. The thin GaN buffer layer is expected to be *a*-plane film [29]. The InN NPs in the other samples are probably oriented along the *c*-axis. However, the spontaneous InN growth along the *c*-axis is not possible on an *a*-plane GaN surface. In this case, InN follows the crystalline structure of the *a*-plane GaN template. However, it has been also suggested that *a*-plane InN NPs could grow on an *a*-plane GaN template at temperature higher than 475°C [27] (which increases the diffusion of In atom on the surface).

All samples were also investigated by HR-XRD to identify the epilayers crystallographic orientation. The 2theta profiles shown in Fig. 9.17 indicate that samples G1376, 1493 and 1495 consist of mixed hexagonal polar *c*-plane (0002) InN and semipolar *s*-plane $\{10\bar{1}1\}$ InN orientations, although G1376 demonstrates preferred *c*-plane (0002) InN orientation. From the investigation of samples G1493 and G1495, HR-XRD revealed that they are oriented in a similar way and none exhibited *a*-plane orientation but the co-existence of the *c*-plane (0002) and *s*-plane $\{10\bar{1}1\}$ InN peaks with preferred $(10\bar{1}1)$ orientation [Fig. 9.17]. III-nitride semiconductors are well known to exhibit higher growth rate along the *c*-axis and this should be responsible for the preferred *c*-axis orientation of the InN NPs of sample G1376. It is believed that the *s*-plane $(10\bar{1}1)$ reflections of sample G1376 emanated from the material deposit in between the NPs. In the case of samples G1493 and G1495, this deposit covered larger areas than the NPs, due to the fact that the used lower growth temperature facilitated coalescence of the initially formed islands, leading to the higher HR-XRD intensity of the $(10\bar{1}1)$ peak observed. Kumagai *et al.* [30] has reported the existence of cubic (001) AlN on nitridated *r*-plane sapphire substrate, and concluded that a thin *c*-AlN layer formed aided *a*-plane InN films' growth on *r*-plane sapphire. In the present experiment, it is observed that whether the *r*-plane sapphire is nitridated or not do not have any effect on the crystal structure of the InN NPs (see samples G1493 and G1495 in Table 9.5 and Fig. 9.17).

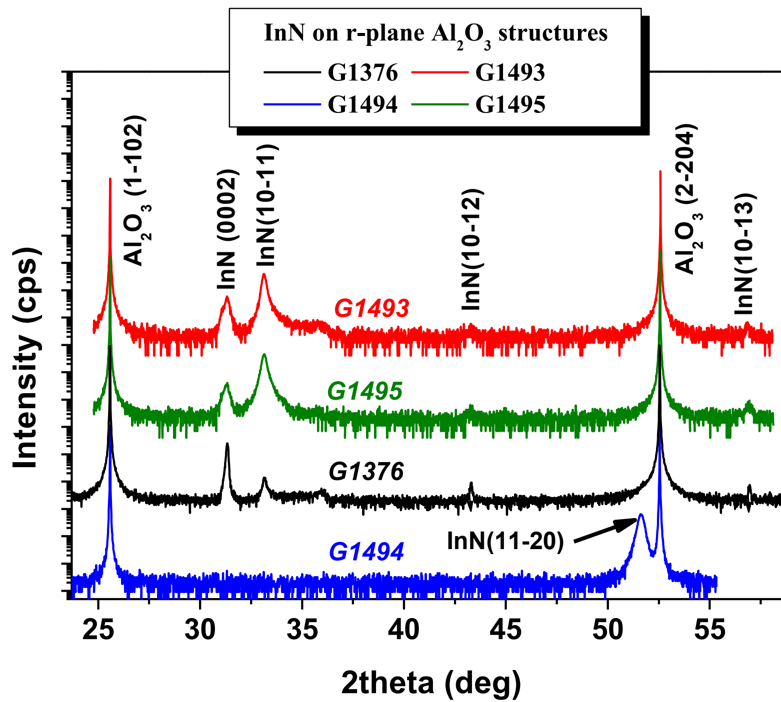

Figure 9.17 *HR-XRD 2theta scan profile of InN grown on r-plane sapphire substrates, using the already optimized growth conditions for InN NPs growth on Si (111). All the InN NPs exhibited mixed InN orientations. Only the InN structure that employed GaN buffer layer resulted to single crystalline a-plane film.*

The HRXRD 2theta measurements of film sample G1494 resulted to only one InN reflection, which corresponds to (11-20) orientation and indicates that the layer is a single crystalline non-polar *a*-plane InN. This result buttresses the fact that InN naturally evolves with *a*-plane (11-20) InN orientation on *r*-plane sapphire substrates whenever GaN wetting layer is used, irrespective of the III/V flux ratio employed for the epilayer InN growth [Section 5.5].

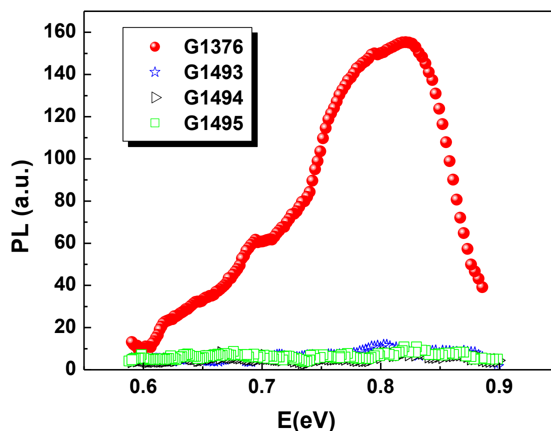

Figure 9.18 *20K PL measurements of InN grown on r-plane sapphire substrates, using the optimum III/V and T_{sub} growth conditions for the growth of InN NPs on Si (111). Only sample G1376 with InN NPs grown spontaneously on r-plane sapphire substrate at a higher T_{sub} of 470^oC exhibited photoluminescence. See the growth conditions of samples G1493 - G1495 in Table 9.5.*

The low temperature PL measurement spectra of the NPs at 20K are shown in Fig. 9.18. Only the InN NPs sample G1376 exhibited PL emissions with energy peak at 0.82 eV. The FWHM of the spectra was determined to be approximately150 meV. These results indicate that the NPs grown at higher T_{sub} undoubtedly demonstrated better crystalline quality. It is note worthy to mention that none of the InN NPs samples G1493 - G1495 exhibit PL emissions [Fig. 9. 18].

9.7 Concluding remarks

The spontaneous growth by PAMBE of InN nanopillars on Si (111) and *r*-plane sapphire substrates has been investigated. The InN NPs are generated due to 3D islands nucleation as a result of lattice mismatch strain energy between the NPs and the substrates. The high surface energy of the nitrogen stabilized (0001) III-nitride surfaces may also stabilize their anisotropic growth. Influences of III/V flux ratio, buffer layer and substrate temperature on the morphology of the NPs were investigated to understand the NPs growth mechanism. The different growth parameters were optimised to obtain well separated NPs, exhibiting PL emission.

Almost in all cases, the growth rate of the InN NPs along the *c*-axis is multiple of the In-limited growth rate. For constant N-flux, the growth rate increases slightly with the In-flux but a significantly lager (multiplication) effect is observed by increasing the N-flux for constant In-flux. Non-uniformity of NPs diameter occurs as column height increases, and it is attributed to temperature aided decomposition and diffusion processes in InN NPs that result to migration of In-adatoms from the base region to the top region of NPs at high growth temperature. The optimum growth temperature determined for spontaneous PAMBE growth of high quality, oriented InN NPs on Si (111) is 500°C under a III/V flux ratio of ~ 0.16. Under these optimum growth conditions, well-aligned, single crystalline NPs with hexagonal InN structure were realized. TEM investigation revealed the formation of unintentional amorphous Si_xN_y layer at the interfacial region in-between the InN NPs and Si. The non-uniformity of the Si_xN_y layer was inevitable under unoptimised growth conditions, leading to the frequently observed NP misorientation or tilt on Si substrates.

An initial deposition of a thin LT-InN nucleation on Si(111) prior to InN NPs growth under the already optimised InN NPs growth conditions resulted to a porous InN layer, indicating that the nucleation and growth of InN NPs on Si is driven by the lattice mismatch strain and chemical differences of InN and Si that favour the 3D growth mode, as well as the formation of amorphous SixNy on the Si surface between the InN nuclei, which is an unfavourable surface for InN nucleation. Use of a thin AlN nucleation layer to grow InN NPs resulted to nanoporous InN structures on Si. However, increasing the N-flux far above that of the optimised conditions for growth directly on Si made possible also the growth of NPs on the AlN layer. All the NPs are pure crystalline wurzite (0002) InN.

The attempt to grow InN NPs directly on *r*-plane sapphire substrates without GaN buffer layers resulted to epilayers that generally exhibited mixed polar (0001) InN and semipolar {10-11} InN orientations. It is anticipated that InN NPs were prefentially oriented along the [0001] axis and the semipolar orientation corresponded to material deposited in the terraces between the NPs. Further characterisation using TEM may be needed to ascertain the exact structure of these samples. A fully

coalesced *a*-plane film structure with rough surface morphology was grown when a GaN buffer layer was initially deposited on a *r*-plane sapphire. The *a*-plane GaN layer reduces the required lattice mismatch strain in between the InN and the substrate, making the realisation of NPs structure difficult.

The InN NPs growth, under optimised conditions, are promising for the fabrication of nanostructure devices as well as for the overgrowth of stress-free epilayers with low threading dislocation density, if the lateral growth and coalescence of NPs can be efficiently accomplished.

References

1. A. Georgakilas, A. Dimoulas, A. Christou and J. Stoemenos, *J. Mater. Res.* **7**, 2194 (1992)
2. A. Kikuchi, M. Tada, K. Miwa and K. Kishino, in "*Quantum Dots, Particles, and Nanoclusters III"*, edited by Kurt G. Eyink, Diana L. Huffaker, *Proc. of SPIE* **6129**, 612905, (2006)
3. F. Natali, F. Semond, J. Massies, D. Byrne, S. Laügt, O. Tottereau, P. Vennéguès, E. Dogheche, and E. Dumont, *Appl. Phys. Lett.* **82**, 1386 (2003)
4. D. Zhu, C. McAleese, M. Häberlen, C. Salcianu, T. Thrush, M. Kappers, A. Phillips, P. Lane, M. Kane, D. Wallis, T. Martin, M. Astles, and C. Humphreys, *Phys. Status Solidi (c)* **7**, 2168 (2010)
5. S. Nakamura, T. Mukai and M. Senoh, *Appl. Phys. Lett.* **64**, 1687 (1994)
6. S. Nakamura, M. Senoh, S. Nagahama, N. Iwasa, T. Yamada, T. Matsushita, H. Kiyoku and Y. Sugimoto, *Japan J. Appl. Phys.* 2 **35** L74 (1998)
7. C. Chèze, L. Geelhaar,B. Jenichen, and H. Riechert, *Appl. Phys. Lett.* **97**, 153105 (2010)
8. C. Chèze, L. Geelhaar, O. Brandt, W. M. Weber, H. Riechert, S. Münch, R. Rothemund, S. Reitzenstein, A. Forchel, T. Kehagias, P. Komninou, G. P. Dimitrakopulos, and T. Karakostas, *Nano Res* **3**, 528 (2010)
9. F. Qian, Y. Li, S. Gradecak, D. L. Wang, C. J. Barrelet and C. M. Lieber, *Nano Lett.* **4**, 1975 (2004)
10. J. Su, G. Cui, M. Gherasimova, H. Tsukamoto, J. Han, D. Ciuparu, S. Lim and L. Pfefferle *Appl. Phys. Lett.* **86**, 13105 (2005)
11. R. Calarco, M. Marso, T. Richter, A. I. Aykanat, R. Meijers, A. V. Hart, T. Stoica and H. Luth *Nano Lett.* **5**, 981 (2005)
12. Y.H. Kim, J.Y. Lee, S.H. Lee, J.E. Oh, H.S. Lee, *Appl. Phys. A* **80**, 1635 (2005)
13. L. E. Jensen, M. T. Björk, S. Jeppesen, A. I. Persson, B. J. Ohlsson and L. Samuelson, *Nano Lett.* **4**, 1961 (2004)
14. A. M. Morales and C. M. Lieber, *Science* **279**, 208 (1998)
15. X. F. Duan and C. M. Lieber *J. Am. Chem. Soc.* **122**, 188 (2000)
16. H.M. Ng, R. Liu and F.A. Ponce, *in "State-of-the-Art Program on Compound Semiconductors XLI and Nitride and Wide Bandgap Semiconductors for Sensors, Photonics and Electronics V"*, Ed. By H. M. Ng, A. G. Baca, Proceedings of the international symposia, pg. 372 (2004)
17. S. Nishikawa, Y. Nakao, H. Naoi, T. Araki, H. Na, Y. Nanishi, *J. Cryst. Growth* **301–302**, 490–495 (2007)
18. X. Wang, S.-B. Che, Y. Ishitani, and A. Yoshikawa, *J. Cryst. Growth* **301**, 496 (2007).
19. T. Stoica, R. J. Meijers, R. Calarco, T. Richter, E. Sutter, and H. Lüth, *Nano Letters* **6**, 1541 (2006).
20. J. Grandal, M.A. Sanchez-Garcia, E. Calleja, E. Luna, and A. Trampert, *Appl. Phys. Lett.* 91, 021902 (2007).
21. C. H. Shen, H. Y. Chen, H. W. Lin, S. Gwo, A. A. Klochikhin, and V. Y. Davydov, *Appl. Phys. Lett.* 88, 253104 (2006).
22. A. O. Ajagunna, A. Adikimenakis, E. Iliopoulos, K. Tsagaraki, M. Androulidaki, and A. Georgakilas, *J. Cryst. Growth* **311**, 2058 (2009)

23. E. Dimakis, E. Iliopoulos, K. Tsagaraki, A. Georgakilas, *Appl. Phys. Lett.* **86**, 133104 (2005)
24. E. Dimakis, E. Iliopoulos, K. Tsagaraki, A. Georgakilas, *Phys. Status Solidi (a)* **203**, 1686 (2006)
25. E. Dimakis, E. Iliopoulos, M. Kayambaki, K. Tsagaraki, A. Kostopoulos, G. Konstantinidis, A. Georgakilas, *J. Electron. Mater.* **36**, 373 (2007).
26. A.P. Vajpeyi, A.O. Ajagunna, G. Tsiakatouras, A. Adikimenakis, E. Iliopoulos, K. Tsagaraki, M. Androulidaki, A. Georgakilas, *Microelectronic Engineering* **86**, 812 (2009)
27. J. Grandal, M. A. Sánchez-García, E. Calleja, E. Gallardo, J. M. Calleja, E. Luna, A. Trampert, and A. Jahn, *Appl. Phys. Lett*. **94**, 221908 (2009)
28. Z. Liliental-Weber, M. Hawkridge, J. Mangum, and O. Kryliouk, *Phys. Status Solidi (c)* **5**, 1795 (2008)
29. A. O. Ajagunna, E. Iliopoulos, G. Tsakatouras, K. Tsagaraki, M. Androulidaki, and A. Georgakilas, *J. Appl. Phys*. **107**, 024506 (2010)
30. Y. Kumagai, A. Tsuyuguchi, H. Naoi, T. Araki, H. Na, and Y. Nanishi, *Phys. Status Solidi (b)* **243**, 1469 (2006)

10 Summary of Results

10.1 Preamble

10.2 InN and InN/InAlN heterostructures on GaN/Al_2O_3 (0001)

10.2.1 InN (0001) films on (0001) GaN/Al_2O_3 (0001)

10.2.2 InN/InAlN heterostructures on (0001) GaN/Al_2O_3 (0001)

10.3 InN on *r*-plane ($1\bar{1}02$) sapphire substrates

10.3.1 The role of buffer layer on InN growth on *r*-plane sapphire

10.3.2 Growth of *a*-plane InN grown on *r*-plane sapphire

10.3.3 Thickness dependent electrical properties of *a*-plane InN

10.4 InN films on Si (111) substrates

10.4.1 Nucleation and buffer layers for InN on Si (111) heteroepitaxy

10.4.2 Optimisation of InN nucleation for direct heteroepitaxy on Si (111)

10.5 InN Nanopillars on Si (111) and *r*-plane ($1\bar{1}02$) Al_2O_3 substrates

10.6 General conclusion for InN heteroepitaxial films

10.7 Possible future works

10.1 Preamble

This dissertation concerns the study of plasma assisted molecular beam epitaxy (PAMBE) of InN heterostructures and nanopillars. Among the group III-nitrides, InN has been the least studied and also the most complex. The investigations basically dealt with the growth and properties of InN on *c*-plane GaN/sapphire (0001), *r*-plane sapphire and Si (111) substrates. The controlled growth and formation of InN/InAlN heterostructures and InN nanopillars was also considered. The detailed investigations on the epitaxy of InN on *c*- and *r*-plane sapphire as well as on Si (111) provide important information for better understanding of the InN growth and properties, and can be of credible assistance towards the growth of device quality InN-based heterostructures. The various studies undertaken and results obtained are briefly mentioned in the following.

10.2 InN and InN/InAlN heterostructures on GaN/Al_2O_3 (0001)

10.2.1 InN (0001) films on (0001) GaN/Al_2O_3 (0001)

The heteroepitaxial growth and properties of InN layer of different thicknesses on MOVPE GaN/ (0001) sapphire pseudo-substrates were investigated. Thickness range of 30 - 5000 nm was considered. The epitaxy of the films proceeded in the step-flow growth mode with surface morphology characterised by monolayer height steps, terraces and spiral hillocks. The early stage of the InN growth is characterised by high density hillocks, which appeared to exhibit increment in size and decrement in density per surface area as the film thickness increases. The hillocks considerably reduced in density (ρ) by two orders from 1.30 x 10^9 cm^{-2} to 1.2 x 10^7 as the InN film thickness increased from 30 nm to 1000 nm, respectively. The visibility of hillocks on the AFM micrographs of the surface is related to the presence of screw dislocation but also to the used growth conditions (substrate temperature and III/V flux ratio).

A roughly constant HR-XRD rocking curve (RC) FWHM of the symmetric (0002) reflection was observed with increasing film thickness while for the case of asymmetric $(10\bar{1}5)$ reflections, the FWHM values significantly reduces with thickness. The symmetric and asymmetric rocking curve (RC) FWHM values obtained for the thickest 5000 nm sample were 450 and 324 arcsec, respectively. Since the FWHM of the HR-XRD symmetric reflection RCs correlates with the density of screw type (including screw component) dislocations (tilt mosaicity) in III-nitride films, this result indicates that the density of screw type dislocations should be almost independent of InN film thickness. On the other hand, the FWHM of assymmetric reflection HR-XRD RCs depends on the density of both edge and screw component dislocations. Since the density of screw type dislocations is expected to be almost contant in the films, the changes observed with thickness in the asymmetric FWHM could only be ascribed to the edge type dislocations (ETD) (including edge-component dislocations), indicating that the density of the ETDs reduces with InN film thickness.

The transport properties investigation by Hall-effect measurements revealed a non-zero surface electron accumulation of 1.58 x 10^{14} cm^{-2} in the InN films. The measured Hall mobility increased monotonically with increasing InN thickness from 242 to 1824 cm^2/V.s as the film thickness increases from 30 nm to 5000 nm and the corresponding apparent electron concentration values decreased simultaneous from 4.45 x 10^{19} to 1.07 x 10^{19} cm^{-3}. The fast increase in the Hall mobility as thickness

increased from 30 nm to 100 nm is due to the weaker contribution of the low mobility surface/interface charge layer to the overall conductivity of the InN layer. The critical thickness at which both electrical quantities (Hall mobility and apparent electron concentration) begin to saturate is 100 nm.

All the InN films exhibited broad 20K photoluminescence spectra due to high carrier concentration, with similar main emission energy and increasing intensity with thickness. Transmittance measurements on the thicker 1000 - 5000 nm InN films revealed a similar absorption edge at approximately 0.80 eV. The deviation of the absorption edge from the ~0.65 eV bandgap of InN is partially attributed to band-filling effect (Burstein-Moss shift) and shift due to compressive in-plane strain resulting from different thermal expansion coefficients of InN and sapphire.

10.2.2 InN/InAlN heterostructures on (0001) GaN/Al_2O_3 (0001)

The controlled growth of InAlN alloys, with InN mole fraction from 0.13 to 0.80, was demonstrated. Ni-based Schottky contacts were successfully fabricated on 10 nm $In_{0.83}Al_{0.17}N$ (InN-rich alloy) layer grown on GaN (0001) buffer layers. Use of a 1 nm AlN barrier enhancement cap layer demonstrated the best diode, leading to a Schottky contact with ideality factor and barrier height of 2.29 and 0.57 eV, respectively. In general, the extracted barrier height and ideality factor are comparable with those already reported for Schottky diodes on AlN-rich $In_{0.17}Al_{0.83}N$.

The advantage of III-nitride band gap engineering between 0.65 eV for InN to 6.2 eV for AlN allows the InAlN to be used as barrier layer and the low bandgap InN material as quantum well layer (channel) for InN-based HEMT heterostructures. An exploratory study was carried out for the growth of InN/InAlN heterostructures on *c*-plane GaN pseudo-substrates, with the main objective of evaluating the potential of developing InN based HEMT transistors. Barrier and cap layers employed consisted of InAlN, InGaN, AlN and GaN. The use of an InN/GaN Multi-Quantum well (MQW) as channel layer was also investigated. Flat and abrupt interfaces were demonstrated by all the heterostructures, according to the theta-2theta symmetric scans. The electron sheet carrier density and Hall mobility of 6.03 x 10^{13} cm^{-2} and 300 $cm^2V^{-1}sec^{-1}$ were achieved, respectively, which are relatively higher than the best values of 2.6 x 10^{13} cm^{-2} and 209 cm^2/Vs reported to date for InN-based heterojunction field-effect transistors.

10.3 InN on sapphire *r*-plane ($1\bar{1}02$) substrates

10.3.1 The role of buffer layer on InN growth on *r*-plane sapphire

The experiments of InN growth on *r*-plane ($1\bar{1}02$) Al_2O_3 substrates revealed that different InN crystallographic orientations could be realized depending on the InN nucleation conditions. Single crystal cubic (001) InN was grown on *r*-plane sapphire by using one-step growth at ~ 400°C with stoichiometric III/V flux ratio, while polar *c*-plane (0001) or semipolar *s*-plane ($10\bar{1}1$) InN were observed by using a two-step growth process with InN nucleation at low temperature under N-rich or near stoichiometric III/V flux ratio conditions, respectively. Pure *a*-plane ($11\bar{2}0$) InN films were realized only when *a*-plane GaN or AlN nucleation-buffer layers were initially grown on *r*-plane sapphire.

10.3.2 Growth of *a*-plane InN grown on *r*-plane sapphire

The growth of *a*-plane InN proceeds in 3D growth mode, resulting to increasing surface roughness with increasing film thickness from 50 to 1000 nm. However, thicker films (e.g 3 μm thick may exhibit improved surface smoothness. This indicates that epitaxial growth of *a*-plane InN may eventually follow a 2D growth mode and the film's surface roughness is mainly limited by initially nucleated and coalesced 3D InN islands. Anisotropic features of surface roughness were not observed in the films, and this is attributed to equivalent diffusivity of the In adatoms along the [0001] and $[1\bar{1}00]$ directions.

Similarly to *c*-plane InN, the structural and electrical properties of *a*-plane InN films improve with increase in growth temperature. A growth window of about 370°C - 420°C, which is slightly lower than that for *c*-plane InN, has been proposed for the epitaxy of *a*-plane InN without InN decomposition.

Investigation of the role of III/V flux ratio from 0.4 to 1 revealed that the surface morphology improves with increasing III/V flux ratio. A stoichiometric or slightly In-rich III/V flux ratio corresponds to the ideal growth conditions for best crystalline quality *a*-plane InN. Intermittent nitridation of the InN surface during growth caused a slight structural degradation in the properties of *a*-plane InN film but offered an improvement of the surface morphology by significantly reducing the 10 x 10 μm^2 AFM rms roughness of 1 μm thick *a*-plane InN films from 10 nm to 2.6 nm.

Moreover, the presence of anisotropy in the structural properties of *a*-plane InN, along the in-plane [0001] and $[1\bar{1}00]$ directions, appears to depend on the type (GaN or AlN) of the used buffer layer and the films exhibited significant structural anisotropy only when an AlN nucleation layer was used. This behaviour is attributed to differences in the introduction of defects for lattice mismatch relaxation at the different hetero-interfaces. However, such a 500 nm film exhibited the highest electron mobility of 630 cm^{2}V^{-1}s^{-1} with a bulk electron concentration of 1.24 x10^{19} cm^{-3}. The lowest FWHM of XRD $(11\bar{2}0)$ rocking curves was 0.40° for a non-anisotropic 1 μm InN film grown on a GaN buffer layer. To the best of our knowledge, these are the best results obtained for *a*-plane InN films even comparing with growth on free-standing *a*-plane GaN substrates.

Overall, the use of a low thickness GaN buffer layer (35 nm) resulted to an *a*-plane InN film that demonstrated the lowest surface roughness, comparably good electrical characteristics, strongest PL and lack of in-plane structural anisotropy. This thin GaN buffer layer is regarded as the optimum for *a*-plane InN growth on *r*-plane sapphire.

TEM investigation of the microstructure of a 500 nm *a*-plane InN film grown on *r*-plane sapphire, using the optimized thin GaN buffer layer, revealed a threading dislocation (TD) density of ~10^{11} cm^{-2}, about two orders of magnitude higher than that obtained for *c*-plane InN. The structural quality of the *a*-plane InN films improved with increasing epilayer thickness as a result of interactions and annihilation of defects. The higher TD density in the *a*-plane InN films is considered responsible for the reduced electron mobility values in *a*-plane InN.

10.3.3 Thickness dependent electrical properties of *a*-plane InN

A comparative study of the thickness dependent electrical properties of *a*-plane InN films grown on *r*-plane Al_2O_3 and *c*-plane InN films grown on GaN/Al_2O_3 (0001) pseudo-substrates, which corresponds to the state-of-the-art InN material, was carried out by room temperature Hall-effect measurements. For both InN orientations, a rather linear increase of the measured electron sheet density (N_{Smeas}) with increasing thickness, consistent with a constant bulk concentration around 1 x 10^{19} cm^{-3}, was observed. The measured electron mobility (μ_{meas}) improved monotonically with increasing thickness of the *a*-plane InN films, and varied from 144 to 500 cm^2/Vs as the thickness increased from 50 nm to 2 μm. Moreover, we observed the same trend for the variation of N_{Smeas}, μ_{meas} and the apparent electron concentration (N_{ap}) versus InN thickness for both the *a*- and *c*-plane InN films. However, the electron mobilities of the *c*-plane InN films were more than three times those of the *a*-plane films, attributed to the presence of significantly higher dislocation density in the *a*-plane InN films. The analysis of the Hall-effect measurements, by considering the contribution of two conducting layers, indicates a similar accumulation of low mobility electrons with $N_S > 10^{14}$ cm^{-2} at the films' surface/interfacial region for both the *a*- and *c*-plane InN films. This result indicates that at least the same defect states are favourable for both surfaces of InN films under exposure to atmospheric air (oxidised InN surfaces).

10.4 InN films on Si (111) substrates

10.4.1 Nucleation and buffer layers for InN on Si (111) heteroepitaxy

In order to optimise the growth of InN films on Si, different intermediate layers comprising of InN, GaN, GaN/AlN and AlN were investigated. The use of GaN/AlN bilayer, prior to the growth of the InN epilayer, resulted to InN films with highly improved surface morphology, structural quality, and electrical properties and excellent interfacial adhesion on Si. Electron concentration and Hall mobility of 1.35 x 10^{19} cm^{-3} and 1210 cm^2/Vs, respectively, were measured for a 2 μm InN film. Moreover, the use of thick (1 μm) GaN buffer layer on the (60 nm) AlN nucleation layer undoubtedly assists to achieve a smooth GaN surface with steps, typical of step-flow growth. The homogeneous nucleation of InN on the smooth GaN surface led to a higher crystal quality InN epilayer and elimination of voids at the InN/GaN interface. TEM study revealed that chemically and structurally sharp InN/GaN interface was achieved on Si. The GaN/AlN buffer/nucleation layer interfaces were effective in reducing the threading dislocation density in the heterostructure by promoting dislocation annihilation interactions. The density of TDs with a *c*-type component and *a*-type component in the InN layer was $8.5x10^9$ cm^{-2} and $4x10^{10}$ cm^{-2}, respectively. Both TD densities were significantly higher in the GaN buffer layer, being $3.5x10^{10}$ cm^{-2} and $8x10^{10}$ cm^{-2}, respectively.

10.4.2 Optimisation of InN nucleation for direct heteroepitaxy on Si (111)

Direct InN growth on Si (111), using the optimum conditions for InN growth on GaN (0001) – substrate temperature 400-450°C and stoichiometric III/V flux ratio-results to 3D growth mode and porous columnar InN epilayers with bad adhesion at the InN/Si interface. A two-step growth process was developed, consisting of nucleating a very thin InN layer on Si at low temperature under N-rich growth

conditions, and the growth of the main epilayer at the optimum InN (0001) growth conditions. The low substrate temperature and excessive N-flux increased the InN nucleation density on the Si surface and full coverage of the substrate surface by coalescence of the InN 3D islands can be achieved at the very early stages of growth, which also limits the extent of unintentional nitridation of the Si surface and formation of an amorphous Si_xN_y interfacial layer. The fast coalescence of the initial 3D islands of InN results to a continuous 20 nm InN film on the Si (111) surface with low 10 x 10 μm^2 AFM rms surface roughness of 0.4 nm, which allows the main epilayer to be overgrown in step-flow growth mode, achieving an atomically smooth surface. The fast coalescence also assists defects annihilation near the InN/Si interface and 0.5 μm films exhibited threading dislocation (TD) density of 4.0x10^9 cm^{-2} for the edge-type and 1.7x10^9 cm^{-2} for the screw-type TDs, which are comparable with reported values for InN grown on GaN/Al_2O_3 (0001) pseudo-substrates. However, in spite of the significant reduction of the TD density in the InN-on-Si film, it exhibits poorer Hall mobility of 784 cm^2/Vs for a carrier concentration of 8.53x10^{18} cm^{-3}, compared to InN films grown on GaN/Al_2O_3 (0001) pseudo-substrates or on Si (111) substrates, using AlN nucleation layer. The deterioration of the electron mobility is consistent with the increased crystal mosaicity of InN films grown directly on Si, as evidenced by higher FWHM values of HRXRD RCs.

10.5 InN Nanopillars on Si (111) and *r*-plane ($1\bar{1}02$) Al_2O_3 substrates

The spontaneous growth of InN nanopillars (NPs) on Si (111) and *r*-plane sapphire substrates was investigated. Optimization of the different growth parameters resulted to well-separated (0001) InN NPs on Si (111) that exhibited photoluminescence. Almost in all cases, the growth rate of the InN NPs along the *c*-axis is multiple of the In-limited growth rate. Non-uniformity of NPs diameter occurs as column height increases, and it is attributed to temperature aided decomposition and diffusion processes in InN NPs that result to migration of In-adatoms from the base region to the top region of NPs at high growth temperature. A non-uniform amorphous Si_xN_y layer was inevitable under unoptimised growth conditions, leading to frequently observed NP misorientation (tilt) on Si substrates. Only *c*-axis oriented InN NPs were formed on the *r*-plane sapphire substrates.

10.6 General conclusion on InN heteroepitaxial growth on different substrates

The InN films exhibited electron concentrations independent from the InN film crystallographic orientation. This suggests that similar surface/interfacial electron accumulation occurs independently of the InN crystallographic orientation, and the bulk donors are not related to the threading dislocations, since significant variations of defect densities occur for the different InN orientations. A SIMS investigation of a *c*-plane InN film exhibiting electron concentration of 1.09 x 10^{20} cm^{-3} excludes hydrogen and silicon as the possible donors since their concentrations were ~ 6.5 x 10^{18} cm^{-3} and ~10^{18} cm^{-3}, respectively. Only oxygen approached a concentration level near 10^{20} cm^{-3} and this might be the unintentionally incorporated donor.

10.7 Possible future works

As far as research on the InN semiconductor is concerned, there are basically three major challenges to overcome at the present time and which could not be handled in this work. These three challenges can be the objectives of future work. First on the list is the problem of surface electron accumulation in all InN films.

The high density (~ 10^{14} cm^{-2}) of electron accumulation at the surface is a major obstacle to overcome for the development of InN-based *pn* junctions for light emitting diodes and solar cells. Inability to obtain electron accumulation free surface from grown non-polar orientation InN films further underscores the difficulty of eliminating this intrinsically charged accumulation layer.

The second challenge concerns the high concentration of unintentionally incorporated donors in the InN crystal. The background electron concentration must be reduced below 10^{17} cm^{-3} to make the controlled *p*-type doping of the material possible. The difficulty is related to the extremely easy incorporation of donor impurities during the InN growth process.

Finally, the third direction of future InN research should deal with the fabrication of InN-based devices that may not need controlled *p*-type doping of the InN layers. This concerns unipolar device applications, such as HEMT transistors and various sensor types that could benefit from the physical and chemical properties of the InN crystal and its surfaces. Bipolar devices may also be considered for InN heterojunctions with other semiconductor that can be controllably doped *p*-type, such as silicon.

Appendices

Appendix 1	Physical parameters of Hexagonal InN, GaN and AlN
Appendix 2	List of peer-reviewed publications in International Journals
Appendix 3	List of peer-reviewed abstracts in International Conferences and Workshops
Appendix 4	List of Invited Talks

Appendix 1

Physical parameters of Hexagonal InN, GaN and AlN

Table I. Recommended values of basic physical parameters of wurtzite InN, AlN, and GaN. Values not referenced were calculated from commonly accepted parameters after Junqiao Wu [J. Appl. Phys. 106, 011101 (2009) and references therein].

Parameter	AlN	GaN	InN
Lattice constant a (T=300 K) (nm)	0.3112[a]	0.3189[a]	0.3533[a]
Thermal expansion $d \ln a/dT$ (10^{-6}/K)	4.2[a]	5.6[a]	3.8[a]
Lattice constant c (T=300 K) (nm)	0.4982[a]	0.5185[a]	0.5693[a]
Thermal expansion $d \ln c/dT$ (10^{-6}/K)	5.3[a]	3.2[a]	2.9[a]
Density (g/cm^3)	3.23[a]	6.15[a]	6.81[a]
Phillips ionicity	0.449[b]	0.500[b]	0.578[b]
Debye temperature (K)	1150[a]	600[a]	660[a]
Melting point (K)	3487[c]	2791[c]	2146[c]
Decomposition temperature (°C)	1040[c]	850[c]	630[c]
Decomposition activation energy (kJ/mol)	414[c]	379[c]	336[c]
Static dielectric constant, $\varepsilon_S/\varepsilon_0$	8.5[a]	8.9[a]	10.5[d]
High-frequency dielectric constant, $\varepsilon_\infty/\varepsilon_0$	4.6[a]	5.4[a]	6.7[e]
Bandgap $E_g(T=0)$ (eV)	6.25[f]	3.51[f]	0.69[g]
Bandgap $E_g(T=300\ \text{K})$ (eV)	6.14[f]	3.43[f]	0.64[g]
Vashni parameter α (meV/K)	1.799[f]	0.909[f]	0.414[g]
Vashni parameter β (K)	1462[f]	830[f]	454[g]
Electron Effective mass at band edge m_e^*/m_0	0.32[f]	0.20[f]	0.07 [h]
Exciton binding energy (meV)	60	34	9
Exciton Bohr radius (nm)	1.4	2.4	8
Mg acceptor binding energy (eV)	0.51[i]	0.17[i]	0.06[j]
Critical point A (eV), $U_3 \rightarrow U_3$		6.36[k]	4.88[k]
Critical point E_1 (eV), $L_{2,4} \rightarrow L_{1,3}$, $M_4 \rightarrow M_{1,3}$	7.97[k]	7.00[k]	5.35[k]
Critical point E_2 (eV), $H_3 \rightarrow H_3$, $M_2 \rightarrow M_1$	8.95[k]	7.96[k]	6.05[k]
Critical point E_3 (eV), $K_{2,3} \rightarrow K_2$		9.25[k]	7.87[k]
A_1(TO) phonon (1/cm)	611[l]	532[l]	447 [l]
A_1(LO) phonon (1/cm)	890[l]	734[l]	586 [l]
E_1(LO) phonon (1/cm)	912[l]	741[l]	593[l]
E_1(TO) phonon (1/cm)	671[l]	559[l]	476[l]
E_2^H phonon (1/cm)	657[l]	568[l]	488[l]
E_2^L phonon (1/cm)	249[l]	144[l]	87[l]

Table II. Physical parameters of wurtzite InN, AlN, and GaN. Values are theoretical except those in parenthesis which are experimental values after Junqiao Wu [J. Appl. Phys. 106, 011101 (2009) and references therein].

Parameter	AlN	GaN	InN
Δ_{cr} (meV)	−169[a]	10[a]	40[a]
Δ_{so} (meV)	19[a]	17[a]	5[a]
$m_e^{\parallel}/m_0$	0.32[b]	0.19[b]	0.065[b]
$m_e^{\perp}/m_0$	0.33[b] (0.29–0.45)	0.21[b] (0.20–0.22)	0.068[b] (0.03–0.085)[c]
$m_A^{\parallel}/m_0$	0.26[a]	1.89[a] (1.76)	1.56[a]
$m_A^{\perp}/m_0$	3.99[a]	0.26[a] (0.35)	0.17[a]
$m_B^{\parallel}/m_0$	3.57[a]	0.44[a] (0.42)	1.54[a]
$m_B^{\perp}/m_0$	0.64[a]	0.33[a] (0.51)	0.17[a]
$m_C^{\parallel}/m_0$	3.54[a]	0.18[a] (0.30)	0.12[a]
$m_C^{\perp}/m_0$	0.64[a]	0.74[a] (0.68)	1.46[a]
A_1	−3.86[a]	−7.21[a]	−8.21[a]
A_2	−0.25[a]	−0.44[a]	−0.68[a]
A_3	3.58[a]	6.68[a]	7.57[a]
A_4	−1.32[a]	−3.46[a]	−5.23[a]
A_5	−1.47[a]	−3.40[a]	−5.11[a]
A_6	−1.64[a]	−4.90[a]	−5.96[a]
A_7 (eV·Å)	0[a]	0.0937[a]	0[a]
Volume deformation potential, a_V (eV)	−10.2[d]	−7.4[d]	−3.7[d]
Bulk modulus, B (kbar)	2158[d] (1850–2079)[b]	2063[d] (1880–2450)[b]	1498[d] (1260–1480)[b]
dE_g/dP (meV/kbar)	4.0[e]–4.2[f] (4.9[g])	3.1[f]–3.9[e] (3.9[h])	1.8[f]–3.3[e] (2.7–3.0)[i]
$E_P^{\parallel}$ (eV)	17.0[j]	17.3[j] (17.8–18.7)[k]	8.7[j]
$E_P^{\perp}$ (eV)	18.2[j]	16.3[j] (16.9–17.8)[k]	8.8[j] 9.7–10[l]
d_{13} (pm/V)	−2.1[a]	−1.6[a]	−3.5[a]
d_{33} (pm/V)	5.4[a]	3.1[a]	7.6[a]
d_{15} (pm/V)	3.6[a]	3.1[a]	5.5[a]
P_{sp} (C/m^2)	−0.090[a]	−0.034[a]	−0.042[a]

Appendix 2

List of peer-reviewed publications in International Journals

1. **InN films and nanostructures grown on Si (111) by RF-MBE**
   A.O. Ajagunna, A. Adikimenakis, E. Iliopoulos, K. Tsagaraki, M. Androulidaki, and A. Georgakilas.
   J. Cryst. Growth 311, 2058-2062 (2009)

2. **Spontaneous growth of III-nitride nanowires on Si by molecular beam epitaxy**
   A.P. Vajpeyi, A. O. Ajagunna, G. Tsiakatouras, A. Adikimenakis, E. Iliopoulos, K. Tsagaraki, M. Androulidaki and A. Georgakilas.
   Microelectronics Engineering 86, 812-815 (2009)

3. **InGaN Nanopillars grown on Silicon substrate using plasma assisted molecular beam epitaxy**
   A.P. Vajpeyi, A. O. Ajagunna, K. Tsagaraki, M. Androulidaki and A. Georgakilas.
   Nanotechnology 20, 325605 (2009)

4. **Microstructure of N-face InN grown on Si (111) by plasma-assisted MBE using a thin GaN-AlN buffer layer**
   G. P. Dimitrakopulos, Th. Kehagias, A. Ajagunna, J. Kioseoglou, I. Kerasiotis, G. Nouet, A. P. Vajpeyi, Ph. Komninou, Th. Karakostas.
   Physica Status Solidi (a) 207(5), 1074 - 1078 (2010)

5. **Epitaxial growth, electrical and optical properties of *a*-plane InN on *r*-plane sapphire**
   A.O. Ajagunna, E. Iliopoulos, G. Tsiakatouras, K. Tsagaraki, M. Androulidaki, and A. Georgakilas.
   J. Appl. Phys. 107, 024506 (2010)

6. **Longitudinal optical phonon energy in InN**
   S. Ardali, E. Tiras, M. Gunes, N. Balkan, A. O. Ajagunna, E. Illiopoulos, and A. Georgakilas
   Physica Status Solidi (c) **8**, 1620-1624 (2011)

7. **Superconductivity in MBE grown InN**
   M. Gunes, N. Balkan, S. Ardali, E. Tiras, A. O. Ajagunna, E. Illiopoulos, and A. Georgakilas
   Physica Status Solidi (c) **8**, 1637-1640 (2011)

8. **Influence of high electron concentration on band gap and effective electron mass of InN**
   Ö. Dönmez, M. Yılmaz, A. Erol, B. Uluğ, M.Ç. Arıkan, A. Uluğ, A. O. Ajagunna, E. Iliopoulos, A. Georgakilas
   Physica Status Solidi (b) **248**, 1172-1175 (2011)

Appendix 3

List of peer-reviewed abstracts in International Conferences and Workshops

1. **Structural anisotropic properties of a-plane (11-20) GaN and InN films grown on *r*-plane sapphire by PAMBE**
   G. P. Dimitrakopulos, A. Lotsari, Th. Kehagias, M. Katsikini, J. Arvanitidis, D. Christofilos, S. Ves, G. Tsiakatouras, A. O. Ajagunna, E. Iliopoulos, and A. Georgakilas, Th. Karakostas, Ph. Komninou
   E-MRS Fall Meeting, Warsaw University of Technology, Warsaw - POLAND, September 2011; Oral

2. **Growth of (0001) GaN films on polycrystalline diamond substrates**
   Adikimenakis, A, Tsiakatouras, G, Ajagunna, A.O., Toth, L, Pécz, B, Dynowska, E, Kaminska, E, Tsagaraki, K, Androulidaki, M, Aretouli, K.E., Georgakilas, A.
   9th International Conference on Nitride Semiconductors (ICNS-9), SECC, Glasgow - UNITED KINGDOM, July 2011; Oral

3. **Structural characterization of nonpolar *a*-plane InN grown on *r*-plane sapphire by MBE**
   A. Lotsari, G. P. Dimitrakopulos, Th. Kehagias, A. O. Ajagunna, E. Iliopoulos, A. Georgakilas, and Ph. Komninou
   9th International Conference on Nitride Semiconductors (ICNS-9), SECC, Glasgow - UNITED KINGDOM, July 2011; Poster

4. **Formation of single-crystal semipolar $(10\bar{1}1)$ InN and polar (0001) InN heterostructures on *r*-plane sapphire**
   A.O. Ajagunna, K. Tsagaraki, A. Lotsari, G. P. Dimitrakopulos, Th. Kehagias, M. Androulidaki, Ph. Komninou, and A. Georgakilas,
   Fourth International Conference on Micro-Nanoelectronics, Nanotechnologies and MEMs (Micro&Nano2010), NCSR Demokritos, Athens – GREECE, December 2010; Poster

5. **Nucleation, growth and microstructure of hexagonal InN with atomically smooth surface on Si (111)**
   A. O. Ajagunna, A. Lotsari, Th. Kehagias, K. Tsagaraki, M. Androulidaki, M. Kayambaki, Ph. Komninou, and A. Georgakilas
   Fourth International Conference on Micro-Nanoelectronics, Nanotechnologies and MEMs (Micro&Nano2010), NCSR Demokritos, Athens – GREECE, December 2010; Oral

6. **Properties of InN films grown on *r*-plane Al_2O_3 by PAMBE**
   A. O. Ajagunna, E. Iliopoulos, A. Lotsari, G. P. Dimitrakopulos, G. Tsiakatouras, K. Tsagaraki, M. Androulidaki, Ph. Komninou, and A. Georgakilas
   19th European Workshop on Heterostructure Technology (HETECH 2010), Fodele Beach-Crete, GREECE, October 2010; Poster

7. **Non-destructive determination of heteroepitaxial InN layer bulk conductivity using FTIR Spectroscopy**
   C. C. Katsidis, A. O. Ajagunna, and A. Georgakilas,
   19th European Workshop on Heterostructure Technology (HETECH 2010), Fodele Beach-Crete, GREECE, October 2010; Oral

8. **Microscopy of GaN grown on diamond**
   B. Pecz, L. Toth, A. Barna, G. Tsiakatouras, A. O. Ajagunna and A. Georgakilas, 19th European Workshop on Heterostructure Technology (HETECH 2010), Fodele Beach-Crete, GREECE, October 2010; Oral

9. **Molecular beam epitaxy of *a*-plane and *s*-plane InN films on *r*-plane sapphire**
   A. O. Ajagunna, E. Iliopoulos, G. P. Dimitrakopulos, A. Lotsari, G. Tsiakatouras, K. Tsagaraki, M. Androulidaki, Th. Kehagias, Ph. Komninou, and A. Georgakilas,
   The 3rd International Symposium on Growth of III-Nitrides (ISGN3), Montpellier, FRANCE, July 2010; Poster

10. **Bandgap and Optical Properties of InAlN Films Lattice Matched to GaN Grown By MOCVD and RF-MBE**
    E. Iliopoulos, A. Adikimenakis, M. Andoulidaki, A.O. Ajagunna, M. Heuken, C. Giesen, J.F. Carlin, M.A. di Forte-Poisson, S.L. Delage, Th. Kehagias, Ph. Komninou, A. Georgakilas,
    The 3rd International Symposium on Growth of III-Nitrides (ISGN3), Montpellier, FRANCE, July 2010; Poster

11. **Scattering analysis of 2D electron gas in undoped GaN/InN/GaN**
    M. Gunes, N. Balkan, O. Donmez, A. Erol, A. O. Ajagunna, E. Illiopoulos, A. Georgakilas and R. Airey
    E-MRS Spring Meeting, Strasbourg, FRANCE, June 2010; Oral

12. **Superconductivity in MBE grown InN**
    M. Gunes, N. Balkan, S. Ardali, E. Tiras, A. O. Ajagunna, E. Illiopoulos, and A. Georgakilas
    E-MRS Spring Meeting, Strasbourg, FRANCE, June 2010; Poster

13. **Longitudinal optical phonon energy in InN**
    S. Ardali, E. Tiras, M. Gunes, N. Balkan, A. O. Ajagunna, E. Illiopoulos, and A. Georgakilas
    E-MRS Spring Meeting, Strasbourg, FRANCE, June 2010; Oral

14. **Influence of high electron concentration on band gap and effective electron mass of InN**
    Ö. Dönmez, M. Yılmaz, A. Erol, B. Uluğ, M.Ç. Arıkan, A. Uluğ, A. O. Ajagunna, E. Iliopoulos, A. Georgakilas
    E-MRS Spring Meeting, Strasbourg, FRANCE, June 2010; Poster

15. **Heteroepitaxial growth of *a*-plane InN films on *r*-plane sapphire by RF-MBE**
    A. O. Ajagunna, G. Tsiakatouras, E. Iliopoulos, K. Tsagaraki, M. Androulidaki and A. Georgakilas
    The 5th International Conference of the African Materials Research Society (IC-AMRS) & 8th Nigerian Materials Congress (NIMACON-2009), Abuja, NIGERIA, December 2009; Oral

16. **High quality (0001) GaN films grown on diamond substrates by molecular beam epitaxy**
    G. Tsiakatouras, A. O. Ajagunna, K. Tsagaraki, M. Androulidaki and A. Georgakilas;
    The 5th International Conference of the African Materials Research Society (IC-AMRS) & 8th Nigerian Materials Congress (NIMACON-2009), Abuja, NIGERIA, December 2009; Oral

17. **Molecular beam epitaxy of *a*-plane InN films on *r*-plane sapphire**
Adebowale O. Ajagunna, Georgios Tsiakatouras, Eleftherios Iliopoulos, Katerina Tsagaraki, MariaAndroulidaki, and Alexandros Georgakilas
8th International Conference on Nitride Semiconductors (ICNS-8), ICC Jeju, KOREA, October 2009; Oral

18. **High Quality (0001) GaN Films Grown on Diamond Substrates by Molecular Beam Epitaxy**
Alexandros Georgakilas, Georgios Tsiakatouras, Adebowale O. Ajagunna, Katerina Tsagaraki, Maria Androulidaki
8th International Conference on Nitride Semiconductors (ICNS-8), ICC Jeju, KOREA, October 2009; Oral

19. **Bandgap and Optical Properties of InAlN Films Lattice Matched to GaN**
E. Iliopoulos, A. Adikimenakis, M. Andoulidaki, A. O. Ajagunna, M. Heuken, C. Giesen, J. F. Carlin, M. A. di Forte-Poisson, S. L. Delage, Th. Kehagias, Ph. Komninou, A. Georgakilas
8th International Conference on Nitride Semiconductors (ICNS-8), ICC Jeju, KOREA, October 2009; Poster

20. **High quality (0001) GaN films grown on diamond substrates by molecular beam epitaxy**
Alexandros Georgakilas, Georgios Tsiakatouras, Adebowale O. Ajagunna, Katerina Tsagaraki, and Maria Androulidaki
E-MRS Fall Meeting, Warsaw University of Technology, POLAND, September 2009; Oral

21. **Thickness dependence of electrical properties of *c*- and *a*-plane InN films**
Adebowale O. Ajagunna, Eleftherios Iliopoulos, Katerina Tsagaraki, George Tsiakatouras, and Alexandros Georgakilas
E-MRS Fall Meeting, Warsaw University of Technology, POLAND, September 2009; Poster

22. **Microstructure of InN grown on Si (111) by plasma-assisted MBE using a double buffer layer**
George P. Dimitrakopulos, Thomas Kehagias, Adebowale Ajagunna, Joseph Kioseoglou, Gerard Nouet, Iordanis Kerasiotis, Alexandros Georgakilas, Theodoros Karakostas, and Philomela Komninou
E-MRS Fall Meeting, Warsaw University of Technology, POLAND, September 2009; Oral

23. **Nanostructured and Bulk III-Nitride Semiconductors in Electrochemical Sensors and Biosensors**
N. Sofikiti, J. Grandal, M. Utrera, M. Sanchez-Garcia, E. Calleja, G. Tsiakatouras, E. Iliopoulos, D. Ajagunna, A. Georgakilas, N. Chaniotakis
Nanotech Conference & Expo 2009, Houston, TX, USA, May 2009; Poster

24. **Spontaneous growth of InN, GaN and InGaN [0001] nanopillars by plasma-assisted molecular beam epitaxy**
A. Georgakilas, A. P. Vajpeyi, A. O. Ajagunna, K. Tsagaraki, M. Androulidaki and E. Iliopoulos
PDI Topical Workshop on MBE-grown Nitride Nanowires, Paul-Drude-Institut für Festkörperelektronik, Berlin – GERMANY, March 2009; Oral

25. **Study of capabilities and limitations of the AlN/GaN HEMT material system**
A. Adikimenakis, M. Alomari, E. Kohn, K. Aretouli, A. Kostopoulos, E. Iliopoulos, K. Tsagaraki, A. O. Ajagunna, G. Konstantinidis and A. Georgakilas
International Workshop on Nitride Semiconductors (IWN 2008), Montreux – SWITZERLAND, October 2008; Poster

26. **High electron mobility transistors based on the AlN/GaN heterojunction**
A. Adikimenakis, M. Alomari, E. Kohn, K. Aretouli, A. Kostopoulos, E. Iliopoulos, K. Tsagaraki, A. Ajagunna, G. Konstantinidis and A. Georgakilas
34th International conference on Micro and Nano Engineering (MNE 2008), Athens – GREECE, September 2008; Poster

27. **Spontaneous growth of III-nitride nanowires on Si by molecular beam epitaxy**
A. P. Vajpeyi, A. O. Ajagunna, G. Tsiakatouras E. Iliopoulos, K. Tsagaraki, and M. Androulidaki and A. Georgakilas
34th International conference on Micro and Nano Engineering (MNE 2008), Athens – GREECE, September 2008; Poster

28. **InN films and nanostructures grown on Si (111) by RF-MBE**
Ajagunna A. O., Adikimenakis A., Iliopoulos E., Tsagaraki K., Androulidaki M., and Georgakilas A.
International Conference on Molecular Beam Epitaxy (MBE 2008), University of British Columbia, Vancouver – CANADA, August 2008; Poster

29. **Molecular beam epitaxy of InN directly on Si (111) substrates**
A. O. Ajagunna, A. Vajreyi, E. Iliopoulos, K. Tsagaraki, M Androulidaki, and A. Georgakilas.
Third international Conference on Micro-Nanoelectronics, Nanotechnology and MEMs, NCSR "Demokritos", Athens – GREECE, November 2007, Poster

30. **Indium Nitride: A new material extending the capability of Solar Cells**
A. O. Ajagunna, E. Iliopoulos, K. Tsagaraki, and A. Georgakilas
30th Annual Conference of the Nigerian Institute of Physics, Lagos State University (LASU), NIGERIA, August 2007; Oral

Appendix 4

List of Invited Talks

1. **"Heteroepitaxial growth of *a*-plane InN films on *r*-plane sapphire by RF-MBE"**
   The 5th International Conference of the African Materials Research Society (IC-AMRS) & 8th Nigerian Materials Congress (NIMACON-2009), Abuja, NIGERIA [13-18 December, 2009]

2. **"The Growth and Properties of InN Heterostructures-Nanostructures"**
   Engineering Materials and Development Institute, Akure (EMDI) & Physics Department, Federal University of Technology, Akure, NIGERIA [07 January, 2009]

3. **"The Growth and Properties of InN Heterostructures-Nanostructures"**
   Obafemi Awolowo University (OAU), Ile-Ife, NIGERIA [06 January, 2009]

4. **"The Growth and Properties of InN Heterostructures-Nanostructures"**
   National Agency for Science and Engineering Infrastructure (NASENI), Abuja, NIGERIA [17 December, 2008].